UNIVERSITÀ DEGLI STUDI DI PARMA
DIPARTIMENTO DI FISICA

Crystal field and vibrational spectroscopy of rare earths in glasses and crystals for photonics

Elisa Buffagni

Thesis submitted for the award of the degree of Ph.D. in Physics
Dottorato di Ricerca in Fisica

Supervisor: Prof. Rosanna Capelletti

XXII Ciclo – Gennaio 2010

A Nicola

INDEX

Introduction 5

1 Theoretical Models

- 1.1 Rare Earths 7
- 1.2 Free ion.. 8
  - 1.2.1 Central field approximation... 8
  - 1.2.2 Perturbative potentials 9
- 1.3 Crystal field (CF).. 11
  - 1.3.1 Expansion of the CF potential 13
  - 1.3.2 Equivalent operator method... 14
- 1.4 Newman’s superposition model 16
- 1.5 Hyperfine interaction.. 17
- 1.6 Line shape... 20
  - 1.6.1 Non-radiative processes.. 22
    - 1.6.1.1 Single phonon processes.. 22
    - 1.6.1.2 Raman processes 23
    - 1.6.1.3 Orbach processes... 25
    - 1.6.1.4 Multiphonon processes.. 25
  - 1.6.2 Line broadening... 25

1.6.3 Line shift 28
1.7 Vibronic transitions 29

2 BaY_2F_8 single crystals

2.1 Introduction 33
2.2 Experimental details 36
2.3 Experimental results 37
2.3.1 Anisotropy 37
2.3.2 Temperature dependence 40
2.3.3 Specific-heat measurements 41
2.4 Discussion 42
2.4.1 Line attribution and crystal field parameters 42
2.4.1.1 Tm^{3+} 44
2.4.1.2 Ho^{3+} 48
2.4.2 Linear dichroism 54
2.4.3 RE^{3+}-local mode interaction 60
2.4.4 Hyperfine structure 70
2.5 Conclusion 72

3 YPO_4 single crystals

3.1 Introduction 75
3.2 Experimental details 77
3.3 Experimental results 78
3.3.1 Temperature dependence 78
3.4 Discussion 83
3.4.1 Line attribution and crystal field parameters 84
3.4.2 Hyperfine structure 93
3.5 Conclusion 100

4 $YAl_3(BO_3)_4$ single crystals

4.1 Introduction 103
4.2 Experimental details 105

4.3 Experimental results ... 106
4.3.1 Anisotropy ... 106
4.3.2 Temperature dependence ... 109
4.4 Discussion ... 111
4.4.1 Line attribution and crystal field parameters ... 111
4.4.2 Linear dichroism ... 118
4.4.3 Electron-phonon interaction ... 121
4.4.4 Fine structure ... 124
4.5 Conclusion ... 126

5 Silica glasses

5.1 Introduction ... 129
5.2 Experimental details ... 130
5.3 Experimental results ... 135
5.3.1 Ce^{3+} doped samples ... 135
5.3.2 Gd^{3+} doped samples ... 137
5.3.3 Ce^{3+}-Gd^{3+} co-doped samples ... 140
5.3.4 Tb^{3+} doped samples ... 142
5.3.5 Yb^{3+} doped samples ... 144
5.3.6 Eu^{3+} doped samples ... 147
5.3.7 TEM and EDS measurements ... 153
5.4 Discussion ... 156
5.4.1 Crystal field spectra ... 156
5.4.2 OH^- and related species ... 160
5.4.2.1 OH^- concentration ... 160
5.4.2.2 Other features ... 164
5.4.3 Vibrational modes ... 167
5.4.3.1 Microreflectivity spectra ... 168
5.4.3.2 IR absorption spectra ... 172
5.5 Conclusion ... 179

6 Conclusions ... 181

Appendix

1 Fourier transform spectroscopy 185
  1.1 Fourier Transform spectrophotometer Bomem DA8 188
  1.2 Accessories 190
    1.2.1 Cryocooler 190
    1.2.2 Polarizer 190
    1.2.3 Microscope 191
2 Other experimental techniques 191
  2.1 Specific-heat measurements 191
  2.2 Luminescence measurements 191
  2.3 AFM measurements 192
  2.4 TEM measurements 192
3 The new polarizer holder 192

References 195

Acknowledgements 203

Publications 205

INTRODUCTION

Rare earth (RE) ions embedded in insulating crystals are characterized by very narrow absorption and emission lines; thus, they can be exploited as microscopic probes sensitive to the environment. In particular, they allow to study the crystal field (CF) interaction, as well as that between different RE's, or RE-impurity, RE-lattice, and the hyperfine one. The knowledge of such interactions, combined with that of other fundamental aspects, as the energy level scheme, is the necessary background to understand and exploit the material optical properties for applications in photonics.

Crystal matrices with large transparency range deserve particular interest. More in details, among the materials analyzed in the present work yttrium fluoride (BaY_2F_8) doped with RE^{3+} ions may work as active systems for new generation lasers emitting in the 2-4 μm range, i.e. in a surgery useful eye-safe region. Yttrium aluminum borate $YAl_3(BO_3)_4$ (YAB) crystals doped with RE^{3+} are good candidates for applications in photonics as materials which exhibit non-linear optical phenomena as self-frequency doubling or self-frequency summing. Although yttrium orthophosphate YPO_4 is a widely investigated material (it has proved to be important for many applications in the field of optical materials and devices), the Ho^{3+} doped one is an almost new material: no very detailed study have appeared in the literature. In all the above crystals the RE^{3+} ion substitutes for the homovalent Y^{3+}, thus the charge compensation is not required: as a consequence a high doping level can be achieved without inducing substantial structural changes. Moreover, since the sizes of the RE^{3+} ions are comparable to those of Y^{3+}, mechanical mismatch is limited (except for Pr^{3+}). The investigated matrices are characterized by rather low crystal symmetries (monoclinic for BaYF, tetragonal for YPO_4, and trigonal for YAB) which, probed by the RE^{3+}, give rise to a variety of often very complex spectra patterns.

In spite of the broader absorption lines induced by the structural disorder, typical of glasses, the spectroscopy supplies valuable information about the nature of the RE^{3+}-related nanoclusters (both ordered and amorphous, Section 5.4.1) and about host matrix modifications caused by doping (Section 5.4.3). In the last decade the research is moving towards the study of nanocomposite materials where the active phase is composed of RE-rich aggregates with dimensions of a few tens of nanometers or less, but the real use of this kind of materials as scintillators requires further investigations. Owing to this, the SiO_2: RE^{3+} (RE=Ce, Gd, Tb, Yb, Eu) glasses are studied as a function of different RE^{3+} doping levels and thermal treatments. The interaction of RE^{3+} with OH^-, an impurity common in sol-gel glasses and responsible for the unwanted luminescence quenching, is also considered (Section 5.4.2).

The main experimental tool applied in the present work is the high resolution (as fine as 0.01 cm^{-1}) Fourier transform absorption spectroscopy in wide wave number (200-25000 cm^{-1}) and temperature (9-300 K) ranges. Complementary techniques (microreflectance, linear dichroism, specific heat, photoluminescence, TEM, EDS, and AFM measurements) were employed to provide a more complete and sound description of the investigated phenomena (see Appendix). The results are discussed in the framework of theoretical models briefly summarized in Chapter 1.

The preliminary necessary step is the determination of the RE^{3+} manifold CF splitting achieved by analyzing the spectra collected as a function of temperature, sample orientation, and incident light polarization (Sections 2.4.1, 3.4.1, and 4.4.1). The experimental energy level fitting according to a single-ion Hamiltonian model supplies a valuable support to unravel the complex energy level scheme originated by the line rich spectra.

On this basis, much finer effects can be investigated, such as the hyperfine (Sections 2.4.4, 3.4.2, and 4.4.4) and roto-electronic (Section 2.4.3) structures exhibited by specific RE^{3+} in crystalline matrices, and the identification of orientations of dipole moments associated with a few transitions (Sections 2.4.2 and 4.4.2).

1 THEORETICAL MODELS

1.1 RARE EARTHS

The Rare Earths (RE), or Lanthanides, are metallic chemical elements with atomic number from 58 (Cerium) to 71 (Lutetium). Their preferential oxidation state is RE^{3+}. Rare earth ions in crystals exhibit spectra which are very similar to free ion spectra, because the shell 4*f*, which can be progressively filled by increasing the atomic number, is shielded from the environment by the outer complete shells.

The RE^{3+} show sharp and narrow emission and absorption bands in the spectral ranges of interest for photonics, thus they are extensively investigated as active ions for solid state lasers and scintillators. Moreover, the very narrow lines allow to use the RE^{3+} as extremely sensitive probes to study microscopic interactions in solids.

A detailed picture of the RE electronic structure is a necessary requirement to understand their absorption spectra. Theoretical models allow predicting the behaviour of the ion embedded in the matrix, but the free ion should be considered before.

1.2 FREE ION

The first approximation is to neglect the contribution of the electrons belonging to the complete shell.

The following sections will particularly refer to Ref. [1].

1.2.1 Central field approximation

The Hamiltonian of an atom with nuclear point charge Ze and N electrons in the incomplete shell is

$$H = \sum_{i=1}^{N}\left(\frac{p_i^2}{2m} - \frac{Ze^2}{r_i}\right) + \sum_{i>j=1}^{N}\frac{e^2}{r_{ij}} \qquad 1.1$$

where m is the electron mass, p_i the i^{th} electron momentum, r_i and r_{ij} the distances from nucleus and j-electron, respectively.

The first term in the right member of eq. 1.1 represents the system kinetic energy, the second one the electron-nucleus interaction energy, and the last one the electron-electron repulsion.

Since the last term does not allow the variable separation in the Schrödinger equation $H\psi = E\psi$, the first step is to consider electrons under the influence of the nucleus and a mean charge distribution producing the mean potential $-U(r_i)/e$ with central symmetry.

In accordance with the central field approximation, the unperturbed Hamiltonian is

$$H_0 = \sum_{i=1}^{N}\left(\frac{p_i^2}{2m} + U(r_i)\right). \qquad 1.2$$

The corresponding Schrödinger equation has eigenfunctions and eigenvectors like

$$\psi_0 = \prod_{i=1}^{N}\psi_{0k_i}(r_i),\ E_0 = \sum_{i=1}^{N}E_{0k_i} \qquad 1.3$$

where k_i is the set of quantum numbers (n_i l_i m_i) of the i^{th} electron.

Due to the potential r dependence, the ψ_{0k} differ from the hydrogen wavefunctions only in the radial part:

$$\psi_{0k}(\underline{r}) = \frac{1}{r} R_{nl}(\underline{r}) Y_{lm}(\theta, \varphi) \tag{1.4}$$

where Y_{lm} are the spherical harmonics and $R_{nl}(r)$ depend on $U(r)$; the eigenstates ψ_{0k} are degenerate with respect of m.

If the spin electron is considered, the Slater determinantal eigenfunctions should work as H_0 eigenstates; as a result, the quantum number set K_j includes also the spin σ_i and

$$\psi_{K_j}(\underline{r_i}) = \psi_{k_j}(\underline{r_i}) \sigma_i . \tag{1.5}$$

The eigenvectors E_{0k} are then degenerate with respect to m and σ.

1.2.2 Perturbative potentials

As a rule, a large number of states with the same unperturbed energy E_0 corresponds to a given configuration. This degeneracy is partially removed by the perturbative potential

$$H - H_0 = \sum_{i=1}^{N} \left(-\frac{Ze^2}{r_i} - U(r_i) \right) + \sum_{i>j=1}^{N} \frac{e^2}{r_{ij}} . \tag{1.6}$$

The first term of the right member can be neglected because it corresponds only to an energy shift (incorporated in the unperturbed Hamiltonian). The real perturbative potential is then

$$H_1 = \sum_{i>j=1}^{N} \frac{e^2}{r_{ij}} . \tag{1.7}$$

The relativistic corrections to the Hamiltonian H can be introduced, in the low electron velocity limit, with the additional spin-orbit term

$$H_{SO} = \sum_i \xi(r_i) \underline{s}_i \cdot \underline{l}_i \tag{1.8}$$

where

$$\xi(r) = \frac{\hbar^2}{2m^2c^2r}\frac{dU}{dr} \qquad 1.9$$

is the spin-orbit coupling coefficient, while $\underline{l}$ and $\underline{s}$ are the angular and spin momenta in $\hbar$ units, respectively. This term expresses the interaction between magnetic field associated with the angular orbital momentum and the spin magnetic dipole.

The total spin momentum $\underline{S}$ and the total orbital momentum $\underline{L}$, defined as

$$\underline{S} = \sum_i \underline{s}_i\,,\ \underline{L} = \sum_i \underline{l}_i\,, \qquad 1.10$$

commute with H_1; then, the eigenvectors of H_0+H_1 are M_L and M_S independent, and their degeneracy is $(2L+1)(2S+1)$.

A set of states belonging to the same eigenvector (then, characterized by a fixed pair SL) is called *term*; the terms are labelled as $^{(2S+1)}L$, where a capital letter is associated with each L value in this way:

L = 0, 1, 2, 3, 4, …
S, P, D, F, G, …

On the other hand, the spin-orbit interaction H_{SO} commutes with the total angular momentum $\underline{J}=\underline{L}+\underline{S}$.

If H_{SO} is negligible, the bases expressed by $|S\ L\ M_S\ M_L>$ and $|S\ L\ J\ M_J>$ are equivalent and it is possible to move from one to the other with the Clebsh-Gordan coefficients. The $\underline{J}$ eigenvalue system is a good basis for H_{SO}, because H_{SO} couples only states with the same J, even belonging to different terms.

Three cases are possible:

1. $H_{SO} << H_1$: H_{SO} gives rise to negligible splittings compared with the energy separations between different spectroscopic terms; so the spin-orbit interaction can be assumed to operate only on a single state with fixed $\underline{L}$ and $\underline{S}$. Then, it can be written as

   $$H_{SO} = \Lambda \underline{L}\cdot\underline{S}\,. \qquad 1.11$$

   It originates a further splitting of the manifolds characterized by J values ranging from $|L\text{-}S|$ to $L+S$ (the new notation is $^{(2S+1)}L_J$) and the residual degeneracy is M_J.

The ground level has $J=|L-S|$ if the shell is less than half-full; it has $J=L+S$ if the shell is more than half-full.

This is the *Russell-Saunders coupling* (RS).

2. $H_{SO} \cong H_1$: it is better to use the whole matrix H_1+H_{SO} and work on the states $|S\ L\ J\ M_J>$.

   This is the *intermediate coupling* (IC).

3. $H_{SO} >> H_1$: it is better to couple the s_i and l_i to each other and then combine the resulting j_i:

$$\underline{J} = \sum_i \underline{j}_i = \sum_i \left(\underline{s}_i + \underline{l}_i \right). \tag{1.12}$$

   This is the *j-j coupling*.

1.3 CRYSTAL FIELD (CF)

When the atom is embedded in a crystalline solid, the surrounding effect on the electronic structure should be considered. This is done in the framework of the Crystal Field Theory (CFT) [1], which is based on two hypotheses:

1. the electrons are localized on the ions, so that the crystal potential can be assumed as a perturbation on the free ion electronic configuration;
2. the neighbouring ion effect is one-body purely electrostatic potential as

$$H_{CF} = -e\sum_i V\left(r_i, \theta_i, \varphi_i\right) \tag{1.13}$$

   where the sum is on the central ion electrons.

This approach is proper for impurities embedded in crystals, and in particular when the impurity is a RE because the 4*f* shell has atomic character.

The crystal field always reflects the local site symmetry in which the ion is placed. This allows, sometimes, an important calculus simplification and the application outside the point charge model.

The CF modifies the electron energy levels in the 4*f* shells depending on the H_{CF} intensity with respect to other H terms.

Three cases are possible:

1. WEAK FIELD

   The CF energy is lower than the splitting between two spin-orbit manifolds $|S\ L\ J\ M>$ and $|S\ L\ J'\ M'>$, and the field removes partially or completely the $2J+1$ degeneracy. J is a good quantum number. The RE and actinides can be studied in this framework due to two facts: the shield on the incomplete $4f$ shell by the external ones and the large separation from the nearest neighbours thanks to the wide spatial distribution of the outer orbitals.

2. INTERMEDIATE FIELD

   The interaction with the CF is stronger than the spin-orbit coupling, then the manifold structure with assigned J vanishes (J is no longer a good quantum number). In accordance with the perturbative theory, the CF effect on a $|S\ L\ M_S\ M_L>$ state should be considered before introducing the spin-orbit coupling. S and L are good quantum number.

3. STRONG FIELD

   The CF energy is higher than the electronic repulsion. L is no longer a good quantum number and CF works directly on a single electron state. New orbitals and a new configuration, called *crystal field configuration*, will result. The electron-electron interaction is introduced as a further perturbation.

In the weak field approximation, the Kramers theorem plays an important role; it states that the electronic levels of a system with an odd number of electrons, even in a low symmetry crystal field, are twofold. Each state is then called *Kramers doublet* (Figure 1.1).

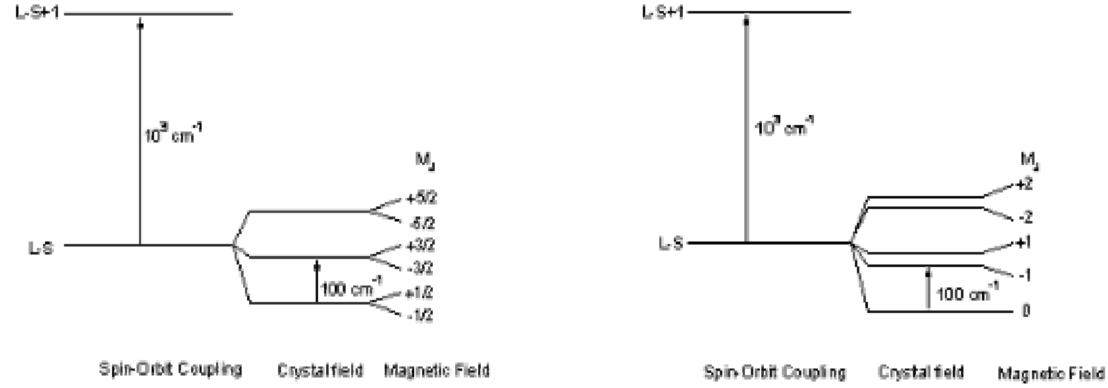

a. Kramers ion

b. non-Kramers ion

Figure 1.1 Energy level diagram for a Kramers (a) and a non-Kramers (b) ion in a weak crystal field.

This degeneracy is due to the system invariance by time reversal; in fact, the application of an external magnetic field, which introduces in the Hamiltonian a term that changes sign by time reversal, lifts the Kramers degeneracy.

1.3.1 Expansion of the CF potential

Due to the point charge approximation, the potential in 1.13 can be written as

$$V(r_i) = -\sum_{k=1}^{N} \frac{Z_k e}{\left|\underline{R}_k - \underline{r}_i\right|} \tag{1.14}$$

where N is the number of ligands, $\underline{r}_i$ is the i^{th} electron position vector, Z_k and $\underline{R}_k$ are the k-ligand effective charge and position vectors, respectively.

In the point charge approximation the CF potential fulfils also the Laplace equation $\Delta V_i = 0$. This is true if $r_i << R_k$, and $V(r)$ can be expanded into Legendre polynomials. The addition theorem for spherical harmonics allows to write

$$H_{CF} = \sum_{i=1}^{n} \sum_{l=0}^{\infty} \sum_{m=-l}^{l} \tilde{A}_l^m \, r_i^l \, Y_l^m(\theta_i, \varphi_i), \tag{1.15}$$

where the coefficient

$$\tilde{A}_l^m = e^2 \frac{4\pi}{2l+1} \sum_{k=1}^{N} \frac{Z_k \, Y_l^{m*}(\theta_k, \varphi_k)}{R_k^{l+1}} \tag{1.16}$$

can be calculated from the system geometry.

On the basis of the general solution

$$c^l(l'\,m', l''\,m'') = \int d\varphi \, d\theta \sin\theta \, Y_{l''}^{m''}(\theta,\varphi) Y_{l'}^{m'}(\theta,\varphi) Y_l^m(\theta,\varphi) \tag{1.17}$$

and the spherical harmonic properties, the following conditions derive:

- $m = m' - m''$
- $l + l' + l''$ even
- $|l' - l''| \leq l \leq l' + l''$.

In the ordinary case of equal electrons, i.e. $l' = l''$, the last two conditions become:

- l even

- $0 \leq l \leq 2l'$

Thus, it is not necessary to consider each term of the expansion.

As a rule the *tesseral harmonics* are exploited, because they represent the spherical harmonic combinations more often used in the CF potential expansion. The tesseral harmonics are:

$$
\begin{aligned}
&Z_l^0 = Y_l^0 \\
&{}^cZ_l^m = \frac{1}{\sqrt{2}}\left[Y_l^{-m} + (-1)^m Y_l^m\right] \qquad m > 0 \\
&{}^sZ_l^m = \frac{i}{\sqrt{2}}\left[Y_l^{-m} - (-1)^m Y_l^m\right] \qquad m < 0
\end{aligned}
\tag{1.18}
$$

Using them, the eq. 1.15 becomes

$$H_{CF} = \sum_{i=1}^{n} \sum_{\substack{l=2 \\ pari}}^{2l'} \sum_{m=-l}^{l} \tilde{A}_l^m \, r_i^l \, Z_l^m(\theta_i, \varphi_i) \tag{1.19}$$

with

$$\tilde{A}_l^m = e^2 \frac{4\pi}{2l+1} \sum_{k=1}^{N} \frac{Z_k \, Z_l^m(\theta_k, \varphi_k)}{R_k^{l+1}} . \tag{1.20}$$

1.3.2 Equivalent operator method

The direct integration of the matrix element 1.19 is very difficult for many electron atoms: in fact, it works on a fundamental degenerate state which is a Slater determinant combination of single electron functions. Then, it is better to work in the subspaces |*S L M_S M_L*> or |*S L J M*> (as for RE).

The Stevens equivalent operator method allows to easily calculate the matrix elements on these states once *L* or *J* contributions are evaluated.

In the framework of this method, in each term of the potential 1.19 the Cartesian coordinates (*x*, *y*, *z*) are substituted by the homologous $\underline{L}$ or $\underline{J}$ components, and r^2 by *L*(*L+1*) or *J*(*J+1*). Henceforward, only *J* will be considered.

Stevens showed that the new CF operators have elements proportional to the original ones, and that only three proportionality constants are useful: α, β, and γ (*Stevens factors*, afterwards simply labelled as Θ_l for $l = 2, 4, 6$, respectively) for terms of 2nd, 4th, and 6th degree, respectively. The Stevens factors are M independent and they are tabulated.

The equivalent Hamiltonian will be

$$H_{CF} = \sum_{\substack{l=2 \\ pari}}^{2l'} \sum_{m=-l}^{l} B_l^m \hat{O}_l^m \tag{1.21}$$

where

$$B_l^m = A_l^m < r^l > \Theta_l \tag{1.22}$$

are the *crystal field parameters*.

They are expressed according to Wybourne normalization [2] and are usually considered as parameters determined by fitting the optical, neutron, and EPR spectroscopic data. The a priori determination may came from

$$A_l^m = \frac{2l+1}{4\pi} S_l^m \tilde{A}_l^m , \tag{1.23}$$

with tabulated S_l^m and

$$< r^l > = \int \left| R_{n'l'}(r) \right|^2 r^l dr \tag{1.24}$$

integral of r^l (calculated between the single electron wavefunction radial parts), but the result is not always satisfactory.

The $\hat{O}_l^m$ are the *Stevens equivalent operators* and they come from the Cartesian expressions of the tesseral harmonics multiplied by r^l but without numerical coefficient. The matrix elements between different states are tabulated [3].

Thanks to the Wigner-Eckart theorem [4], the formula 1.21 is valid even if the point charge hypothesis does not any longer hold. It is enough to substitute the equivalent operator $\hat{O}_l^m$ with the *tensorial operators* C_Q^K, whose property is to transform as the spherical harmonics of K degree and Q order do.

Whatever the crystal field origin is, the potential 1.13 can be expanded in terms of tensor operators

$$C_Q^K = \left(\frac{4\pi}{2K+1} \right)^{1/2} \sum_{i=1}^{n} Y_K^Q(i) . \qquad 1.25$$

The Hamiltonian is therefore

$$H_{CF} = \sum_{K,Q} B_Q^K \, C_Q^K . \qquad 1.26$$

The expansion of H_{CF} in tesseral harmonics is particularly useful if it operates within manifolds with fixed L or J, while the tensor operator method is better when different manifolds are mixed (*J-mixing*).

1.4 NEWMAN'S SUPERPOSITION MODEL

The Newman's Superposition Model (SPM) is a semi-phenomenological procedure for the calculation of the CF parameters from the position of the nearest neighbours around the considered ion. The so-calculated CF parameters can be compared with those obtained by fitting the experimental energy levels with a single-ion Hamiltonian; this procedure supplies useful information on the active site and its surroundings [5-7]. The three main assumptions of the SPM are:

1. the CF potential at the RE site is exclusively due to the nearest neighbours;
2. it is the sum of individual ligand contributions;
3. the single-ion contributions are cylindrically symmetric around the axis which links the ligand and the central ion.

In this framework, the CF parameters B_Q^K in H_{CF} can be expressed as

$$B_Q^K = N_Q^K \left\langle r^K \right\rangle \sum_i \overline{A}_K\left(R_i\right) K_K^Q\left(\theta_i, \varphi_i\right). \qquad 1.27$$

where K_K^Q are the coordination factors, R_i is the distance between the central ion and the i^{th} ligand, and $\overline{A}_Q^K\left(R_i\right)$ is an intrinsic parameter, whose distance dependence is usually supposed to follow the power low

$$\overline{A}_K\left(R\right) = \overline{A}_K\left(R_0\right)\left(\frac{R_0}{R}\right)^{t_K} \qquad 1.28$$

with t_K and $\overline{A}_K\left(R_0\right)$ as adjustable parameters, and R_0 as a conveniently defined “standard ligand distance” [8].

The rare earth ions are good systems for the SPM when embedded in insulating covalent crystals (oxides, fluorides, and chlorides in particular), due to the well shielded 4*f* shell. On the contrary, in ionic crystals the hypothesis 1. is no longer fulfilled.

1.5 HYPERFINE INTERACTION

A further splitting of a degenerate energy level of given *J* can be due to the hyperfine interaction between the electrons and the nuclear spin $\underline{I}$ (for non-degenerate states, the hyperfine splitting is forbidden in the first-order approximation by time reversal symmetry [9]). It enters the system Hamiltonian with the term

$$H_{hf} = 2\mu_B \mu_N g_I \underline{I} \cdot \sum_i \frac{\underline{N}_i}{r_i^3} \qquad 1.29$$

where *i* labels the electrons of the ion,

$$\underline{N}_i = \underline{l}_i - \underline{s}_i + \frac{3\underline{r}_i\left(\underline{r}_i \cdot \underline{s}_i\right)}{r_i^2}, \qquad 1.30$$

μ_B is the Bohr magneton, μ_N is the nuclear magneton, g_I is the g nuclear factor (i.e., the ratio between nuclear magnetic moment, in μ_N unit, and *I*).

Since the matrix elements of $\underline{N}$ are proportional to those of $\underline{J}$ within a single ${}^{2S+1}L_J$ multiplet, the eq. 1.29 can be written as

$$H_{hf} = A_j \underline{J} \cdot \underline{I} \tag{1.31}$$

where A_J is the hyperfine coupling constant for the considered multiplet.

Some specific isotopes of RE, such as Pr^{3+}, Ho^{3+}, and Tm^{3+}, doped into crystals, are good candidates for the spectroscopic investigation of the hyperfine structure of ions embedded in a solid matrix, since they are endowed with a nuclear magnetic momentum and they exhibit very narrow absorption and emission lines [10].

An example of hyperfine analysis is given by $YAl_3(BO_3)_4$ (YAB): Ho^{3+} system [10].

YAB: Ho^{3+} is a good candidate to investigate the hyperfine structure (hfs), due to the trigonal structure of the matrix (which does not remove completely the manifold degeneracy) and the features of the RE^{3+} embedded (nuclear spin I=7/2, natural abundance 100%, and lowest manifold with high J values).

The monitored hfs showed different pattern, as displayed in the two figures here reported (see Figure 1.2 and Figure 1.3): it is possible to distinguish one (panels (c) in both Figures), eight (panels (a) and (d) in Figure 1.2, and panels (a) and (b) in Figure 1.3), or nine (panel (b) in Figure 1.2) components, either evenly spaced or not (panels (d) and (a) in Figure 1.2, respectively). All those cases were explained considering the transitions between two electronic levels split by the hyperfine interaction. As a first order approximation, eq. 1.31 can be written as

$$H_{hf} = -\underline{\mu}_i \cdot \underline{H}_0 , \tag{1.32}$$

where μ_i is the magnetic moment of the nucleus and $\underline{H}_0$ is the magnetic field created at the ion's nucleus by electrons in a given state. In this framework, the hyperfine field splits each E electronic doublet into eight equally spaced components (I_z=−7/2, ..., +7/2, I_z being the nuclear spin components along the magnetic field), while it does not affect the A_1 and A_2 singlets. Thus, a transition between two A-type levels will result in a single line (panels (c) in Figure 1.2 and Figure 1.3, and panel (a) in Figure 1.4), while transitions between E- and A-type levels should result in eight lines (panels (a) in Figure 1.2 and Figure 1.4) due to the selection rule ΔI_z=0.

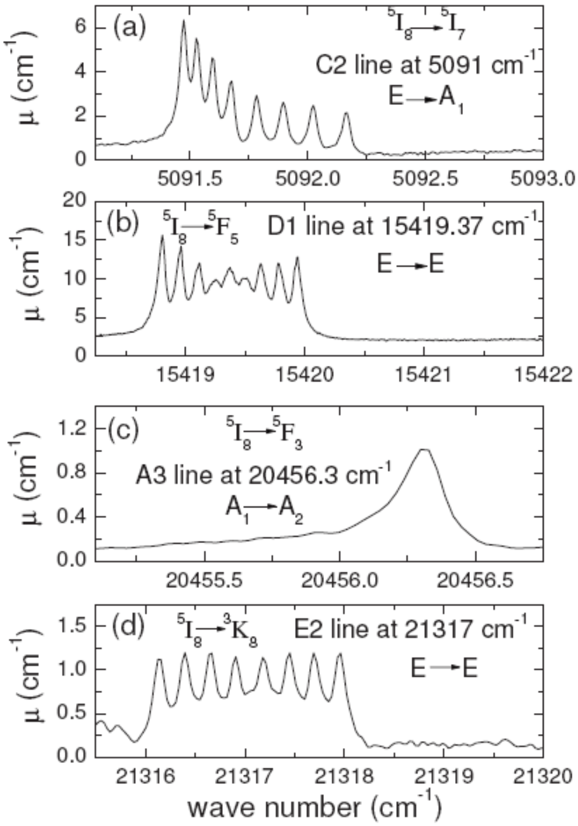

Figure 1.2 Examples of hfs patterns displayed by absorption lines in different wave number ranges [10].

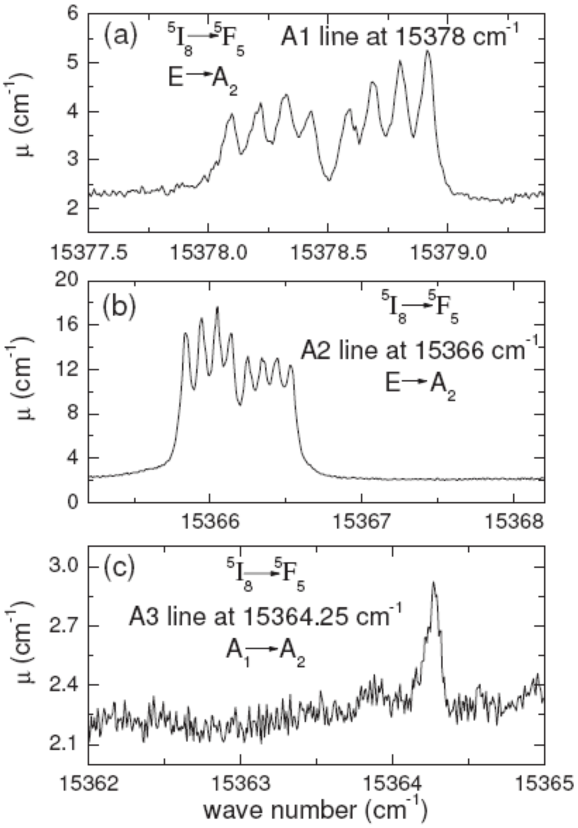

Figure 1.3 Examples of hfs patterns displayed by absorption lines starting from the first three sublevels (*E*, *E*, and A_1) of the ground manifold $^5I_8$ to the same sublevel (A_2) of the $^5F_5$ excited state [10].

The situation is more complex in the case of transitions between two *E* doublets. Calling Δ_i and Δ_f the overall hyperfine splitting of the initial and final electronic level, respectively, the presence of electric (ED) and magnetic dipole (MD) contributions at the same time should give rise to the presence of 16 hyperfine lines: 8 with hyperfine splitting $\Delta_{ED}=|\Delta_i+\Delta_f|/(2I)$ and 8 with hyperfine splitting $\Delta_{MD}=|\Delta_i-\Delta_f|/(2I)$ (panel (b) in Figure 1.4). However, a situation in which all the 16 lines are observable and well resolved is never achieved in practice, not only because the MD contribution might be much smaller than the ED one, but also because of the hyperfine energy gap values. If Δ_i is much larger than Δ_f or vice versa, $|\Delta_i+\Delta_f|/|\Delta_i-\Delta_f|\sim 1$; therefore, only eight lines (each one a superposition of two unresolved transitions between hyperfine levels) should be observable (panel (d) in Figure 1.2). On the other hand, if $\Delta_i \sim \Delta_f$, then $|\Delta_i-\Delta_f|\sim 0$, and a ninth line (superposition of eight lines), due to the MD contribution, is observable at the centre of the hyperfine structure (panel (b) in Figure 1.2).

A second order hyperfine interaction could also occur. As expected from perturbation theory, this term may have a significant effect on groups of electronic levels separated by small energy gaps. This gives rise to a contribution to the hyperfine splitting, which is proportional to I_z^2 rather than to I_z, i.e., a pseudoquadrupolar coupling with strength inversely proportional to the energy separation between the levels considered [11]. This contribution may add to the first-order hyperfine splitting if at least one *E*-type doublet is concerned in the process, or give rise to a pure pseudoquadrupolar splitting if two singlets, one of A_1- and one of A_2-type, are close enough (an A_n singlet is not connected to another A_n singlet of the same type by any matrix element).

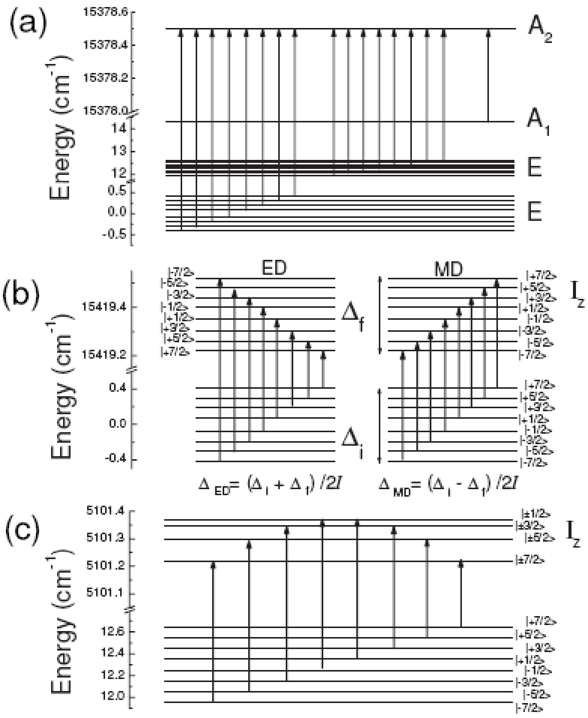

Figure 1.4 Examples of transitions originating different hfs pattern [10].

1.6 LINE SHAPE

The optical absorption or emission spectra of free atom (or molecule) consist of extremely sharp lines with a Lorentzian shape associated with the possible transitions between the energy levels. When they are embedded in a solid the electronic structure changes, as described in previous paragraphs, and the line shape is modified by two mechanisms [4]:

1. inhomogeneous broadening: it is due to the disorder of the host matrix, and thus gives a Gaussian shape (characteristic of random events) to the absorption lines. It derives from the fact that each ion probes a slightly different crystal field in dependence of its position, then it is particularly related to the equilibrium lattice defects. It is time independent;
2. homogeneous broadening: it is caused by the electron-phonon interaction. The temperature plays a key role on the population of the vibration levels, thus it affects the line width. The line shape is Lorentzian.

When both mechanisms are active, the resulting shape is a Voigt profile, i.e. the convolution between the Gaussian and Lorentzian line shapes (Figure 1.5). At very low temperature the former can be considered the dominant contribution and the latter can be assumed as negligible. By increasing the temperature, the vibrational energy levels get populated and induce homogeneous broadening and shift. The ligand charge acts on the ion by modulating the crystal field and changes consequently its energy levels. The Hamiltonian term describing the crystal field distortion caused by the lattice vibrations is a function of the local strain and can therefore be expanded in powers of the strain term ε:

$$H_{\text{int}} = V_0 + V_1\varepsilon + V_2\varepsilon^2 + \ldots\ldots \tag{1.33}$$

with

$$\varepsilon = \left.\frac{\partial u}{\partial x}\right|_{x\approx 0} = i\sum_q \left(\frac{\hbar\omega_q}{2Mv^2}\right)^{1/2} \left(b_q - b_q^+\right) \tag{1.34}$$

where u is the displacement, M is the crystal mass, b_q and b_q^+ are respectively the annihilation and the creation operators of the q^{th} oscillator, ω_q is its frequency, and v is the sound velocity in the crystal. The static term V_0 can be included in the single ion Hamiltonian since it does not depend on the temperature.

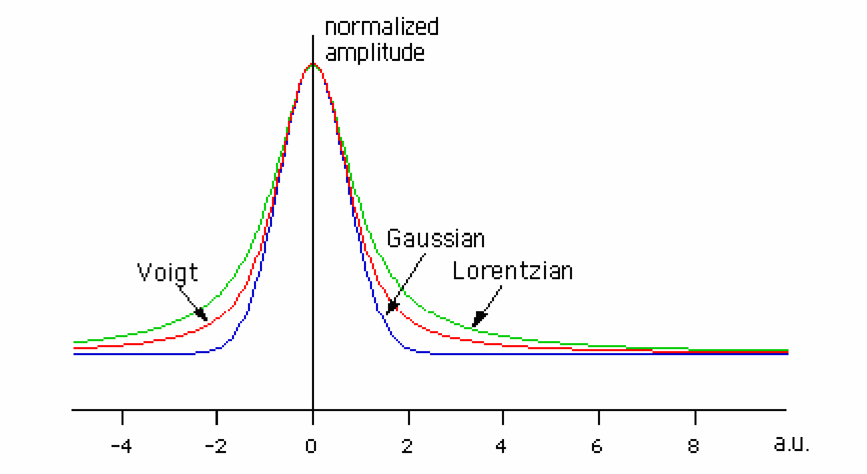

Figure 1.5 Gaussian, Lorentzian and Voigt shapes.

1.6.1 Non-radiative processes

Examples of non-radiative processes in crystals which cause homogeneous broadening phenomena are described in the following subsections [4].

1.6.1.1 Single phonon processes

They involve the absorption or the emission of a single phonon. It means that the interaction matrix element of 1.33 is

$$M = \langle f | H_{\text{int}} | i \rangle \propto \langle \psi_f^{el} | V_1 | \psi_i^{el} \rangle \langle n_q - 1 | b_q | n_q \rangle \qquad 1.35$$

where n_q is the occupation number of the q^{th} phonon state.

Assuming the Debye phonon distribution, the absorption probability of a single phonon with frequency ω_r is then

$$W_{abs} = \frac{3\omega_r{}^3}{2\pi\rho v^5 \hbar} \left| \langle \psi_f^{el} | V_1 | \psi_i^{el} \rangle \right|^2 n_r \qquad 1.36$$

where $n_r = \left(e^{\hbar\omega_r / k_B T} - 1 \right)^{-1}$, ψ_i^{el} and ψ_f^{el} are the electronic initial and final wavefunctions, respectively, and $\rho = M/V$ is the crystal density. Similarly

$$W_{emi} = \frac{3\omega_r^3}{2\pi\rho v^5\hbar} \left| \left\langle \psi_f^{el} \middle| V_1 \middle| \psi_i^{el} \right\rangle \right|^2 (n_r + 1) \qquad 1.37$$

represents the probability of a single phonon emission. It contains a temperature dependent part which is equal to W_{abs} and a temperature independent term describing the spontaneous emission phenomenon.

1.6.1.2 Raman processes

In the Debye approximation, the density $D(\omega)$ of vibrational occupied states is

$$D(\omega) = n(\omega)\rho(\omega) \propto \frac{\omega^2}{e^{\frac{\hbar\omega}{k_B T}} - 1} \qquad 1.38$$

and it has a maximum at $\omega \approx k_B T / \hbar$. If the energy gap between the initial and final electronic states is $\hbar\omega_r << k_B T$, the number of phonons available for the single phonon decay is very small. In this case, Raman scattering processes take place. They consist in a non-resonant absorption of a phonon with frequency ω_a and a subsequent emission of a phonon ω_e such that $\omega_r = \omega_e - \omega_a$. In these processes practically all the phonons of the spectrum are involved.

At the first order the two phonon Raman scattering is described by the diagram portrayed in Figure 1.6 and the associated matrix element is

$$\left\langle f \middle| H_{\text{int}} \middle| i \right\rangle^I = \left\langle \psi_f^{el} \middle| V_2 \middle| \psi_i^{el} \right\rangle \left\langle n_a - 1, n_e + 1 \middle| \varepsilon^2 \middle| n_a, n_e \right\rangle \qquad 1.39$$

where V_2 and ε are given by eq. 1.33.

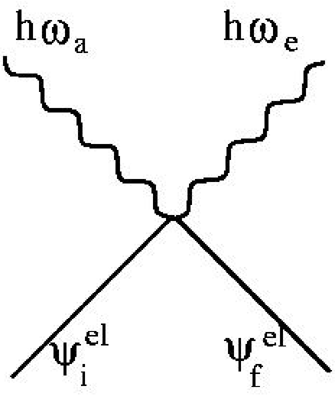

Figure 1.6 Diagram illustrating the first order two phonon Raman scattering according to eq. 1.39: the $h\omega_a$ quantum is absorbed while the $h\omega_e$ is emitted.

The relevant second order matrix element is

$$\langle f|H_{\mathrm{int}}|i\rangle^{II} = \sum_{l}\left[\frac{\langle \psi_f^{el}; n_a-1, n_e+1|H_{\mathrm{int}}|\psi_l^{el}; n_a, n_e+1\rangle \times \langle \psi_l^{el}; n_a, n_e+1|H_{\mathrm{int}}|\psi_i^{el}; n_a, n_e\rangle}{-\hbar\omega_e-(E_l^{el}-E_i^{el})} + \right.$$
$$\left. + \frac{\langle \psi_f^{el}; n_a-1, n_e+1|H_{\mathrm{int}}|\psi_l^{el}; n_a-1, n_e\rangle \times \langle \psi_l^{el}; n_a-1, n_e|H_{\mathrm{int}}|\psi_i^{el}; n_a, n_e\rangle}{-\hbar\omega_a-(E_l^{el}-E_i^{el})}\right] \qquad 1.40$$

where the system goes through a virtual state ψ_l^{el} as if the two phonon Raman scattering were subdivided into two single phonon non resonant processes (Figure 1.7).

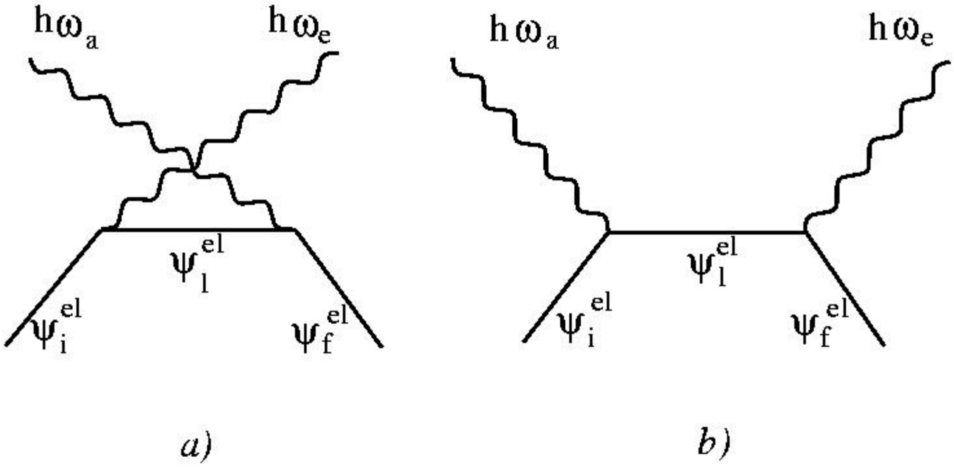

Figure 1.7 Diagram illustrating the possible second order Raman scattering according to eq. 1.40. Panel a): the first step is the emission of a $h\omega_e$ quantum and the second one is the absorption of $h\omega_a$; panel b): the first step is the absorption of $h\omega_a$ quantum and the second one is the emission of $h\omega_e$.

Taking into account both the first and second order matrix elements, the transition probability is then

$$W = A\left(\frac{T}{T_D}\right)^7 \int_0^{T_D/T} \frac{x^6 e^x}{\left(e^x-1\right)^2}dx \qquad 1.41$$

where $T_D = \hbar\omega_D / k_B$ is the Debye temperature and

$$A=\frac{9}{\rho^2 v^{10} 8\pi^3}\left|2\left\langle\psi_f^{el}\left|V_2\right|\psi_i^{el}\right\rangle+2\sum_l\left[\frac{\left\langle\psi_f^{el}\left|V_1\right|\psi_l^{el}\right\rangle\left\langle\psi_l^{el}\left|V_1\right|\psi_i^{el}\right\rangle}{E_i^{el}-E_f^{el}}\right]\right|^2, \qquad 1.42$$

which can be considered as a coupling coefficient between the energy levels of the ion and the lattice vibrations.

1.6.1.3 Orbach processes

They are resonant two phonon processes. The energy gap between the two involved electronic levels is in the range of the maximum vibrational energy k_BT_D. For this reason the Orbach processes are important only in the case of non-radiative relaxation between Zeeman states (i.e. states split by a magnetic field) in which the 1. and 2. processes (Section 1.6) have a lower probability to occur.

1.6.1.4 Multiphonon processes

The gap between the electronic levels involved in these processes are higher than k_BT_D and more than two phonons are simultaneously absorbed and emitted. The probability associated with these events, given by the higher orders of the perturbation theory, is practically independent of the temperature and negligible in the 9-300 K range.

An in-depth analysis of both the Orbach and Multiphonon processes can be found in Ref. [4].

1.6.2 Line broadening

This section deals with the effect of the temperature on the width and position of sharp spectral lines induced by electronic transitions [4].

The different mechanisms which broaden the optical absorption lines are the following.

1) Phonon non-radiative decay by spontaneous or induced emission of one or more phonons; this process takes place when the ion in an excited state decays to a lower level by transforming its energy into vibrational energy.
2) Phonon excitation of an ion to a more energetic state; it can involve one or more phonons as well.

3) Raman relaxation of an ion to a lower energy state. The difference between the frequencies of the absorbed phonon and re-emitted higher phonon is equal to the frequency difference between the initial and final electronic state of the ion.
4) Raman excitation of an ion to a higher state by means of two phonons. This process takes place in the opposite direction with respect to the previous one.
5) Vibronic decay of an ion from an excited state. This process involves the emission of a photon and the absorption or emission of one or more phonons. This contribution can be generally considered small.
6) Raman scattering of phonons by an ion in an excited state. In this process the ion remains in the same electronic state.

All processes, since they involve phonons, are temperature dependent.

A very important distinction has to be done among the described processes, i.e. the first five processes remove the ion from its starting state while the last maintains the ion in the same electronic configuration. It means that the first five processes affect the line width by shortening the lifetime of the electronic state, while the last one (two phonon Raman scattering) affects the width but not the lifetime.

The line width of sharp lines, as evaluated from the fluorescence spectra, is generally much larger than the reciprocal of the fluorescence lifetime (e.g. for R1 line of ruby the lifetime induced broadening is $\approx 2\cdot 10^{-9}$ cm^{-1}, while the room temperature line width is ≈ 10 cm^{-1} [4]). Therefore, the most important mechanism is that which broadens the energy level without removing the electrons from it.

The first four processes have been already discussed (see Section 1.6.1). As a rule, the contribution of the vibronic decay to the line width may be considered weak.

Being the two phonon Raman scattering the main contribution to the line broadening, the width ΔE_i (with respect to the width at T=0) of the i^{th} line can be written [4], according to eq. 1.41 and 1.42, as

$$\Delta E_i = \alpha \left(\frac{T}{T_D} \right)^7 \int_0^{T_D/T} \frac{x^6 e^x}{\left(e^x - 1\right)^2} dx \qquad 1.43$$

where the electron-phonon (e$^-$-ph) coupling parameter α

$$\alpha = \frac{1}{c}\frac{9}{\rho^2 v^{10} 2\pi^3}\left(\frac{k_B T_D}{\hbar}\right)^7 \left[\sum_{j\neq i}\frac{\left|\left\langle \psi_i^{el}\right|V_1\left|\psi_j^{el}\right\rangle\right|^2}{E_i - E_j} + \left\langle \psi_i^{el}\right|V_2\left|\psi_i^{el}\right\rangle\right]^2 \tag{1.44}$$

is intrinsically positive (c is the velocity of the light). The line shape produced by such a process is Lorentzian.

By analyzing the temperature induced line broadening in the absorption spectra of different RE^{3+} ions in LiYF$_4$ matrix, Ellens and co-workers [12] demonstrated that the same T_D=250 K was the best value to fit the experimental RE^{3+} line broadening.

They also considered the role played by the one phonon direct processes on the broadening of absorption line induced by RE^{3+} in LiYF$_4$. As first step, the α coefficients for different Eu^{3+} lines were derived as fitting parameters according to eq. 1.43. By taking into account both the two phonon Raman scattering and the one phonon direct absorption and emission [4] the “thermal” width of a line can be expressed as follows:

$$\begin{aligned}\Delta E_i = {} & \alpha\left(\frac{T}{T_D}\right)^7 \int_0^{T_D/T}\frac{x^6 e^x}{\left(e^x - 1\right)^2}dx + \\ & + \frac{1}{c}\sum_{j<i}\beta_{ij}\left(\frac{e^{\Delta E_{ij}/k_B T}}{e^{\Delta E_{ij}/k_B T} - 1}\right) + \frac{1}{c}\sum_{j>i}\beta_{ji}\left(\frac{1}{e^{\Delta E_{ji}/k_B T} - 1}\right)\end{aligned} \tag{1.45}$$

with

$$\beta_{ij} = \frac{3\omega_{ij}^3}{2\pi\rho v^5 \hbar}\left|\left\langle \psi_i^{el}\right|V_1\left|\psi_j^{el}\right\rangle\right|^2 \tag{1.46}$$

and α given by eq. 1.44. Since the evaluation of the β_{ij} by fit the experimental data to eq. 1.45 is a difficult task, especially when a large number of energy levels are present, in Ref. [12] simulation of the line width data has been done on the basis of eq. 1.45. Comparing the fitting and simulation results, Ellens and co-workers concluded that neglecting the one phonon direct process introduces considerable error in the fitting parameters, but the electron-phonon coupling strength remains of the same order of magnitude. Therefore, if the aim is to compare the e$^-$-ph coupling for different lines of the same ion or different lines induced by different ions, the one phonon direct processes may be neglected.

On the other hand, if the T_D is known and the one-parameter fitting according to eq. 1.43 fails, a single phonon coupling model [13] can be applied.

In the framework of the single phonon coupling model, the line width can be written

$$\Delta E_i = \frac{2(\delta\omega)^2}{\gamma} \frac{e^{h\omega_0/k_B T}}{\left(e^{h\omega_0/k_B T} - 1\right)^2} \tag{1.47}$$

where $h\omega_0$ and γ are energy and width of the coupled phonon band, and $\delta\omega$ is the coupling constant (which is assumed to be smaller than γ).

1.6.3 Line shift

It has been experimentally demonstrated that the absorption lines due to magnetic ions in crystals may change their position by increasing the temperature. Since several mechanisms are responsible for this change, the shift can be treated by means of perturbation theory. The 1.33 electron-phonon interaction Hamiltonian gives a non zero contribution only at the second order so that the displacement δE_i of the i^{th} energy level can be written as

$$\delta E_i = \sum_{j \neq i} \frac{\langle i | V_1 \varepsilon | j \rangle \langle j | V_1 \varepsilon | i \rangle}{E_i - E_j} + \langle i | V_2 \varepsilon^2 | i \rangle . \tag{1.48}$$

Therefore, for a given absorption line the resulting line shift is given by

$$\delta E = \beta \left(\frac{T}{T_D} \right)^4 \int_0^{T_D/T} \frac{x^3}{e^x - 1} dx \tag{1.49}$$

with

$$\beta = \frac{3}{4\pi^3 \rho v^5 c} \left(\frac{k_B T_D}{\hbar} \right)^4 \left[\sum_{j \neq i} \frac{\left| \langle \psi_i^{el} | V_1 | \psi_j^{el} \rangle \right|^2}{E_i^{el} - E_j^{el}} + \langle \psi_i^{el} | V_2 | \psi_i^{el} \rangle \right] \tag{1.50}$$

Depending on the relative weight and sign of the two terms in square brackets, the line shift may be either positive or negative [14].

On the other hand, in the framework of the single phonon coupling model [13], the line shift can be written as

$$\delta E_i = \frac{\delta\omega}{e^{h\omega_0/k_B T} - 1} \qquad 1.51$$

The fitting of experimental data according to eq. 1.47 and 1.51 provides $h\omega_0$ and γ; the former is an important parameter, because it can be compared with the phonon energy values coming from IR absorption and/or Raman spectroscopy.

1.7 VIBRONIC TRANSITIONS

In the previous sections the electron-phonon interaction has been discussed as responsible of the shape, width, and position of zero phonon lines. The e^--ph interaction is revealed even by the presence in the absorption spectra of new lines attributed to vibronic transitions. They involve simultaneously two events: a change in the electronic and the vibrational states of the system. The study of vibronic transitions by optical spectroscopy provides information about the interaction between the optical active ion and the surrounding. Since insulating materials doped with RE^{3+} ions are employed in several applications in photonics, it is of interest to investigate how this interaction depends both on the ion and on the surrounding. The rare earths with optical $4f \rightarrow 4f$ transitions belong to the weak interaction case. For a general outline of the theory of vibronic transitions we refer to Ref. [15].

An absorption vibronic transition takes place between the states $\psi(a,n)$ and $\psi(b,n')$ where the final vibrational state n' differs from the initial one n, and a and b are the ground and excited electronic states, respectively. The transition matrix element is then:

$$\left\langle \psi(b,n') \middle| \mu \middle| \psi(a,n) \right\rangle \qquad 1.52$$

where μ is the proper operator (electric or magnetic dipole).

The optical transition from a to b consists of several vibronic transitions between the involved vibrational states $n - n'$. Using the Condon approximation, eq. 1.52 can be written as

$$\langle \psi(b) | \mu | \psi(a) \rangle \langle \chi(n') | \chi(n) \rangle \qquad 1.53$$

where χ denotes the vibrational wavefunctions.

At low temperature only the vibrational level n=0 is occupied in the ground state a. The transition to n'=0 is called *zero phonon* (ZP) transition and it originates a very sharp line.

The electronic matrix element in eq. 1.53 vanishes for electric dipole transitions within $4f^n$ configuration (as in the case of RE^{3+} ions). Since for n=0, $\chi(0)$ has the totally symmetric representation, the eq. 1.53 does not vanish only if $\chi(n')$ has the same representation of the electric dipole operator μ. Therefore, parity forbidden electric dipole transitions can become in part allowed by interaction with vibrational modes.

From eq. 1.53 the selection rule $\Delta J \leq 2$ can be also inferred, where ΔJ is the difference between the total angular quantum numbers of the ground and excited electronic state. Two processes M and Δ (Figure 1.8) contributes to the vibronic transition probability [15]. The former describes a “vibronically” forced electric dipole (ED) induced transition, while in the latter the vibronic transition is due to a change in the equilibrium position of the ion in the excited state with respect to that in the ground state (Frank-Condon process). Not many theoretical approaches are available in the literature and the majority of them neglects the Δ contribution, because the parabola offset, in the configurational coordinate diagram, is assumed to be zero. In Ref. [15] Blasse compared the theoretical models with several experimental data, mainly concerning Gd^{3+} in different crystal lattices. The Gd^{3+} ion has a non-degenerate ground state $^8S_{7/2}$, thus the emission from an excited state, e.g. $^6P_{7/2}$, is represented by a single line. It simplifies the separation of the vibronic tail from the zero phonon lines and allows the calculation of the vibronic transition intensities. Blasse stated that, according to the theoretical calculations, the strongest vibronic lines derive from the coupling with the vibrational modes having the most intense IR absorptions and the vibronic intensities increase with increasing the covalency. But he also found that the assumption to neglect the Δ contribution is in some cases incorrect [15, 16].

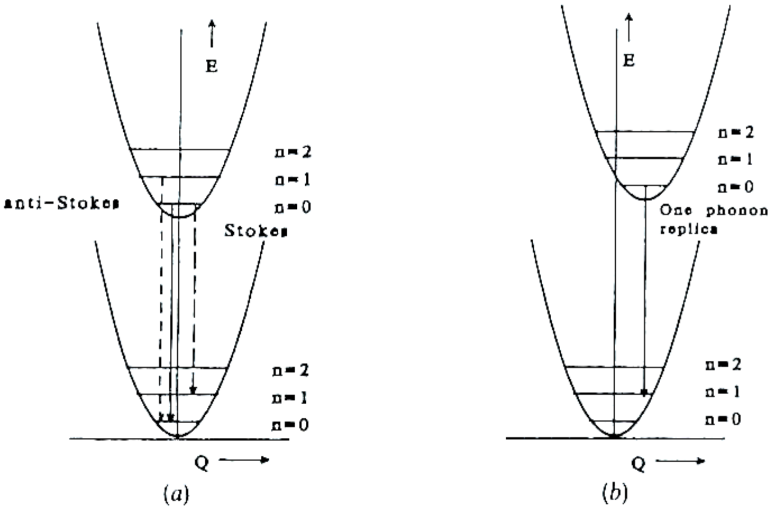

Figure 1.8 The *M* (panel (a)) and Δ (panel (b)) contributions to vibronic transitions.

The vibronic transition probability is thus the sum of the two contributions coming from the *M* and Δ processes:

$$A_{vib} = A_{vib}(M) + A_{vib}(\Delta). \qquad 1.54$$

Theoretical calculations of transition probability predict that the *M* process term is the sum of a static and a dynamic contribution [17]. In both the *M* and Δ cases, the covalency increasing determines an increasing of the vibronic intensities, as experimentally observed.

The analysis of the vibronic tails in crystals doped with RE^{3+} may give indications about electron-phonon coupling along the lanthanide series, but, being the vibronic intensity evaluation a very difficult task in systems with a large number of ZP lines, it is not expected to provide quantitative information. The vibronic tails in laser materials are also relevant in view of tuning and extending the laser emission to energies below that of the ZP emission lines [18].

2 BaY_2F_8 SINGLE CRYSTALS

2.1 INTRODUCTION

Yttrium fluoride single crystals doped with trivalent rare earth (RE^{3+}) ions are good candidates as active materials for new generation lasers emitting in the 2-4 μm range. They are characterized by large transparency range (from 9 μm up to 200 nm, i.e. ~1100-50000 cm^{-1}) [19] and low phonon energy ($h\nu_{max}$~450 cm^{-1}, lower than in garnets and oxides) [20]. These features make BaY_2F_8 (BaYF) interesting for applications requiring long-lived metastable levels, because their lifetime is limited only by non-radiative energy transfer processes.

For example, the emission at 2.8 μm of BaYF: Er^{3+} crystals can be absorbed by the OH groups of the living tissues, then exploited in medicine, especially in surgery [21]. Tunable 1.94-μm BaYF: Tm^{3+} laser has various applications because this is considered an eye-safe wavelength interval, thus reducing the risk of injury during the propagation through the atmosphere [22]. BaYF: Ho^{3+} offers not only the transition at 2 μm, but also laser lines at 2.4 and 2.9 μm [23]. Also co-doped Tm-Ho crystals emit in the same eye-safe region; in this case, the role of Tm is to absorb the diode laser emission and, through a cross relaxation and an energy transfer process, efficiently feed the Ho upper laser level [24, 25].

The BaYF crystal structure was determined by means of X-ray diffraction at room temperature [26]: it is monoclinic and belongs to the space group C2/m. The unit cell (Figure 2.1) contains two formula units and the lattice parameters are:

$a = 6.9829(5)$ Å

$b = 10.5190(10)$ Å

$c = 4.2644(4)$ Å

$\alpha = \gamma = 90°$

$\beta = 99.676(8)°$.

RE^{3+} substitutes for Y^{3+} (confirmed also by atomistic modelling [27]), which probes a C_2 local symmetry; thus, it is surrounded by a polyhedron of eight F^- ions (Figure 2.2). Since the RE^{3+} substitutes for the homovalent Y^{3+}, the charge compensation is not required, thus a high doping level can be reached without inducing substantial structural changes. Moreover, since the dimensions of the RE^{3+} ions are comparable to those of Y^{3+}, mechanical mismatch is limited.

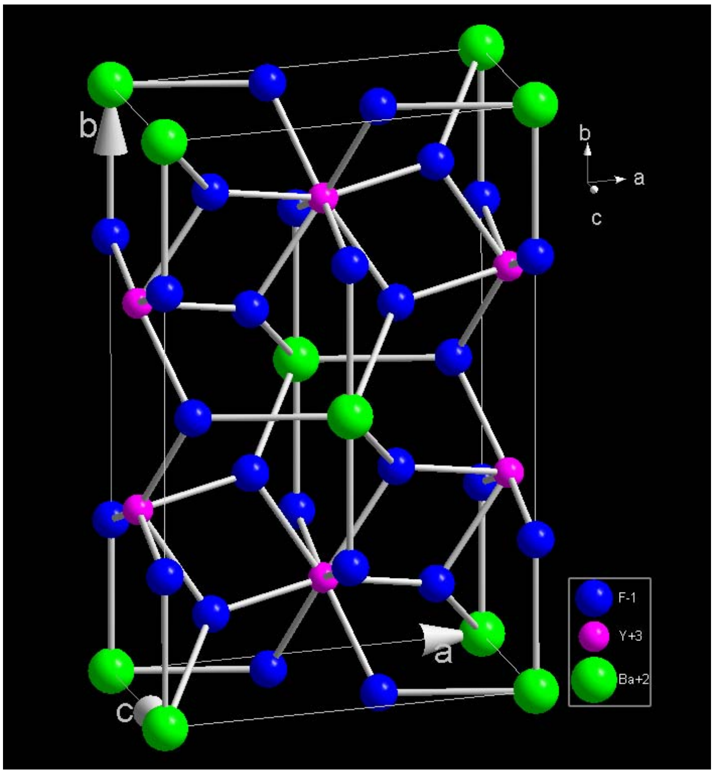

Figure 2.1 BaYF unit cell. Blue: Fluorine; pink: Yttrium; green: Barium. The bonds are indicated by sticks and the axes by gray arrows.

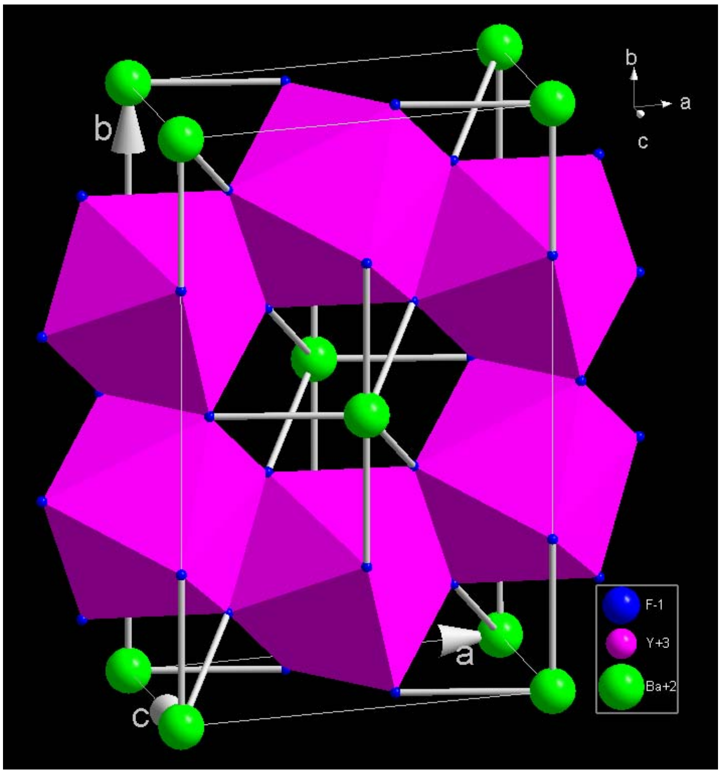

Figure 2.2 BaYF unit cell. Blue: Fluorine; pink: Yttrium; green: Barium. The F^- polyhedra are made evident and the axes are indicated by gray arrows.

In the present work BaYF single crystals doped with Tm^{3+} or Er^{3+} and co-doped with Tm^{3+} and Ho^{3+} are studied by means of high resolution Fourier transform spectroscopy in the wave number range 500-25000 cm^{-1} and in the temperature range 9-300 K.

The energy level schemes of Ho^{3+} and Tm^{3+} in BaYF are refined with respect to Ref. [28] (Section 2.4.1).

A detailed analysis of dichroic spectra of Er^{3+} and Tm^{3+} doped samples allows determining the orientation of the dielectric ellipsoid and of the transition dipole moments (Section 2.4.2). Specific heat measurements performed on the Er^{3+} doped samples, coupled with optical-absorption spectra, allows to identify "roto-electronic" transitions, i.e. the simultaneous excitation of a crystal field (CF) transition and a rotational-like mode of the RE^{3+}-F^- group [29] (Section 2.4.3).

An unexpected hyperfine structure of Ho^{3+} absorption lines is also monitored and analyzed (Section 2.4.4).

2.2 EXPERIMENTAL DETAILS

The BaYF single crystals were grown at the Physics Department of the University of Pisa (Prof. M. Tonelli and co-workers) by a computer-controlled Czochralski technique under a purified argon atmosphere [25, 30, 31]. The list of analyzed samples is reported in Table 2.1; the sample thickness ranges between 0.9 and 19 mm. The RE^{3+} doping level is given in terms of atomic fraction (at%), i.e. the ratio between the numbers of RE^{3+} and Y^{3+} ions.

A nominally pure sample was also analyzed as reference.

The samples were oriented by means of X-ray diffraction, cut, and polished for spectroscopic investigation.

Table 2.1 Analyzed samples.

Dopant	C_{RE} (at%)	C_{RE} (at%)
Er^{3+}	0.5 2 12 20	
Tm^{3+}	0.5 1 5	
Tm^{3+}, Ho^{3+}	5.2	0.5

The optical absorption spectra were monitored in the wave number range 500-25000 cm^{-1} with a non-apodized resolution as fine as 0.01 cm^{-1} (see Appendix 1.1) and in the temperature range 9-300 K (see Appendix 1.2.1). Measurements with linearly polarized light (see Appendix 1.2.2) were performed at 9 K in the infrared (IR) region 4000-10000 cm^{-1}.

The specific heat of Er^{3+} doped samples was also measured in the 1.5-25 K range by Prof. G. Carini and co-workers at the Physics Department of the University of Messina (see Appendix 2.1).

2.3 EXPERIMENTAL RESULTS

2.3.1 Anisotropy

Due to its monoclinic structure, BaYF is an optically anisotropic media (biaxial) [26]. Thus, spectra measured with light travelling along different crystallographic directions are different. Figure 2.3 displays three spectra measured at 9 K on a Tm^{3+} 1at% doped sample in the region of the $^3H_6 \rightarrow {}^3F_4$ transition: when the radiation is propagating along the *b* axis (curve c) the peaks labelled with A2 and C1 are very weak and the D1 peak is practically negligible. Spectra measured with the beam travelling along the *c* axis (curve b) or perpendicular to the *b*-*c* plane (i.e., very close to the *a* axis; curve a) are very similar one to each other.

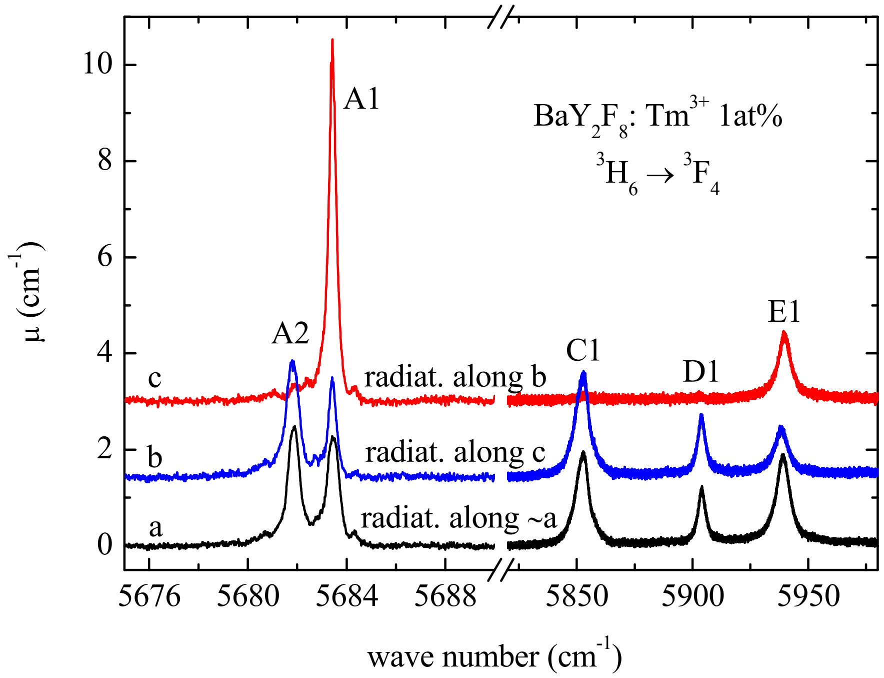

Figure 2.3 Optical absorption spectra of a BaYF: Tm^{3+} 1at% sample in the region of the $^3H_6 \rightarrow {}^3F_4$ transition measured at 9 K with radiation propagating along different axes.

Owing to this observation, measurements along the three directions and with linearly polarized light were performed. Figure 2.4 shows an example of spectra measured at 9 K with light electric field E_l travelling along the *c* axis and polarization angle θ=90° (curve a), θ=0° (curve b), and θ=45° (curve c) with respect to the *b* axis. A spectrum with unpolarized light is reported for reference (curve d). The A1 peak is strong when E_l is perpendicular to the *b* axis, while A2 is weak; on the contrary, if E_l is parallel to the *b* direction, the A2 line is strong and A1 is weak. Spectra measured with the beam travelling along the *b* axis show only the A1 line, independently of the light polarization (Figure 2.5 and Figure 2.3).

Similar considerations can be done for Er^{3+} doped samples.

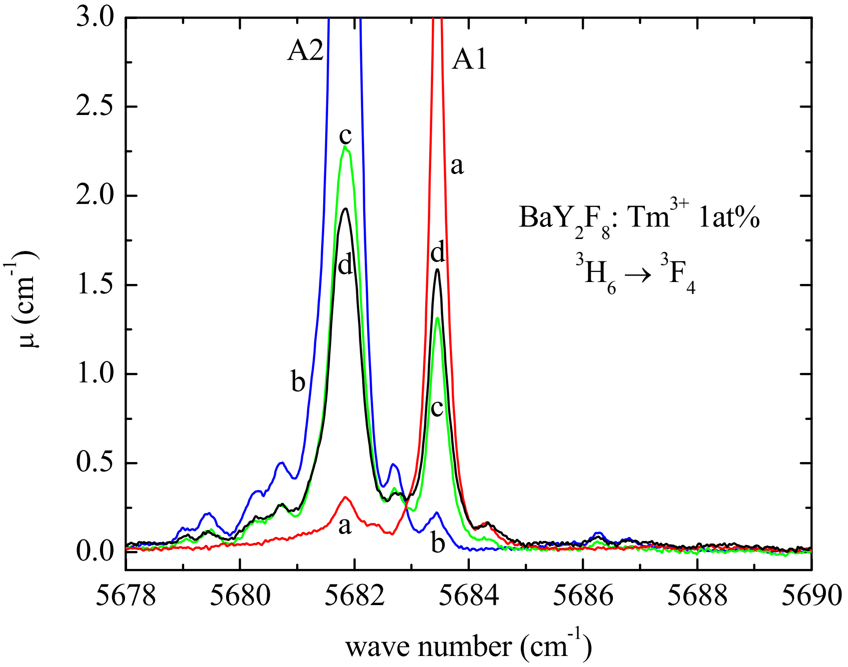

Figure 2.4 Optical absorption spectra of a BaYF: Tm^{3+} 1at% sample in the region of the $^3H_6 \rightarrow {}^3F_4$ transition measured at 9 K with radiation propagating along the *c* axis. Curve a (red): θ=90°; curve b (blue): θ=0°; curve c (green): θ=45°; curve d (black): unpolarized light.

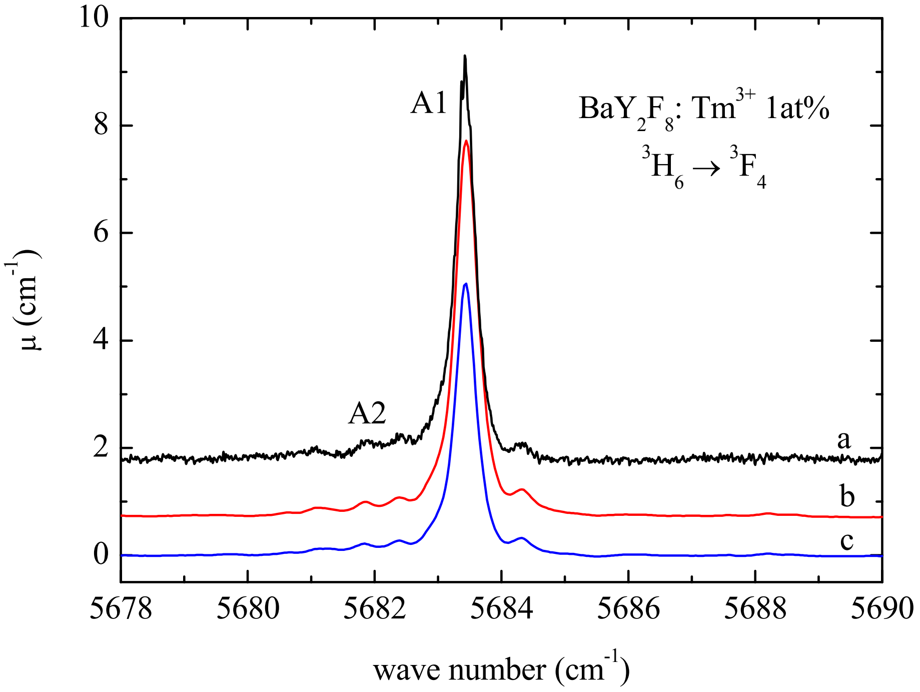

Figure 2.5 Optical absorption spectra of a BaYF: Tm^{3+} 1at% sample in the region of the $^3H_6 \rightarrow {}^3F_4$ transition measured at 9 K with radiation propagating along the *b* axis. Curve a (black): unpolarized light; curve b (red): θ=0°; curve c (blue): θ=90°.

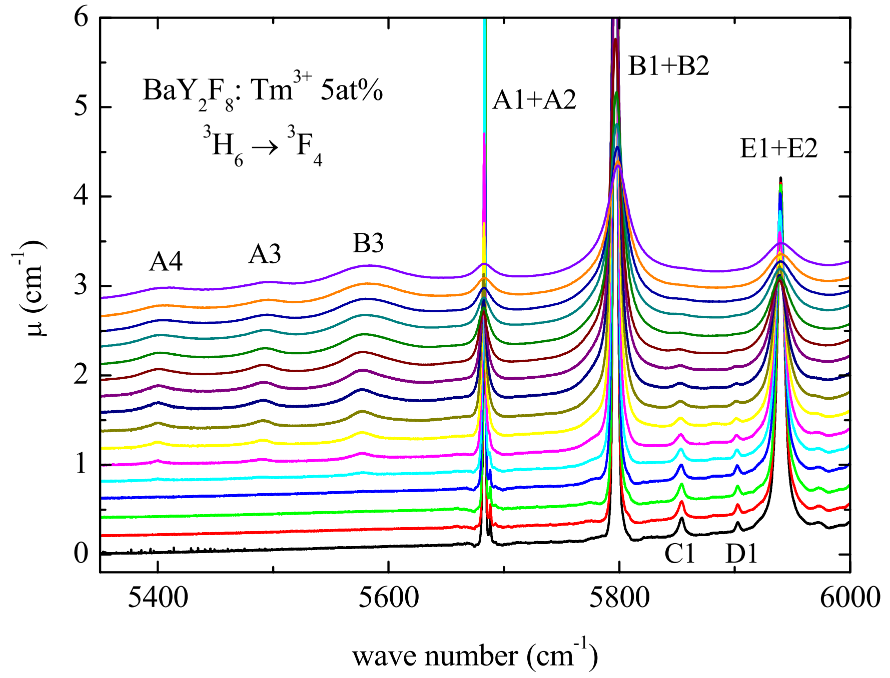

Figure 2.6 Optical absorption spectra measured at different temperatures on a BaYF: Tm^{3+} 5at% sample in the region of the $^3H_6 \rightarrow {}^3F_4$ transition. Lower curve (black): 9 K; upper curves (from red to violet): temperature increasing from 20 to 300 K by 20 K steps (from the bottom).

2.3.2 Temperature dependence

The absorption lines change their width and position with increasing the temperature (see Section 1.6). Figure 2.6 shows the spectra measured at different temperatures (from 9 to 300 K) on a BaYF: Tm^{3+} 5at% sample in the region of the $^3H_6 \rightarrow {}^3F_4$ transition. Figure 2.7 displays the spectra measured at 9, 20, 80, 140, and 300 K on a BaYF: Tm^{3+} 5.2at%, Ho^{3+} 0.5at% in the region of the Ho^{3+} $^5I_8 \rightarrow {}^5I_7$ transition. In both cases, at 9 K the lines are sharp and structured; by increasing the temperature they broaden and new lines grow in the low wave number side. At 300 K the lines are much weaker and broader.

The temperature dependence of the line shape is summarized in Figure 2.8. Some lines behave as the line at 5683.6 cm^{-1} (panel A) associated with a Tm^{3+} absorption: they become weaker and broaden by increasing the temperature. Some other lines behave as the line at 5156 cm^{-1} (panel B), associated with an Ho^{3+} absorption: they initially increase with the temperature, and then decrease and broaden. It is important to notice that the former shifts towards lower wave numbers, while the latter towards higher wave numbers.

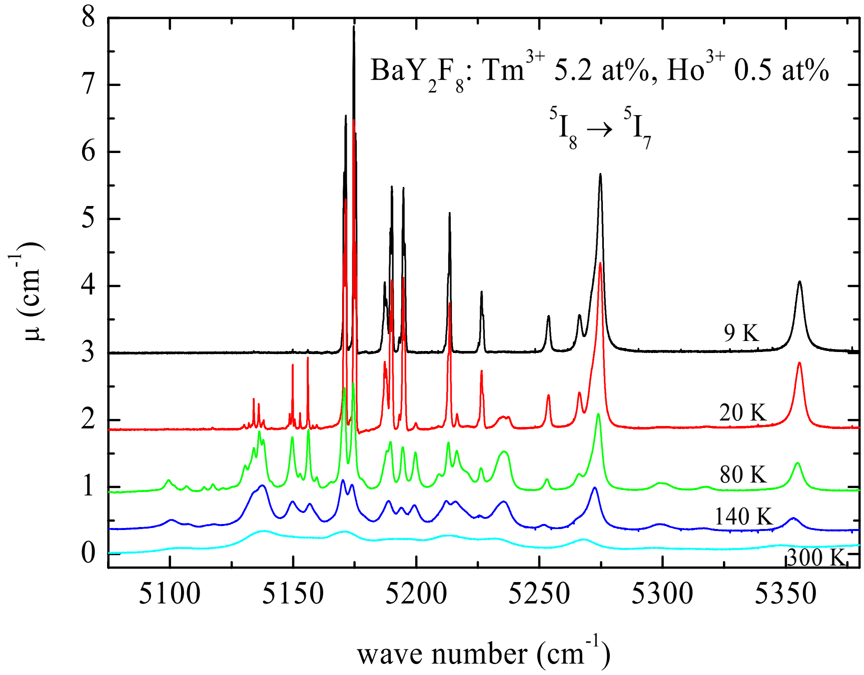

Figure 2.7 Optical absorption spectra measured at 9, 20, 80, 140, and 300 K on a BaYF: Tm^{3+} 5.2at%, Ho^{3+} 0.5at% sample in the region of the $^5I_8 \rightarrow {}^5I_7$ Ho^{3+} transition.

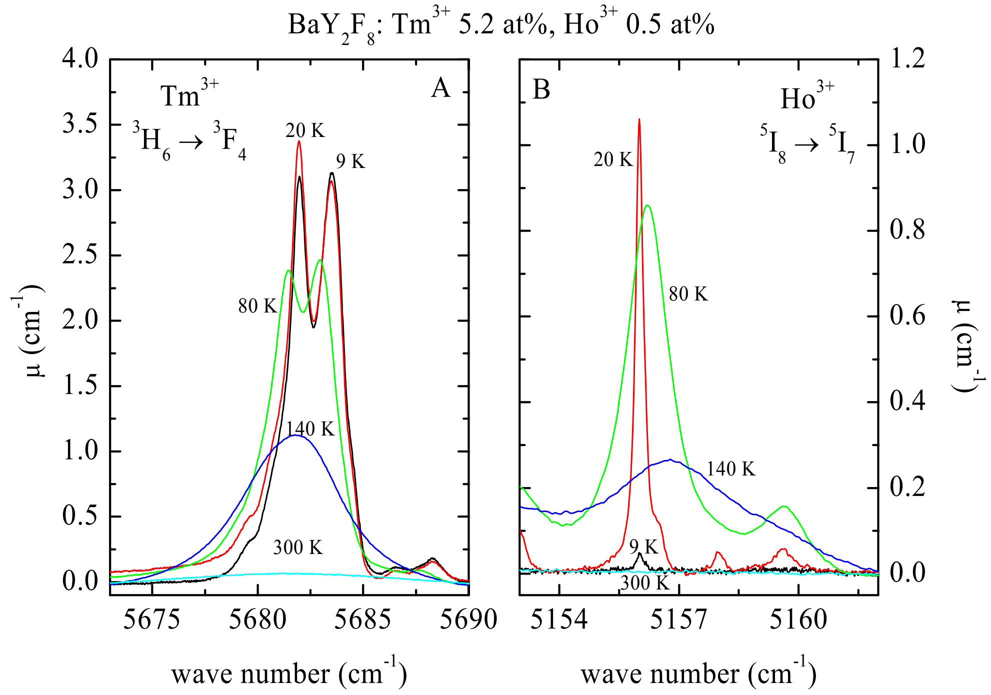

Figure 2.8 Optical absorption spectra measured at 9, 20, 80, 140, and 300 K on a BaYF: Tm^{3+} 5.2at%, Ho^{3+} 0.5at% sample in the regions of the Tm^{3+} $^3H_6 \rightarrow {}^3F_4$ (panel A) and Ho^{3+} $^5I_8 \rightarrow {}^5I_7$ (panel B) transitions.

2.3.3 Specific-heat measurements

Figure 2.9 displays the specific-heat measurements performed on a nominally pure sample (■) and three Er^{3+} doped samples with different doping levels: 0.5at% (●), 12at% (▲), and 20at% (▼). Above 20 K the specific heat (C_p) is nearly the same for BaYF samples both pure and doped with different Er^{3+} concentrations. Below 20 K, the C_p of the pure and 0.5at% doped samples are still coincident, while in samples containing 12 and 20at% of Er^{3+} it exceeds that of the undoped one, becoming about two orders of magnitude larger at the lowest temperatures. Data taken in different experimental runs always reproduced the same trend.

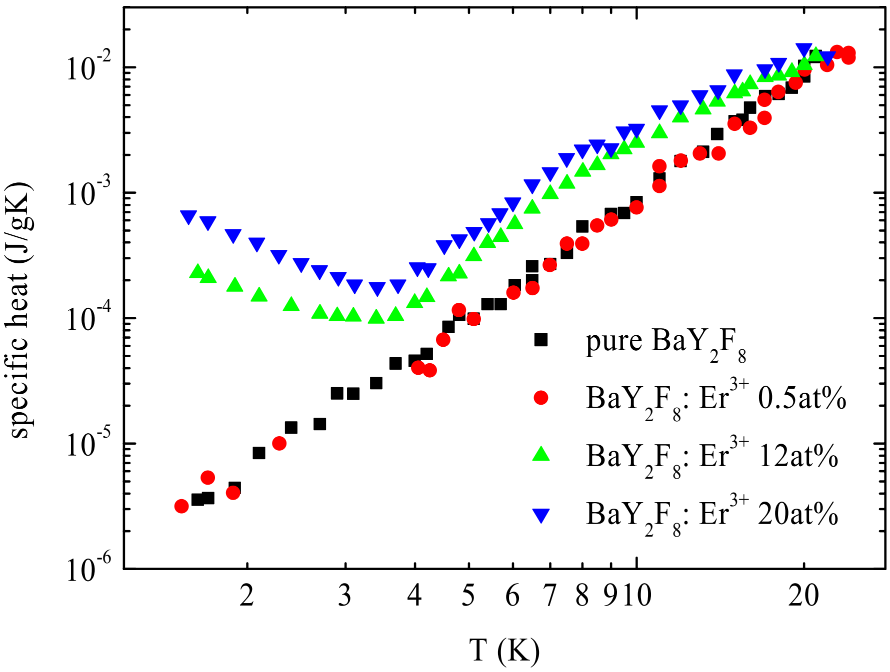

Figure 2.9 Specific heat measured as a function of temperature in the range 1.5-22 K on four BaYF samples. ■: nominally pure sample; ●: 0.5at% Er^{3+} doped sample; ▲: 12at% Er^{3+} doped sample; ▼: 20at% Er^{3+} doped sample.

2.4 DISCUSSION

2.4.1 Line attribution and crystal field parameters

The line attribution for non-Kramers ions, as Ho^{3+} ($4f^{10}$) and Tm^{3+} ($4f^{12}$), is quite difficult due to the large number of sublevels (up to $2J+1$) into which a manifold of a given J can be split by low symmetry crystal field (as in the case of monoclinic BaYF). A careful analysis of the spectra as a function of temperature, sample orientation, and incident light polarization is the way to obtain a correct attribution of the absorption lines and to build the energy sublevel scheme for every manifold. Moreover, the fitting of the experimental energy levels with a CF model supplies a valuable aid (see Section 1.3).

The energy levels are conventionally indicated with letters X=A, B, C, ... for the excited manifolds and with numbers i=1, 2, 3, ... for the ground one from which the absorption starts. Thus, in the spectra each absorption line is labelled by Xi as well as the associated transition.

At low temperature the absorption lines in the spectra are due to transitions from the lowest sublevels of the ground manifold (the only ones which are populated) to all the sublevels of the excited manifolds; among them, the X1 lines should be the strongest. By increasing the temperature, even higher sublevels of the ground manifold become gradually populated. Then, the amplitude of the lines detectable at 9 K decreases (see Figure 2.8, panel A) and new lines rise in the lower wave number side (see Figure 2.8, panel B); see also Figure 2.6 and Figure 2.7. These new lines are called *hot bands* and their amplitude first increases, then decreases. The separation between the X1 line position and that of the X2, X3, ... ones gives the energy separation of the sublevels 2, 3, ... from the lowest sublevel 1 in the ground manifold (whose energy has been assumed as zero). Thus, the energy position of the excited sublevels within the ground manifold can be averaged over several pairs of X1-Xi (i=2, 3, ...) line separations.

In the present work the absorption line attribution and the energy level scheme were refined for Tm^{3+} and Ho^{3+} in BaYF with respect to [28].

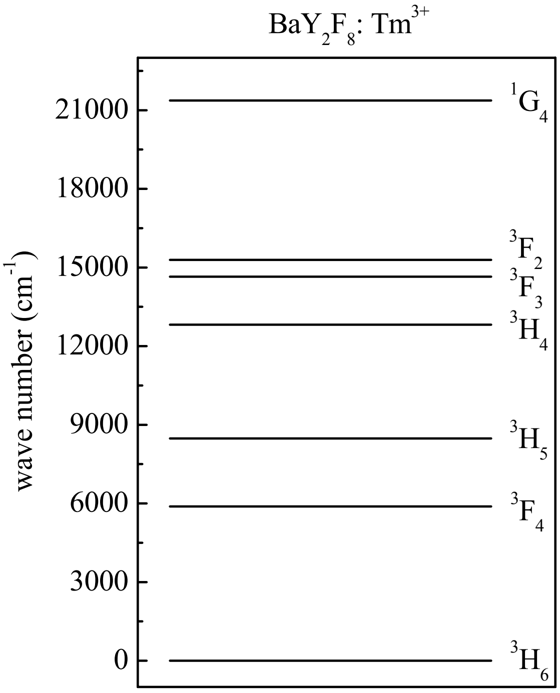

Figure 2.10 Energy level scheme of the first seven manifolds for Tm^{3+} in BaYF.

2.4.1.1 Tm^{3+}

The $4f^{12}$ configuration of the free Tm^{3+} ion is split into 13 manifolds by the electrostatic and spin-orbit interaction [32]. The ground state is $^3H_6$, and it is further split into 13 sublevels by the low symmetry CF probed in BaYF. Figure 2.10 displays the first seven manifolds (from $^3H_6$ to $^1G_4$): those which were investigated in the present work.

With the attribution method described in Section 2.4.1, the energy values of the sublevels related to the ground $^3H_6$ and to the excited $^3F_4$, $^3H_5$, $^3H_4$, $^3F_3$, $^3F_2$, and $^1G_4$ manifolds were derived. The values obtained are displayed in Table 2.2, third column.

Due to the small separation between the first two sublevels of the ground manifold (see Figure 2.8, panel A), in some cases it was impossible to discriminate between X1 and X2; these cases are indicated in italic type in Table 2.2.

Table 2.2 Sublevel positions (cm^{-1}) for Tm^{3+} ground and excited manifolds in BaYF as derived from optical absorption measurements (third column) and theoretical calculations (fourth column). Experimental values from Ref. [28] are reported for comparison (last column).

$^{2S+1}L_J$	Level	Exp. (cm^{-1})	Fit. (cm^{-1})	Exp. (cm^{-1})
$^3H_6$	1	0	-0.56	0
	2	1.6±0.1	0.21	1.6±0.1
	3		265.80	187±10
	4	281±7	271.44	282±5
	5		293.06	
	6	307±2	302.31	
	7		435.24	
	8		457.29	
	9		469.54	
	10	478±6	478.01	
	11		483.44	
	12		500.85	
	13		511.10	
$^3F_4$	A	5683.41	5704.90	5683.5
	B	5798.04	5797.99	5796.7
	C	5852.8	5880.71	5852.8
	D	*5903.8*	5908.36	5904.1
	E	5939.7	5936.19	5939.3
	F	*6044.8*	6034.26	-
	G	*6056.6*	6043.90	6045.1
	H	*6084.4*	6080.23	6056.2
	I	*6092.4*	6105.99	6085.6

$^{2S+1}L_J$	**Level**	**Exp. (cm^{-1})**	**Fit. (cm^{-1})**	**Exp. (cm^{-1})**
$^3H_5$	A	8296.75	8278.71	8296.8
	B	8297.43	8278.94	8297.5
	C	8520.9	8504.23	-
	D	8533.4	8511.57	-
	E	8546.3	8513.88	8521.1
	F	*8549.5*	8522.86	8533.4
	G	8565.5	8602.25	8580.3
	H	8579.7	8602.89	8595.8
	I	*8595.7*	8633.45	8608.8
	L	*8606.8*	8647.85	8622.6
	M	8647.0	8652.32	8646.2
$^3H_4$	A	12662.65	12644.29	-
	B	12665.36	12670.83	12665.3
	C	*12738.7*	12774.65	12739.2
	D	*12805.8*	12815.27	12807.8
	E	12843.9	12853.92	12843.5
	F	*12885.5*	12877.84	12886.4
	G	*12919.7*	12930.23	12918.4
	H	*12954.8*	12964.76	12954.6
	I	*12980.2*	13014.16	12981.2
$^3F_3$	A	*14582.5*	14587.68	14582.8
	B	*14637.0*	14637.95	14638.8
	C	*14663.0*	14648.00	14665.1
	D	*14669.2*	14663.52	14669.3
	E	*14673.8*	14670.36	14674.4
	F	*14701.9*	14681.07	14704.0
	G	14724.2	14719.88	14723.5
$^3F_2$	A	15205.0	15223.17	15204.9
	B	*15239.3*	15230.52	15240.2
	C	15320.4	15310.65	15319.6
	D	*15340.5*	15342.45	15341.6
	E	-	15380.20	15393.7
$^1G_4$	A	21051.6	21087.63	21400 barycenter
	B	*21203.8*	21210.46	
	C	*21368.9*	21371.34	
	D	*21383.7*	21379.06	
	E	*21605.0*	21398.26	
	F	*21614.1*	21572.75	
	G	*21620.0*	21601.30	
	H	*21653.8*	21662.40	
	I	*21695.0*	21667.48	

A further support to the line attribution came from the presence of a very small amount of Tm^{3+} in the sample BaYF: Er^{3+} 0.5at%: the low concentration minimizes the line broadening and overlapping, and avoids the presence of additional lines due to RE^{3+}-RE^{3+} interaction [31]. Thus, it is possible to determine precisely the position of the strongest X1 and X2 lines.

At 9 K only the X1 and X2 lines are detectable, due to the small separation (1.6 cm^{-1}) between the first two sublevels within the ground manifold and the large one of the third sublevel (~281 cm^{-1}). The X3 lines grow at T≥80 K (see, for example, Figure 2.6); at so high temperatures the lines are already broad. This fact justifies the large error which affects the determination of the highest sublevel positions within the ground manifold. Moreover, the two sublevels at 281 and 478 cm^{-1} come from the average of two groups of sublevels very close one to each other. This hypothesis is confirmed by theoretical fittings with a single-ion Hamiltonian model (Table 2.2, fourth column): the calculations support the presence of three and seven sublevels around 281 and 478 cm^{-1}, respectively.

The atomic part of the single-ion Hamiltonian used to fit experimental data is

$$\begin{aligned}\hat{H}_{FI} = E_{av} + \sum_q F^q \hat{f}^q + \zeta \hat{H}_{SO} + \alpha \hat{L}\left(\hat{L}+1\right) + \beta \hat{G}\left(G_2\right) + \\ + \gamma \hat{G}\left(R_7\right) + \sum_i T^i \hat{t}_i + \sum_j M^j \hat{m}_j + \sum_q P^q \hat{p}_q\end{aligned} \qquad 2.1$$

while the crystal field one is

$$\hat{H}_{CF} = \sum_{k,q} B_q^k C_q^k . \qquad 2.2$$

where q=2, 4, 6; i= 2, 3, 4, 6, 7, 8; j=0, 2, 4; ζ is related to spin-orbit interaction; α, β, γ are related to two-body interaction; T^i to three-body interaction; M^j to the spin-other-orbit interaction; P^q to electrostatically correlated magnetic interactions (see Section 1.3 and [5, 7]). Since the free ion parameters are generally expected to be very similar in all phases, only Coulomb and spin-orbit among them were varied to fit experimental data starting from the values obtained by Carnal *et al.* for Tm^{3+} in LaF_3 [33]: other free ion parameters (which are weak corrective potentials) were kept fix at the values obtained in Ref. [33]. Moreover, the CF parameters are expected not to change drastically if different RE are embedded in the same host. Thus, only the three CF parameters B_q^0 were varied freely, while the ratio B_q^k / B_q^0 was kept fix (related values indicated with * in Table 2.3) at the values obtained for Er^{3+} in Ref. [31], being Er^{3+} near Tm^{3+} in the periodic table. The B_q^0 starting values were those of Er^{3+} in Ref. [31]. These choices were made to avoid over-parameterization. The parameters so obtained are listed in Table 2.3.

The agreement between experimental and calculated energy levels is good, with a root mean square deviation $\sigma \sim 20$ cm^{-1}.

Table 2.3 Coulomb, spin-orbit and CF parameters obtained for Tm^{3+} from experimental data fitting.

Parameter	Data fit
F^2	99980±130
F^4	69770±110
F^6	55980±320
ζ	2632±1
B_2^0	-449±27
B_4^0	-1250±35
B_6^0	420±25
B_2^2	60*
B_4^1	306*
B_4^2	96*
B_4^3	4*
B_4^4	358*
B_6^1	-223*
B_6^2	-45*
B_6^3	-71*
B_6^4	337*
B_6^5	-331*
B_6^6	223*

* **Value related to the fixed ratio (see text).**

The last column of Table 2.2 lists the preliminary values obtained from Ref. [28] for comparison. The most important difference is the presence of a sublevel of the ground manifold at 187 cm^{-1}: it was definitely not observed. The overall accuracy improvement attained in the present work with respect to Ref. [28] is related to the higher number of samples with different Tm^{3+} concentrations and orientations, and to the measurements performed with linearly polarized light.

2.4.1.2 Ho^{3+}

The Ho^{3+} is a non-Kramers ion with $4f^{10}$ configuration which is split into 107 manifolds by the electrostatic and spin-orbit interactions [32]. The ground state is $^5I_8$, and the transitions investigated in the present work were $^5I_8 \rightarrow {}^5I_7$, $^5I_6$, $^5I_5$, $^5I_4$, $^5F_5$, $^5S_2$, $^5F_4$, $^5F_3$, $^5F_2$, $^3K_8$, $^5G_6$, and $^5F_1$. Due to the high J values of the low energy lying manifolds, a large number of lines was expected for them (see Figure 2.7).

With the attribution method described in Section 2.4.1 and the support of theoretical approach (Table 2.4, fourth column; see Section 2.4.1.1), the energy values of the sublevels related to all the quoted manifolds were derived. The values obtained are displayed in Table 2.4, third column. Unfortunately, in this case only the BaYF sample co-doped with Tm^{3+} and Ho^{3+} was suitable for the attribution and level scheme determination. Thus, in some cases overlapping between Tm^{3+} and Ho^{3+} transitions occurred (as shown in Figure 2.11). In addition, the Ho^{3+} absorption lines were weak due to the low concentration. The large number of manifolds and lines added further difficulties.

Table 2.4 Sublevel positions (cm^{-1}) for Ho^{3+} ground and excited manifolds in BaYF as derived from optical absorption measurements (third column) and theoretical calculations (fourth column). Experimental values from Ref. [28] are reported for comparison (last column).

$^{2S+1}L_J$	Level	Exp. (cm^{-1})	Calc. (cm^{-1})	Exp. (cm^{-1})
$^5I_8$	1	0	-9.08	0
	2	0.62±0.05	-5.31	0.60±0.06
	3	37.2±0.4	41.84	37.3±0.2
	4	39.3±0.3	46.17	53.9±0.2
	5	54.1±0.3	49.51	57.1±0.7
	6	57.5±0.3	74.68	
	7	88.7±0.3	83.05	
	8	-	124.93	
	9	-	222.90	
	10	-	278.23	
	11	-	300.65	

$^{2S+1}L_J$	**Level**	**Exp. (cm^{-1})**	**Calc. (cm^{-1})**	**Exp. (cm^{-1})**
	12	-	309.63	
	13	-	323.75	
	14	-	334.58	
	15	-	339.60	
	16	-	368.77	
	17	-	370.59	
$^5I_7$	A	5171.3	5161.50	-
	B	5175.4	5164.68	5171.4
	C	5186.4	5177.20	5175.3
	D	5187.9	5182.64	5187.9
	E	5190.1	5192.69	5190.1
	F	*5193.1*	5194.31	5195.3
	G	5195.3	5209.44	5213.6
	H	5213.6	5217.96	5226.5
	I	5227.1	5247.47	5253.8
	L	5253.7	5249.45	5253.8
	M	*5266.2*	5259.81	-
	N	*5270.8*	5264.33	-
	O	*5274.7*	5265.65	5266.2
	P	*5355.6*	5352.08	5355.7
	Q	*5355.6*	5352.17	5355.7
$^5I_6$	A	8686.8	8690.18	8686.8
	B	8696.3	8694.02	8696.3
	C	8701.4	8696.12	8701.4
	D	*8702.3*	8698.21	8702.3
	E	8708.7	8700.42	8708.8
	F	8711.9	8708.32	8711.9
	G	8715.5	8718.60	8715.4
	H	8741.1	8743.06	8741.1
	I	8746.0	8745.63	8746.0
	L	8752.8	8750.45	8755.8
	M	8755.8	8754.51	8755.8
	N	*8851.7*	8856.61	8851.9
	O	*8851.7*	8856.77	8851.9
$^5I_5$	A	-	11255.04	-
	B	11258.4	11261.32	-
	C	11266.1	11265.68	11258.4
	D	11277.3	11275.75	11266.1
	E	11283.1	11275.88	11277.2
	F	11284.0	11284.41	11283.1
	G	11289.4	11290.41	11284.0
	H	11291.3	11296.44	11291.3
	I	11314.2	11311.48	11313.7

$^{2S+1}L_J$	**Level**	**Exp. (cm^{-1})**	**Calc. (cm^{-1})**	**Exp. (cm^{-1})**
	L	*11387.9*	11393.53	11387.8
	M	*11387.9*	11396.54	11387.8
$^5I_4$	A	13212.2	13215.58	13211.9
	B	13247.4	13253.96	13247.1
	C	-	13313.29	-
	D	-	13353.16	13356.6
	E	*13356.4*	13363.57	13356.6
	F	*13370.4*	13375.95	13370.3
	G	*13403.7*	13402.95	13403.5
	H	-	13512.76	-
	I	-	13568.77	-
$^5F_5$	A	15496.4	15498.52	15496.4
	B	15500.5	15501.97	15500.6
	C	-	15525.50	-
	D	15530.3	15534.64	15530.3
	E	15580.6	15577.41	15580.6
	F	*15622.3*	15627.03	15622.3
	G	-	15629.53	-
	H	*15654.6*	15648.64	15654.6
	I	*15682.9*	15677.95	15682.9
	L	*15697.6*	15695.12	15697.9
	M	*15712.6*	15709.38	15712.7
$^5S_2$+$^5F_4$	A	18505.6	18516.22	18505.6
	B	18509.8	18517.70	18509.7
	C	18538.4	18542.05	18538.4
	D	18549.8	18550.89	18549.8
	E	18553.8	18553.70	18553.9
	F	18589.1	18586.42	18589.1
	G	18597.7	18598.90	18597.7
	H	*18649.3*	18651.33	18649.3
	I	*18686.1*	18684.55	18686.1
	L	*18697.4*	18696.16	18697.4
	M	*18706.6*	18704.39	18706.6
	N	*18717.6*	18716.60	18717.6
	O	*18717.6*	18717.46	18717.6
	P	*18744.0*	18743.94	18744.0
$^5F_3$	A	20652.2	20645.95	20652.3
	B	20654.0	20659.79	20654.1
	C	20678.9	20675.16	20679.1
	D	*20769.2*	20763.24	20769.4
	E	*20769.2*	20763.48	20769.4
	F	*20780.6*	20783.19	20780.8
	G	*20785.1*	20788.11	20785.2

$^{2S+1}L_J$	**Level**	**Exp. (cm^{-1})**	**Calc. (cm^{-1})**	**Exp. (cm^{-1})**
$^5F_2$+$^3K_8$	A	-	21155.94	21400 barycenter
	B	-	21156.52	
	C	-	21188.32	
	D	-	21231.54	
	E	-	21234.43	
	F	-	21381.00	
	G	21388.2	21385.79	
	H	21388.2	21387.46	
	I	21395.1	21388.97	
	L	21402.4	21403.83	
	M	21405.1	21407.60	
	N	21422.4	21410.31	
	O	21426.6	21417.41	
	P	*21431.8*	21441.09	
	Q	-	21479.34	
	R	-	21491.48	
	S	21496.3	21493.24	
	T	*21501.4*	21504.21	
	U	*21507.1*	21506.40	
	V	*21511.0*	21507.27	
	W	*21522.6*	21530.55	
	Y	*21522.6*	21530.70	
$^5G_6$+$^5F_1$	A	22144.8	22150.87	22310 barycenter
	B	22144.8	22151.53	
	C	22179.5	22190.68	
	D	22190.2	22196.40	
	E	22212.9	22208.04	
	F	22214.4	22209.78	
	G	-	22304.26	
	H	*22327.6*	22308.37	
	I	*22333.7*	22326.27	
	L	*22341.4*	22349.62	
	M	*22382.8*	22398.50	
	N	*22382.8*	22399.23	
	O	*22415.2*	22405.59	
	P	-	22411.09	
	Q	*22458.2*	22429.49	
	R	-	22495.48	

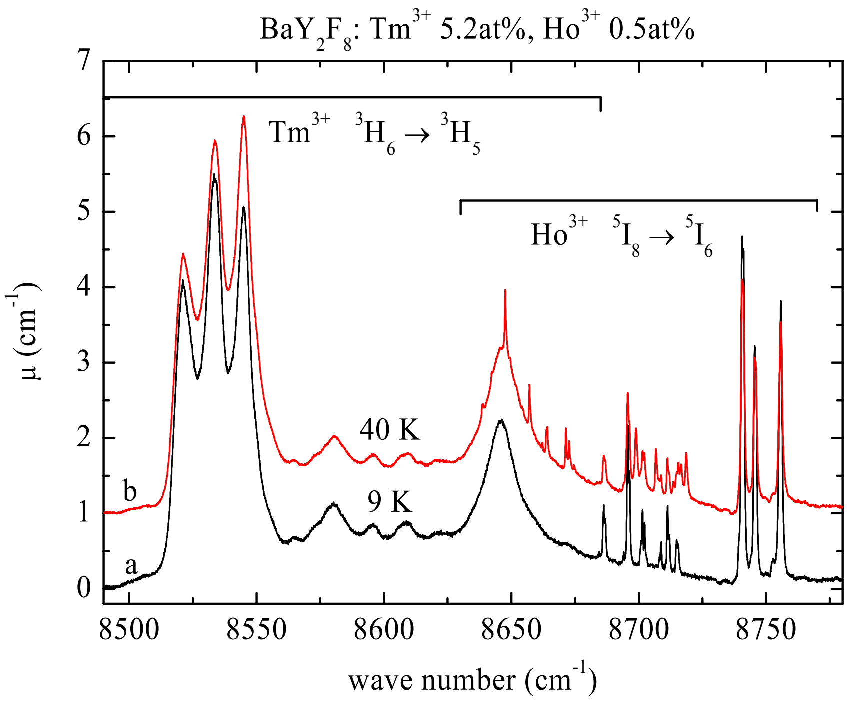

Figure 2.11 Optical absorption spectra measured at 9 (curve a) and 40 K (curve b) on a BaYF: Tm^{3+} 5.2at%, Ho^{3+} 0.5at% sample in the region of the Tm^{3+} $^3H_6$ → $^3H_5$ and Ho^{3+} $^5I_8$ → $^5I_6$ transitions.

It is important to notice that the high resolution spectroscopy at 9 K allowed separating some sublevels very close one to each other, as the first two sublevels of the ground manifold. Due to this small separation (0.6 cm^{-1}), it was very difficult to distinguish between X1 and X2 lines; in the third column of Table 2.4 are indicated in italic type these lines.

While the position of the sublevels 3, 4, 5, 6, and 7 was derived only from the analysis of the $^5I_8$ → $^5I_7$ transition, the separation between the first two sublevels of the ground manifold was averaged over 55 pairs X1-X2. A lot of hot bands related to transitions from sublevels higher than the seventh within the ground manifold were detectable in the high temperature spectra measured in the $^5I_8$ → $^5I_7$ transition range (see Figure 2.7). However, it is difficult to do an unequivocal attribution of these lines, due to the absence of measurements at different temperatures in the ranges of other transitions.

The positions of the energy levels of the excited manifolds were fitted with a single-ion Hamiltonian (Table 2.4, fourth column) and a root mean square deviation $\sigma = 5.5\ cm^{-1}$

was obtained. Then, the agreement is good, and, in particular, it is better than that achieved in Ref. [28].

The energy sublevel values tabulated in Ref. [28] are reported in the last column for comparison. The most important refinements obtained in the present work are the determination of two more sublevels within the ground state (39.3 and 88.7 cm^{-1}) and the attribution of the lines of the $^5I_8 \rightarrow {}^5F_2+{}^3K_8$ and $^5G_6+{}^5F_1$ transitions.

Table 2.5 Coulomb, spin-orbit and CF parameters obtained for Ho^{3+} from experimental data fitting.

Parameter	Data fit
F^2	94325±42
F^4	66294±75
F^6	52001±42
ζ	2142±1
B_2^0	-555±16
B_4^0	-1204±18
B_6^0	492±7
B_2^2	74*
B_4^1	295*
B_4^2	93*
B_4^3	4*
B_4^4	345*
B_6^1	-262*
B_6^2	-52*
B_6^3	-84*
B_6^4	408*
B_6^5	-387*
B_6^6	262*

*** Value related to the fixed ratio (see text).**

Table 2.5 lists the Coulomb, spin-orbit and CF parameters obtained from experimental data fitting. To calculate the CF parameters, due to the large number of them, only the three B_q^0 were varied freely, while the ratio B_q^k / B_q^0 was kept fix (related values indicated with * in Table 2.5) at the value obtained for Er^{3+} in Ref. [31], being Er^{3+} near Ho^{3+} in the periodic table. The other free ion parameters were kept fix to the values obtained for Ho^{3+} in LaF_3 by Carnall *et al.* [33]. It is possible to compare these parameters with those obtained for Tm^{3+} (Section 2.4.1.1), Nd^{3+}, Dy^{3+}, and Er^{3+} [6, 7, 31] (Table 2.6). They follow the expected trend: the free ion parameters slightly increase with the atomic number, while the CF ones slightly decrease or remain more or less constant along the series.

Table 2.6 Coulomb, spin-orbit and CF parameters obtained for different RE^{3+} from experimental data fitting.

Parameter	Nd^{3+}(a)	Dy^{3+}(a)	Ho^{3+}(b)	Er^{3+}(c)	Tm^{3+}(b)
F^2	72625	90000	94325±42	96354	99980±130
F^4	53086	65060	66294±75	68601	69770±110
F^6	35425	48267	52001±42	53204	55980±320
ζ	880	1911	2142±1	2362	2632±1
B^0_2	-620	-500	-555±16	-450	-449±27
B^0_4	-1123	-1580	-1204±18	-1430	-1250±35
B^0_6	780	650	492±7	470	420±25
B^2_2	-120	-10	74	60	60
B^1_4	240	450	295	350	306
B^2_4	60	60	93	110	96
B^3_4	700	-130	4	5	4
B^4_4	470	440	345	410	358
B^1_6	-190	-230	-262	-250	-223
B^2_6	10	50	-52	-50	-45
B^3_6	-240	-20	-84	-80	-71
B^4_6	890	430	408	390	337
B^5_6	-610	-390	-387	-370	-331
B^6_6	-90	100	262	250	223

(a) From Ref. [6].
(b) Present work.
(c) From Ref. [31].

2.4.2 Linear dichroism

Figure 2.4 shows the effect of the polarization of the incident electric field E_l on the absorption spectra of Tm^{3+} in BaYF in the region of the $^3H_6 \rightarrow {}^3F_4$ transition.

Being BaYF a monoclinic crystal, it was possible to follow the approach described in Ref. [34] to determine the orientation of the dielectric ellipsoid and of the dipole moments μ associated with each transition. Figure 2.12 visualizes the positions of dielectric principal axes *X*, *Y*, and *Z*, the incident electric field E_l, and the transition moment μ with respect to the crystallographic axes *a*, *b*, and *c*. In the monoclinic structure the *b* axis coincides with the *Y* axis [26], thus the axes *X* and *Z* lie in the *a*-*c* plane. If the incident radiation enters the crystal along the direction parallel to the *b* axis (i.e. perpendicular to the sample) it will not be refracted and E_l belongs to the same *a*-*c* plane (see Figure 2.12).

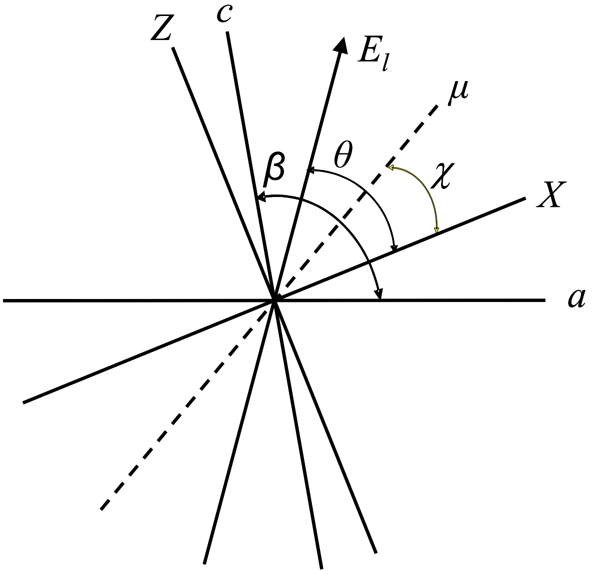

Figure 2.12 Positions of dielectric principal axes *X* and *Z*, incident electric field E_l, and transition moment μ with respect to the crystallographic axes *a* and *c*. The *b* and *Y* axes are perpendicular to the plane.

If the incident light is polarized at an angle θ with respect to the *X* axis, the absorbance α can be expressed as a function of θ as:

$$\begin{aligned}\alpha(\theta) &= -\log\frac{I}{I_0} = -\log\left(T_X\cos^2\theta + T_Z\sin^2\theta\right) = \\ &= -\log\left(10^{-\alpha_X}\cos^2\theta + 10^{-\alpha_Z}\sin^2\theta\right)\end{aligned} \qquad 2.3$$

where I_0 and I are the incident and transmitted radiation intensities, respectively, $T_{X,Z}$ are the principal transmittances, and $\alpha_{X,Z}$ are the principal absorbances.

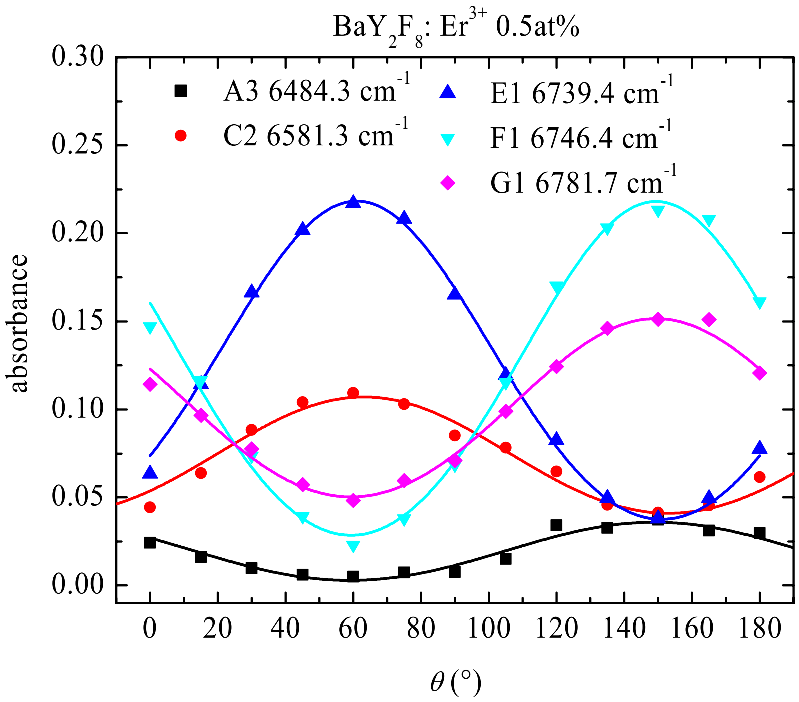

Figure 2.13 Angular dependence on E_l for the maximum of a few lines detected in the spectra measured at 9 K on a BaYF: Er^{3+} 0.5at% sample. The beam travels along the *b* axis and θ is the angle between E_l and the normal to the *a* axis.

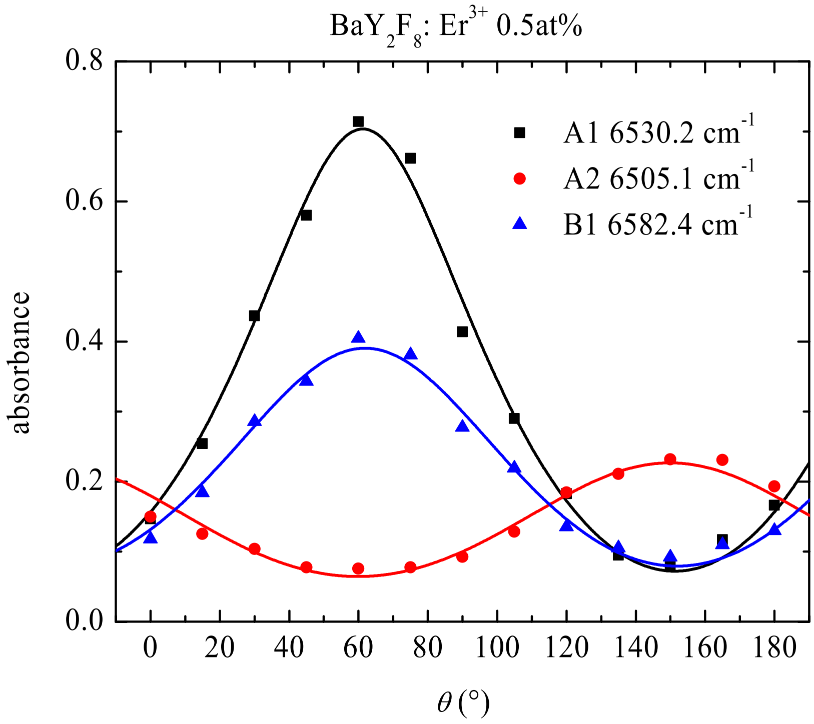

Figure 2.14 Angular dependence on E_l for a few strong lines (see text) detected in the spectra measured at 9 K on a BaYF: Er^{3+} 0.5at% sample. The beam travels along the *b* axis and θ is the angle between E_l and the normal to the *a* axis.

Figure 2.13 and Figure 2.14 display the angular dependences on E_l for a few lines detected in the spectra measured at 9 K on a BaYF: Er^{3+} 0.5at% sample with the light travelling along the *b* axis and being θ the angle between E_l and the perpendicular to the *a* axis. The data were fitted according to eq. 2.3. The $\alpha(\theta)$ for the lines is displayed in Figure 2.14 by plotting the amplitude taken not at the peak (either out of scale or affected by the detector nonlinearity because too high) as for the weak lines in Figure 2.13 but on the line tail at 0.1 cm^{-1} from the peak position.

All the lines have the maximum or the minimum in the same position (see Table 2.7, third column), i.e. θ_M~(60.6±1.4)° with respect to the normal to the *a* axis; then, θ_M~(29.4±1.4)° with respect to the *a* axis. This value is in good agreement with that reported in literature: 22° [26]; the difference can be in part accounted for by the different temperatures at which the measurements were performed.

Table 2.7 Angles θ_M and χ for different lines of the Er^{3+} transition $^4I_{15/2} \rightarrow {}^4I_{13/2}$.

Line	Position (cm^{-1})	θ_M (°)	Error θ_M (°)	χ (°)
A3	6484.3	59	2	74.15
A2	6505.1	60	2	61.94
A1	6530.2	61.3	0.8	17.74
B3	6536.2			45
C2	6581.3	63	2	31.76
B1	6582.4	62	1	24.26
D1	6695.5			45
E1	6739.4	61	0.5	22.54
F1	6746.4	59.4	0.7	70.12
G1	6781.7	59.3	0.9	60.05

On the other hand, from the values of α_X and α_Z derived from the fitting according to eq. 2.3, it was possible to calculate also the angle χ between the projection of the dipole moment μ (electric dipole matrix element associated with a given transition between sublevels of different manifolds) and the *X* axis. In fact, the dichroic ratio

$$D = \frac{\alpha_X}{\alpha_Z} = \sqrt{\frac{\varepsilon_Z'}{\varepsilon_X'}} \cot^2 \chi = \frac{n_Z}{n_X} \cot^2 \chi \qquad 2.4$$

links $\alpha_{X,Z}$ with χ through the real parts of the dielectric constant $\varepsilon_{X,Z}'$, then through the refractive indices along the principal axes $n_{X,Z}$ [34]. Taking into consideration the difficulties in aligning the sample and in evaluating the line amplitude, it was allowed to approximate $n_Z / n_X \sim 1$, also considering the weak dependence of the refractive index on the wavelength as evaluated by means of the Sellmeier coefficients [35]. The values derived according to eq. 2.4 for the lines displayed in Figure 2.13 and Figure 2.14 are listed in Table 2.7, last column. The B3 and D1 lines do not change with the polarization angle, thus the direction of the dipole moment should be at 45°. Figure 2.15 plots the values obtained as a function of the line position; two values derived from the spectra measured on a Er^{3+} 20at% doped sample are also reported. The values are grouped around five discrete angles: 20, 33, 45, 60, and 70° with respect to the *X* axis, i.e. $\beta_{\pm}=22°\pm\chi$ with respect to the *a* axis (Table 2.8).

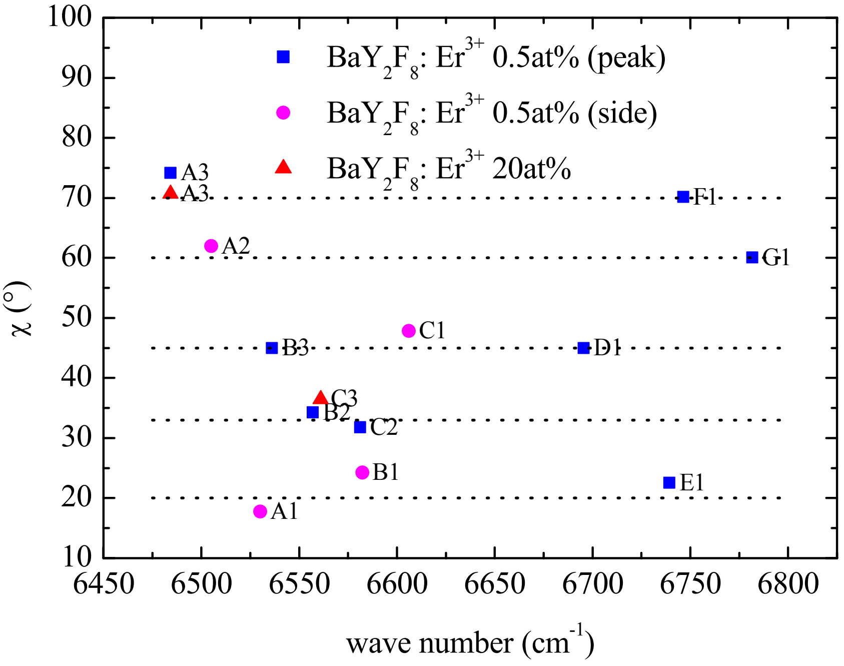

Figure 2.15 Values of the χ angle as a function of the position of the associated line.

Table 2.8 Discrete χ values derived from Figure 2.15 and related $\beta_\pm$ angles and absorption lines.

χ (°)	β_+ (°)	β_- (°)	Lines
20	42	2	A1, B1, E1
33	55	-11	B2, C2, C3
45	67	-23	B3, C1, D1
60	82	-38	A2, G1
70	92	-48	A3, F1

To better understand the arrangement of the dipole moments in the BaYF structure, Figure 2.16 shows the projection of the primitive cell on the *a*-*c* plane and of the dipole moments: the latter are applied to a Y^{3+} ion. Only in the cases of 55, -11 (panel B), and 67° (panel C) there is a correspondence with the projection of a Y^{3+}-F^- bond.

This approach cannot be applied to BaYF: Ho^{3+} due to the large overlapping between different Xi lines. In the case of Tm^{3+} doped samples, there were one more difficulty: at 9 K only the X1 and X2 absorption lines are detectable and in most cases it was not possible to discriminate between them.

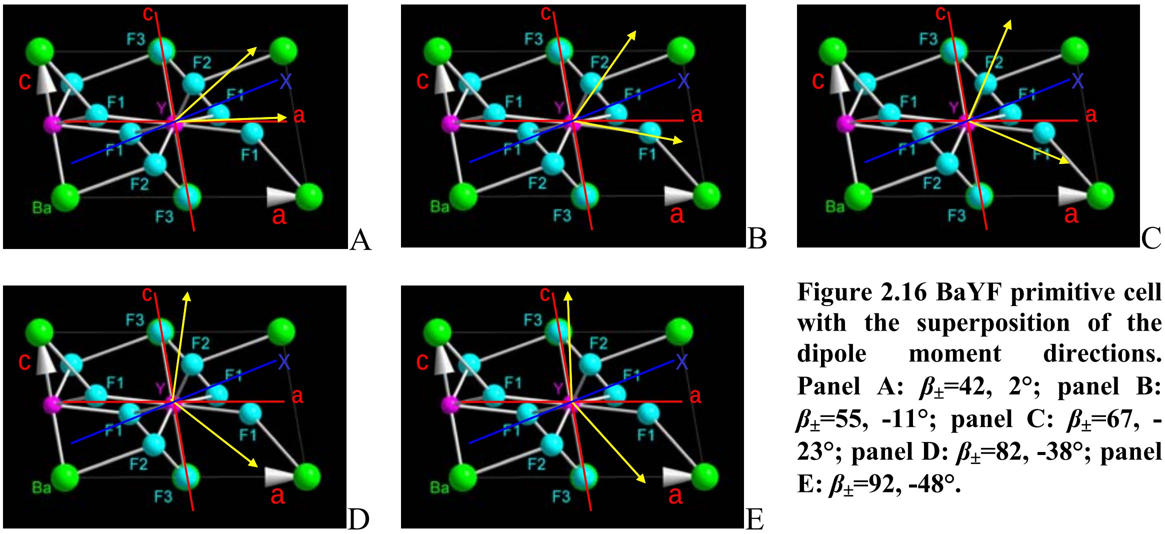

Figure 2.16 BaYF primitive cell with the superposition of the dipole moment directions. Panel A: $\beta_\pm$=42, 2°; panel B: $\beta_\pm$=55, -11°; panel C: $\beta_\pm$=67, -23°; panel D: $\beta_\pm$=82, -38°; panel E: $\beta_\pm$=92, -48°.

2.4.3 RE^{3+}-local mode interaction

Analyzing the absorption spectra measured on Er^{3+} and Tm^{3+} doped samples, a series of weak, extremely narrow (0.03-0.1 cm^{-1}), and closely spaced (~0.2-0.8 cm^{-1}) lines, was detected on both sides of the narrowest zero-phonon (ZP) lines (i.e. the lines induced by a pure electronic transition from a sublevel of the ground manifold to a sublevel of an excited manifold). This fine structure (FS) covers a few cm^{-1} range around the ZP lines, and was analyzed as a function of RE^{3+} concentration, temperature, and polarization angle.

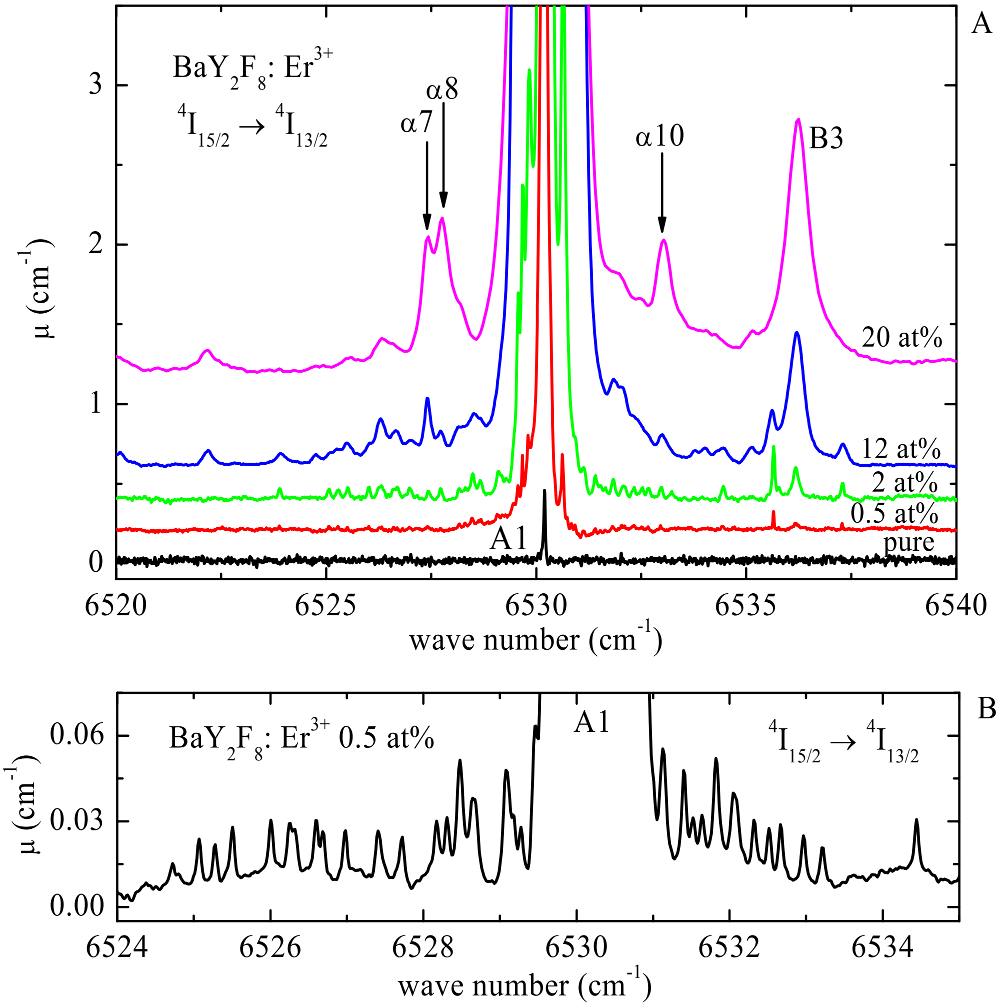

Figure 2.17 Optical absorption spectra, measured at 9 K on BaY_2F_8 samples doped with different Er^{3+} concentrations, in the region of the $^4I_{15/2}\rightarrow{}^4I_{13/2}$ transition. Panel A: nominally pure sample, 0.5, 2, 12, and 20 at%. The solid arrows indicate the α lines due to Er^{3+} clusters. Panel B: magnification of the weak lines displayed in panel A for the Er^{3+} 0.5at% doped sample.

Figure 2.17, panel A displays the FS which accompanies the A1 line at 6530.2 cm^{-1} ($^4I_{15/2} \rightarrow ^4I_{13/2}$ transition) in BaYF samples doped with different Er^{3+} concentrations: from 0.5 to 20at%. A nominally pure sample spectrum is also reported; it shows the very weak and narrow A1 line due to Er^{3+} traces. In panel B there is a magnification of the weakest between the FS lines in the spectrum of the Er^{3+} 0.5at% doped sample: the excellent signal-to-noise ratio allows seeing even the finest details of the structure, and FS lines separated only by 0.34-0.4 cm^{-1} from the A1 line can be distinguished. Curves in Figure 2.17, panel A show how the FS lines increase by increasing the doping level. This suggests the FS line are related to the RE^{3+} presence. In spectra of high concentration samples the FS lines were affected both by inhomogeneous broadening and by the overlapping of bands due to Er clusters (α lines indicated by arrows in panel A) [31], then they were less resolved and distinguishable.

The fine structure was detectable also near other lines, both in the same transition (as A2, B1 B2, and C1) and in the $^4I_{15/2} \rightarrow ^4I_{11/2}$ transition, even if the high energy of the reached sublevel in the ZP transition induced an absorption line increase that hides the nearest among the FS lines.

By increasing the temperature, the FS line amplitude gradually decreases and most of the FS lines is no longer detectable yet at 30 K.

The spectra of Tm^{3+} doped samples displayed similar FS patterns, as shown by line A1 and A2 in Figure 2.4; in this case too, the FS lines were present near other ZP lines of the same transition or in other. However, in the Tm^{3+} case the FS lines vanished at 60 K, i.e. at a higher temperature than the Er^{3+} case. Moreover, due to the closeness of the A1 and A2 lines, it was difficult to assign each FS line to a given ZP line, by simply analyzing the unpolarized spectra. Figure 2.18, panel A reports the angular dependence on E_l of the A1 and A2 ZP lines and of some FS lines close to them detected in a Tm^{3+} 1at% doped sample in the region of the $^3H_6 \rightarrow ^3F_4$ transition. The FS lines exhibit the same angular dependence on E_l of the ZP line they are associated with. The same behaviour is shown in Figure 2.18, panel B in the case of an Er^{3+} doped sample. The data displayed in Figure 2.18 were analyzed according to the procedure described in Section 2.4.2 to estimate the orientation of both the index ellipsoid principal axis and of the dipole moment associated with a given transition; the angles obtained are, within the experimental error, the same for a ZP line and the relative FS lines. In this way it was possible to associate unequivocally the FS lines with their ZP line.

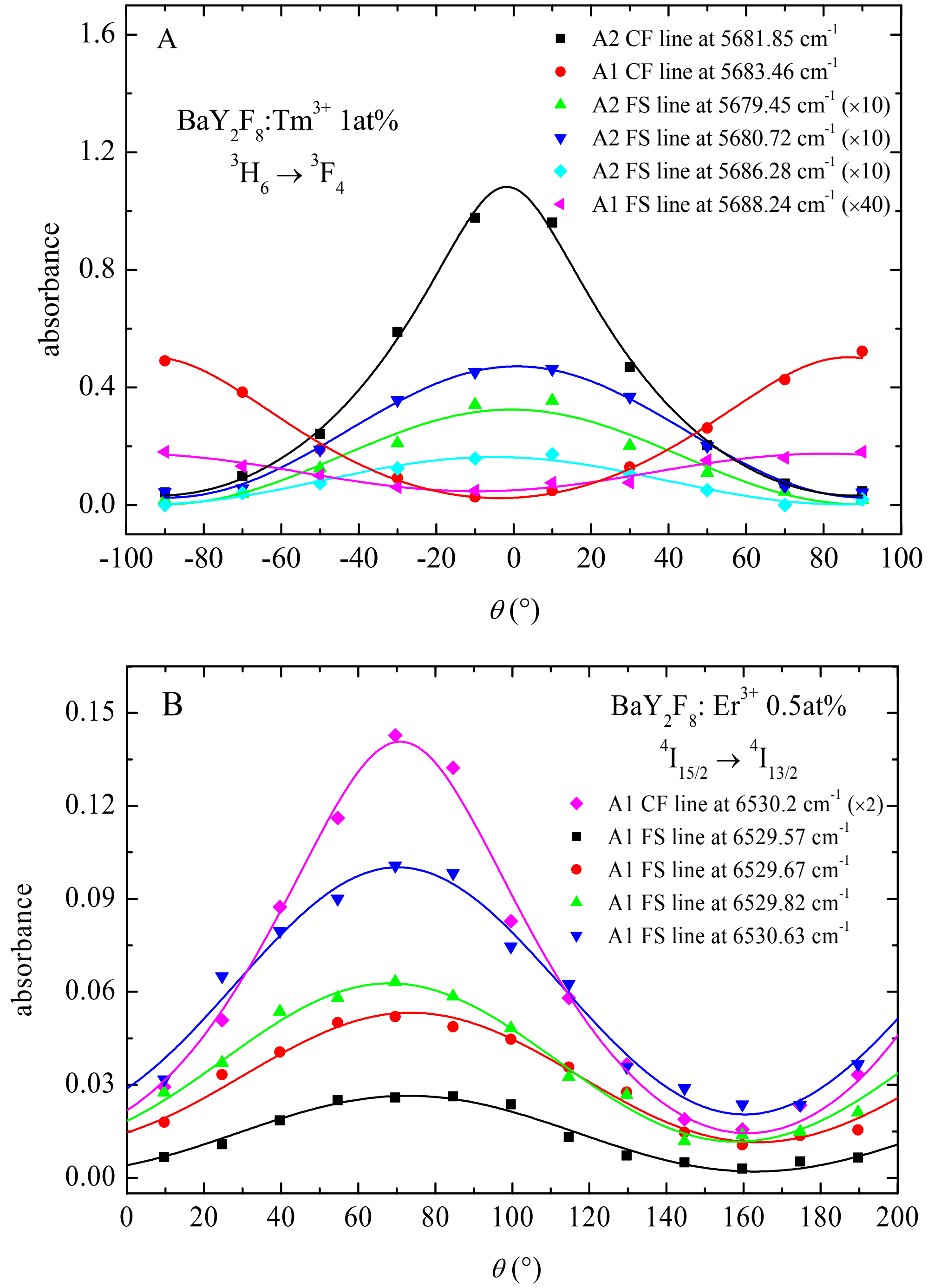

Figure 2.18 Angular dependence on the light electric field E_l orientationfor a few lines detected in the spectra measured at 9 K. Panel A: BaY$_2$F$_8$: Tm^{3+} 1at% sample in the region of the $^3H_6 \rightarrow {}^3F_4$ transition. The beam travels along the *c* axis and θ is the angle between E_l and the *b* axis. Panel B: BaY$_2$F$_8$: Er^{3+} 0.5at% sample in the region of the $^4I_{15/2} \rightarrow {}^4I_{13/2}$ transition. The beam travels along the *b* axis and θ is the angle between E_l and the *c* axis.

The hypotheses formulated to explain the origin of the FS lines were:

1. hyperfine interaction or isotopic effects: the number of expected lines due to hyperfine interaction ($2I+1$, where $I = 7/2$ and $1/2$ are the nuclear spin of Er^{3+} and Tm^{3+}, respectively) and isotope effects (one line for each RE^{3+} isotope, in the case of Er^{3+}) is much lower than that observed [36]. Moreover, hyperfine interaction should be excluded because, once the value of the coupling constant and the CF eigenfunctions for a given RE^{3+} in the host crystal are known, its associated features and energy splitting should follow precise quantitative and qualitative patterns [9, 10] which are not compatible with the present observations;
2. vibronic transitions: the FS lines cannot be induced by vibronic transitions (transitions in which a photon and a phonon are simultaneously absorbed [15, 37]) because the separations between them and the relative ZP lines are small and the density of states for lattice modes of such low energies is negligible;
3. RE^{3+}-RE^{3+} interaction: as shown in Figure 2.19, where the amplitudes of the FS line at 6530.63 cm^{-1} (the most intense among the FS lines), the G1 ZP line, and the α line (i.e. a line due to Er^{3+} clusters [31]) at 6522.2 cm^{-1} are displayed as a function of the temperature. The FS line exhibits a much faster temperature decay with respect the other two types of absorption lines. This suggests a different origin. The G1 line was chosen as representative of the ZP lines, instead of the A1, because its amplitude was comparable with that of the FS line at 6530.63 cm^{-1}, while that of the A1 was very high, thus cannot be evaluated correctly over the whole temperature range (it was affected by the detector non-linearity);
4. isolated perturbed sites: since the RE^{3+} substitutes for the homovalent Y^{3+}, charge compensating defects are not required; thus, no defect is expected to neighbour the RE^{3+}. Moreover, the random distribution of isolated perturbed sites (e.g., vacancies and interstitial ions) is expected to induce an inhomogeneous broadening of the ZP lines rather than the well-defined FS pattern. Finally, the statistical weight of satellite lines due to defects should change from sample to sample and in different parts of the same sample. This is not the case of FS lines: see Figure 2.17, panel A, where spectra of different samples are displayed and, in particular, compare the spectrum of the Er^{3+} 0.5at% thin sample in panel A with that of a thick sample in panel B;

5. off-centre position: to rule out this hypothesis as the main responsible for the FS lines (suggested by the CF parameter analysis in Ref. [5]), measurements on a Er^{3+} 2at% sample were performed at 9 K after submitting the sample to two different cooling procedures. In fact, a slow cooling should reduce the number of ions located in off-centre positions with respect to a fast cooling, thus the FS line amplitude should decrease. There were no differences between the two measurements.

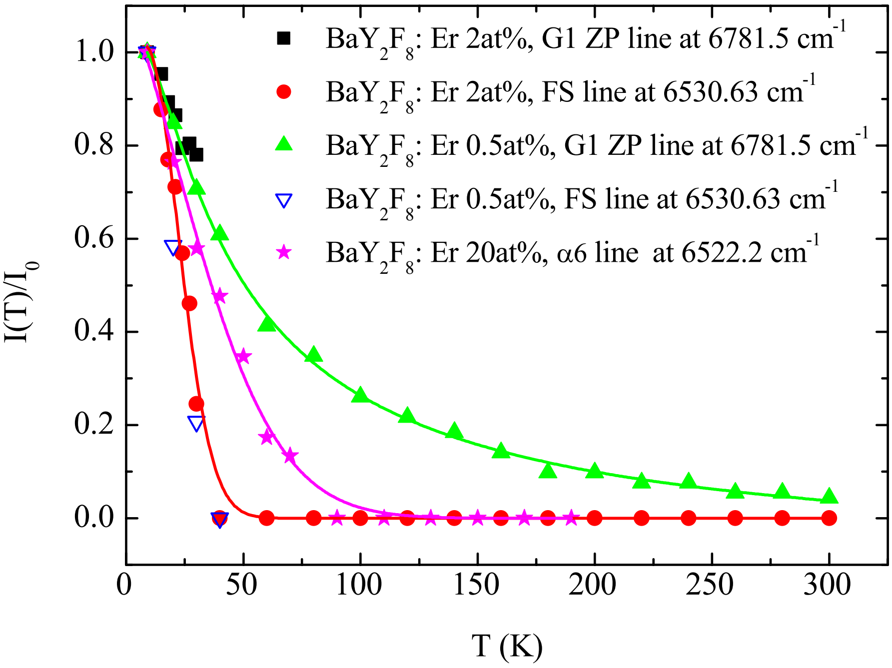

Figure 2.19 Temperature dependence of the amplitude for a few lines detected in BaY_2F_8 samples doped with different Er^{3+} concentrations (0.5, 2, and 20at%). The solid lines are guides for the eyes.

The FS lines were attributed to a simultaneous excitation both of an electronic and a local mode (see, for example, [38-40]). Since the energy quanta involved are small (~10^{-4} eV), good candidates for the local mode are hindered rotations or librations within the eight fluorine cage surrounding the Y^{3+} site. Among the fluorine ions, four are classified as F1, two as F2, and two as F3 on the basis of their position, distance from Y^{3+}, and thermal parameters. Two different considerations could justify the possibility of librational motion of RE-F3 group.

1. The rather large thermal parameter suggests that the F3 anion may be slightly out of the binary axis and may benefit of some mobility [26].
2. The F-F distances are larger than the sum of the ionic radii, providing some room for possible F oscillations [26].

Some of the lines were located at the same distance on both sides of the relative ZP line. The presence of lines even in the low-energy side in the 9 K spectra was consistent with the fact that possible rotational-like energy excited states may be already populated at low temperature, due to their small separation from the ground state. Among the FS lines, those located symmetrically with respect to the related ZP line and common to more than one ZP line (i.e., present at the same distance from different ZP line, also in different transitions and samples), were selected (due to their large statistical weight) and their separation from the ZP line was plotted as a function of a quantum number *n* (Figure 2.20).

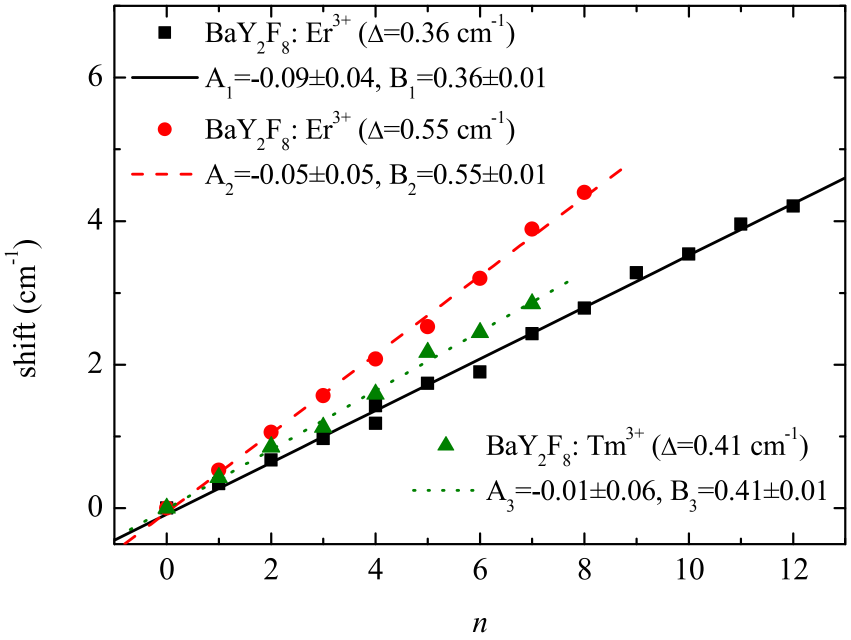

Figure 2.20 FS line sequences observed in BaYF samples doped with Er^{3+} (■ and ●) and Tm^{3+} (▲). The separation of the FS lines from the related ZP is plotted vs a quantum number *n*. The straight lines are the linear fits of the experimental data.

Two sequences of nearly equispaced FS lines were identified for Er^{3+} doped samples, and two for Tm^{3+} doped samples (one of them is not displayed in Figure 2.20 for clarity, since it practically overlaps the black squares sequence). The data were fitted according to straight lines y=A_i+B_i: the resulting slopes B_i for Er^{3+} doped samples were (0.36±0.01) and (0.55±0.01) cm^{-1}, and (0.355±0.003) and (0.41±0.01) cm^{-1} for Tm^{3+} doped samples. The equispaced sequences suggest a free-rotator like behaviour [41]; in this case, the slope of the straight line provides the separation 2*B*, where *B* is the rotational constant $B = \hbar^2 / 2M_I$, with $\hbar$ the reduced Planck's constant and M_I the moment of inertia.

2*B* could be evaluated as 2*B*=0.39 cm^{-1} for the Er-F3 group from the separation *d*=2.242 Å [26] and ion masses. Comparable values were obtained for the Er-F1 and Er-F2 complexes, and for similar complexes in BaYF: Tm^{3+}. The value is in excellent agreement with those supplied by the straight line fitting. The differences could be due to the fact that the RE-F separations were derived from X-ray diffraction measurements performed at room temperature, while the FS lines were monitored at 9 K. Being the thermal expansion coefficients anisotropic, a distortion of the BaYF unit cell could take place (confirmed by CF parameter analysis [5]).

Further support come from the analysis of the specific heat measurements performed on BaYF: Er samples (Figure 2.9). As already observed in Section 2.3.3, the specific heat (C_p) above 20 K is nearly the same for the four samples, suggesting that only lattice vibrations contribute to C_p. In insulating crystals phonons usually dominate the thermal properties: both pure and Er^{3+} 0.5at% doped samples showed a C_p which, below 12 K, follow strictly the Debye T^3-law. From the slope of the related straight line in the log-log plot a Debye temperature T_D=388 K could be extracted. Below 20 K, as a rule, C_p of insulating crystals doped with paramagnetic ions may include also a contribution C_{CF}, coming from the CF, in addition to the vibrational one C_{Vib}, i.e. $C_p = C_{Vib}+C_{CF}$. To evaluate the C_p excess displayed by Er^{3+} 12 and 20at% doped samples and its temperature dependence, the specific heat of the undoped sample is assumed to supply the vibrational contribution (C_Y=C_{Vib}) and it is subtracted from that of heavy doped samples (C_{Er}). The resulting ΔC=C_{Er}-C_Y provides an estimate of the anomalous contributions (Figure 2.21, panel A). Both contributions exhibit a bump at about 17 K, whose magnitude increases by increasing the Er^{3+} concentration, and a further upturn at temperatures lower than about 3.5 K, which follows a T^{-2} dependence. The specific-heat excess ΔC is divided by the nominal number of Er^{3+} moles and by R (the universal gas constant). The so-obtained $\Delta C_m/R$ data for both concentrations (Figure 2.21, panel B) overlapped (particularly at T>5 K) within the experimental error, showing ΔC divided by the concentration. Both the low (below 3.5 K) and high temperature (at about 17 K) contributions to ΔC_m exhibit the characteristics of a Schottky anomaly, which is well known to grow exponentially with temperature and, at sufficiently high temperatures, to decrease as T^{-2}. Thus, the influence of the low temperature anomaly on the maximum amplitude of the high temperature one is small. The anomaly maximum at about 17 K suggests a splitting of about 40.9 K or 28.4 cm^{-1}, a value little higher than the separation of Δ_1=25 cm^{-1} between the first two sublevels of the ground $^4I_{15/2}$ manifold determined in Ref. [31]. On the other hand, Δ_1 between two levels with the same degeneracy (Kramers doublet) is not sufficient to fit the maximum amplitude (0.61-0.66) of $\Delta C_m/R$ at about 17 K. Thus, the electronic transitions towards the second excited doublet above the ground state (at 46 cm^{-1} [31]) are also considered (Δ_2) and the following expression for the specific heat was deduced:

$$\frac{\Delta C_m}{R} = \left(\frac{\Delta_0}{2T}\right)^2 + \left\{ \frac{\left(\frac{\Delta_1}{T}\right)^2 \exp\left(-\frac{\Delta_1}{T}\right) + \left(\frac{\Delta_2}{T}\right)^2 \exp\left(-\frac{\Delta_2}{T}\right) + \left(\frac{\Delta_2 - \Delta_1}{T}\right)^2 \exp\left(-\frac{\Delta_1 + \Delta_2}{T}\right)}{\left[1 + \exp\left(-\frac{\Delta_1}{T}\right) + \exp\left(-\frac{\Delta_2}{T}\right)\right]^2} \right\} \qquad 2.5$$

where the T^{-2} behaviour of ΔC_m observed below 3 K is accounted for by considering the high temperature tail of a single Schottky anomaly with a Δ_0 splitting. The data of Er^{3+} 12at% in Figure 2.21, panel B are fitted according to eq. 2.5 (curve a) with the splittings deduced from spectroscopy: Δ_0=0.79 K (0.55 cm^{-1}), Δ_1=36 K (25 cm^{-1}), and Δ_2=66.2 K (46 cm^{-1}). To fit Er^{3+} 20at% data it is necessary to introduce an additional low-temperature Schottky anomaly: $\Delta_{0,a}$=0.52 K (0.36 cm^{-1}), suggested again by spectroscopy measurements (Figure 2.20). Both fits can be considered satisfactory, by considering that the accuracy of the ΔC values decreases with rising the temperature above about 17 K. The difference between the curves a and b for T<3.5 K can be tentatively explained by the increased statistical weight of Er clusters in Er^{3+} 20at% doped sample: as demonstrated in Ref. [31], the electronic sublevels of clusters do not change meaningfully (Table VII in Ref. [31]), while the rotational-like frequencies of the Er-F groups could be more affected, for example, by the slight lattice distortions caused by an additional neighbouring Er^{3+}.

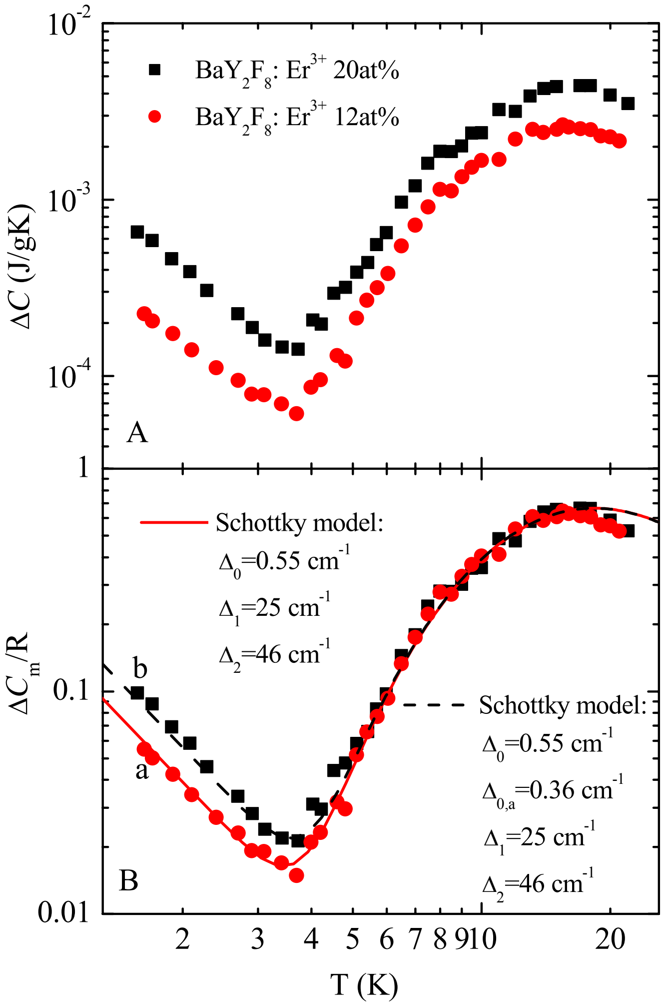

Figure 2.21 Temperature dependence of the excess contribution to the specific heats $\Delta C = C_{Er} - C_Y$ (panel A) and to the specific heats per mole Er (ΔC_m) with respect of a nominally pure sample (panel B) of two BaYF: Er^{3+} samples doped with 12 (●) and 20at% (■). The solid and dashed lines are the results of different fitting approaches according to eq. 2.5 using three (curve a) and four (curve b) Schottky contributions, respectively.

Thus, the fit shows that the anomalous specific heat at T>3.5 K is due to electronic transitions between the first three sublevels of the Er^{3+} ground manifold. The level separation of a few tenths of cm^{-1} extracted from the T^{-2} behaviour monitored at T<3.5 K confirmed a contribution given by rotational-like levels of the Er-F complex. Unfortunately, the limited temperature range explored (down to 1.5 K) prevents a complete evaluation of the magnitude of the low temperature Schottky anomalies.

Specific heat measurements on Tm^{3+} doped samples were not performed, because the separation between the two lowest sublevels of the ground $^3H_6$ manifold is only 1.6 cm^{-1} (see Section 2.4.1.1): the electronic contribution is expected to overlap that coming from the rotational-like levels (Δ=0.36÷0.41 cm^{-1}), thus precluding any clear cut interpretation.

The description of Er-F as a free rotator is too näive and does not consider all the other not equispaced FS lines.

A hindered rotator model [42, 43] predicts line rich roto-vibrational absorption spectra that resemble the FS pattern in the present work. At low temperatures the lines are fewer and not equally spaced (unless the energy barrier V_0 vanishes and/or the temperature is high enough to allow free rotations); some of them are due to librations of the molecular group within the potential wells: in this case the librational absorption lines appear on the high energy side, well separated from the central line. For $k_BT<<V_0$ the molecular group occupies levels below the top of the barrier and the energy levels are those of a harmonic oscillator of frequency ν_{libr} (in cm^{-1}) which depends on V_0 (in cm^{-1}) and on the rotational constant B (in cm^{-1}) as [44]

$$\nu_{libr} = 2\sqrt{V_0 B} \,. \qquad 2.6$$

This equation was originally obtained by Pauling [45] for a potential

$$V = \frac{1}{2} V_0 \left(1 - \cos 2\vartheta\right) \qquad 2.7$$

where ϑ is the angle between the molecular group and a reference axis.

Tunneling across the energy barrier is also expected. There is no contradiction between the two descriptions: the closely spaced energy levels of hindered rotator (a model suitable for low or medium potential energy barriers) converge to those expected on the basis of tunneling between different minima (suitable for higher energy barriers) [43, 46]. The hindered-rotator model expresses the rotational motion as a linear combination of spherical harmonic wave functions, while the tunneling model calculates the same energy levels by allowing localized harmonic oscillator wave functions to overlap the equivalent wave functions in neighbouring potential wells [46].

In the case of Tm^{3+} doped samples, it was possible to identify the librational lines associated with A1 and A2 lines as the main ones within the two groups on the higher energy side, separated from the associated ZP lines by 4.5 and 4.7 cm^{-1}, respectively (see Figure 2.4). They peak at 5688.24 and 5686.28 cm^{-1}, and have the same polarization dependence as the A1 and A2 lines, respectively (see Figure 2.18, panel A). Also if the potential given by the eq. 2.7 is not the same probed by the Tm-F group in BaYF, V_0 may be roughly estimated by assuming the librational frequencies as ν_{libr}=4.5 and 4.7 cm^{-1} and $2B$ as 0.41 cm^{-1}. The resulting values of V_0 are about 25 and 27 cm^{-1} (of the order of 3×10^{-3} eV), i.e. the energy barrier ‘seen’ by the librating Tm-F molecular group, when the Tm^{3+} electronic transition starts from the first two sublevels of the ground $^3H_6$ manifold, respectively, to reach the first sublevel of the excited $^3F_4$ manifold (A1 and A2 lines). The low values of V_0 explain why the FS lines are no longer detectable yet at T>60 K. At higher temperature, the free rotator line spectrum should be detected; this was not possible due to the simultaneous line broadening. At low temperatures the barrier can be crossed only by tunneling and the Tm-F molecular group performs only small angular oscillations (librations) within the well.

In BaYF: Er^{3+} spectra it was difficult to identify unequivocally a librational line, from whose position V_0 might be, at least roughly, estimated according to eq. 2.6. This could be due to the fact that the Er^{3+} FS lines are no longer detectable at 40 K, then the energy barrier which separates different orientations of the Er-F group is still less than that estimated for the Tm-F complex. Thus, 9 K is probably a temperature high enough to forbid the librational line detection.

2.4.4 Hyperfine structure

Some absorption lines of the Ho^{3+} $^5I_8 \rightarrow {}^5I_7$ transition show the shape displayed in Figure 2.22: the peak is split in four components (see B1 line at 5175.4 cm^{-1}). The width Δ (see Section 1.5) of the structured lines ranges between 0.34 and 0.46 cm^{-1}. Some other absorption lines do not show clearly this structure but a squared top that suggests it.

The structure resembles that reported in Figure 1.3 [10], thus it could be induced by hyperfine (hf) interaction (see Section 1.5).

As already stated in Section 1.5, Ho^{3+} is the best candidate among RE^{3+} for a hf structure (hfs) analysis. On the other hand, the monoclinic structure of BaYF removes completely the manifold degeneracy and the hf interaction does not affect singlet states. Notwithstanding this, a second order hf interaction (pseudoquadrupolar coupling) could take place when groups of electronic levels are separated by small energy gaps. Such a coupling gives rise to a pure pseudoquadrupolar splitting if two singlets are involved in the transition.

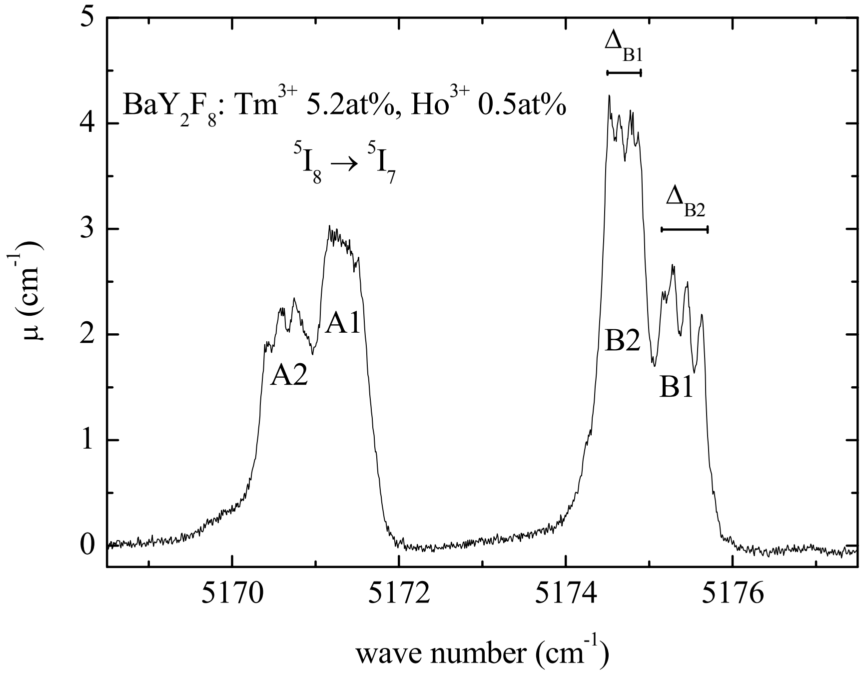

Figure 2.22 Optical absorption spectrum measured at 9 K on a BaYF: Tm^{3+} 5.2at%, Ho^{3+} 0.5at% sample in the region of the Ho^{3+} $^5I_8 \rightarrow {}^5I_7$ transition.

This could be the case of BaYF: Ho^{3+}, where the separation between the first two sublevels of the ground manifold is only 0.6 cm^{-1}. In this framework, the hf splitting of the fundamental and first excited sublevel of the ground manifold can be evaluated (see Section 1.5 and 3.4.2), from example from Δ_{B1} and Δ_{B2} (see Figure 2.22), as Δ_i^1=0.34±0.01 and Δ_i^2=0.45±0.01 cm^{-1}, respectively.

Theoretical calculations of the energy spectra by numerical diagonalization of the full matrix representing each multiplet in the nuclear- and electronic-moment product space are still in progress to verify this hypothesis. The values of the free ion and crystal field parameters used in this calculation will be fixed at those obtained from the fitting of the experimental energy levels (see Table 2.5 and Section 2.4.1.2).

2.5 CONCLUSION

BaY_2F_8 (BaYF) single crystals doped with Tm^{3+} or Er^{3+} and co-doped with Tm^{3+} and Ho^{3+} were studied by means of high resolution Fourier transform spectroscopy in the wave number range 500-25000 cm^{-1} and in the temperature range 9-300 K. Since BaYF is a biaxial crystal, measurements with linearly polarized light were also performed.
Analyzing the large number of high resolution spectra (up to 0.01 cm^{-1}) as a function of temperature, sample orientation, and incident light polarization angle the absorption line attribution and the energy level scheme were refined for Tm^{3+} and Ho^{3+} in BaYF with respect to Ref. [28] (Table 2.2 and Table 2.4, respectively; see Section 2.4.1). The data fitting in the framework of a single-ion Hamiltonian model supported the validity of the attribution and provided the free ion and crystal field (CF) parameters (Table 2.3 and Table 2.5). Comparing the parameters with those obtained for Nd^{3+}, Dy^{3+}, and Er^{3+} in BaYF [31, 6, 7] the expected trend was found (Table 2.6): the free ion parameters slightly increase by increasing the atomic number, while the CF ones slightly decrease or remain more or less constant along the series.
Dichroic spectra were also exploited to determine the orientation inside the BaYF matrix of both the dielectric ellipsoid and of the dipole moments μ associated with each transition (see Section 2.4.2). The direction found for the dielectric ellipsoid with respect to the *a* axis (θ_M~(29.4±1.4)°) is in good agreement with that reported in literature (22°) [26]. The dipole moments seem to be oriented along discrete directions (see Figure 2.16).
Moreover, spectra measured on Er^{3+} and Tm^{3+} doped samples made evident series of weak, extremely narrow (0.03-0.1 cm^{-1}), and closely spaced (~0.2-0.8 cm^{-1}) lines appearing on both sides of the narrowest electronic absorption lines (see Section 2.4.3 and Figure 2.17). In this study, the high resolution was fundamental. These fine structure (FS) lines were attributed to a simultaneous excitation both of an electronic transition and of a local mode, specifically a hindered rotation or libration of a RE^{3+}-F^- group. As a first approximation, the RE^{3+}-F^- complexes were regarded as free rotators; the rotational constants of 0.36-0.55 cm^{-1} were derived from the spectra analysis (Figure 2.20) and found in agreement with those calculated from the inertia momenta. The rotational-like contribution should induce energy levels with a separation from the

electronic one of only a few tenths of cm^{-1}. Specific heat measurements performed on Er^{3+} doped samples confirmed the presence of those sublevels. In the more realistic framework of hindered rotations [42-46], the potential barrier, which separates different orientations of the RE^{3+}-F^- group, was determined (~26 cm^{-1}) from the analysis of the FS decorating the A1 and A2 lines of the Tm^{3+} $^3H_6 \rightarrow {}^3F_4$ transition. For Er^{3+} doped samples it was not possible to evaluate the energy barrier: it was probably too low to be 'seen' even at 9 K.

This is the first time, to our knowledge, that the structure due to the simultaneous excitation of an electronic transition and hindered rotation modes was resolved so clearly; compare, for example, the results in Ref. [38, 44] for roto-vibrational spectra.

Finally, an unexpected hyperfine structure of a few Ho^{3+} absorption lines was detected (see Section 2.4.4): it was probably due to a second order hyperfine interaction (pure pseudoquadrupolar coupling, see Section 1.5). Theoretical calculations are still in progress to analyze this hypothesis.

3 YPO_4 SINGLE CRYSTALS

3.1 INTRODUCTION

Yttrium orthophosphate YPO_4 is a widely investigated crystal that has proved to be important for many applications in the field of optical materials and devices. For instance, undoped YPO_4 has been recently demonstrated to be a stimulated Raman scattering active crystal with non-linear laser properties with possible applications in the visible, near- and mid-infrared (IR) spectral ranges [47]. On the other hand, YPO_4 doped with trivalent rare earth ions (Ce^{3+}, Pr^{3+}, and Nd^{3+} in particular) shows strong 5*d*-4*f* luminescence in the UV [48-50], and therefore can find applications in the field of fast scintillating materials.

Although the 4*f*-4*f* spectroscopy of RE^{3+} in YPO_4 is rather well known, in the case of the Ho^{3+} ion no very detailed studies have appeared in the literature. Absorption measurements were performed 40 years ago on $HoPO_4$ and YPO_4 doped with Ho^{3+} 10% [51]: crystal field energies and parameters have been extracted [52, 53]. However, YPO_4: Ho^{3+} has been reported to be non-luminescent at room temperature [54] and so far only the multiphonon relaxation rate of the Ho^{3+} excited levels ($^5F_4$, $^5S_2$) has been investigated in detail [55].

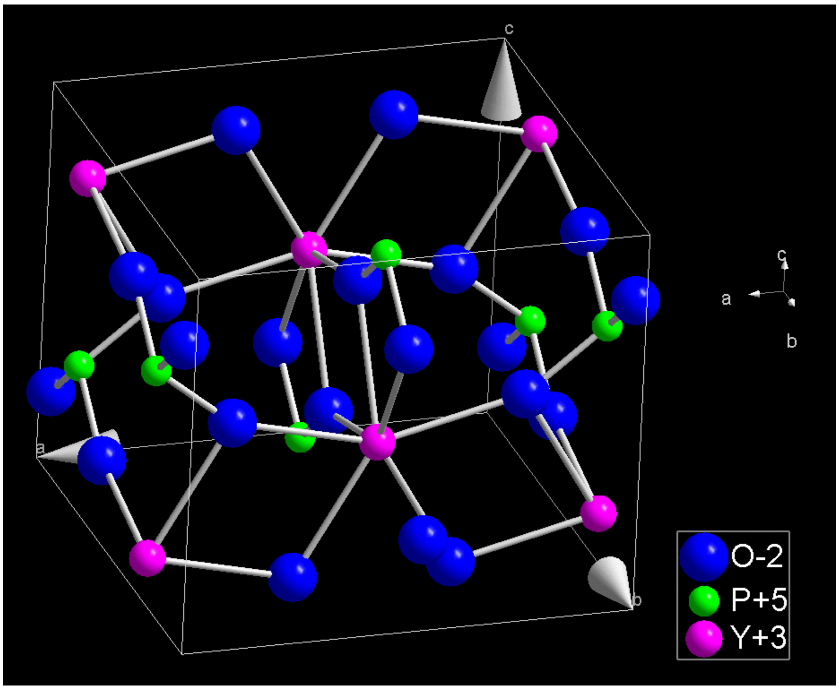

Figure 3.1 YPO_4 unit cell. Blue: Oxygen; pink: Yttrium; green: Phosphate. The bonds are indicated by sticks and the axes by gray arrows.

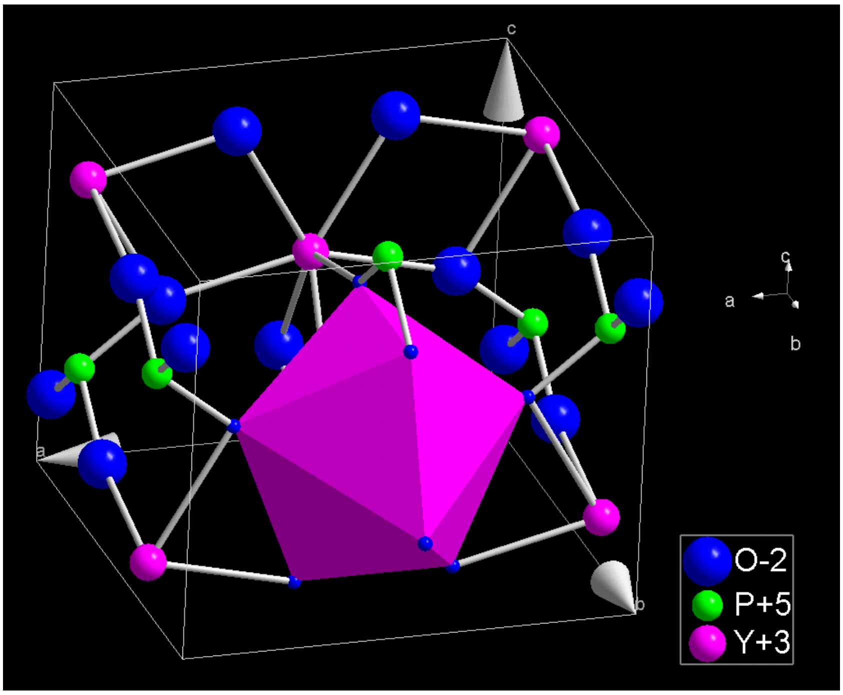

Figure 3.2 YPO_4 unit cell. Blue: Oxygen; pink: Yttrium; green: Phosphate. The O^- polyhedra are made evident and the axes are indicated by gray arrows.

The YPO_4 crystal has tetragonal structure and belongs to the space group D^{19}_{4h}–$I4_1/amd$ (n. 141) [47]. The unit cell (Figure 3.1) contains four formula units and the lattice parameters are:

$a = b = 6.8817(5)$ Å

$c = 6.0177(6)$ Å

$\alpha = \beta = \gamma = 90°$

RE^{3+} substitutes for the eight-fold coordinated Y^{3+} and probes a D_{2d} site symmetry; thus, it is surrounded by a polyhedron of eight O^- ions (Figure 3.2). Since Y^{3+} and RE^{3+} are homovalent, no charge compensation is required; thus, no further local symmetry lowering can be caused by charge compensating defect(s). Moreover, since the dimensions of the RE^{3+} ions are similar to those of Y^{3+}, mechanical mismatch is reduced.

The first aim of the investigations is the energy level scheme determination for Ho^{3+} in YPO_4, with the theoretical support of crystal field calculations based on a single-ion model (Section 3.4.1). On this basis, the study of an expected hyperfine structure made evident by high resolution absorption spectra can be performed (Section 3.4.2).

3.2 EXPERIMENTAL DETAILS

Single crystals of YPO_4 were grown at the Solid State Physics Laboratory of the University of Verona by spontaneous nucleation from a PbO-P_2O_5 flux (1:1 molar ratio). The reagents employed were $NH_4H_2PO_4$, PbO (both reagent grade), Y_2O_3 (99.99 %) and Ho_2O_3 (99.99 %). The growing procedure is described in Ref. [47]. Single crystals of good optical quality were obtained, having a size up to $1.0\times0.8\times8$ mm^3 and elongated in the direction of the *c* axis of the tetragonal structure. The Ho^{3+} nominal concentration in the YPO_4 samples employed in the present work was 1% m.f..

All the measurements here reported were performed on samples 0.42 mm thick.

The optical absorption spectra were monitored in the wave number range 500-25000 cm^{-1} with a non-apodized resolution as fine as 0.01 cm^{-1} (see Appendix 1.1) and in the temperature range 9-300 K (see Appendix 1.2.1).

Photoluminescence spectra were also measured at 10 K by Prof. J. Garcia Solé and co-workers at the Material Physics Department of the Universidad Autonoma de Madrid (see Appendix 2.2).

3.3 EXPERIMENTAL RESULTS

3.3.1 Temperature dependence

In the wave number range analyzed (500-25000 cm^{-1}) several Ho^{3+} electronic transitions from the ground manifold $^5I_8$ to the excited manifolds are expected, i.e. $^5I_8 \rightarrow {}^5I_{7,6,5,4}$, $^5F_5$, $^5S_2$, $^5F_{4,3,2}$, $^3K_8$, $^5G_6$+$^5F_1$,and $^5G_5$ [56].

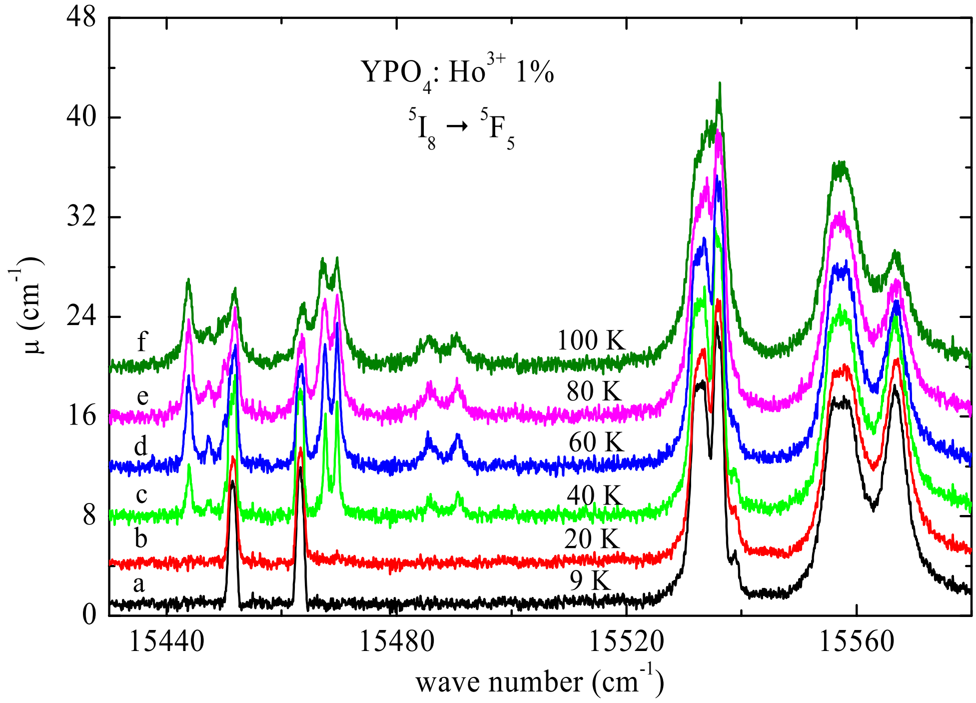

Figure 3.3 Optical absorption spectra measured at 9 K (curve a) and from 20 to 100 K by 20 K steps (curves from b to f) on a YPO$_4$: Ho^{3+} 1% sample in the region of the Ho^{3+} $^5I_8 \rightarrow {}^5F_5$ transition.

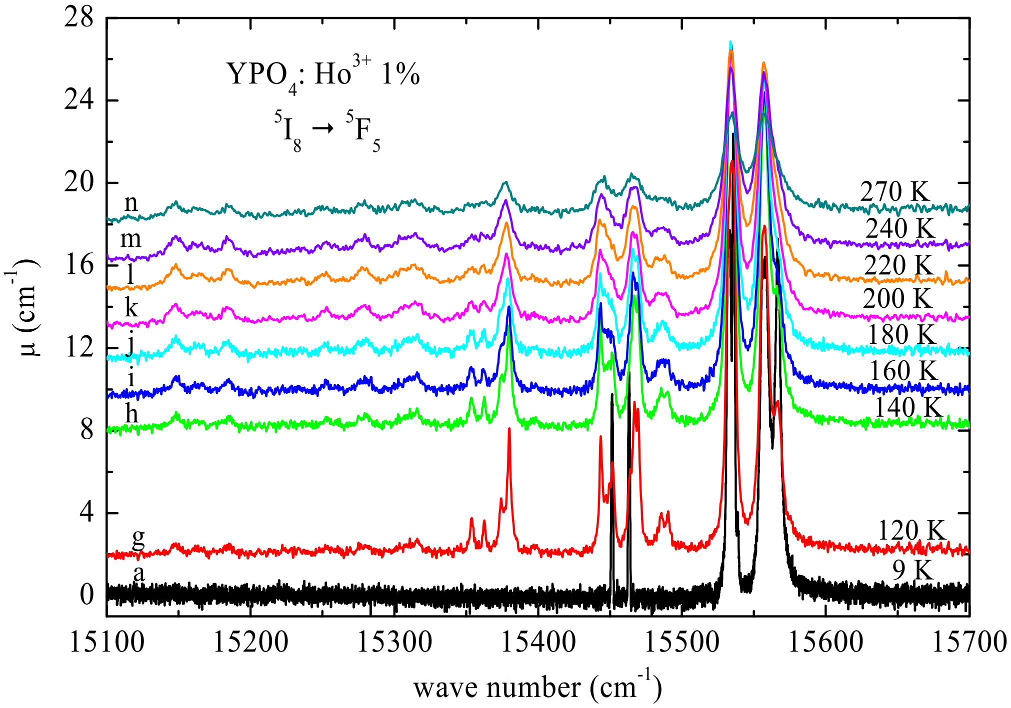

Figure 3.4 Optical absorption spectra measured at temperatures of 9 K (curve a), from 120 to 240 by 20 K steps (curves from g to m), and 270 K (curve n) on a YPO$_4$: Ho^{3+} 1% sample in the region of the Ho^{3+} $^5I_8 \rightarrow {}^5F_5$ transition.

An example of high resolution absorption spectra in the 9-300 K range is displayed in Figure 3.3 and Figure 3.4: it is related to the $^5I_8 \rightarrow {}^5F_5$ transition, which covers the 15430-15580 cm^{-1} range. At 9 K only seven lines are present (Figure 3.3, curve a): two of them, at 15451.5 and 15463.2 cm^{-1}, are rather narrow (FWHM~1.5 cm^{-1}), while two (at 15532.7 and 15557.2 cm^{-1}) are much broader, squared, and apparently show a structure, which, however, cannot be resolved, in spite of the high instrumental resolution employed. No changes are monitored at 20 K (curve b). By increasing the temperature in the 40-100 K ranges (curves c-f), new lines grow on the low energy side, while the original ones displayed at 9 K gradually decrease. A further temperature increase up to 300 K (Figure 3.4) causes the appearance of other lines at even lower energies and a general broadening and weakening of the whole spectrum.

Figure 3.5 displays some spectra measured at 9, 40, 80, and 120 K (curves from a to d, respectively) in the region of the first transition: $^5I_8 \rightarrow {}^5I_7$. In this region the lines detected at 9 K are very narrow, and some of them are seemingly affected by noise.

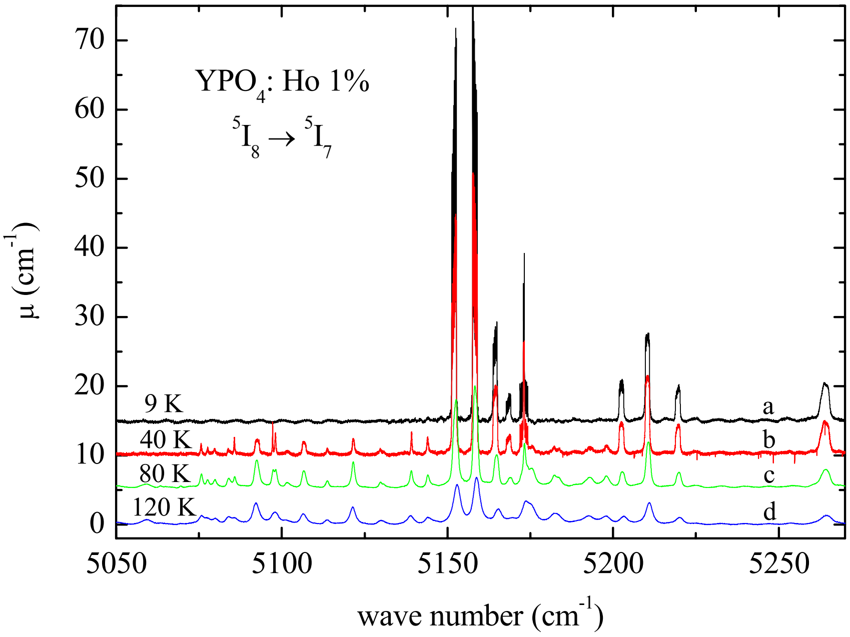

Figure 3.5 Optical absorption spectra measured at 9, 40, 80, and 120 K (curves from a to d, respectively) on a YPO_4: Ho^{3+} 1% sample in the region of the Ho^{3+} $^5I_8 \rightarrow {}^5I_7$ transition.

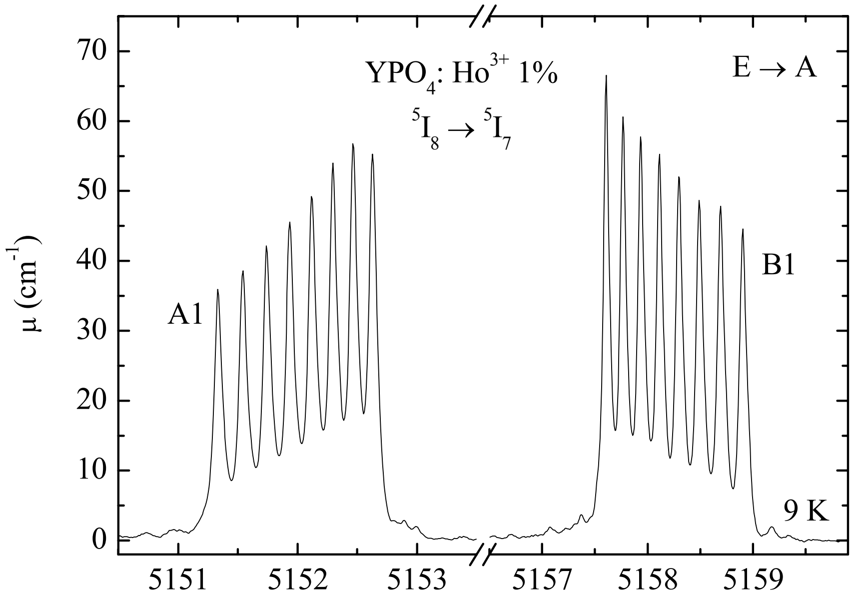

Figure 3.6 Hyperfine structures displayed by the absorption lines at ~5152 and 5158 cm^{-1} in the region of the Ho^{3+} $^5I_8 \rightarrow {}^5I_7$ transition. The spectrum is measured at 9 K with a non-apodized resolution of 0.01 cm^{-1}.

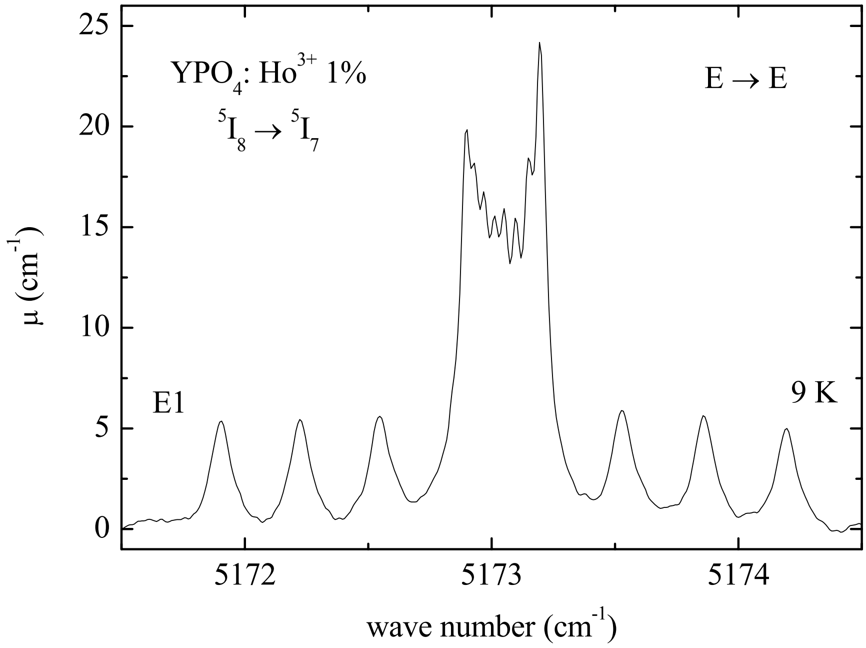

Figure 3.7 Hyperfine structure displayed by the absorption line at ~5173 cm^{-1} in the region of the Ho^{3+} $^5I_8 \rightarrow {}^5I_7$ transition. The spectrum is measured at 9 K with a non-apodized resolution of 0.01 cm^{-1}.

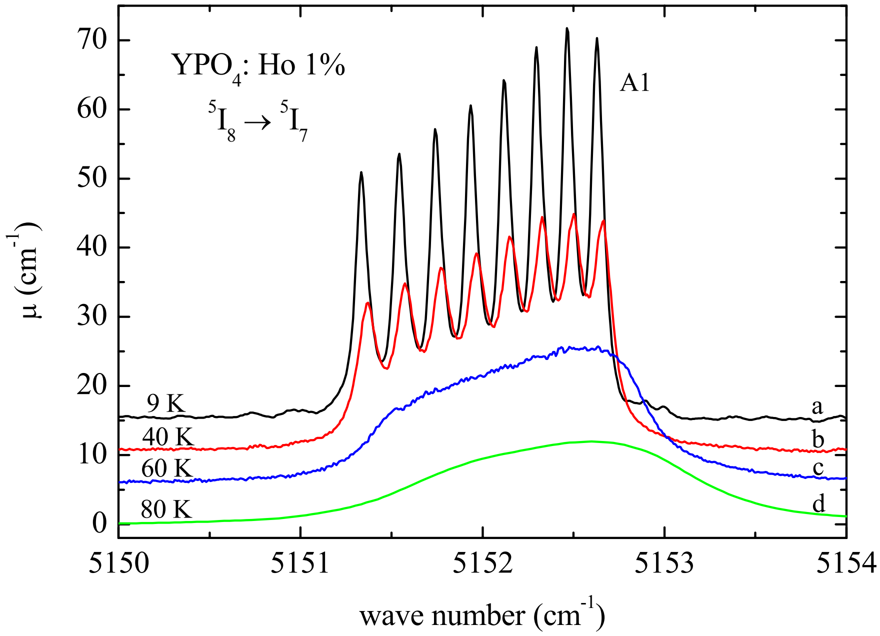

Figure 3.8 Hyperfine structure displayed by the absorption line at ~5152 cm^{-1} in the region of the Ho^{3+} $^5I_8 \rightarrow {}^5I_7$ transition. The spectra are measured at 9, 40, 60, and 80 K (curves from a to d, respectively).

The magnifications of three of them displayed in Figure 3.6 and Figure 3.7 show complex hyperfine structures (see Section 1.5). Also in this case, by increasing the temperature new peaks appear at lower wave numbers, while those monitored at 9 K decrease. The hyperfine structures (hfs) are no longer detectable at 60 K; in Figure 3.8 the hfs of the line at ~5152 cm^{-1} is displayed for different temperatures from 9 to 80 K: the measurement performed at 20 K is omitted because it practically overlaps that taken at 9 K. At 40 K the hfs can be still clearly distinguished (curves b), while at 60 K all the hfs components merge in a unique rather broad line (curve c). Only in some cases at 60 K weak features remind hfs.

Similar features characterize all the spectra measured at closely spaced temperature steps in the region of the other Ho^{3+} transitions investigated, i.e. $^5I_8 \rightarrow {}^5I_{6,5,4}$, $^5S_2$, $^5F_{4,3,2}$, $^3K_8$, $^5G_6$+$^5F_1$, and $^5G_5$. Many of the lines monitored exhibit beautiful hfs patterns at temperatures below 60 K.

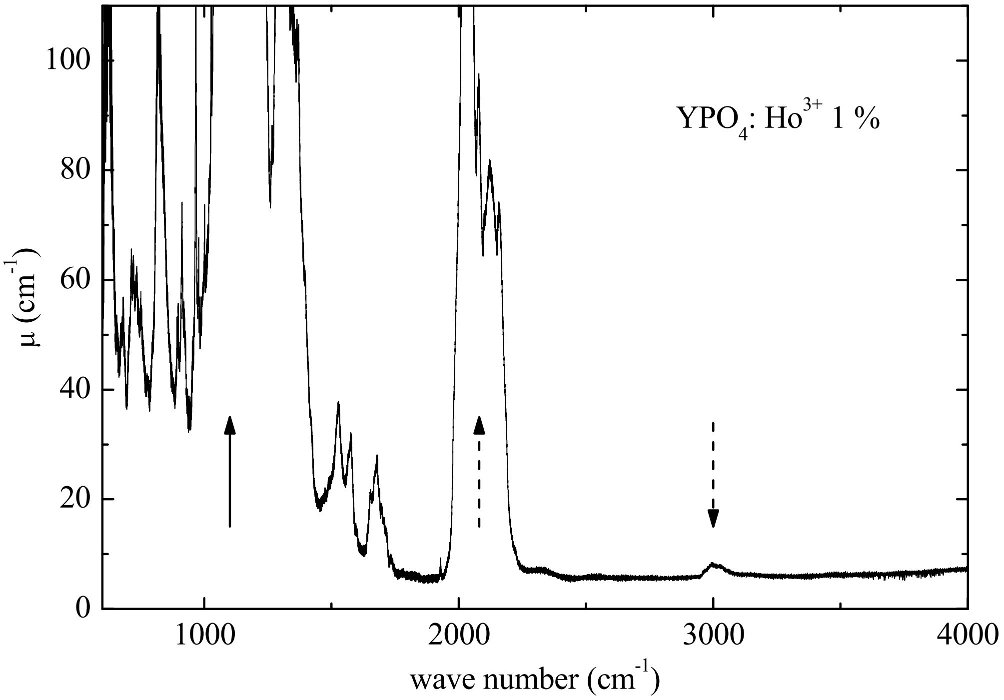

Figure 3.9 Optical absorption spectrum measured at 9 K in the 500-4000 cm^{-1} range.

Measurements were performed even in the region of the IR active groups PO$_4^{3-}$ (600-4000 cm^{-1}). The spectrum at 9 K displayed in Figure 3.9 shows very strong absorptions around 1100 cm^{-1}, strong ones at ~2080 cm^{-1}, and a much weaker one at ~3000 cm^{-1}.

Finally, luminescence measurements were performed to support absorption spectra. Figure 3.10 shows the 10 K unpolarized emission spectrum in the 15100-15500 cm^{-1}

range, obtained upon excitation at 540 nm (18518.5 cm^{-1}), i.e. into the $^5I_8 \rightarrow {}^5S_2$ transition of Ho^{3+} ions. It involves transitions from the $^5F_5$ manifold (at ~15500 cm^{-1}) to the sublevels within the $^5I_8$ manifold.

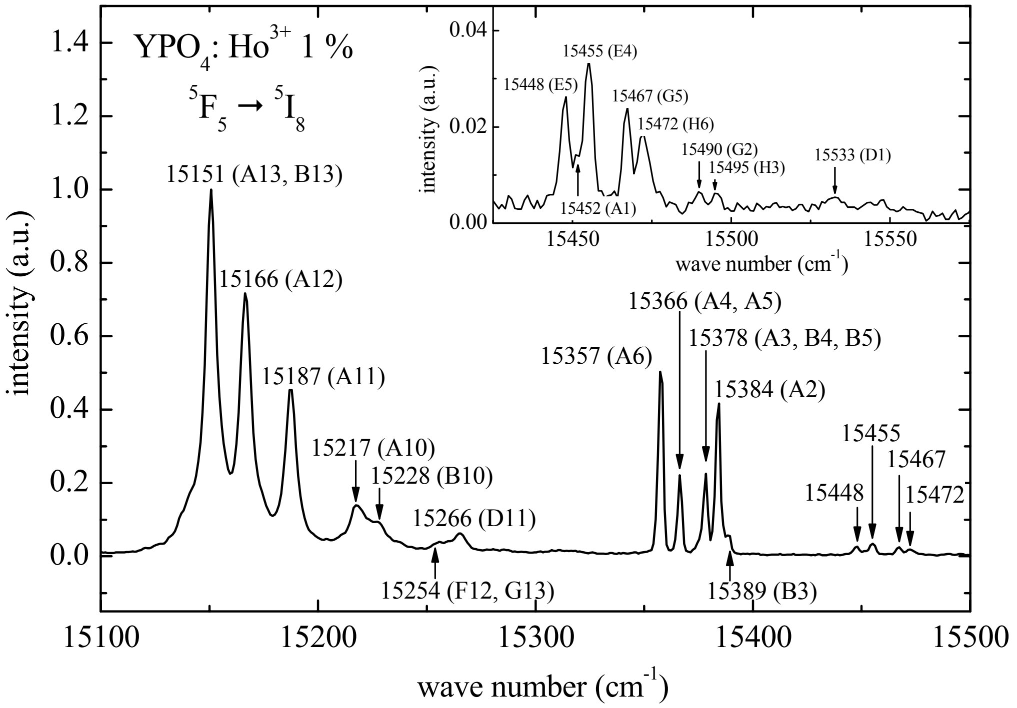

Figure 3.10 Unpolarized emission spectrum, in the range 15100-15500 cm^{-1}, measured at 10 K upon excitation at 540 nm. The insert shows a magnification of the spectrum in the 15400-15600 cm^{-1} range.

3.4 DISCUSSION

The first step of the analysis will be to determine the attribution of the large number of lines arising from the transitions connecting the sublevels of the ground manifold $^5I_8$ to those of the excited ones and to fit the experimental data by a single ion Hamiltonian. The crystal field parameters will be also determined (Section 3.4.1). Thus, the variety of hfs patterns will be analyzed and interpreted in terms of electric dipole and/or magnetic dipole allowed transitions and interaction between rather close sublevels (Section 3.4.2).

3.4.1 Line attribution and crystal field parameters

As already stated above, in the wave number range analyzed (500-25000 cm^{-1}) several Ho^{3+} electronic transitions from the ground $^5I_8$ to the excited manifolds occurs: $^5I_8 \rightarrow$ $^5I_7$, $^5I_6$, $^5I_5$, $^5I_4$, $^5F_5$, $^5S_2$, $^5F_4$, $^5F_3$, $^5F_2$, $^3K_8$, $^5G_6$+$^5F_1$,and $^5G_5$ [56]. Moreover, being Ho^{3+} a non-Kramers ion (configuration $4f^{10}$), each manifold of given J can be split by low symmetry crystal field in a large number of sublevels (up to $2J$+1).

The energy level scheme and the attribution of the lines originated by such transitions were obtained by measuring the absorption spectra as a function of the temperature and fitting the experimental energy levels with a single ion Hamiltonian model, according to the procedure already described in Section 2.4.1.

A further support to the line attribution within the $^5I_8 \rightarrow$ $^5F_5$ transition came from luminescence spectra.

Being Ho^{3+} and Y^{3+} homovalent ions, the substitution in the unique available site in the lattice does not require any charge compensation. Such conditions allow a more precise analysis. Moreover, the lines are usually expected to be rather narrow. In fact, a small electron-phonon coupling can be predicted for Ho^{3+}, as suggested by an extended analysis of RE^{3+} spectra of LiYF$_4$ single crystals, where the coupling was found to be strong at the beginning and at the end of the lanthanide series and weak in the middle [12]: Ho^{3+} falls in the region where the coupling should be rather weak (see Section 1.6).

The energy levels are conventionally indicated with letters X=A, B, C, ... for the excited manifolds and with numbers i=1, 2, 3, ... for the ground one from which the absorption starts. Thus, in the spectra each absorption line is labelled Xi as the associated transition.

According to the attribution method described in Section 2.4.1, absorption spectra were analyzed and the temperature dependences of the line amplitudes are exemplified in Figure 3.11 for three lines belonging to the $^5I_8 \rightarrow$ $^5F_5$ transition. The amplitude of fundamental lines (i.e. lines due to transition from the fundamental sublevel of the ground manifold to sublevels of excited manifolds) continuously decreases as a function of the temperature; the amplitude of hot bands (i.e. lines due to transitions from excited sublevels of the ground manifold to sublevels of excited manifolds), after an initial growth, then decreases.

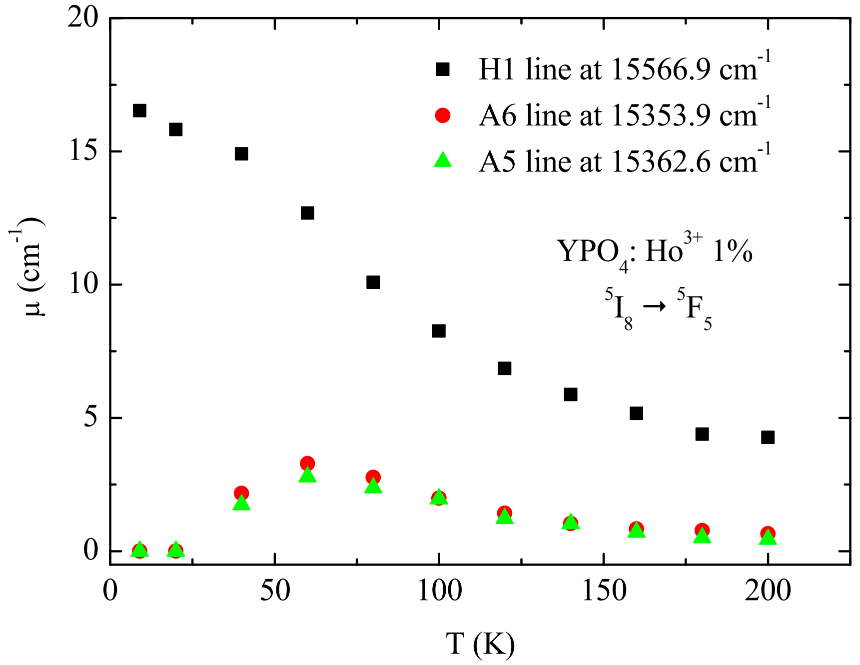

Figure 3.11 Temperature dependence of the amplitude for a few lines. Squares: H1 line at 15566.9 cm^{-1}; circles: A6 line at 15353.9 cm^{-1}; triangles: A5 line at 15362.6 cm^{-1}.

In spite of the complications originated by the hf splitting of many lines, it was possible to identify nearly all the X1 lines (i.e. the fundamental ones) and to determine the positions of the sublevels of the ground manifold (thanks to measurements performed at closely spaced temperature steps). The results are collected in Table 3.1, third column.

The ground manifold sublevel positions were determined by averaging a large number of ‘separations’ related to different lines and different manifolds. For example the 66.5±0.7 cm^{-1} value was obtained by averaging 50 separations between X1 and X2 lines. Due to this rather high separation between the first two sublevels of the ground manifold, no hot bands were detected in the 9 and 20 K spectra (see curves a and b in Figure 3.3): they grow only at 40 K (see curve c). It is important to notice that only the high resolution and the large number of measurements at different temperatures allowed to distinguish the very close 2-8 sublevels within the ground manifold (compare third and sixth column in Table 3.1).

Table 3.1 Sublevel positions (cm^{-1}) for Ho^{3+} ground and excited manifolds in YPO_4 as derived from optical absorption measurements (third column), theoretical calculations (fourth column), and luminescence (fifth column). Experimental values from Ref. [51] are reported for comparison (last but one column). In the last column are listed the hf separations calculated (see Section 3.4.2).

$^{2S+1}L_J$	Level	Exp. (cm^{-1})	Fit. (cm^{-1})	Lum. (cm^{-1})	Exp.[a] (cm^{-1})	$\Delta_{hf}^{exp.}$
$^5I_8$	1	0	5.3 D	0	0	1.29±0.04
	2	66.5 ±0.7	60.1	67	66.58	0.97±0.04
	3	71.2 ±0.5	74 D	73	71.73	
	4	80.6 ±0.6	81.7	81	80.86	
	5	88.7 ±0.5	88.2	89	89.21	
	6	94.9 ±1.6	101.1	94	160.42	
	7	105.3 ±1.8	143.9		188.09	
	8	112.8 ±1.9	144.6		250.21	
	9	161.5 ±2.2	199 D		279.36	
	10	233.7 ±3.1	244.5	235		
	11	264.5 ±4.0	246.4	266		
	12	283.1 ±2.6	262.9 D	285		
	13	304.3 ±1.5	278	306		
$^5I_7$	A	5152 *	5147 D			
	B	5158 *	5150.6			
	C	5164.4 *	5153.9			0.144
	D	5168.3 *	5166.5 D			
	E	5173 *	5168.3			0.994
	F	5202 *	5189.6			
	G	5210 *	5200.2 D			0.21
	H	5219.5 *	5212.9			
	I	5262.6	5255.7			
	L	5264 *	5257.1 D			0.08
	M		5257.6			
$^5I_6$	A	8650 *	8641.9			
	B	8652 *	8643.3			
	C	8673 *	8682.5			
	D		8685.5 D			
	E	8680 *	8698.6			
	F	8689.4 *	8699.8			
	G	8703.3 *	8704.1 D			0.81
	H	8749 *	8741.4			0.49
	I	8757.5	8757.8 D			
	L	8788	8765.9			
$^5I_5$	A	11215.5	11213.4 D			0.87
	B	11233.2	11251.1 D			
	C	11251.4 *	11254.6			
	D	11261 *	11258.9			

$^{2S+1}L_J$	Level	Exp. (cm^{-1})	Fit. (cm^{-1})	Lum. (cm^{-1})	Exp.^{a} (cm^{-1})	$\Delta_{hf}^{exp.}$
	E		11267.2			
	F	11288.5	11294.4			
	G	11305.1 *	11302.8 D			
	H	11376.2	11322.6			
$^5I_4$	A	13231	13262.5 D			
	B		13280.1			
	C	13286.6 *	13285.2			
	D		13307.7			
	E	13330	13349.6			
	F		13390.1 D			
	G		13482.1			
$^5F_5$					15432.11	
	A	15451.5	15429	15452	15452.27	
	B	15463.2	15432.7 D	15463	15463.68	
	C	15477.6	15438.4	-	-	
	D	15532.7 *	15514.9 D	15533	15532.79	0.57
	E	15535.9 *	15523.9	15536	15336.26	
	F	15539	15527.1		15539.05	
	G	15557.2 *	15542.1 D	15557	15557.01	1.68
	H	15566.9	15558	15567	15567.29	
$^5S_2$+$^5F_4$	A		18430.6			
	B		18433.2		18437.29	
	C	18438.7	18433.9 D		18443.84	
	D	18445	18448.6		18446.29	
					18461.95	
	E	18512	18511.6			
	F	18518.2	18539.3 D		18518.89	
					18545.88	
	G	18571	18563.9 D		18571.50	
	H	18577	18586		18593.33	
	I	18619	18594.5		18619.70	
	L	18621.6	18617.2		18620.11	
	M	18624	18626.7		18625.01	
$^5F_3$	A	20583.5 *	20578.4		20584.04	
	B	20601.4 *	20585 D		20601.85	
	C	20644.2 *	20635.5		20644.30	
	D	20668	20667.2 D		20668.71	
	E	20675.4	20672.9		20675.57	
$^5F_2$	A	21060	21070.5		21049.43	
	B	21077	21081.8 D		21077.99	
	C	21083	21086.1		21083.44	
	D	21138	21146.5		21139.71	
$^3K_8$	A	21331 *	21322.6		21331.45	

$^{2S+1}L_J$	Level	Exp. (cm^{-1})	Fit. (cm^{-1})	Lum. (cm^{-1})	Exp.[a] (cm^{-1})	$\Delta_{hf}^{exp.}$
	B	21332.3	21330.6 D		21332.69	0.6
	C	21347.2	21338.1		21347.65	
	D	21355.5	21340.7		21355.93	
	E	21358.4	21357.4 D		21358.67	
	F	21372.7 *	21378.8		21373.19	
	G	21377.5 *	21379.1		21377.94	
	H		21392.2			
	I		21393.2			
	L	21407 *	21399.7		21408.19	
	M	21409 *	21406.3 D		21409.69	
	N	21411	21411.3		21411.46	
					21417.78	
	O	21445	21429.8 D		21445.31	
$^5G_6$+$^5F_1$	A		22047.1			
	B	22043 *	22050.7 D		22043.76	
					22043.85	
	C	22075	22083.8		22075.18	
	D	22121.2 *	22122.2 D		22121.47	
	E	22142	22130			
	F	22147.9	22155.9		22148.33	
	G	22157	22183.6		22157.96	
	H	22173	22220.8		22173.23	
	I	22200	22220.9 D			
	L	22248	22246.9		22253.52	
	M	22265	22274.3		22262.04	
	N	22285	22345.2 D		22286.62	
					22295.85	
					22334.35	
$^5G_5$					23898.95	
	A	23907.5	23930.4		23907.76	
	B	23925	23943.5 D		23925.64	
	C	23987.9 *	23965.3		23988.09	
	D	23996.2	23993.9		23996.56	
	E	24007	24001 D		24008.52	
	F	24022	24014.3			
	G	24029 *	24027.2 D		24030.16	
	H	24063.2	24031.3		24057.27	

[a] From Ref. [51].

*** Hyperfine structure.**

D Doublet.

Fourth column of Table 3.1 lists the energy level positions derived by fitting the experimental data (third column) with a single-ion Hamiltonian (see Sections 1.3 and 2.4.1.1). Since the free ion parameters are generally expected to be very similar in all phases, only Coulomb and spin-orbit among them were varied to fit experimental data starting from the values obtained by Carnal *et al.* for Ho^{3+} in LaF_3 [33]: other free ion parameters (which are weak corrective potentials) were kept fix at the values obtained in Ref. [33] and they are listed in Table 3.2. Moreover, the CF parameters are expected not to change drastically if different RE are embedded in the same host; thus, the B_q^0 starting values were those of Dy^{3+} in Ref. [57], being Dy^{3+} near Ho^{3+} in the periodic table. These choices were made to avoid over-parameterization. The parameters so obtained are listed in Table 3.3. The agreement between experimental and calculated energy levels is good, with a root mean square deviation $\sigma \sim 14$ cm^{-1}.

Table 3.2 Free ion parameters [33] fixed in the experimental data fitting.

Parameter	Data fit
α	17150
β	-607.9
γ	1800
T^2	400
T^3	37
T^4	107
T^6	-264
T^7	316
T^8	336
M^0	2.54
M^2	1.422
M^4	0.787
P^2	605
P^4	302.5
P^6	60.5

Table 3.3 Coulomb, spin-orbit and CF parameters obtained from experimental data fitting.

Parameter	Data fit
E_{ave}	48370±8
F^2	93883±62
F^4	66272±101
F^6	51923±61
ζ	2145.8±0.8
B_2^0	-443±27
B_4^0	-170±40
B_6^0	623±29
B_4^4	-651±25
B_6^4	163±31

In spite of the complexity of the spectra, due to hfs (the lines that show hfs are indicated with * in the third column of Table 3.1) and the above mentioned vicinity of seven sublevels within the $^5I_8$ manifold, it was possible to identify the 13 sublevels, predicted on the basis of symmetry considerations for Ho^{3+} in the tetragonal YPO_4 lattice. In fact, the calculations performed in the framework of a single-ion model (see above) show that four among the $^5I_8$ expected sublevels (i.e. 2J+1=17) are doubly degenerate (doublets, labelled with D in the fourth column of Table 3.1): the manifold degeneracy cannot be completely removed by the crystal field experienced by Ho^{3+}, sitting in a D_{2d} symmetry site, within the tetragonal YPO_4 lattice.

The whole set of level positions (Table 3.1, third column) were compared with the experimental values obtained from absorption measurements performed on $HoPO_4$ and YPO_4: Ho^{3+} 10% samples at two temperatures (4.2 and 85 K) [51] (last but one column). There is an overall excellent agreement for the sublevel figures related to the common investigated transitions, i.e. $^5I_8 \rightarrow {}^5F_5$, $^5S_2$, $^5F_4$, $^5F_3$, $^5F_2$, $^3K_8$, $^5G_6+{}^5F_1$, and $^5G_5$. Nevertheless, there are very few exceptions, because more sublevels are reported according to Ref. [51]. Some of them can be accounted for by considering that Ho^{3+} substitutes 100 and 10% of Y^{3+}, respectively, in Ref. [51] samples in comparison with the 1% of the present ones, thus weak absorptions may be there emphasized by the higher Ho^{3+} concentration. Some of the additional sublevels may be ascribed to possible Ho^{3+} clusters in the 10% Ho^{3+} doped sample, as already reported for Er^{3+} heavily doped

BaY_2F_8 [31]. Due to the YPO_4 optical anisotropy, the presence of some lines depends on the crystal direction along which the spectrum is measured [51] and/or on the light beam polarization (see, for example, the case of BaY_2F_8 analyzed in Chapter 2), as proved, for example, by the 21347.65, 21411.46, and 21417.78 cm^{-1} lines, which, being listed in Table 2 [51], do not appear in Fig. 1 of the same paper. Those peaking at 18545.88 and 21049.43 cm^{-1} are hot lines rather than fundamental ones, because they were detected at 85 K [51], where some of the excited sublevels of the ground manifold are already populated, as shown for example in Figure 3.3 and Figure 3.5. For what concerns the 6-9 sublevels within the ground manifold, $^5I_8$, the discrepancy between the present data and those reported in Ref. [51] may arise from the analysis of spectra measured only at two temperatures (4.2 and 85 K). The rather closely temperature spaced sequence of spectra, measured in the present work by 20 or 30 K steps over the 20-240 and 240-300 K ranges, respectively, is a necessary requirement to follow the progressive growth of the hot bands and to evaluate correctly the positions of all sublevels within the ground manifold.

A further support to the $^5I_8$ and $^5F_5$ manifold splitting comes from the luminescence measurements (see Figure 3.10 and fifth column of Table 3.1).

It should be remarked that difficulties are usually met to detect luminescence in YPO_4, due to a tight coupling between Ho^{3+} and the lattice [55]. In addition, part of the excitation energy is known to be delivered to lattice vibrations in terms of multiphonon (MP) process [55]. The MP transition rate for Ho^{3+} was found to be very high in YPO_4 and much higher with respect to similar host matrices as $YAsO_4$ and YVO_4, compare Fig. 7 with Figs. 5 and 6 in Ref. [55]. In the present case, measurements performed in the range of fundamental absorption of PO_4^{3-} group modes (Figure 3.9) allow to analyze the nature of phonons involved in these processes. Figure 3.9 shows absorptions at ~1100, 2080, and 3000 cm^{-1}. Absorption peaks at 1070, 1030, 643.1, and 526.3 cm^{-1} were monitored in room temperature IR spectra of YPO_4-KBr (or CsI) pellets [58]; they were attributed to PO_4^{3-} ionic group vibrations: the first two to stretching modes, while the last two to bending modes. Recent Raman scattering measurements have shown two peaks at ~1002 and 1058 cm^{-1}, which were attributed to totally symmetric $A_{1g}(\nu_1)$ and antisymmetric $B_{1g}(\nu_3)$ stretching vibrations of the PO_4^{3-} complexes, respectively [47]. Thus the bands detected around 1100 cm^{-1} (solid arrow in Figure 3.9) can be attributed to the fundamental absorption of IR active modes of PO_4^{3-} groups. The peaks at ~2080 and 3000 cm^{-1} in the same figure (dashed arrows) can be regarded as due to absorptions of first and second overtones of PO_4^{3-} IR active modes and of their combinations with Raman active modes, in analogy with the multi-mode absorptions of tetrahedral groups in sillenites [59, 60]. Thus, part of the excitation energy may be spent to change the vibrational state of one or more of the PO_4^{3-} complexes neighbouring Ho^{3+} in tetragonal YPO_4. The vibrational modes of tetrahedral VO_4^{3-} and AsO_4^{3-} units should occur at lower frequencies, as observed indeed in sillenites [60], due to the larger atomic masses of V and As with respect to that of P. Such a consideration may account for the already mentioned lower MP transition rate for Ho^{3+} in $YAsO_4$ and YVO_4, with respect to YPO_4 [55]. In principle, OH^- groups might also be responsible for luminescence quenching [15]; however the spectrum displayed in Figure 3.9 does not show any absorption which can be attributed to OH^- modes (see, for comparison, Figure 5.4).

On the basis of the sublevel positions determined from the absorption spectra analysis and listed in Table 3.1 (third column) it was possible to assign practically all the transitions originating the single emission lines portrayed in Figure 3.9 (they are labelled according to the terminology adopted for the corresponding absorption lines). Only in a few cases, it was difficult to determine unequivocally the final state, as for the 15366 and 15378 cm^{-1} lines because the two possible final states (4 and 5, fifth column of Table 3.1) are rather close. Moreover, an A3 line contribution might be hidden under the 15378 cm^{-1} line. For the strongest line at 15151 cm^{-1}, the starting sublevel may be either A or B: the line, being rather broad, may indeed arise from the superposition of both A13 and B13 lines. Lines due to transitions starting from all the $^5F_5$ manifold sublevels (listed in the third column of Table 3.1) were identified. The strongest lines are those appearing on the low energy side of the emission spectrum and are originated by transitions having as final states the highest sublevels of the $^5I_8$ manifold, i.e. X13, X12, and X11 lines. Only the weak lines at 15452 and 15533 cm^{-1} correspond to transitions reaching the lowest sublevel of the ground manifold: they are the A1 and D1 lines, respectively. According to the above attribution it was possible to extract the position of the sublevels within the ground manifold, as the difference between the energy of the starting sublevel within the $^5F_5$ manifold (evaluated from the absorption measurements) and the energy at which each emission line is detected: the results are collected in Table 3.1, fifth column. The agreement with the figures obtained from the absorption spectra as a function of temperature (Figure 3.3 and Figure 3.4) is excellent (compare third and fifth column in Table 3.1).

3.4.2 Hyperfine structure

The hyperfine (hf) interaction depends both on the nuclear spin $\underline{I}$ and on the total angular momentum $\underline{J}$ of the 4*f* electrons, being expressed as $H_{hf} = A_j \underline{J} \cdot \underline{I}$ within a single manifold, where A_J is the hyperfine coupling constant for the considered multiplet (see Section 1.5). In most cases, the hf structure (hfs) of energy spectra can be well understood by considering H_{hf} as a perturbation acting on degenerate electronic states.

YPO_4 doped with Ho^{3+} is an ideal system to study the hfs for a few reasons:

1. Ho^{3+} has the highest nuclear spin (I=7/2) among the rare earths (configuration $4f^{10}$);
2. ^{165}Ho has a natural abundance of 100%;
3. all the low-lying manifolds of Ho^{3+} are characterized by large J values (up to J=8 for the ground state);
4. the D_{2d} crystal field symmetry probed by Ho^{3+}, substituting for the eight-fold coordinated Y^{3+}, in tetragonal YPO_4 is not low enough to remove completely the manifold sublevel degeneracy;
5. the Y^{3+} site is the only one which can be occupied by Ho^{3+};
6. the substitution of Ho^{3+} for homovalent Y^{3+} does not require any charge compensation, thus a single Ho centre is expected to occur;
7. the weak phonon coupling allows the absorption lines to be very narrow at low temperatures (see above and Section 1.6).

As a rule, in the past, the hfs was put in evidence only in restricted wave number ranges and for a few transitions, as for tetragonal $LiYF_4$ [9, 61-63], CaF_2 [64-66], or $CsCdBr_3$ [67] doped with Ho^{3+}, with the exception of YAB: Ho^{3+} [10].

In the present work a large number of absorption lines, monitored at temperatures lower than 60 K and belonging to almost all the investigated transitions, appeared ‘decorated’ by beautiful and clear hfs patterns (they are labelled with * in the third column of Table 3.1). Three examples were reported in Figure 3.6 and Figure 3.7. In other cases the lines showed a nearly squared top which suggests they are affected by hf splitting, as the line at 15557.2 cm^{-1} in Figure 3.3; the structure cannot be resolved even with high instrumental resolution. Only the transitions $^5I_8 \rightarrow {}^5I_4$, $^5S_2$, and $^5F_4$ does not allow to distinguish unequivocally any hfs, since the lines are very weak and thus affected by noise. Furthermore, even at 9 K the lines broaden by increasing the energy at which they fall, due to excited state lifetime shortening, thus the hfs is blurred as a consequence of the single component overlap.

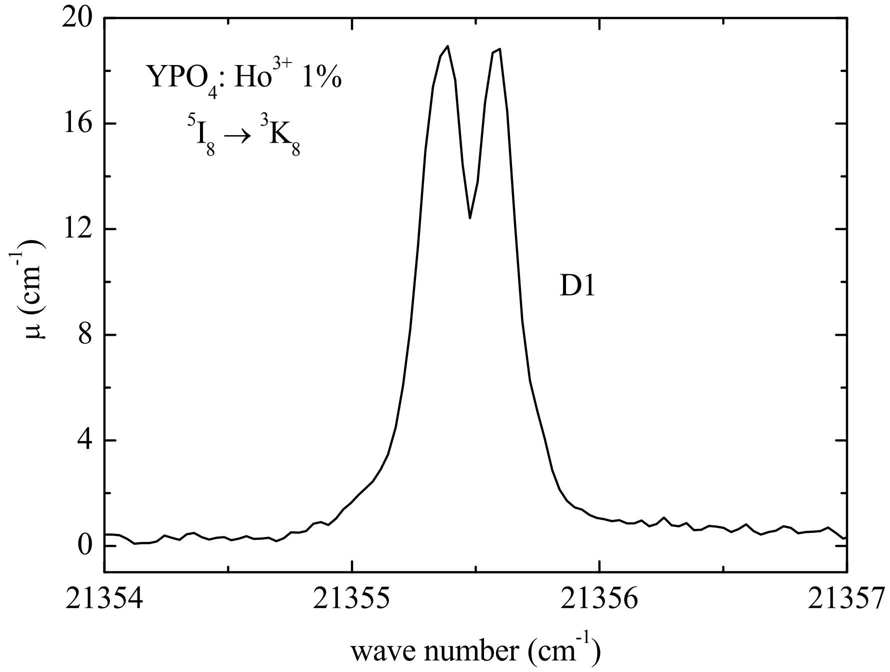

Figure 3.12 Hyperfine structure displayed by the absorption line at ~21355.5 cm^{-1} in the region of the Ho^{3+} $^5I_8 \rightarrow {}^3K_8$ transition.

According to Section 1.5, different patterns can be distinguished: a single narrow line, two components (Figure 3.12), eight components (Figure 3.6) and a more complicated pattern (Figure 3.7 and Figure 3.13). Moreover, the hfs components can be either evenly spaced or not, of equal or different amplitude (Figure 3.6 and Figure 3.7).

The large number of fundamental lines split by hfs can be explained only by a doubly degenerate (*E*) starting level. Then, in the case of simple hfs with eight components, i.e. transitions from a doublet to a singlet (*E*→*A*) (Figure 3.6), it is possible to derive the separation Δ_i of the fundamental state (see Section 1.5). The value so derived by averaging the widths of 18 lines was $\Delta_i^1=1.29\pm0.04$ cm^{-1}.

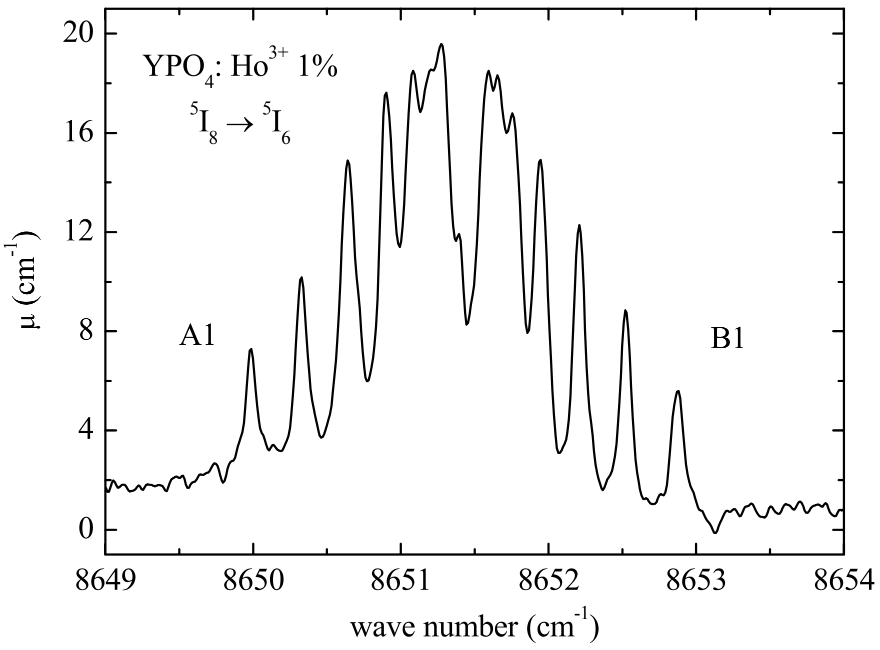

Figure 3.13 Hyperfine structure displayed by the absorption lines at ~8650 and 8652 cm^{-1} in the region of the Ho^{3+} $^5I_8 \rightarrow {}^5I_6$ transition.

In the case of the close lines at ~5152 and 5158 cm^{-1}, whose components are separated by ~0.19 cm^{-1}, a lorentzian decomposition was performed: the results are displayed in Figure 3.14 and Figure 3.15. The lorentzian shape confirms a negligible contribution of inhomogeneous broadening (see Section 1.6). Plotting the separation (ν_{n+1}-ν_n) between each (n+1)th and nth component as a function of n, the result is a straight line (Figure 3.16). This confirms not only that the lines are not evenly spaced, but also that the separation varies linearly. A non-equispaced pattern can be explained by a second order hyperfine interaction (see Section 1.5), which gives rise to a contribution to the hf splitting proportional to I_z^2 rather than I_z, and have a significant effect on groups of electronic levels separated by small energy gaps. When at least one *E*-level is involved in the considered transition, the effect of this pseudoquadrupolar coupling is a non evenly spaced lying series of components (see Figure 1.4).

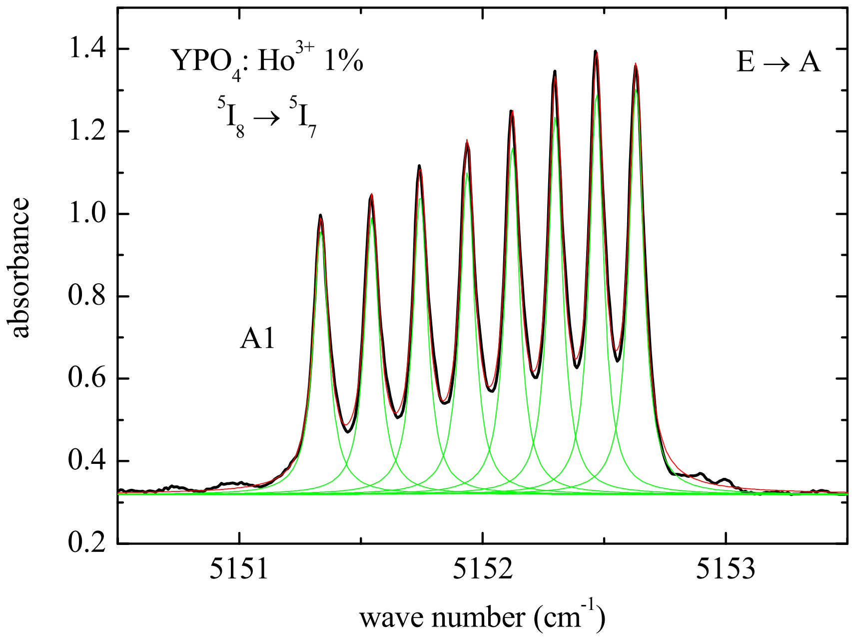

Figure 3.14 Lorentzian decomposition of the hyperfine structure displayed by the absorption line at ~5152 cm^{-1} in the region of the Ho^{3+} $^5I_8 \to {}^5I_7$ transition. Black curve: experimental data; green curves: lorentzian components; red curve: fit.

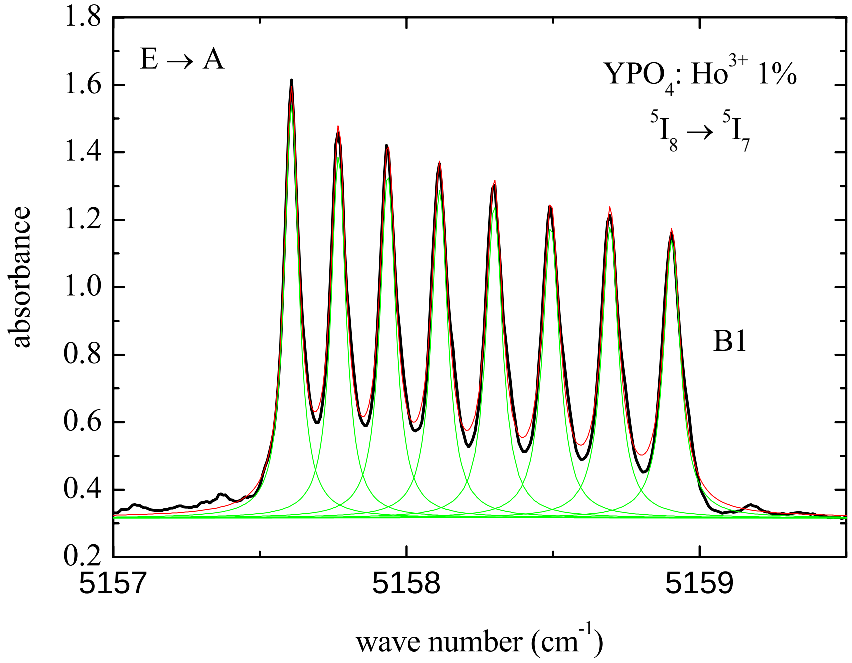

Figure 3.15 Lorentzian decomposition of the hyperfine structure displayed by the absorption line at ~5158 cm^{-1} in the region of the Ho^{3+} $^5I_8 \to {}^5I_7$ transition. Black curve: experimental data; green curves: lorentzian components; red curve: fit.

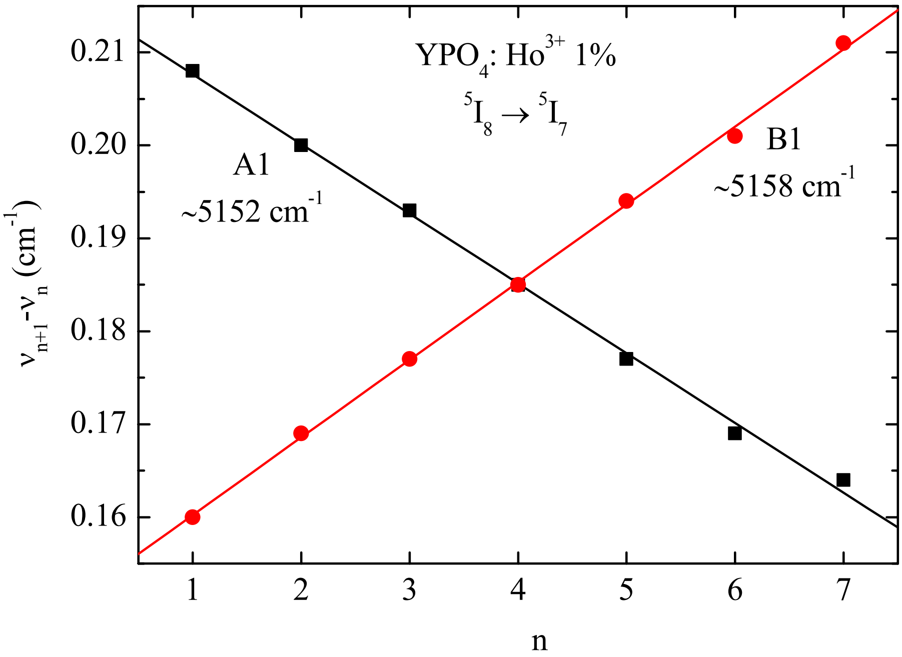

Figure 3.16 Hfs component separation ν_{n+1}-ν_n as a function of n for the lines at ~5152 and 5158 cm^{-1}. The lines are linear fitting.

A more complicated pattern, as those in Figure 3.7 and Figure 3.13, could arise from either the superposition of ED and MD contributions to hfs ($E \rightarrow E$ transition, see Section 1.5), or from two singlet lines with simple hfs so close one to each other to be practically overlapped (e.g. the lines at ~8650 and 8652 cm^{-1}, in Figure 3.13), respectively.

The line at ~5173 cm^{-1} represents the most interesting case: in addition to the 8 components due to ED contribution ($\Delta_{ED}=|\Delta_i+\Delta_f|/(2I)$), the 8 central components due to the MD contribution ($\Delta_{MD}=|\Delta_i-\Delta_f|/(2I)$) appear. It is the first time, to our knowledge, of a clear evidence of such complex well resolved structure.

The values derived from the spectrum, Δ_{ED}=2.29 and Δ_{MD}=0.3 cm^{-1}, allowed to obtain Δ_i=1.295 and Δ_f=0.994 cm^{-1}. The value Δ_i=1.295 cm^{-1} is in excellent agreement with that derived from the analysis of the doublet-to-singlet transitions (Δ_i^1=1.29±0.04 cm^{-1}); this confirms the soundness of the approach. The same procedure was applied to the line at ~5164.4 cm^{-1}: starting from Δ_{ED}=1.43 and Δ_{MD}=1.14 cm^{-1}, Δ_i=1.284 and Δ_f=0.144 cm^{-1} was obtained. Once more, the value of Δ_i=1.284 cm^{-1} was obtained.

Owing to this, a width of the line affected by hfs larger than ~1.29 cm^{-1} suggests the presence of the MD contribution, even if it is not as evident as shown in Figure 3.7. The value of Δ_f was derived fixing Δ_i=1.29 cm^{-1} in the equation $\Delta_{ED}=|\Delta_i+\Delta_f|/(2I)$. The results are listed in the last column of Table 3.1.

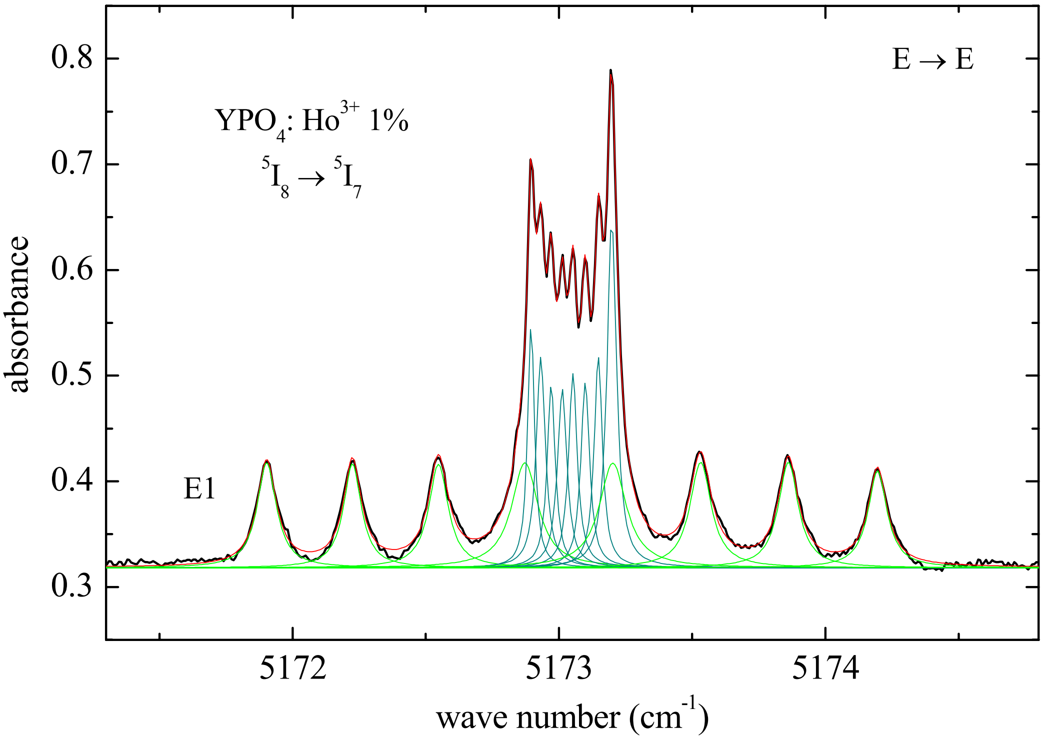

Figure 3.17 Lorentzian decomposition of the hyperfine structure displayed by the absorption line at ~5173 cm^{-1} in the region of the Ho^{3+} $^5I_8 \rightarrow {}^5I_7$ transition. Black curve: experimental data; green curves: ED lorentzian components; olive curves: MD lorentzian components; red curve: fit.

The lorentzian decomposition of the line at ~5173 cm^{-1} was also performed (Figure 3.17); the result is a straight line. Figure 3.18 portrays the separation (ν_{n+1}-ν_n) between each (n+1)th and nth component as a function of n; data are fitted according to a straight line. Thus, also in this case a small pseudoquadrupolar coupling contribution can be supposed, probably due to the proximity of the D1 line at ~5168.3 cm^{-1}.

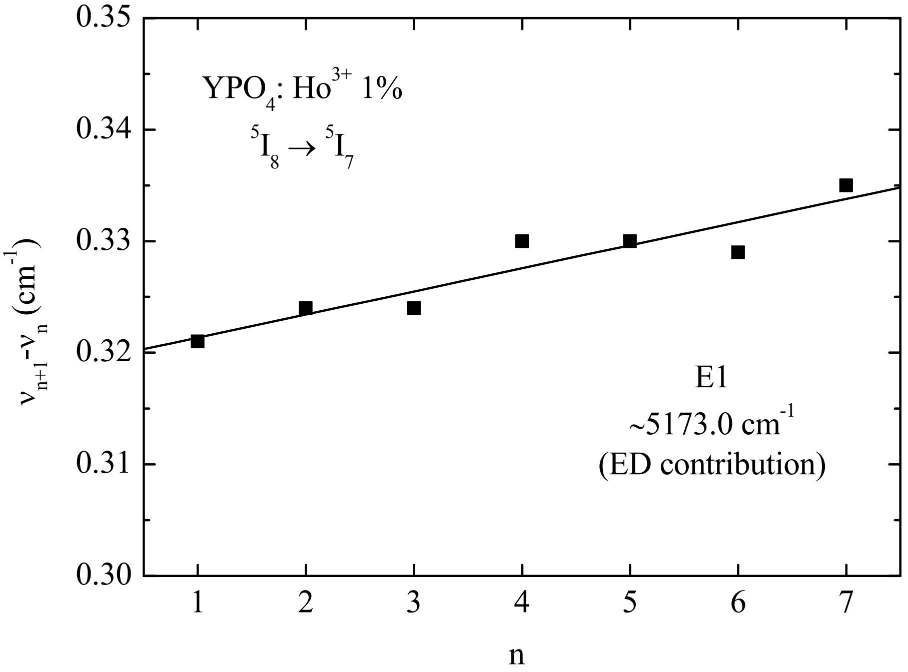

Figure 3.18 Hfs component separation ν_{n+1}-ν_n as a function of n for the line at ~5173 cm^{-1}. The line is a linear fitting.

Since in YPO4 the Ho^{3+} hfs survives up to rather high temperatures (40 K), at variance with the case of YAB [10], even some hot lines display the hfs, notwithstanding the first two excited sublevels of the ground manifold is as large as 66.5 and 71.2 cm^{-1} (see third column of Table 3.1), respectively. This allowed to determine the hf separation of the second excited sublevel, averaging the results coming from three X3 lines of the transition $^5I_8 \rightarrow {}^5I_7$: Δ_i^3=0.97±0.04 cm^{-1}.

To support the above considerations, theoretical calculations are in progress. By fitting the experimental energy levels with a single-ion Hamiltonian (see Section 3.4.1), the free ion and crystal field parameters, and the symmetry of the wave function related to each sublevel will be determined. Thus, the energy spectra will be calculated by numerically diagonalizing the full matrix representing each multiplet in the nuclear- and electronic-moment product space, to derive the expected separation for each degenerate sublevel [10].

3.5 CONCLUSION

The high resolution absorption spectra of a YPO_4: Ho^{3+} 1% m.f. single crystal, measured over wide wave number (500-25000 cm^{-1}) and temperature (9-300 K) ranges, have been analyzed in detail, taking advantage also of luminescence measurements (in the 15100-15500 cm^{-1} range) and theoretical calculations.

Thanks to rather closely temperature spaced sequences of spectra, measured by 20 or 30 K steps over the 20-240 and 240-300 K ranges, respectively, the large number of detected lines was attributed (Section 3.4.1): the scheme of the energy sublevels involved in the $^5I_8 \rightarrow {}^5I_7$, $^5I_6$, $^5I_5$, $^5I_4$, $^5F_5$, $^5S_2$, $^5F_4$, $^5F_3$, $^5F_2$, $^3K_8$, $^5G_6$+$^5F_1$,and $^5G_5$ transitions was supplied (see third column of Table 3.1). In particular, all the 13 expected sublevels of the ground manifold $^5I_8$ were assigned. In spite of the spectral complexity, the experimental energy levels were successfully fitted in the framework of a single-ion model (see fourth column of Table 3.1) and the crystal field parameters were derived (see Table 3.3 and Table 3.2).

Moreover, the employed high resolution allowed to detect the hyperfine structure which decorates a high number of absorption lines in a wide wave number range (up to ~24000 cm^{-1}; Section 3.4.2): in the past, the hfs was detected only for a few transitions ($^5I_8 \rightarrow {}^5I_7$, $^5I_6$, and $^5F_5$), as for tetragonal $LiYF_4$ [9, 61-63], CaF_2 [64-66], or $CsCdBr_3$ [67] doped with Ho^{3+}, with the exception of YAB: Ho^{3+} [10]. In the present work only the transitions $^5I_8 \rightarrow {}^5I_4$, $^5S_2$, and $^5F_4$ does not allow to distinguish unequivocally any hfs. On the other hand, at variance with the case of YAB [10], the hfs survives in YPO_4 up to rather high temperatures (40 K). Thus, a careful analysis of the low temperatures spectra (see Section 1.5) allowed to determine the hf splitting of the fundamental and second excited (71.1 cm^{-1}) sublevels of the ground manifold, and of some sublevels of the excited manifolds (see last column of Table 3.1).

Among the various hfs patterns detected (one, two, eight or more components, evenly spaced or not), a line with 16 hf well resolved components due to the electric and magnetic dipole contributions (Figure 3.7 and Figure 3.17) was monitored for the first time to our knowledge.

Theoretical calculations are still in progress to determine the symmetry of the wave function related to each sublevel and, then, to derive the expected separation of each degenerate sublevel [10]. The values so obtained will be compared with those extracted from the analysis of the experimental data (last column of Table 3.1).

4 $YAl_3(BO_3)_4$ SINGLE CRYSTALS

4.1 INTRODUCTION

Yttrium aluminum borate $YAl_3(BO_3)_4$ (YAB) is a crystal characterized by high hardness [68], broad optical transmission range (2500-50000 cm^{-1}) [69], and absence of colour centres. Moreover, it has a high non-linear optical coefficient.

Owing to this, YAB crystals doped with RE^{3+} are good candidates for applications in photonics as materials which exhibit non-linear optical phenomena as self-frequency doubling (SFD) or self-frequency summing (SFS). In particular, YAB: Nd^{3+} (NYAB) is an excellent material for infrared-to-visible up-conversion by SFD of the fundamental infrared line at 1.06 μm [70]. Furthermore, YAB: Yb^{3+} can provide tunable green [71] and yellow [72] outputs. On the other hand, it was demonstrated that YAB single crystals doped with Pr^{3+}, unlike other hosts as, for example, Cs_2NaYCl_6 [73], shows no *f-d* luminescence in the UV region, and therefore it is not exploitable as UV laser crystal [74].

The YAB crystal structure was determined by means of Rietveld refinement of neutron- and X-ray powder diffraction at room temperature [75]: it belongs to the hexagonal space group R32 (n. 155) with trigonal symmetry. The unit cell (Figure 4.1) contains three unit formulas, and the lattice parameters are:

a = 9.293(2) Å

c = 7.236(8) Å.

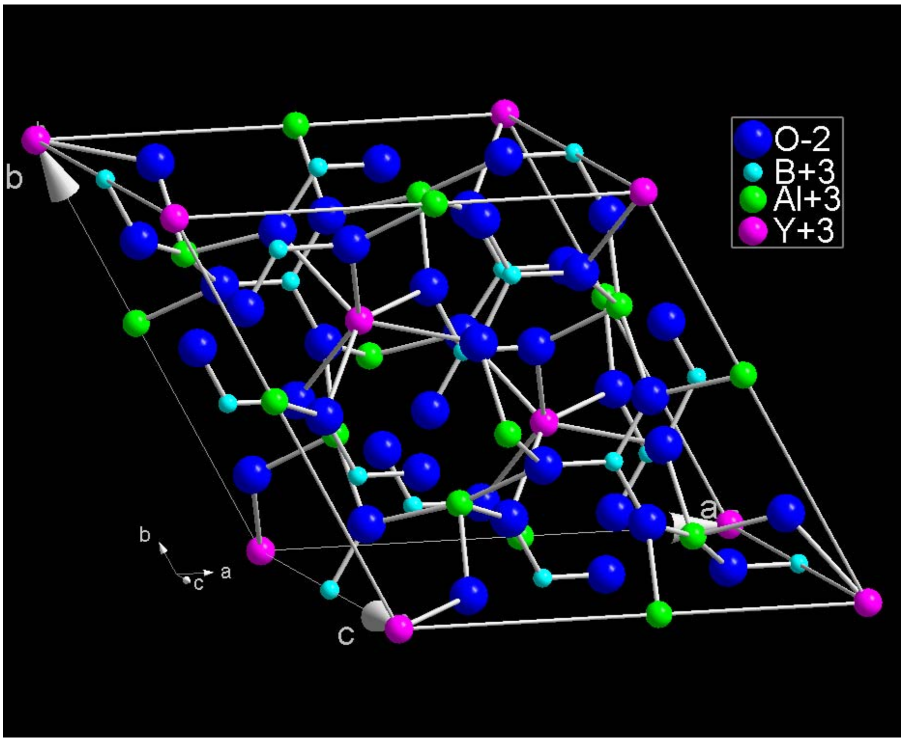

Figure 4.1 YAB unit cell. Blue: Oxygen; pink: Yttrium; green: Aluminium; cyan: Barium. The bonds are indicated by stickd and the axes by gray arrows.

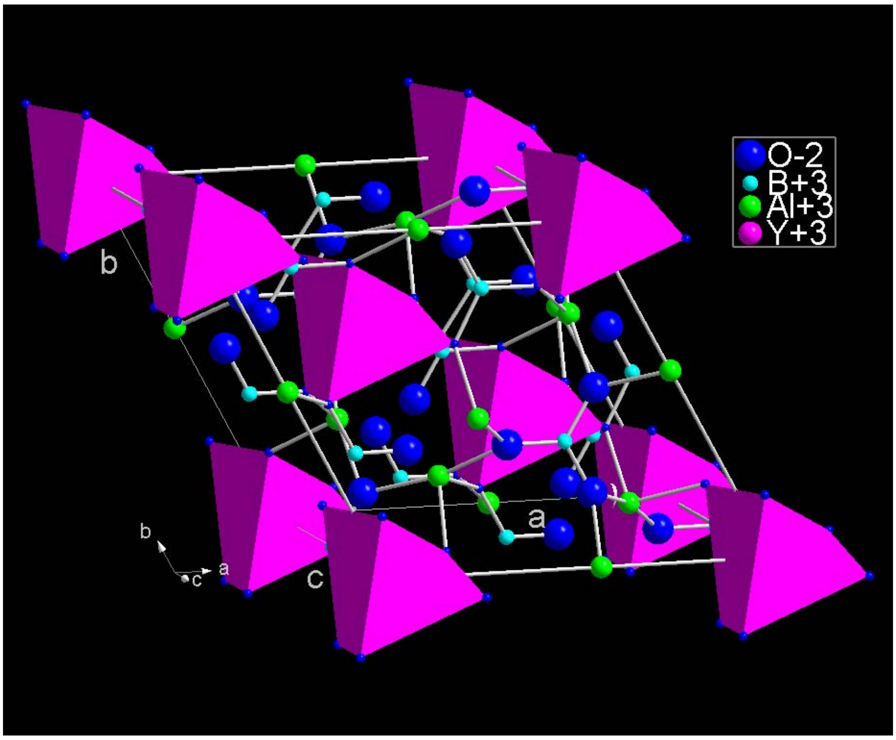

Figure 4.2 YAB unit cell. Blue: Oxygen; pink: Yttrium; green: Aluminium; cyan: Barium. The O^- polyhedra are made evident and the axes are indicated by gray arrows.

RE^{3+} substitutes for Y^{3+}, which probes a D_3 local symmetry; thus, it is surrounded by a trigonal prism of six O^{2-} ions (Figure 4.2). Since the RE^{3+} substitutes for the homovalent Y^{3+}, the charge compensation is not required, thus a high doping level can be reached without inducing substantial structural changes.

In the present work YAB: Pr^{3+} single crystals are studied. A careful analysis of the measured spectra allows to determine the energy level scheme of Pr^{3+} in YAB (Section 4.4.1) and to study the electron-phonon interaction (Section 4.4.3); moreover, measurements performed with linearly polarized incident light enable to identify the orientation of the dielectric ellipsoid and of the transition dipole moments inside the cell (Section 4.4.2). A fine structure showed by a few absorption lines is also studied (Section 4.4.4).

4.2 EXPERIMENTAL DETAILS

YAB single crystals were grown at the Research Institute for Solid State Physics and Optics of Budapest (Hungary) by the top-seeded solution growth (TSSG) from the $K_2O/MoO_3/B_2O_3$ mixed flux. The doping Pr^{3+} ions are added as Pr_2O_3 [76]. The crystals were X-ray oriented, cut, and polished for spectroscopic investigations.

Three samples were analyzed: two with 1mol% and one with 4mol% Pr^{3+} (concentrations expressed in terms of molar fractions); these nominal values were very close to the real ones, according to the atomic absorption analysis. The samples had different thicknesses (1-2 mm) and orientations: the Pr^{3+} 4mol% and one of the 1mol% samples were z-cut (i.e. with the *c* axis perpendicular to the sample plane, thus along the beam direction), while the latter 1mol% sample was x-cut (i.e. with the *c* axis in the plane of the sample, thus perpendicular to the beam). Figure 4.3 reports the optical microscope pictures collected by positioning the samples between crossed polarizers to make apparent possible striations due to twinning or internal strains [77].

The optical absorption spectra were monitored in the wave number range 500-25000 cm^{-1} with a resolution as fine as 0.02 cm^{-1} (see Appendix 1.1) and in the temperature range 9-300 K (see Appendix 1.2.1). Measurements with linearly polarized light (see Appendix 1.2.2) were also performed at 9 K in the infrared (IR) region 500-10000 cm^{-1}.

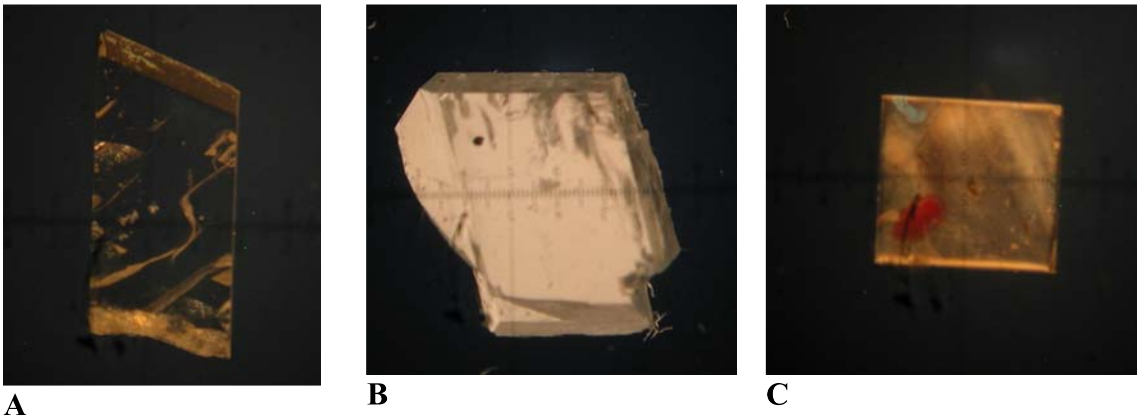

Figure 4.3 Pictures of the YAB: Pr^{3+} 1 (panels A and B) and 4mol% samples (panel C). The first sample (panel A) is x-cut, while the other two (panels B and C) are z-cut.

4.3 EXPERIMENTAL RESULTS

4.3.1 Anisotropy

Since YAB is a uniaxial crystal, it is expected that the Pr^{3+} transitions exhibit a strong dependence both on the sample orientation and on the light polarization (as in the case of BaYF, see Section 2.3.1).

Figure 4.4 reports the spectra measured at 9 K on the two 1mol% samples in the region of the $^3H_4 \rightarrow {}^3H_5$, $^3H_6$, $^3F_2$ transitions: while the spectrum of the z-cut sample (curve a) shows a strong absorption below 3000 cm^{-1}, the x-cut one (curve b) allows to monitor the lines originated by the first transition ($^3H_4 \rightarrow {}^3H_5$). Another example of anisotropy is displayed in Figure 4.5, which shows the spectra of two samples characterized by different doping levels and orientations. The z-cut YAB: Pr^{3+} 4mol% sample (curve b) exhibits a few strong absorption lines and other very weak ones. Although curve a represents the spectrum of a 1mol% doped sample, thanks to the different orientation (x-cut), it shows a large number of lines: some of them are weaker or absent in the

4mol% spectrum. Furthermore, for a few lines the amplitude is comparable to that of the strongest lines displayed by curve b, despite of the lower dopant concentration. Owing to this considerations, most of the measurements were performed on the x-cut YAB: Pr^{3+} 1mol%.

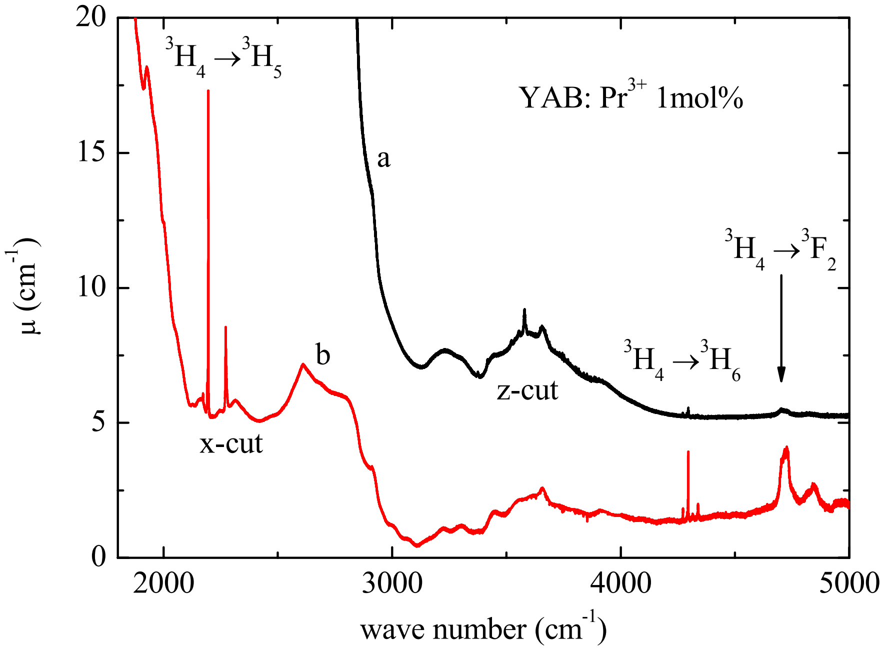

Figure 4.4 Optical absorption spectra of two YAB: Pr^{3+} 1mol% samples measured at 9 K in the region of the $^3H_4 \rightarrow {}^3H_5$, $^3H_6$, $^3F_2$ transitions with radiation propagating parallel (curve a) and perpendicular (curve b) to the *c* axis.

Thus, spectra with linearly polarized light were collected. Figure 4.6 shows an example of spectra measured at 9 K in the region of the $^3H_4 \rightarrow {}^3F_2$ transition with light electric field E_l travelling along one of the two-fold axes (i.e. perpendicular to the *c* axis) and polarization angle θ=0, 30, 60, and 90° with respect to the *c* axis. For E_l parallel to the *c* axis (θ=0°) the line at 5187 cm^{-1} dominates the spectrum. Rotating the electric field by 30° steps, it becomes weaker and weaker until, for E_l perpendicular to the *c* axis (θ=90°), it is only a weak shoulder. On the contrary, the bands at 5080, 5103, and 5206 cm^{-1} are weak at 0° and reach their maximum at 90°.

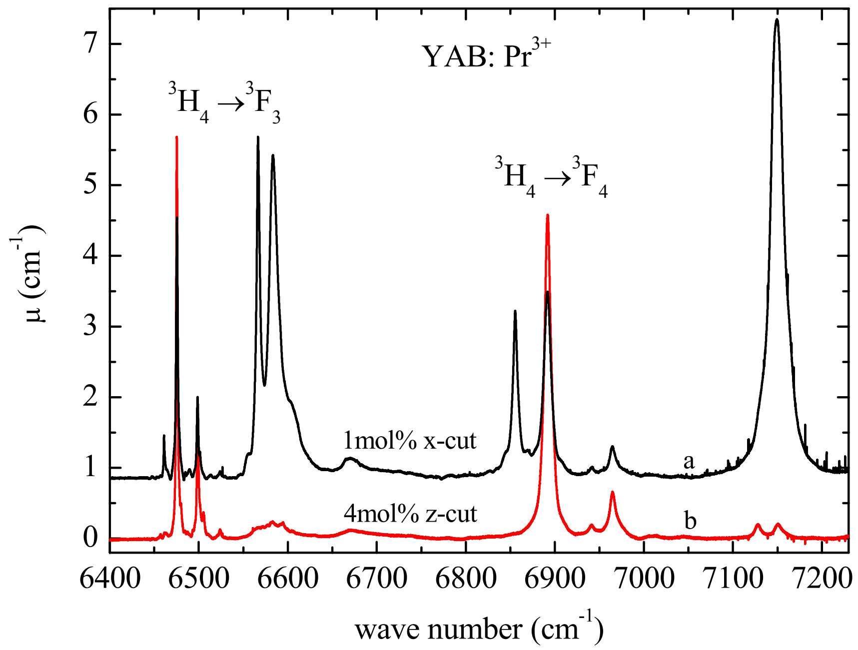

Figure 4.5 Optical absorption spectra of YAB: Pr^{3+} 1 (x-cut, curve a) and 4mol% (z-cut, curve b) samples measured at 9 K in the region of the $^3H_4 \to {}^3F_3$, $^3F_4$ transitions.

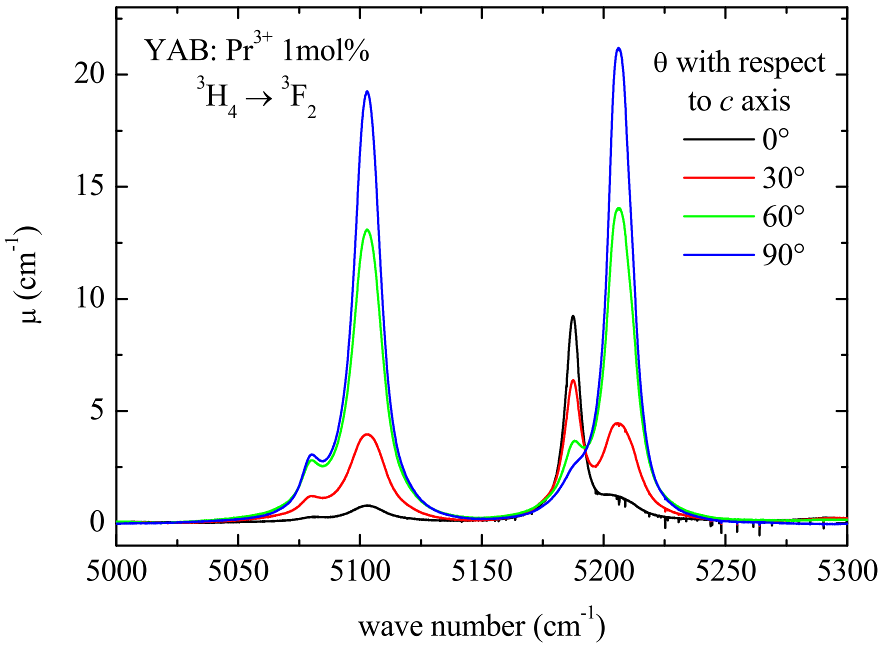

Figure 4.6 Optical absorption spectra of a YAB: Pr^{3+} 1mol% sample in the region of the $^3H_4 \to {}^3F_2$ transition measured at 9 K with linearly polarized radiation propagating perpendicular to the *c* axis and polarization angle θ=0, 30, 60, and 90°.

4.3.2 Temperature dependence

Measurements at different temperatures were performed on all the samples. An example of the results obtained from the 4mol% sample in the region of the $^3H_4 \rightarrow {}^3H_6$ transition is displayed in Figure 4.7: at 9 K (curve a) there are only some structures, the two strongest at 4295.5 and 4338.6 cm^{-1} being split into two components whose separations are about 0.4 and 1.1 cm^{-1}, respectively. By increasing the temperature up to 40 K (curves b and c), their amplitude decreases while other lines, shifted by ~23 cm^{-1} with respect to each of the structures monitored at 9 K, increase exhibiting the same splittings: 0.4 cm^{-1} for the line at 4272.3 cm^{-1} and 1.1 cm^{-1} for that at 4315.3 cm^{-1}. A further increase of the temperature up to 100 K (curve d) causes a decrease of all the lines, until, at 300 K (curve e), the spectrum is composed of a unique broad and weak band. By increasing the temperature, even the line position slightly changes: see for example behaviour of the line at 4295.5 cm^{-1} (it shifts at 4295.1 cm^{-1} at 100 K).

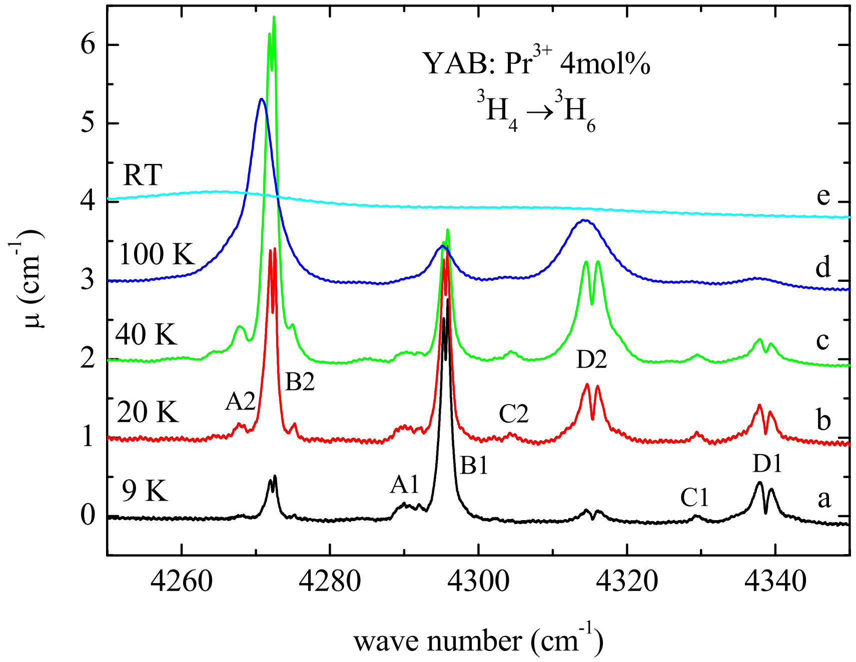

Figure 4.7 Optical absorption spectra measured at different temperatures on a YAB: Pr^{3+} 4mol% sample in the region of the $^3H_4 \rightarrow {}^3H_6$ transition. Curve a: 9 K; curve b: 20 K; curve c: 40 K; curve d: 100 K; curve e: RT.

Measurements at different temperatures (9-300 K) were performed on the x-cut 1mol% sample in the regions of Pr^{3+} transitions $^3H_4 \rightarrow {}^3H_5$, $^3H_6$, $^3F_2$, $^3F_3$, $^3F_4$, $^1G_4$, $^1D_2$, $^3P_0$, $^3P_1$, and $^1I_6$ [56]. The line behaviour by increasing the temperature is well represented in

Figure 4.8 and Figure 4.9 for the $^3H_4 \rightarrow {}^3F_3$ transition. Figure 4.8 displays the spectra measured at temperatures up to 80 K: also in this case at 9 K (curve a) only few lines are present. By increasing the temperature up to 20 K (curve b) the bands at 6485.1, 6498.6, 6524, 6581, and 6591 cm^{-1} decrease, while those at 6469, 6475, 6501, 6555, and 6566 cm^{-1} increase, reach their maximum amplitude at 40 K (curve c) and start decreasing at 60 K. At 80 K (curve d) the lines displayed in curve a become weaker and broader, while new lines appear on the lower energy side of the spectrum at 6244, 6270, 6332, 6361, and 6421 cm^{-1}. In Figure 4.9 the higher temperature spectra are shown (120-300 K). Besides a strong line broadening and weakening, the temperature increasing up to 300 K induces the growth of other structured bands.

The splitting of some lines into two components shown in Figure 4.7 is not detectable in this region, but it is present elsewhere (separation ranging between 0.4 and 3.1 cm^{-1}).

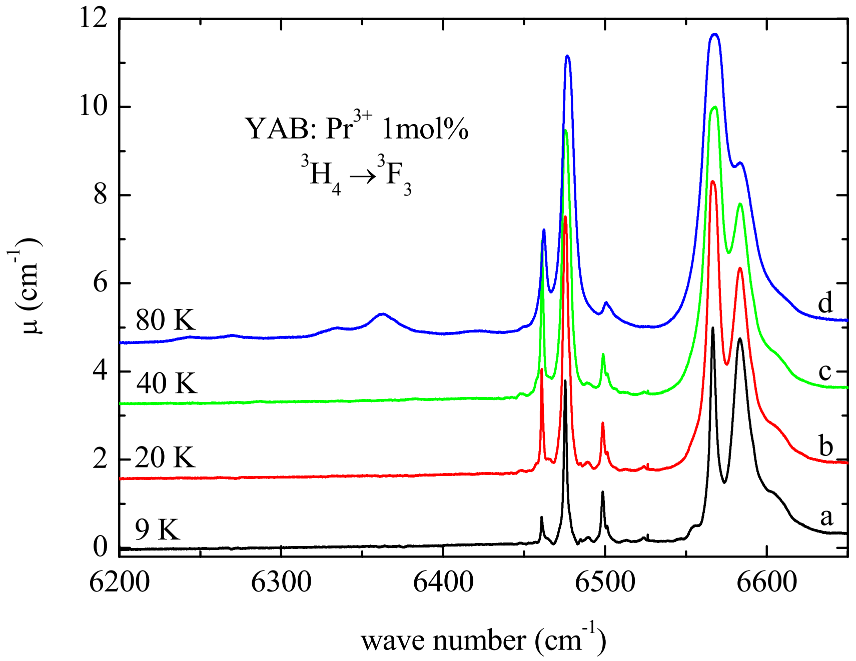

Figure 4.8 Optical absorption spectra measured at 9, 20, 40, and 80 K (curves from a to d, respectively) on a YAB: Pr^{3+} 1mol% sample in the region of the $^3H_4 \rightarrow {}^3F_3$ transition.

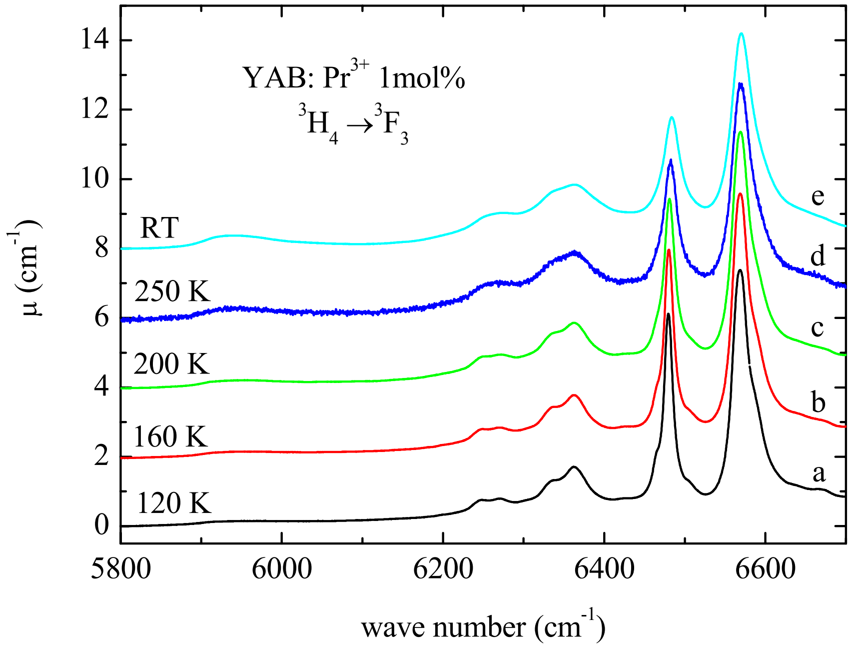

Figure 4.9 Optical absorption spectra measured at 120, 160, 200, 250 K, and RT (curves from a to e, respectively) on a YAB: Pr^{3+} 1mol% sample in the region of the $^3H_4 \rightarrow {}^3F_3$ transition.

4.4 DISCUSSION

4.4.1 Line attribution and crystal field parameters

As already reported in the cases of BaYF: Ho^{3+} and Tm^{3+} (Section 2.4.1) and YPO_4: Ho^{3+} (Section 3.4.1), the line attribution for a non-Kramers ion, as Pr^{3+} ($4f^2$), is quite difficult due to the large number of sublevels (up to $2J+1$) into which a manifold of given J can be split by low symmetry crystal field. The $4f^2$ configuration level of the free Pr^{3+} ion is split into 13 manifolds by the electrostatic and spin-orbit interaction [32]. For the ion embedded in a crystal host, the transitions expected in the range analyzed in the present work are those from the fundamental manifold $^3H_4$ to the excited ones $^3H_5$, $^3H_6$, $^3F_2$, $^3F_3$, $^3F_4$, $^1G_4$, $^1D_2$, $^3P_0$, $^3P_1$, and $^1I_6$ [56]. A further difficulty in the line attribution comes from the fact that the Pr^{3+} absorption lines in YAB are structured (see Figure 4.7) and rather broad, if compared with those induced by other RE^{3+} at the same concentration (see for example the low temperature spectra of YAB: Dy^{3+} 1mol% in

Ref. [78]). Nevertheless, the accurate analysis (according to the procedure described in Section 2.4.1) of the spectra as a function of Pr^{3+} doping level, sample orientation, temperature and incident light polarization allowed identifying most of the X1 lines and the Stark splitting of the $^3H_4$ ground manifold.

Table 4.1 Sublevel positions (cm^{-1}) for Pr^{3+} ground and excited manifolds in YAB as derived from optical absorption measurements (third column) and theoretical calculations (last but one column). Experimental values from Ref. [74] are reported for comparison (fourth column). Last column lists the hf separations evaluated from the spectra (see Section 4.4.4).

$^{2S+1}L_J$	Level	Exp. (cm^{-1})	Exp.[a] (cm^{-1})	Level	Fit. (cm^{-1})	$\Delta_{hf}^{exp.}$
$^3H_4$	1	_0_	0	1'	-8.13	
	2	_23.7_±1.4	150	2'	22.684 D	
	3	_140.6_±1.7	231	3'	168.214	
	4	_228.8_±2.2	332	4'	246.491 D	
	5	_332_±5	-	5'	444.341 D	
	6	_560_	560	6'	538.187	
$^3H_5$	A	2191.1		A'	2156.525 D	
	B	2194				
	C	_2196.1_*		B'	2219.512 D	0.53±0.01
	D	2198.4				
	E	_2272_		C'	2258.561	
				D'	2388.411	
	F	_2478_		E'	2425.848 D	
				F'	2562.643 D	
				G'	2621.159	
$^3H_6$	A	4290.9*				
	B	_4295.5_*		A'	4330.564	0.4
	C	4329.4				
	D	_4338.6_*		B'	4357.499 D	1.11±0.05
				C'	4363.669	
				D'	4440.863 D	
				E'	4462.181	
				F'	4646.161	
	E	4703				
	F	_4715_		G'	4717.693 D	
	G	4724				
	H	4817.8				
	I	_4845_		H'	4866.86 D	
				I'	4914.481	
$^3F_2$	A	_5103_	5080	A'	5050.072	
	B	_5187_	5178	B'	5086.62 D	
	C	_5206_	5200	C'	5188.052 D	

$^{2S+1}L_J$	Level	Exp. (cm^{-1})	Exp.[a] (cm^{-1})	Level	Fit. (cm^{-1})	$\Delta_{hf}^{exp.}$
$^3F_3$	A	_6465_	6463	A'	6475.072 D	
	B	_6485.1_	6487	B'	6478.422	
	C	6498.6				
	D	_6524_	6528	C'	6534.157 D	
	E	_6581_	6555	D'	6579.125	
	F	6591	6590			
	G	_6607_		E'	6603.515	
$^3F_4$	A	6671				
	B	_6855.5_	6843	A'	6852.088 D	
	C	_6891.3_	6879	B'	6860.212	
	D	_6965_	6928	C'	6994.397 D	
			6980	D'	7058.479	
	E	_7150.4_*	7115	E'	7138.049 D	
	F	_7160_	7135	F'	7165.535	
$^1G_4$	A	_9707.4_		A'	9676.354 D	1.23
	B	_9749_*		B'	9777.989	
	C	_9909_		C'	9931.078 D	
				D'	10073.98	
	D	_10178_		E'	10180.6	
	E	_10216_		F'	10214.14 D	
	F	10256				
$^1D_2$	A	16512*	16525			1.53
	B	_16754_*	16769	A'	16737.34 D	
				B'	16856.18	
	C	_17150_	17156	C'	17188.4 D	
$^3P_0$	A	_20603_*	20619	A'	20602.66	
$^3P_1$+$^1I_6$	A	_20985_		A'	20960.63	
	B	_21008_		B'	20967.32	
	C	_21013_*		C'	21052.35 D	3.1
	D	_21145_		D'	21147.83 D	
	E	_21153_*		E'	21188.68 D	2.8
	F	21163*	21176			
	G	21219				
	H	_21247_*	21236	F'	21275.06	
	I	_21330_		G'	21372.65	
	L	21353				
				H'	21485.25	
				I'	21640.07 D	
	M	_21816_		L'	21791.19 D	
	N	_21889_		M'	21844.2	
$^3P_2$	A	22260	22274			
	B	_22365_	22379	A'	22421.85	

$^{2S+1}L_J$	Level	Exp. (cm^{-1})	Exp.[a] (cm^{-1})	Level	Fit. (cm^{-1})	$\Delta_{hf}^{exp.}$
	C	*22460*		B'	22474.17 D	
	D	*22710*	22418	C'	22641.55 D	

*** Line split into two components.**
[a] From Ref. [74].
D=doublet.

The experimental energy levels are summarized in Table 4.1, third column and compared with the experimental values obtained by Bartl and co-workers [74] from optical absorption spectra measured with a resolution of 5 cm^{-1} in the visible range (fourth column). The majority of the experimental values reported in Ref. [74] are comparable, within the used resolution, to those found in the present work. The most important discrepancy is in the determination of the $^3H_4$ ground manifold splitting: Bartl and co-workers did not find the sublevel at 23.7 cm^{-1}, probably because only two temperatures were analyzed (10 and 298 K). Although this level has never been quoted in Ref. [74], the presence of this sublevel is beyond any doubt: in the present work it was derived from differences between the positions of about 30 X1-X2 line pairs in the 1mol% sample, and from 42 ones in the 4mol% sample. Moreover, the relative lines show a behaviour, as a function of the temperature, characteristic of hot bands. As an example, panels A, B, and C in Figure 4.10 show the temperature dependence of the line amplitude for a few X1-X2 line pairs monitored in the 1mol% sample. For the lines which exhibit the doublet structure (indicated by * in Table 4.1) at T≤40 K (as the B1 line at 4295.5 cm^{-1} displayed in Figure 4.7), three sets of data are reported, i.e. the values of the two components (up and down triangles) and their average (squares and circles). The X1 lines at 2196.1, 4295.5 and 5103 cm^{-1} (squares) decreases by increasing the temperature, while the related hot-bands at 2172.8, 4272.3, and 5080 cm^{-1} (circles) are absent or weaker at 9 K, increase by increasing the temperature until they reach the maximum between 40 and 60 K, and then decrease. Since in Ref. [74] the sublevel at 23.7 cm^{-1} was not evidenced, some other discrepancies with the present work find an explanation: a few lines related in Ref. [74] to transitions starting from the lowest level of the ground manifold, are here attributed to hot-bands starting from the first excited level of the ground manifold. An example is the A2 line at 5080 cm^{-1} (see Figure 4.6).

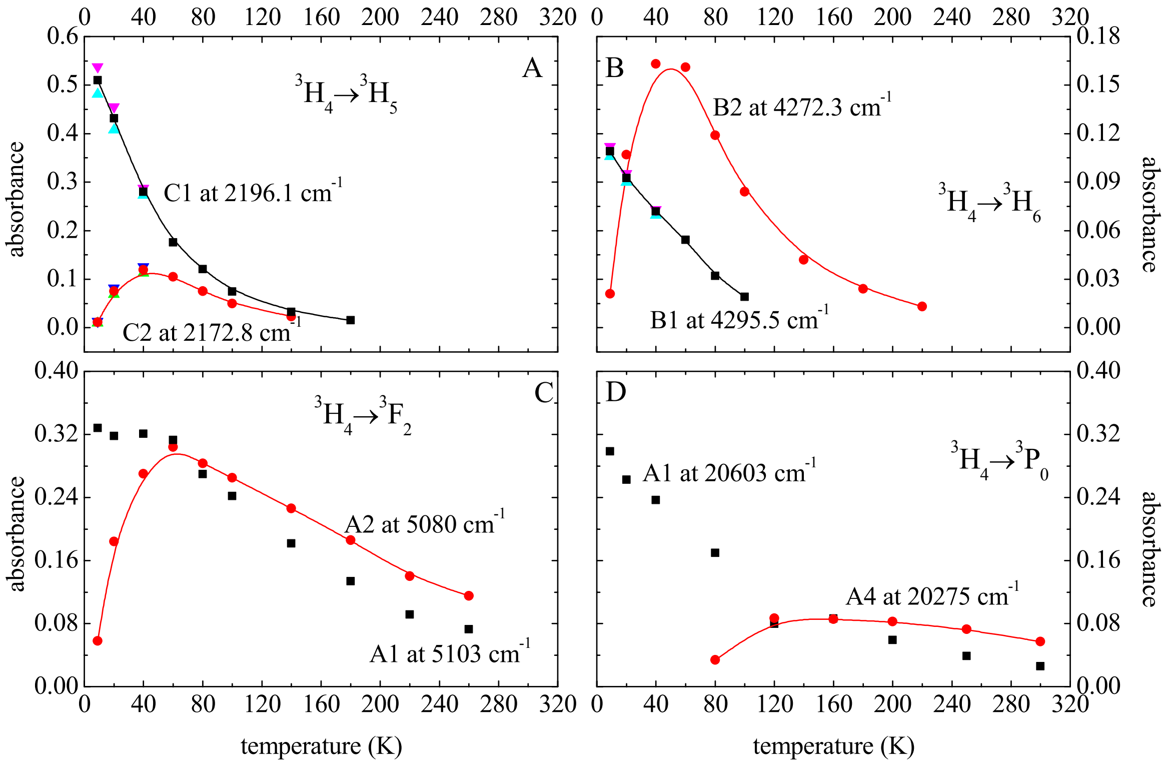

Figure 4.10 Temperature dependence of the line amplitude for a few X1-X2 line pairs (panels A, B, and C) and a pair A1-A4 (panel D) detected in spectra of the 1mol% sample. The lines are guides for the eyes.

In panel D in Figure 4.10 the A1 (at 21603 cm^{-1} squares) and A4 (at about 21275 cm^{-1} circles) lines ($^3H_4 \rightarrow {}^3P_0$ transition) are displayed. Since the final manifold of this transition is characterized by J=0, it should be a singlet; thus, the low temperature spectra in that region should exhibit a single fundamental line (A1) and should allow the unequivocal identification of the related hot-bands (A2, A3, ...). Figure 4.11 shows the spectra measured at different temperatures on a x-cut 1mol% sample: the orientation is the necessary requisite for making evident the fundamental line A1 because, according to Ref. [74], it has a π polarization. The spectrum measured at 9 K (curve a) shows a very intense line at 20603 cm^{-1}, attributed to the A1 transition, accompanied by a weak satellite separated by ~23 cm^{-1}, at about 20580 cm^{-1} and attributed to the A2 hot-band. At 80 K (curve b) other bands grow on the lower energy side, separated by 140 and 228 cm^{-1} from the A1 line and attributed to the A3 and A4 transitions, respectively. In fact, their amplitudes increase by increasing the temperature up to 160 K (curve c; see also panel D in Figure 4.10). In the 200 K spectrum (curve d) also the A5 hot-band can be detected at 20276 cm^{-1}, separated from the fundamental A1 line by 327 cm^{-1}. Although the A1 line at 20603 cm^{-1} at 9 K should be very simple, being originated by a transition connecting the lowest sublevel of the ground manifold to the $^3P_0$ singlet, it presents an unexpected complex structure (with components at 20599, 20600.6, and 20603.4 cm^{-1}), showed in the inset of Figure 4.11.

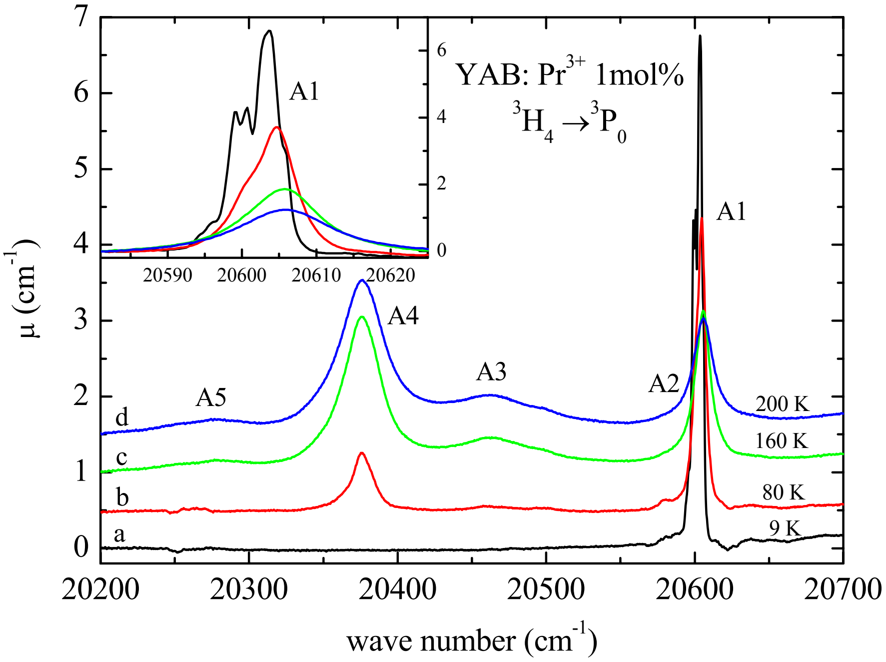

Figure 4.11 Optical absorption spectra measured at 9, 80, 160, and 200 K (curves from a to d, respectively) on a YAB: Pr^{3+} 1mol% sample in the region of the $^3H_4 \rightarrow {}^3P_0$ transition. Magnification of the A1 line region in the inset.

Several other discrepancies were found between the experimental energy leves and the theoretical calculations.

Last but one column in Table 4.1 lists the values obtained from fitting the experimental data according to the crystal-field (CF) theory (see Section 1.3 and Section 2.4.1.1): they are labelled with i' and X' in the fifth column. Since the free ion parameters are generally expected to be very similar in all phases, only Coulomb and spin-orbit among them were varied to fit experimental data starting from the values obtained by Carnal *et al.* for Tm^{3+} in LaF_3 [33]: other free ion parameters (which are weak corrective potentials) were kept fix at the values obtained in Ref. [33]. The starting CF parameters came from Ref. [74]. The best fit was obtained by excluding some experimental data which the calculations are not able to reproduce; the values exploited for the fitting are those in italic in the third column of Table 4.1. The parameters so obtained are listed in Table 4.2.

Table 4.2 Coulomb, spin-orbit and CF parameters obtained for Pr^{3+} from the fitting of the experimental data in italic in the third column of Table 4.1.

Parameter	Data fit
E_{ave}	10083±4
F^2	67973±40
F^4	49600±140
F^6	32663±93
ζ	755.7±2.2
B_2^0	548±33
B_4^0	165±70
B_6^0	362±92
B_4^3	1336±49
B_6^3	457±67
B_6^6	-243±81

Despite all the efforts, the agreement is poor (σ~35.7 cm^{-1}) and the correspondence is missing both in the numerical values and in the position within the sublevel sequence (compare second and third columns with fifth and sixth ones, respectively, in Table 4.1). In a few cases, as for $^3H_4 \rightarrow {}^3F_3$, $^3P_1+{}^1I_6$, $^3P_2$ transitions, the number of experimental levels is larger than that expected from the theoretical calculations.

On the other hand, strong discrepancies were found between experimental and theoretical values in several crystals doped with Pr^{3+} ions [79, 80]. In those cases, the discrepancies were mainly limited to a few transitions ($^3H_4 \rightarrow {}^1G_4$, $^1D_2$ in particular), independently of the host matrix, and could be significantly reduced by introducing additional contributions in the Hamiltonian: a two-electrons correlation-crystal field interaction [79] or a crystal-field induced interconfigurational mixing [80].

The difficulties found in the experimental data fitting might come from some peculiar characteristics of Pr^{3+} ions. The ionic radius, of Pr^{3+} coordinated with 6 oxygen ions, is 0.99 Å, thus larger than that of Y^{3+} (0.9 Å) which Pr^{3+} substitutes for [81]. This could induce some deformations in the surrounding and distortions of the local symmetry. The fact, already mentioned, that, for comparable doping levels, the Pr^{3+} absorption lines in YAB are much broader than those due to others RE^{3+} [78], might support a higher Pr^{3+} interaction with nearest and next-nearest neighbours.

Further theoretical attempts to improve the fit are still in progress.

4.4.2 Linear dichroism

Figure 4.6 is an example of dichroism exhibited by Pr^{3+} absorption lines in YAB in the region of the $^3H_4 \rightarrow {}^3F_2$ transition.

Following an approach similar to that described in Section 2.4.2 for the monoclinic structure of BaYF, the dichroic spectra can be exploited to identify the orientation of the dielectric ellipsoid and of the dipole moments μ associated with each transition. In the present work, spectra were measured on a x-cut 1mol% sample oriented with the binary a_1 axis parallel to the incident light beam: the incident light electric field E_l forms an angle θ with the c axis.

The absorbance α can be expressed as a function of θ [34]:

$$\alpha(\theta) = -\log\left(10^{-\alpha_Z}\cos^2\theta + 10^{-\alpha_Y}\sin^2\theta\right) \qquad 4.1$$

where $\alpha_{Z,Y}$ are the absorbances along the principal dielectric axes Z and Y, respectively. Figure 4.12 displays the angular dependences for the A1, A2, and B1 lines ($^3H_4 \rightarrow {}^3F_2$ transition) detected in the spectra measured at 9 K; the data were fitted according to eq. 4.1 and θ_M (abscissa of the maximum), α_Z and α_Y, obtained as fitting parameters, are listed in Table 4.3 (fourth, fifth, and sixth columns, respectively). Thus, averaging all the θ_M values, the angle between the crystallographic axis c and the principal dielectric axis Z results $\theta_M \sim (-5.2 \pm 0.99)°$. In the trigonal symmetry, the two axes, c and Z, are usually assumed as coincident [82]; the small misalignment found here might be due to the difficulties in aligning a small specimen in the sample holder.

All the analyzed X1-X2 line pairs exhibit the same behaviour as a function of the polarization angle; for example, both the A1 and A2 lines of the $^3H_4 \rightarrow {}^3F_2$ transition portrayed in Figure 4.12 have the maximum at ~85° and the minima at ~-5 and 175°. This means that the lowest and first excited sublevels of the ground manifold have the same character. This represents a further discrepancy between experimental data and theoretical calculations: in fact, the last predict that the two first sublevels of the ground manifold are a singlet and a doublet, respectively (see last but one column of Table 4.1). Thus, the X1 and X2 lines should have different polarizations, according to the selection rules for D3 symmetry [74].

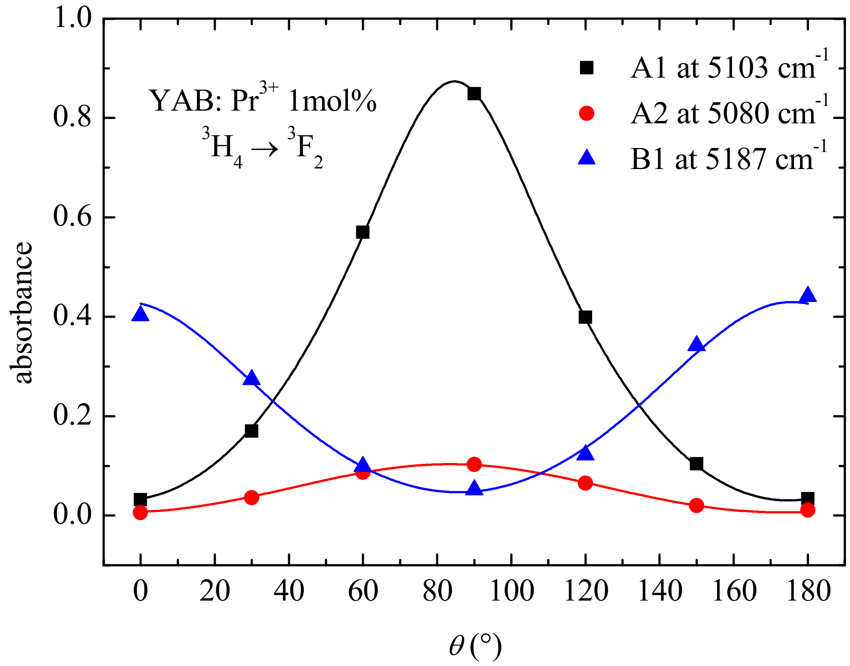

Figure 4.12 Angular dependence of the amplitude of the A1, A2, and B1 lines ($^3H_4 \rightarrow {}^3F_2$ transition) detected in the spectra measured at 9 K on a x-cut 1mol% sample. The beam travels along the a_1 axis and θ is the angle between E_l and the *c* axis.

From α_Z and α_Y derived from the fitting according to eq. 4.1, it is possible to calculate the angle χ between the *Z* axis and the projection on the *Y-Z* plane of the dipole moment μ (electric dipole matrix element associated with a given transition between sublevels of different manifolds). In fact, the dichroic ratio *D*

$$D = \frac{\alpha_Z}{\alpha_Y} = \sqrt{\frac{\varepsilon_Y '}{\varepsilon_Z '}} \cot^2 \chi = \frac{n_Y}{n_Z} \cot^2 \chi \qquad 4.2$$

links $\alpha_{Z,Y}$ with χ, $\varepsilon'_{Z,Y}$ (real parts of the dielectric constant), and $n_{Z,Y}$. (refractive indices along the principal axes). Taking into consideration the difficulties in aligning the sample and in evaluating the line amplitude, it is allowed to approximate $n_Y/n_Z \sim 1$, despite the dependence of the refractive index on the propagation direction and on the wavelength [83, 84]. The values derived according to eq. 4.2 are listed in last column of Table 4.3; they can be grouped around four discrete values: $\chi_1=(11.5\pm1.8)°$, $\chi_2=(17.6\pm2.2)°$, $\chi_3=(70.5\pm1.8)°$, and $\chi_4=(82.3\pm1.6)°$, which can be compared, to understand how the dipoles are arranged in the YAB structure, to the angles between the Y^{3+}-O^{2-} (or Pr^{3+}-O^{2-}) bonds and the Z axis. Figure 4.13 shows a projection of the YAB primitive cell on the *Y*-*Z* plane (usually *Y* coincides with the binary axis a_1 [82]) and of dipole moment vectors (forming angles $\pm\chi_i$ with the *Z* axis) applyed to the Y^{3+} ions. Only the dipole moment projection characterized by χ_2 is close, within the standard deviation, to the that of a Y^{3+}-O^{2-} bond. The other dipole moments are located in the "empty spaces", either between the planes of oxygens ($\pm\chi_3$ and $\pm\chi_4$) or almost perpendicular to them pointing towards the boron ions ($\pm\chi_1$). Since the observed absorption lines are not related to charge transfer transitions, the electrons are not necessary located along the bond directions. On the contrary, intraconfigurational transitions require a change in the electronic distribution and they may occur more likely along directions not occupied by the bonds.

Table 4.3 Angles θ_M and χ for different lines of Pr^{3+} transitions.

Transition	**Line**	**Position (cm^{-1})**	**θ_{MAX} (°)**	**χ (°)**
$^3H_4 \rightarrow {}^3H_6$	B2	4272.8	-5.08384	12.29386
	A1	4290.9	-4.11573	17.66363
	B1	4295.5	-4.92385	12.55914
	D2	4315.3	-5.8343	8.404291
	D1	4338.6	-4.68892	15.17997
$^3H_4 \rightarrow {}^3F_2$	A2	5080	-6.56194	13.77385
	A1	5103	-5.35056	10.54555
	B1	5187	-4.29835	71.65241
	C1	5206	-5.44874	9.60057
$^3H_4 \rightarrow {}^3F_3$	B2	6460.9	-5.55883	68.34873
	C2	6475	-5.56287	12.2917
	C1	6498.6	-5.42244	17.18813
	D2	6501	-5.56529	20.47365
	F2	6566	-5.72231	82.64375
$^3H_4 \rightarrow {}^3F_4$	B1	6855.5	-5.76276	83.76062
	C1	6891.3	-4.92779	10.87275
	D1	6965	-7.18447	13.41853
	E1	7150.4	-5.71926	80.57602
$^3H_4 \rightarrow {}^1G_4$	E1	10216	-2.57573	71.38728

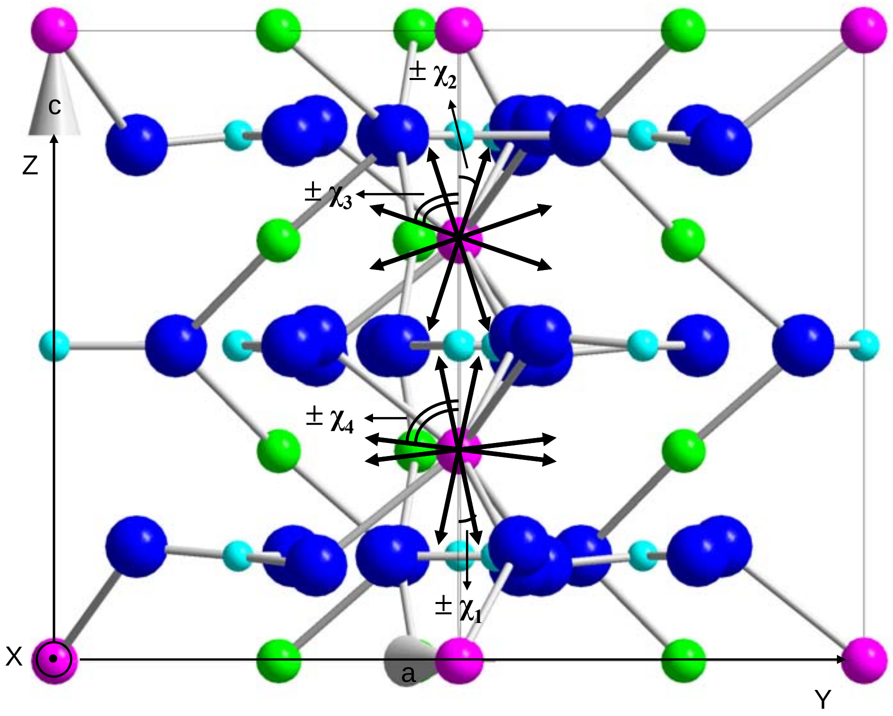

Figure 4.13 YAB primitive cell with the superposition of dipole moments in different directions. Blue: Oxygen; pink: Yttrium; green: Aluminium; cyan: Barium.

4.4.3 Electron-phonon interaction

The spectra temperature dependence was exploited to determine the energy level scheme of Pr^{3+} in YAB (see Section 4.4.1). It is possible to analyze the line full width at half maximum (FWHM) and position (POS) to obtain information about the electron-phonon coupling (see Sections 1.6.2 and 1.6.3). To do this, the line broadening and shift is fitted according to models based on either the single phonon coupling (SPC) or the two-phonon Raman scattering (TPRS). The choice of the proper model depends on the Debye temperature of the crystalline host, the energies of the involved phonons with respect to the upper limit of the phonon spectrum, and the inhomogeneous broadening occurring at low temperatures [7].

The SPC model was already applied on YAB samples to fit the shift and broadening of the absorption lines induced by rare earth ions [7] and OH^- stretching modes [85]. In this framework, the shift δE_i and broadening ΔE_i for a given i^{th} line are expressed according to eq. 1.51 and 1.47, respectively.

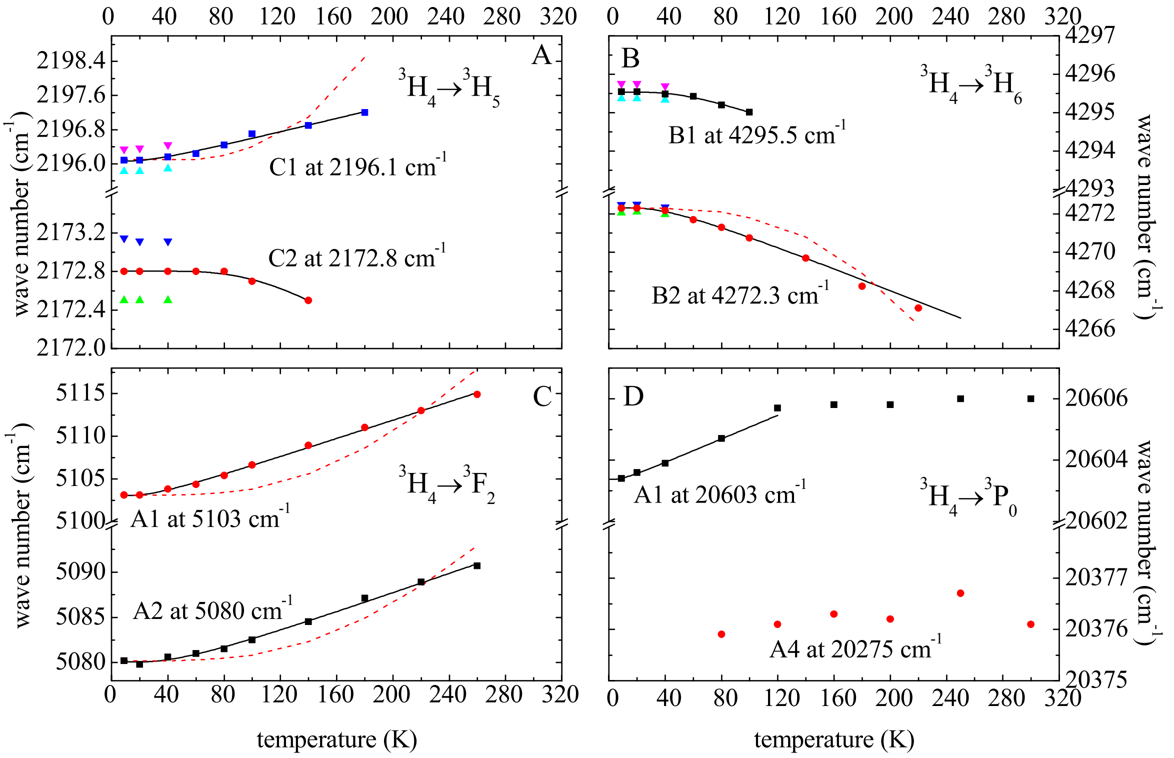

Figure 4.14 Position temperature dependence for a few absorption lines. Solid lines: fitting according to SPC model. Dashed lines: fitting according to TPRS.

The full width at half maximum cannot be evaluated for most of the lines in YAB, because they are either split into two components or superimposed to the neighbouring lines. Furthermore, the lines are affected by inhomogeneous broadening. The frequency shift is thus a more reliable parameter than the line width. Figure 4.14 displays some examples of POS temperature dependence for four X1-X2 line pairs (the same already analyzed in Figure 4.10). In two cases, panel A and B, the considered lines were split, thus both values related to the two components (up and down triangles) and their average are portrayed (squares and circles). Panel D shows the data related to the A1 and A4 lines of the $^3H_4 \rightarrow {}^3P_0$ transition (Figure 4.11): being the A1 line structured, only the position of the strongest component is reported. Since for temperature higher than 80 K the components merge in a unique band, the line temperature dependence analysis becomes difficult. Thus, the fitting was performed only in the range 9-80 K.

As already stated in Section 1.6.3, the line shift can be either positive or negative. In some cases both the fundamental line and the hot-band shift towards lower energies (see panel B in Figure 4.14), while in other cases both shift towards higher energies (see panel C). In panels A and D the fundamental lines, C1 and A1, respectively, exhibit blue-shift, while the relative hot-bands shift towards lower energies (C2 line in panel A) or do not move by increasing the temperature (A4 line in panel D).

The position fitting in the framework of the SPC model according to eq. 1.51 is represented by the solid lines in Figure 4.14 and the related parameters are listed in Table 4.4. The agreement with the experimental data is very good. Among the fitting parameters, the frequency σ of the phonon involved in the line shift (fifth column of Table 4.4) can be compared with the vibrational frequencies evaluated by Raman and IR spectra of YAB matrix (sixth and last but one columns, respectively) [69, 86]. It is worth noting that, except for the A1 line at 20603 cm^{-1}, the phonon energies practically coincide with those of a few Raman or IR active modes (sixth and last but one columns of Table 4.4, respectively). Furthermore, the same phonon values were derived from the vibronic replica of zero-phonon lines in YAB: Dy^{3+} 1mol% (last column of Table 4.4) [69]. The figure of the phonon involved in the shift of A1 line at 20603 cm^{-1} is supported by the vibronic replica monitored in YAB: Dy^{3+} [69].

Table 4.4 Parameters (second, third and fourth columns) obtained from the fitting according to eq. 1.51 of the lines in Figure 4.14. Fifth column: frequency of the phonon involved. The last three columns compare values coming from Raman, IR, and vibronic spectra.

Line	POS(0) (cm^{-1})	δω (cm^{-1})	$\hbar\omega/k_b$ (K)	σ (cm^{-1})	Raman (RT)[a]	IR (9 K)[b]	Vibronic shift (9K)[b]
C2	2172.804±0.008	-6.2±3.3	427±71	296.9±49	308	308	306.4±0.5
C1	2196.07±0.04	0.6±0.3	76.6±53.3	53.3±21.3	51		50.03±1.63
B2	4272.31±0.03	3.4±0.4	115.9±8.8	80.6±6.1	86		86±1.2
B1	4295.53±0.02	-2.6±1.0	177.3±30.8	123.2±21.4	123.8	125.8	122.9±1.7
A2	5080.1±0.2	7.5±0.5	136±22	94.6±15.2	94	95.4	93.05±1.56
A1	5103.0±0.1	4.4±0.8	81±56	56.0±8.8	51		50.03±1.63
A1	20603.38±0.08	0.5±0.4	26.1±17.9	18.2±12.4			18.81±1.37

[a] **From Ref. [86].**
[b] **From Ref. [69].**

The line position was also fitted in the framework of the two-phonon Raman scattering (TPRS) according to eq. 1.49, by assuming a Debye temperature of T_D=820 K (directly evaluated for YAB by means of specific heat measurements in the range 1.5-25 K [7]). The results are represented by the dotted curves in Figure 4.14.

By comparing the fits according to SPC and TPRS models (solid and dashed curves in Figure 4.14, respectively), it is clear that the latter fails in reproducing the thermally induced line shift. This might be due to the low energy of the phonons involved in the shifts (up to 296 cm^{-1}, see fifth column of Table 4.4) with respect to the upper value of the phonon band (~1400 cm^{-1} [87]) and to the narrowness of the lines [7].

4.4.4 Fine structure

As shown in Figure 4.7, in the YAB: Pr^{3+} spectra there are lines which exhibit a doublet structure (indicated by * in the third column of Table 4.1); this happens not only in the region of the $^3H_4 \rightarrow {}^3H_6$ transition, but it is monitored over the whole analyzed range (500-25000 cm^{-1}), with a separation of the two components ranging between 0.4 and 3.1 cm^{-1}. The temperature dependence of some split lines is shown in panels A and D in Figure 4.10 and Figure 4.14: by increasing the temperature from 9 to 40 K, both the amplitude (Figure 4.10) and position (Figure 4.14) of the two components (up and down triangles) exhibit the same trend. At 60 K the two components merge, due to the temperature induced homogeneous broadening.

Since the hyperfine (hf) interaction can be expressed as $H_{hf} = A_J \underline{J} \cdot \underline{I}$ and it acts on degenerate levels (see Section 1.5), it could be detected, on principle, also in YAB: Pr^{3+} for several reasons:

1. $^{141}Pr^{3+}$ has a natural abundance of 100%;
2. Pr^{3+} has nuclear spin I=5/2;
3. Pr^{3+} has, at least in the lower energy manifolds, a rather high electronic total angular momentum (J=4, 5, 6);
4. YAB has the hexagonal symmetry of the space group R32 [75], thus the crystal field experienced by the Pr^{3+} ions does not remove completely the level degeneracy (see last but one column of Table 4.1).

Actually, the hf splitting of Pr^{3+} energy levels has been detected in different matrices, as CaF_2 [88], $CsCdBr_3$ [89, 90], and $LiYF_4$ [91, 92]. The hf interaction acts on degenerate state by splitting the Pr^{3+} levels into three doublets in the cubic CaF_2 symmetry [88] or in six levels in matrices with a lower symmetry [89, 90]. In a few cases, the central gap is wider than the others and this might be due to a low symmetry perturbation [89], rather than a pseudo-quadrupolar interaction or an exchange interaction with neighbouring Pr^{3+}, as in the case of Ho^{3+} in $LiYF_4$ [9, 61].

Thus, the structure of some of the Pr^{3+} absorption lines in YAB can be due to hyperfine interaction and a additional one which splits the hf components in two groups. Moreover, as already pointed out in the previous sections, the lines are affected at 9 K by broadening, induced by the combined effect of the electron-phonon interaction (see Section 4.4.3) and of a site symmetry perturbation (see Section 4.4.1); it could hide the splitting, merging the components of the two groups into a doublet. A small energy gap separating the hf levels of Ho^{3+} in two groups of four levels each, was already observed in YAB, denoting a slight distortion of the site symmetry D_3 [10].

The hyperfine separations Δ (see Sections 1.5 and 3.4.2) have been evaluated for different doublets over the whole Pr^{3+} spectrum and the values, reported in the last column of Table 4.1, range from 0.4 to 3.1 cm^{-1}. A few experimental values are obtained averaging the hyperfine separation of the fundamental lines and the relative X2 hot-bands. The fact that the separation remains the same between the X1-X2 line pairs (see Section 4.3.2) means that both the lowest sublevels of the ground manifold are non-degenerate and the splitting comes from the final state. This does not agree with the level degeneracy evaluated from calculations based on the present data (see last but one column in Table 4.1), but agrees with the linear dichroism results (Section 4.4.2).

This is a further evidence of the limit of the single-ion model in predicting the energy level scheme of Pr^{3+} in YAB. In any case, additional attempts to improve the theoretical approach to this system are in progress, in order to derive the symmetry of each state and thus the possible hf splitting.

4.5 CONCLUSION

$YAl_3(BO_3)_4$ (YAB) single crystals doped with 1 and 4% m.f. of Pr^{3+} were analyzed in a wide wave number range (500-6000 cm^{-1}) and at different temperatures (9-300 K) by means of high resolution Fourier transform spectroscopy (see Appendix 1). Since YAB is a uniaxial crystal, measurements with linearly polarized incident light were also performed.

The spectra showed some peculiar features:

1. the absorption lines are rather broad with respect to those induced by other RE^{3+} in the same host (see for example Ref. [78]);
2. a few lines are split into a doublet (see Figure 4.7).

Although these features made the spectra analysis more complicated, the line attribution and the energy level scheme were obtained for the transitions connecting the fundamental manifold $^3H_4$ with the excited ones $^3H_{5,}$ $^3H_6$, $^3F_2$, $^3F_3$, $^3F_4$, $^1G_4$, $^1D_2$, $^3P_0$, $^3P_1$, and $^1I_6$ (see Section 4.4.1). Moreover, the orientation of the dielectric ellipsoid and of the dipole moments μ associated with each transition were determined (see Table 4.3 and Figure 4.13) starting from the dichroic spectra (see Section 4.4.2).

Fitting of the line shift as a function of the temperature according with either the single phonon coupling model (SPC) or the two-phonon Raman scattering one (TPRS) (see Section 1.6) demonstrated that the latter model is unable to reproduce the experimental data (see Section 4.4.3). According to the SPC model, the energies of the phonon involved were derived; they practically coincide with those of a few Raman or IR active modes (see Table 4.4).

The line broadening could account for the doublet structure shown by a few absorption lines. In fact, the line splitting only into two “components” (each due to the merging of three true hf components) could be induced by hyperfine interaction and additional contributions coming, for example, from pseudoquadrupolar coupling and/or local symmetry perturbation (see Section 4.4.4). The presence of a hf interaction might envisaged a new application of YAB: Pr^{3+} in the quantum information processing [93]. Good results were already obtained for Pr^{3+} embedded in Y_2SiO_5 [94] and $LiYF_4$ [91, 92] by exploiting the $^3H_4 \rightarrow {}^1D_2$ transition.

At variance with the cases of RE^{3+} embedded in BaYF and YPO_4 (see Chapters 2 and 3, respectively), for YAB: Pr^{3+} the agreement between experimental results and theoretical calculations was not found satisfactory (see Table 4.1). Other discrepancies came from the dichroic spectra analysis (Section 4.4.2) and from the same hf splitting of the X1-X2 line pairs (Section 4.4.4). The difficulties in the theoretical modelling of the Pr^{3+} embedded in a crystal host were already encountered in other matrices, as CaF_2 [88], $CsCdBr_3$ [89, 90], and $LiYF_4$ [91, 92].

Further attempts to improve the theoretical approach are still in progress.

5 SILICA GLASSES

5.1 INTRODUCTION

The interest in scintillating materials, i.e. luminescent materials which absorb ionizing radiation efficiently and convert it into radiation with a wavelength in or around the visible spectral region, is one century old [95]. Fundamental requirements for those materials are low density, high transparency, high luminescence efficiency, radiation hardness, and fast scintillation decay. They find applications in several fields [96, 97] like medicine [98], high energy physics [99], and security controls [100]. Recently, in alternative to the currently employed scintillator crystals, glasses were considered due to their good mechanical properties (because of their amorphous isotropic structure), good chemical stability, easy shape modelling [101] and, in principle, due to the possibility of doping with several activators even in large amounts. Moreover, the compatibility with the silica based photonics technology is higher and the glass synthesis techniques are less expensive than those of crystals.

Studies on rare earths (RE) doped glasses produced from powder melting [99, 100] evidenced a rather low luminescence efficiency and a poor radiation hardness, due to the low energy transfer from the glass matrix to the luminescent ions and to the presence of non-radiative paths competing with the radiative decay of the activators. In this respect, recently it was observed that co-doping with Gd^{3+} ions could increase the energy transfer to the luminescent ions (Ce^{3+}, Tb^{3+} or Eu^{3+}, for example) [102, 103].

Moreover, the sample preparation by means of the sol-gel technique could improve the luminescence properties [104-106]. About non-radiative channels, particular attention was given to the OH^- groups (due to their high energy vibrational modes, 0.4-0.45 eV) and to possible ways to reduce them [107, 108]. These groups together with H_2O remain in the samples during the preparation process. While free molecular water H_2O can be completely removed at high densification temperatures, OH^- present as silanol groups (Si–OH) remain, even after high temperature treatments. The OH^- content can be lowered by proper physical/chemical treatments, e.g. with fluorine [109].

In the last decade, the research is moving towards the study of nanocomposite materials where the active phase is composed of RE-rich aggregates with dimensions of a few tens of nanometres or less [110], but the real use of this kind of materials as scintillators requires further investigations. For example, in the case of SiO_2 doped with Ce^{3+}, one of the most employed activators, the formation of aggregates was monitored; unfortunately, these aggregates were CeO_2 clusters, and Ce^{4+}, due to its $4f^0$ configuration, does not originate radiative emission [108, 111, 112]. This is a further non-radiative channel in addition to OH^-. The presence of tetravalent ions can be removed by means of a sinterization process under reducing atmosphere [113].

In the present work Gd^{3+}, Tb^{3+}, Yb^{3+}, Ce^{3+}, Eu^{3+}, and co-doped Gd^{3+}-Ce^{3+} SiO_2 glasses are studied to investigate the cluster formation (Section 5.4.1), the OH^- content (Section 5.4.2), the matrix modifications (Section 5.4.3) owing to the RE^{3+} incorporation.

5.2 EXPERIMENTAL DETAILS

The glass samples were prepared at the Department of Materials Science of the University of Milano-Bicocca by the sol-gel method [111]; the densification temperature was 1050 °C for all the investigated samples. Ce^{3+} doped samples were submitted to a sinterization process in reducing atmosphere to avoid the presence of Ce^{4+} [113]. Discs of approximately 2 cm diameter were obtained; sometimes the disc was already broken at the end of the growth process. Several samples were submitted to a further post-densification rapid thermal treatment (RTT) by an oxidizing oxygen-hydrogen flame (marked with x in the last column of Table 5.1). Such a treatment typically features a very fast (2-4 s) temperature increase up to 1500-1800 °C, where the sample is kept for approximately 10 s before a rapid cooling in air. The temperature was monitored by an optical pyrometer (Impac IE 120) working at 5140 nm emission.

The list of analyzed samples is reported in Table 5.1; thickness ranges between 0.20 and 20 mm. The RE^{3+} doping level is given in terms of molar percentage (mol%), i.e. the ratio between the moles of RE^{3+} and the total moles of RE^{3+} and Si^{4+} [mol% = (moles of RE / (moles of RE + moles of Si))×100]. Pure SiO_2 samples were measured as references; they were submitted to the same thermal treatments of the samples doped with Eu^{3+} or Yb^{3+}.

Most of the samples are transparent, but some of them show a “foggy” or partially “milky” region (see, for example, SiO_2: Eu^{3+} 0.001mol% in Figure 5.1); the extreme case is the Eu^{3+} 10mol% sample (Figure 5.2): it is almost completely milky, only some fragments are partially transparent. After RTT, some samples kept the same appearance; some other samples changed drastically: they practically “exploded”, completely or partially (see, for example, the pictures in Figure 5.3).

Table 5.1 Analyzed samples.

Dopant	C_{RE} (mol%)	C_{RE} (mol%)	RTT
Gd^{3+}	0.05		x
	0.1		x
	0.5		x
	1		x
	3		x
	8		x
Eu^{3+}	0		x
	0.001		x
	0.003		x
	0.01		x
	0.03		x
	0.1		x
	0.3		x
	1		x
	3		x
	10		

Dopant	**C_{RE} (mol%)**	**C_{RE} (mol%)**	**RTT**
Tb^{3+}	0.001		x
	0.003		x
	0.01		x
	0.03		x
	0.1		x
	0.3		x
	1		x
	3		x
	10		x
Yb^{3+}	0		
	0.005		x
	0.01		x
	0.02		
	0.05		x
	0.1		
	0.2		x
	0.5		x
	1		x
	4		x
Ce^{3+}	0		
	0.001		
	0.003		
	0.01		
	0.03		
	0.1		
	0.3		
	1		
	3		
	10		
Gd^{3+}, Ce^{3+}	0.1	1	
	0.5	1	
	1	1	x
	3	1	x
	5	1	
	8	1	x
	0.1	0.1	
	0.5	0.1	
	1	0.1	x
	3	0.1	x
	5	0.1	x
	8	0.1	x

Figure 5.1 Picture of the SiO_2: Eu^{3+} 0.001mol% sample: it is characterized by a “foggy” region on the left.

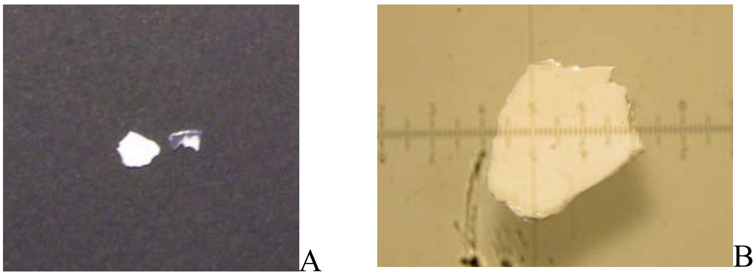

Figure 5.2 Pictures of the SiO_2: Eu^{3+} 10mol% sample. A: two fragments, one milky and the other partially transparent; B: magnification (8x) of the former sample.

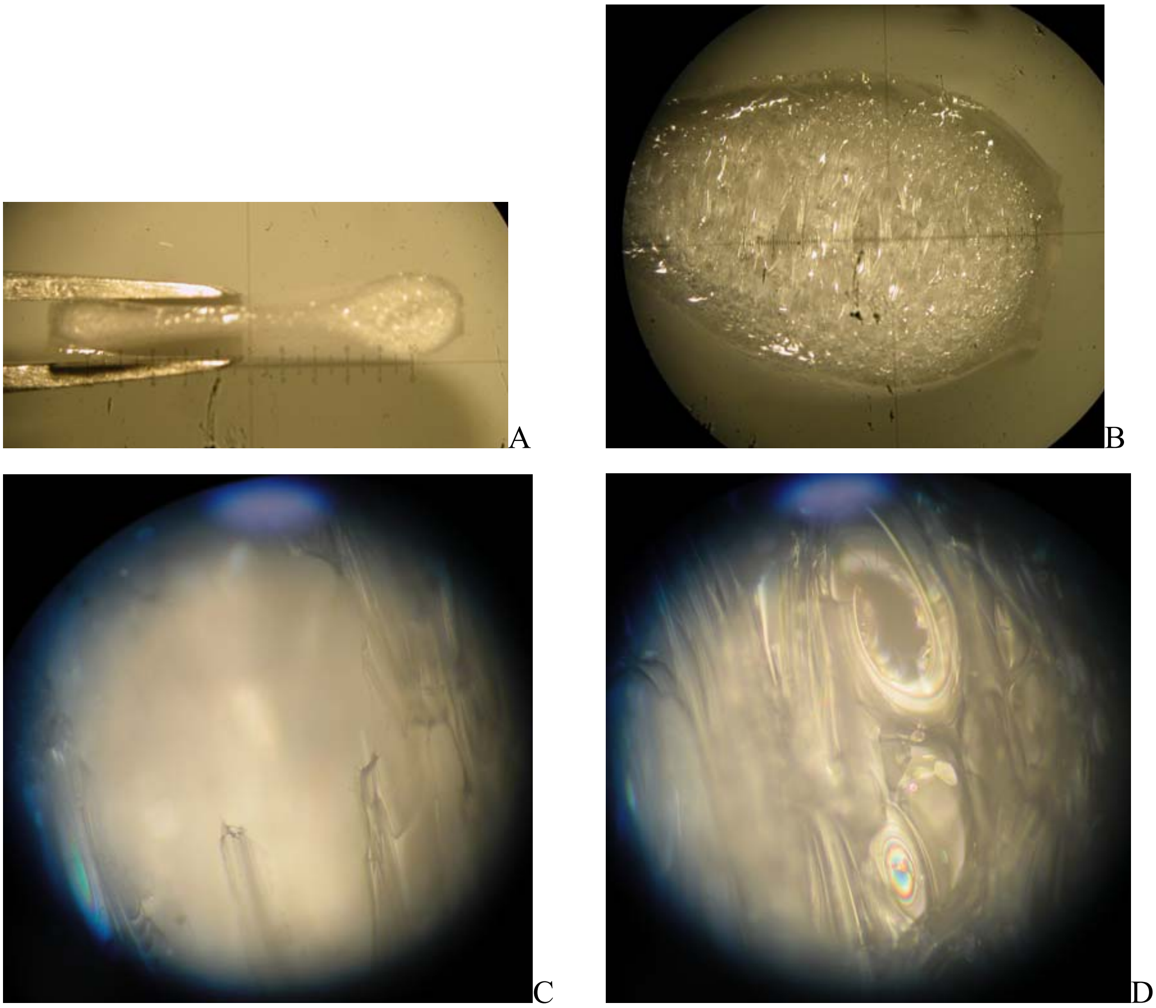

Figure 5.3 Pictures of the SiO_2: Eu^{3+} 0.01mol% sample. A: sample side image (8x); B: magnification 32x; C and D: magnifications 225x in two different positions.

The spectra of different compounds were measured for comparison with those of doped silica. They are:

1. RE^{3+} oxides, $(RE)_2O_3$ with RE= Eu, Gd, Tb, Yb (actually Tb_4O_7), purchased from Aldrich;
2. RE^{3+} oxyorthosilicate, $(RE)_2SiO_5$ with RE= Eu, Gd, Tb, Yb, prepared at the Department of Materials Science of the University of Milano-Bicocca; Gd-oxyorthosilicate was a crystalline sample doped with Ce^{3+} 0.2mol% (from Hitachi Chemicals).

Pellets were employed to measure the absorption spectra of powdered RE^{3+}-compounds (oxyorthosilicates and oxides) and of silica (RE^{3+} doped or undoped) in the spectral ranges where the massive samples exhibit very high absorption coefficients. Thus, chips of samples were ground and mixed with CsI or KBr powders. The weight ratio (W.R.) was ~0.6÷20 mg sample over 100 mg CsI or KBr.

The optical absorption spectra were monitored in the wave number range 200-14000 cm^{-1} with a resolution of 1 cm^{-1} (see Appendix 1.1) at room temperature (RT). Some samples were also measured in the temperature range 9-300 K (see Appendix 1.2.1) with a resolution as fine as 0.1 cm^{-1}, to made evident possible sharp lines due to RE^{3+} in ordered arrangements. The microreflectance measurements were performed at RT in the 500-6000 cm^{-1} range with a resolution of 1 cm^{-1} (see Appendix 1.2.3); the reflectance standard was a gold layer.

The surface morphology of the SiO_2: Eu^{3+} 10mol% sample were investigated by acquiring atomic force microscopy (AFM) topographic images (see Appendix 2.3).

Transmission electron microscopy (TEM) images were taken in the framework of a cooperation with the Department of Materials Science of the University of Milano-Bicocca (Prof. A. Vedda and co-workers) (see Appendix 2.4).

5.3 EXPERIMENTAL RESULTS

5.3.1 Ce^{3+} doped samples

Since Ce^{3+} has one more electron with respect to a closed shell configuration (i.e., it is characterized by a $4f^1$ configuration), it exhibits only one CF transition: $^2F_{5/2} \rightarrow {}^2F_{7/2}$. It is expected in the region of 2600 cm^{-1} [56].

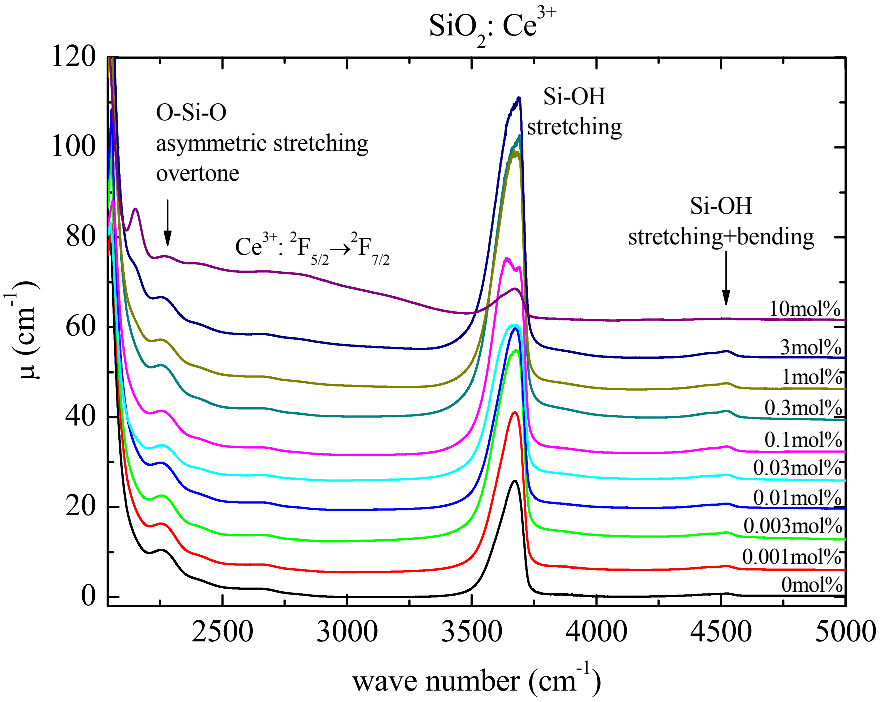

Figure 5.4 Optical absorption spectra of SiO_2 samples doped with different amount of Ce^{3+} (0-10mol%) measured at RT in the region of the $^2F_{5/2} \rightarrow {}^2F_{7/2}$ transition and OH^- vibrational modes.

Figure 5.4 displays the spectra measured at RT on Ce^{3+} doped samples (0-10mol%) in the 500-6000 cm^{-1} range; the spectra are displayed starting from ~2000 cm^{-1} because at lower wave number the absorbance is out of scale. By increasing the Ce^{3+} concentration from 0 (pure sample) to 10mol% the absorption spectra show that:

1. broad and weak bands grow in the region of the $^2F_{5/2} \rightarrow {}^2F_{7/2}$ transition;
2. the peak at ~2260 cm^{-1} related to O–Si–O asymmetric stretching overtone [114] decreases;

3. the two peaks related to Si–OH modes (stretching at ~3670 cm^{-1} and combination stretching+bending at ~4520 cm^{-1} [115]) first increase, then decrease.

Owing to the presence of bands due to the Ce^{3+} $^2F_{5/2} \rightarrow {}^2F_{7/2}$ transition, measurements at 9 K were performed on heavy doped samples (1-10mol%); Figure 5.5 displays the spectra measured on the sample doped with 10mol% Ce^{3+} at RT and 9 K. The absorption bands remain broad even at low temperature.

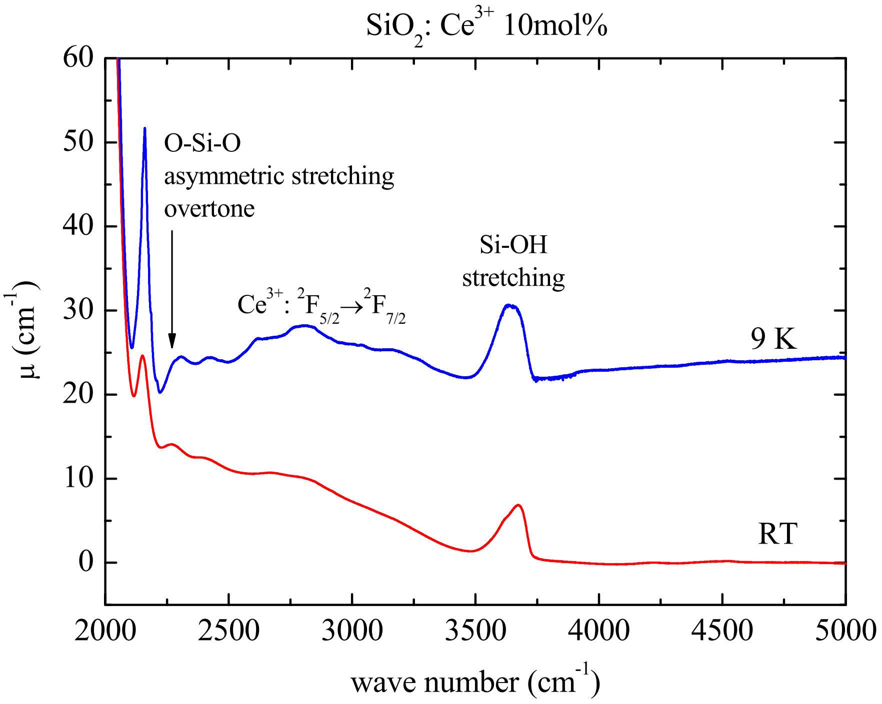

Figure 5.5 Optical absorption spectra of SiO$_2$: Ce^{3+} 10mol% measured in the region of the $^2F_{5/2} \rightarrow {}^2F_{7/2}$ transition and OH$^-$ vibrational modes at RT and 9 K.

To investigate the changes induced by the Ce^{3+} doping on the SiO$_2$ intrinsic fundamental modes, microreflectance measurements were performed at RT. Figure 5.6 displays the spectra (normalized to the reflectivity maximum at ~1123 cm^{-1} to emphasize the differences) of pure sample and three doped ones (1, 3, and 10mol%); spectra of low Ce^{3+} concentration samples are not reported for clarity, by considering that they practically coincide with the pure sample spectrum. The modifications induced by increasing the doping level are:

1. the shift towards low wave numbers of the reflectivity maximum at ~1123 cm^{-1};
2. the increase of the dip at ~1200 cm^{-1};

3. the appearance of bands in the 860-950 cm^{-1} region;
4. the increase of the band at ~780 cm^{-1}.

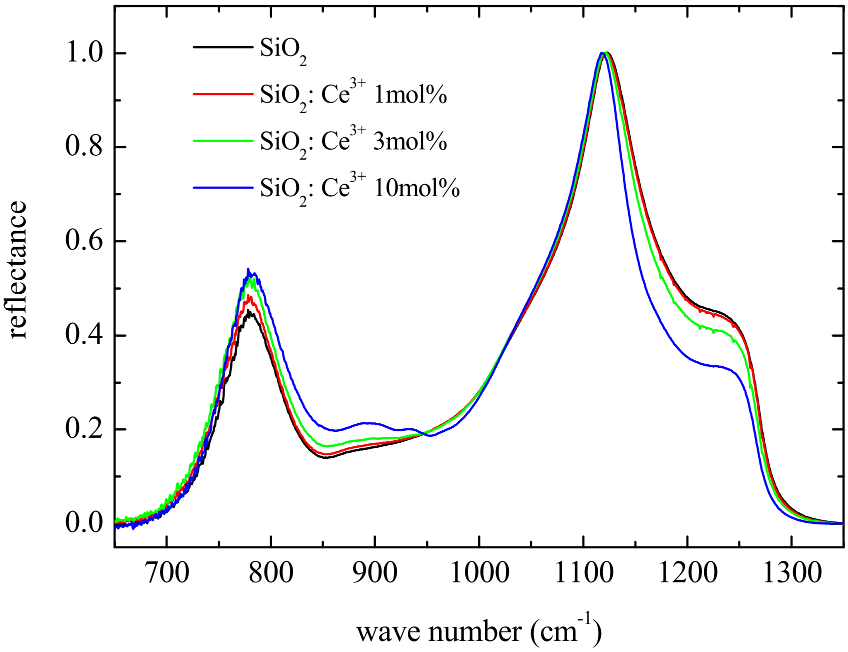

Figure 5.6 Microreflectance spectra of SiO$_2$ samples: pure and doped with different amounts of Ce^{3+} (1, 3, and 10mol%). All the spectra are normalized to the maximum.

5.3.2 Gd^{3+} doped samples

Gadolinium is the RE in the middle of the Lanthanide series: its configuration is $4f^7$, thus the fundamental manifold is $^8S_{7/2}$ and the first excited one, $^6P_{7/2}$, is expected at ~32000 cm^{-1}, i.e. in the UV region [56]. Thus, no absorption lines due to crystal field transitions should be detected in the investigated regions.

The main features in the region of the OH$^-$ modes (see Figure 5.7) are:

1. the appearance of a weak band at ~4250 cm^{-1} (indicated by an arrow) in addition to the peak due to Si–OH combination stretching+bending mode at ~4520 cm^{-1} [115]. It disappears in sample submitted to RTT;
2. the drastic decrease of the Si–OH bands in the Gd^{3+} 8mol% sample.

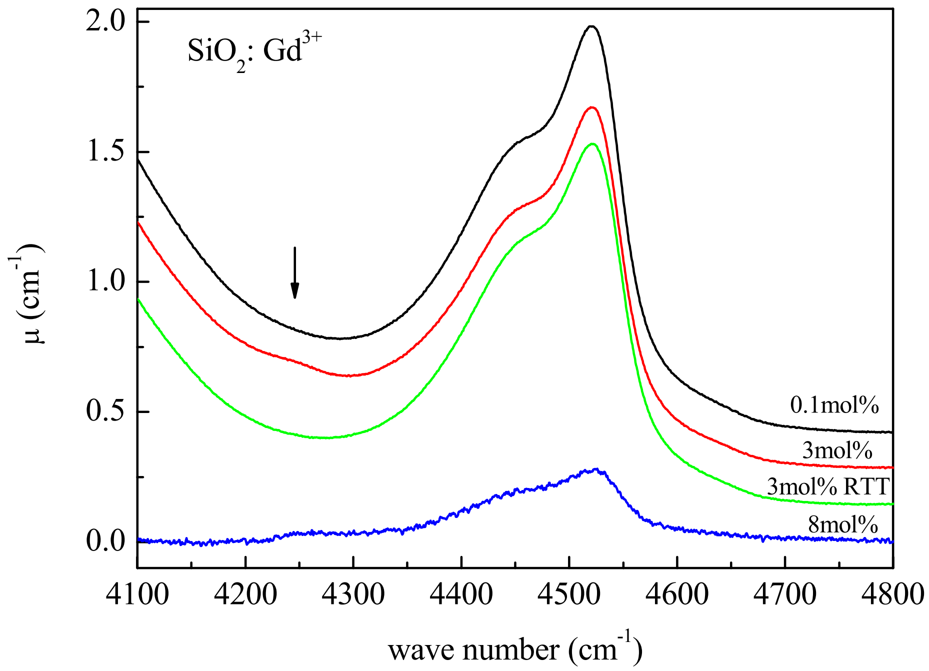

Figure 5.7 Absorption spectra measured in the region of the OH combination mode on SiO_2 samples doped with different amount of Gd^{3+}. The spectrum of a sample submitted to RTT is reported too.

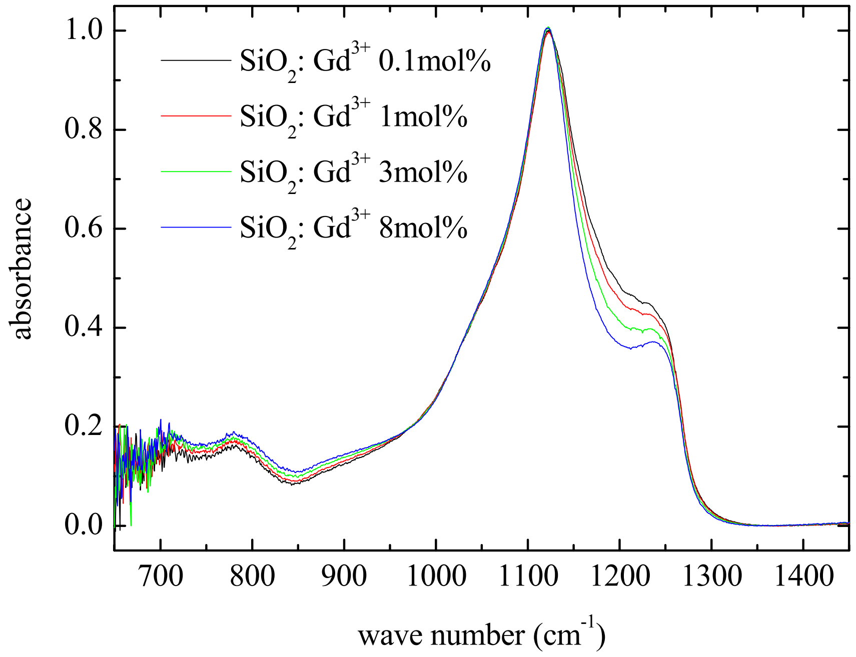

Figure 5.8 Microreflectance spectra of SiO_2 samples doped with different amounts of Gd^{3+} (0.1, 1, 3, and 8mol%). All the spectra are normalized to the maximum.

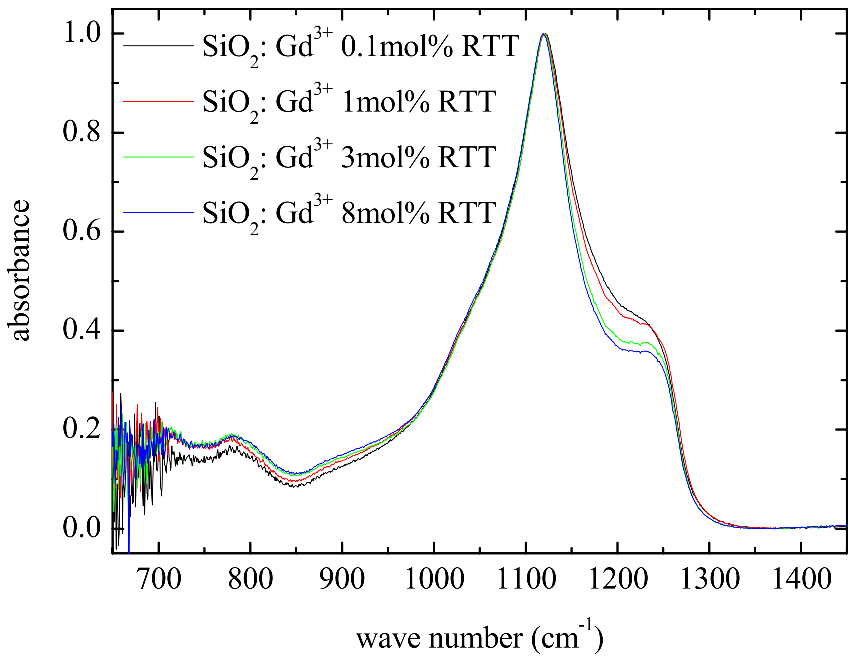

Figure 5.9 Microreflectance spectra of SiO_2 samples doped with different amounts of Gd^{3+} (0.1, 1, 3, and 8mol%) submitted to RTT. All the spectra are normalized to the maximum.

To investigate the changes induced by the Gd^{3+} doping on the matrix intrinsic fundamental modes, both microreflectance (on massive samples) and absorption (on pellets) measurements were performed. Figure 5.8 and Figure 5.9 displays the spectra (normalized to the reflectivity maximum) of four doped samples (0.1, 1, 3, and 8mol%), before and after RTT, respectively. In both cases, the increase of Gd^{3+} doping induces an increase both of the dip at ~1200 cm^{-1} and of the band at ~780 cm^{-1}. The spectra of the same samples (before RTT) diluted in CsI (W.R. 0.5 mg of sample over 100 mg of CsI) are reported in Figure 5.10 (curves b-e); spectra of pellets of a pure silica (diluted in KBr, curve a) and of a GSO: Ce 0.2mol% crystal (diluted in CsI, curve f) are also displayed for reference. The peaks at ~797 and 1105 cm^{-1} are related to symmetric and antisymmetric O–Si–O stretching mode absorptions [116], respectively. It is important to notice the growth of a shoulder at ~880 cm^{-1} whose amplitude increases with the Gd^{3+} concentration.

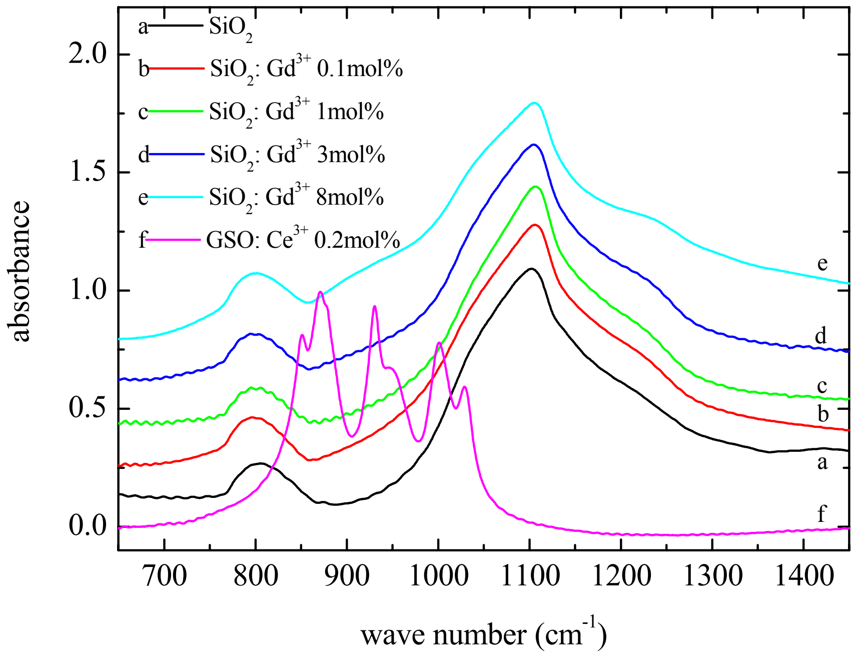

Figure 5.10 Absorption spectra measured in the region of the SiO_2 intrinsic stretching modes on pellets. Curve a: SiO_2; curves b-e: SiO_2: Gd^{3+} 0.1, 1, 3, and 8mol%, respectively; curve f: GSO: Ce^{3+} 0.2mol%.

5.3.3 Ce^{3+}-Gd^{3+} co-doped samples

Co-doped samples are very interesting due to the possibility to increase the luminescence efficiency of the active Ce^{3+} ions thanks to the energy transfer from Gd^{3+} (see Section 5.1).

Spectra of co-doped samples measured in the region of the OH^- combination stretching+bending mode at ~4520 cm^{-1} showed the same additional peak at ~4250 cm^{-1} already monitored in Gd^{3+} doped samples (Figure 5.7). Also in this case the peak amplitude increases with the RE^{3+} concentration, and disappears after RTT (Figure 5.11).

Furthermore, spectra measured in the region of the SiO_2 intrinsic stretching modes on pellets of co-doped samples diluted in KBr confirm the observations done for the Gd^{3+} doped samples: a shoulder appears at ~880 cm^{-1}, it increases with the concentration of Gd^{3+} and it still remains after RTT.

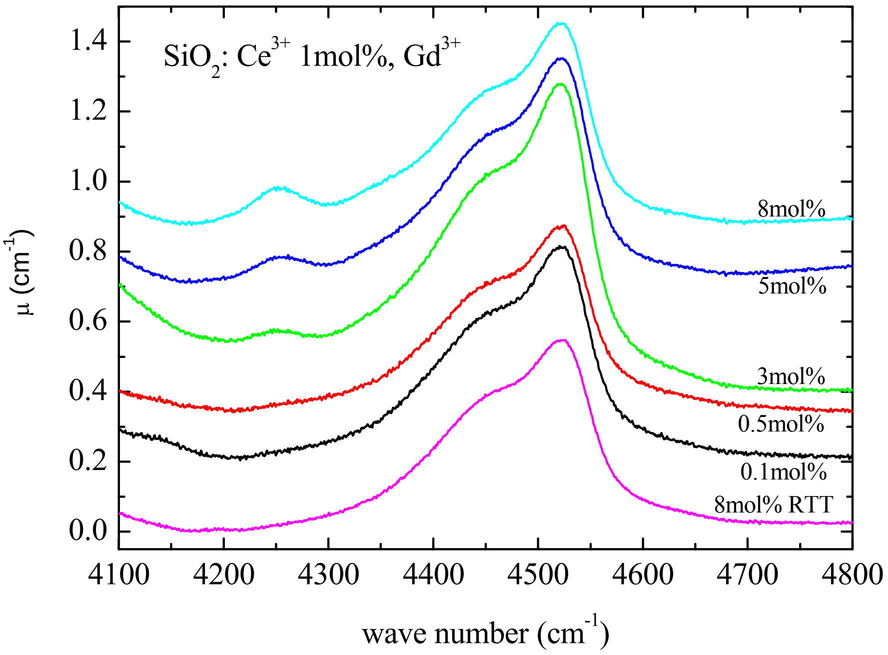

Figure 5.11 Absorption spectra measured in the region of the OH$^-$ combination mode on SiO$_2$: Ce^{3+} 1mol%, Gd^{3+} co-doped samples with different amount of Gd^{3+} (0.1, 0.5, 3, 5, and 8mol%). The spectrum of the sample co-doped with Gd^{3+} 8mol% and submitted to RTT is reported too.

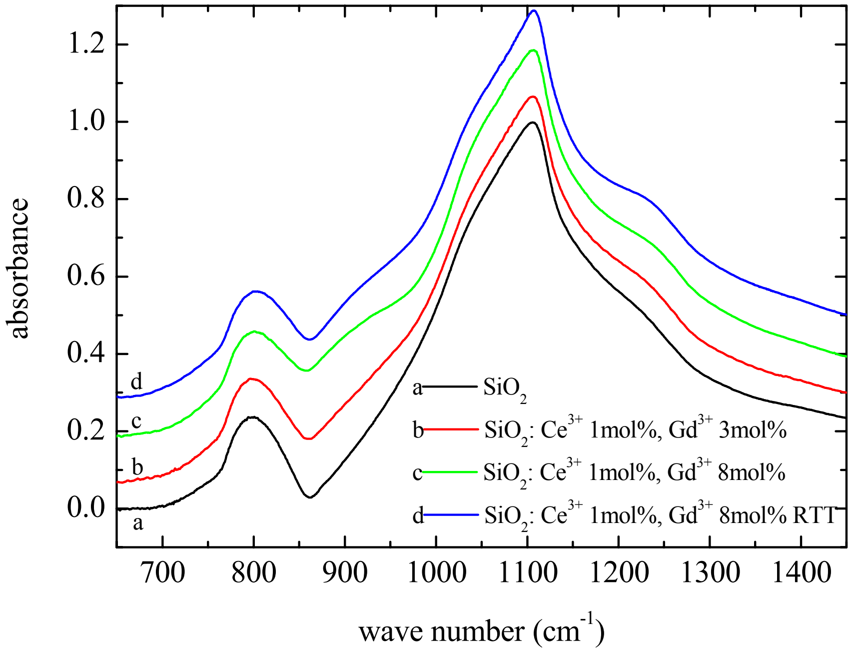

Figure 5.12 Absorption spectra measured in the region of the SiO$_2$ intrinsic stretching modes on pellets. Curve a: SiO$_2$; curves b and c: SiO$_2$: Ce^{3+} 1mol%, Gd^{3+} 3 and 8mol%, respectively; curve d: SiO$_2$: Ce^{3+} 1mol%, Gd^{3+} 8mol% RTT.

5.3.4 Tb^{3+} doped samples

Terbium is the element which follows Gd in the periodic table. For Tb^{3+} the electronic configuration is $4f^8$, thus the fundamental manifold is $^7F_6$. Six different excited manifolds are expected in the region between 2000 and 6000 cm^{-1} [56], thus this is the range first analyzed. Figure 5.13 shows the RT absorption spectra measured in this region on Tb^{3+} 1, 3, and 10mol% doped samples; for the last concentration, also the RTT sample spectrum is reported. The 10mol% sample was measured also at 9 K. The main features are:

1. the presence of broad bands in the region of the Tb^{3+} $^7F_6 \rightarrow {}^7F_{3,2,1}$ transitions whose amplitude increases with the RE^{3+} concentration (even in RTT samples); the bands are still broad at low temperature;
2. the peak related to Si–OH stretching at ~3670 cm^{-1} is too strong, thus out of the linearity range of the MCT detector (see Appendix 1.1), while that due to the combination stretching+bending at ~4520 cm^{-1} is overlapped to crystal field absorption bands.

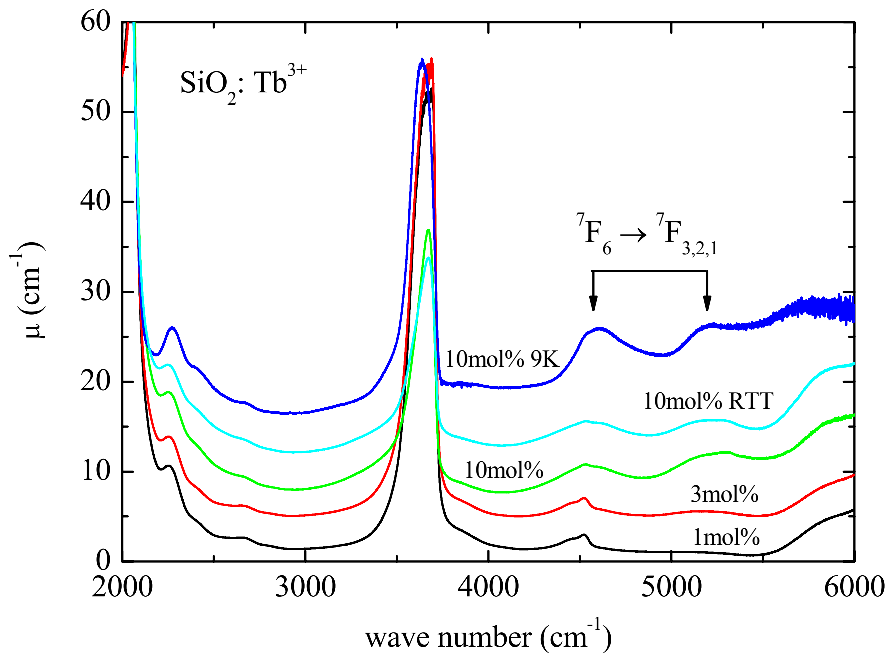

Figure 5.13 Absorption spectra measured in the region of the Tb^{3+} $^7F_6 \rightarrow {}^7F_{3,2,1}$ transitions and SiO_2 intrinsic stretching modes on SiO_2: Tb^{3+} samples.

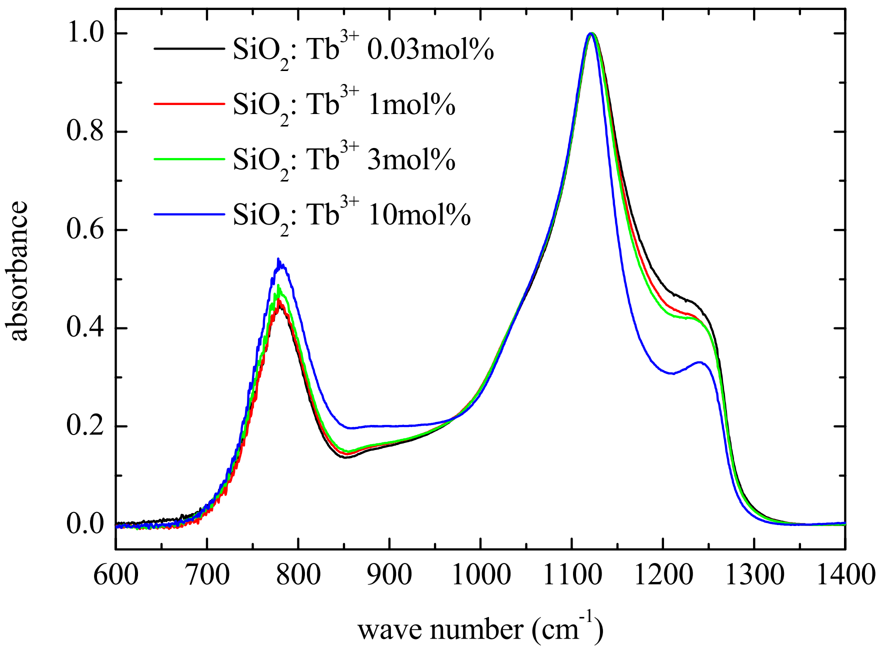

Figure 5.14 Microreflectance spectra of SiO_2 samples doped with different amounts of Tb^{3+} (0.03, 1, 3, and 10mol%). All the spectra are normalized to the maximum.

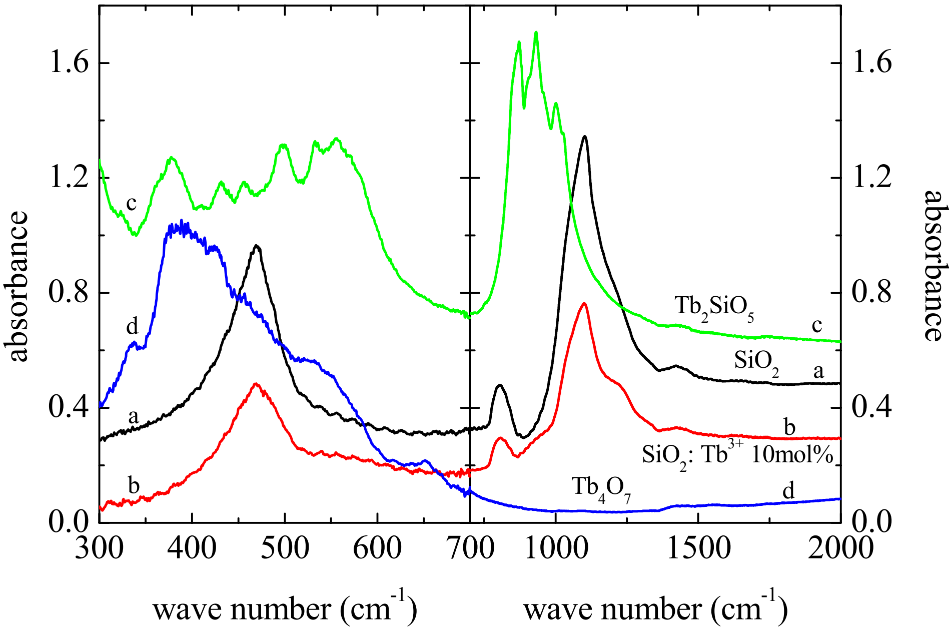

Figure 5.15 Optical absorption spectra measured at RT on CsI pellets. Curve a: undoped SiO_2; curve b: SiO_2: Tb^{3+} 10mol%; curve c: Tb_2SiO_5; curve d: Tb_4O_7. The wave-like behaviour in the range 300-700 cm^{-1} is due to the interference fringes in a thin sample.

Microreflectance measurements on all the Tb^{3+} doped samples were performed: Figure 5.14 displays only some of them for clarity; as already mentioned for Gd^{3+} and Ce^{3+}, by increasing the doping level, both the dip at ~1200 cm^{-1} and the band at ~780 cm^{-1} increase. The measurements not reported in the figure follow the same trend. Samples submitted to RTT show a further enhancement of these effects.

To complement the information acquired from microreflectance spectra about the influence of Tb^{3+} doping on fundamental vibrational silica modes, measurements on CsI pellets were performed in the 300-2000 cm^{-1} range. Figure 5.15 collects the spectra of two silica samples, the former pure (curve a) and the latter doped with Tb^{3+} 10mol% (curve b); the spectra are compared with those of Tb-oxyorthosilicate (Tb_2SiO_5, curve c) and Tb-oxide (Tb_4O_7, curve d). The main changes induced by Tb^{3+} (curve b) with respect to the undoped silica sample (curve a) are:

1. the marked decrease of the absorption in all the regions of O–Si–O fundamental vibrations (W.R. being the same for both pellets, 0.6/100 mg), i.e. the bands at ~1100, 800, and 470 cm^{-1} [117, 118];
2. the small shift (about 3 cm^{-1}) of peaks;
3. two shoulders growing around ~940 and ~554 cm^{-1}.

5.3.5 Yb^{3+} doped samples

Ytterbium is the last element of the Lanthanide series; for Yb^{3+} the electronic configuration is $4f^{13}$. The fundamental manifold is $^2F_{7/2}$, and the excited manifold $^2F_{5/2}$ is expected at ~9500 cm^{-1} [56]. Thus, the analysis was extended up to 14000 cm^{-1}.

Figure 5.16 reports the spectra measured at RT on samples doped with different Yb^{3+} concentrations (0.1, 0.2, 0.5, 1, and 4mol%) just in the region of the Yb^{3+} $^2F_{7/2} \rightarrow {}^2F_{5/2}$ transition. The amplitude of the broad band at ~10240 cm^{-1} and the shoulder at ~10750 cm^{-1}, related to the CF transitions, increase with the Yb^{3+} concentration, while their shape remains practically unchanged over the whole concentration range examined (0.05-4mol%). At 9 K the bands are still broad (Figure 5.17).

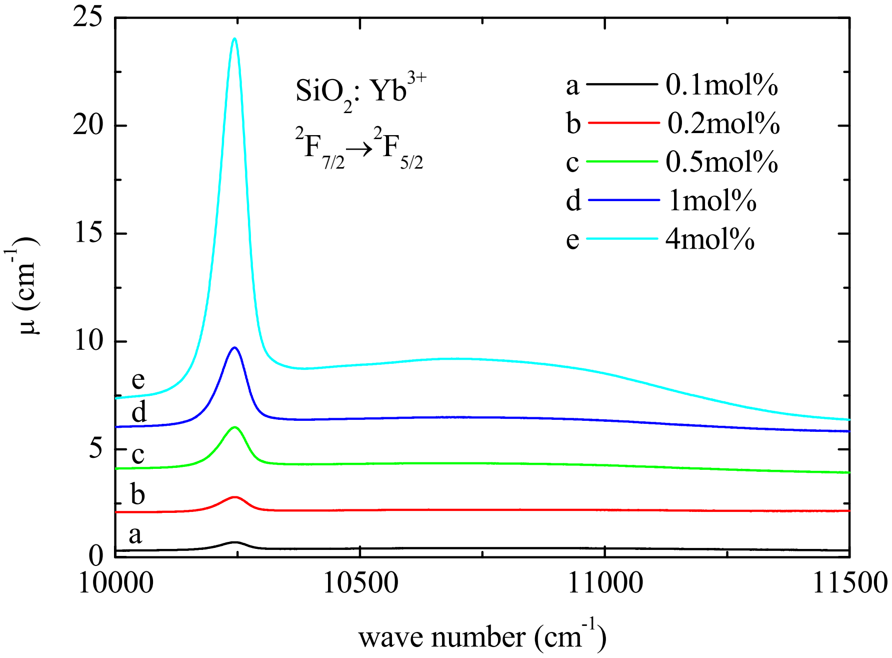

Figure 5.16 Optical absorption spectra measured at RT on SiO_2 samples doped with different Yb^{3+} concentrations in the region of Yb^{3+} $^2F_{7/2} \rightarrow {}^2F_{5/2}$ transition. Curve a: 0.1mol%; curve b: 0.2mol%; curve c: 0.5mol%; curve d: 1mol%; curve e: 4mol%.

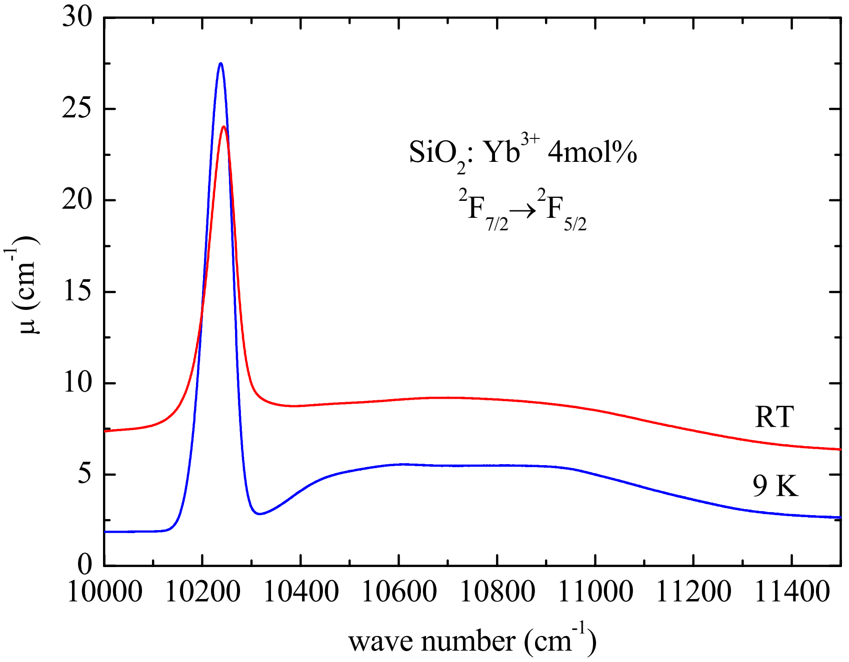

Figure 5.17 Optical absorption spectra measured at RT and 9 K on the SiO_2: Yb^{3+} 4mol% sample in the region of Yb^{3+} $^2F_{7/2} \rightarrow {}^2F_{5/2}$ transition.

The behaviour of the bands related to Si–OH stretching and combination modes are displayed in Figure 5.18: their amplitude is larger than that of the undoped sample (curve a), but it decreases as a function of the Yb^{3+} content.

The microreflectance spectra performed also for this series of samples show the same behaviour already described for other RE^{3+}, even if less marked: the increase of the dip at ~1200 cm^{-1}. For this reason they are not here reported. Nevertheless, spectra measured on CsI pellets in the region of fundamental vibrational silica modes are displayed in Figure 5.19: the spectra of the undoped sample (curve a) and of Yb^{3+} 4mol% doped one (curve b) practically coincide. Spectra of Yb-oxyorthosilicate (Yb_2SiO_5, curve c) and Yb-oxide (Yb_2O_3, curve d) are added for comparison.

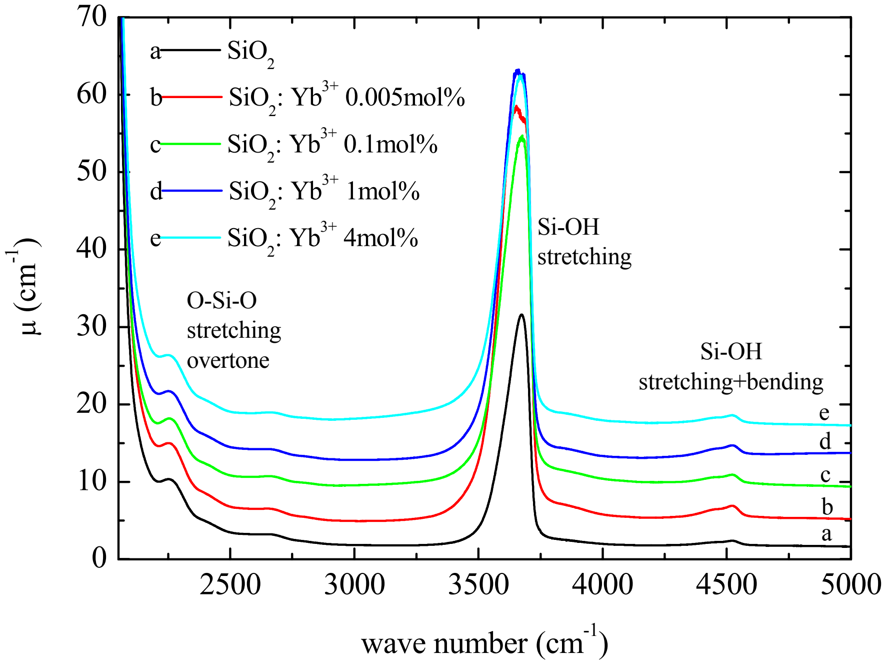

Figure 5.18 Optical absorption spectra measured at RT on SiO_2 samples doped with different amount of Yb^{3+} (0-4mol%) in the region of Si–OH vibrational modes.

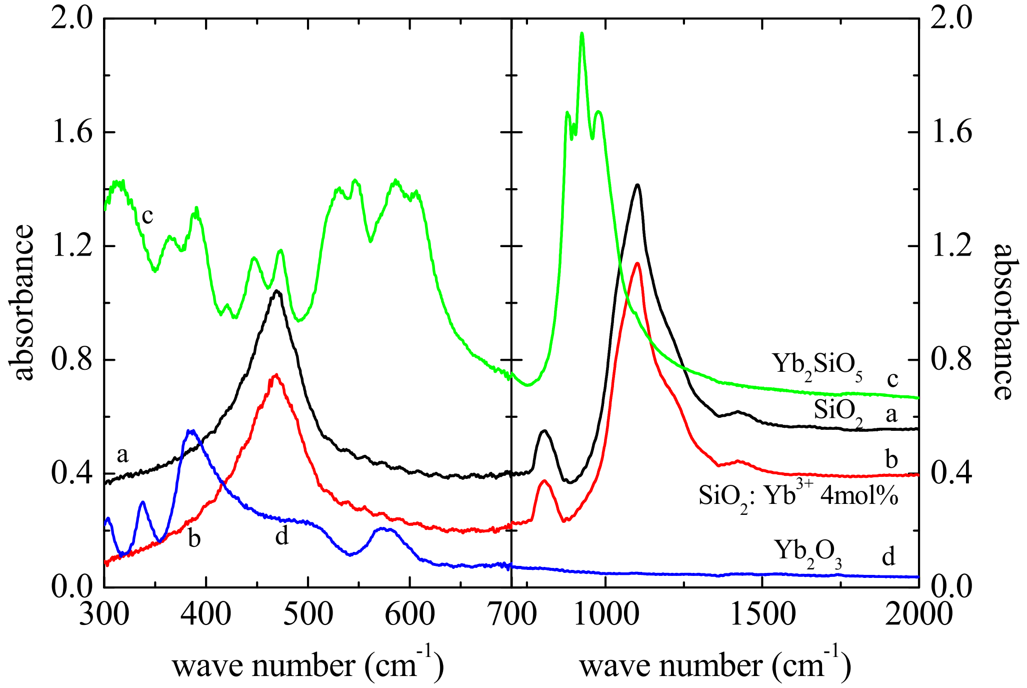

Figure 5.19 Optical absorption spectra measured at RT on CsI pellets. Curve a: undoped SiO_2; curve b: SiO_2: Yb^{3+} 4mol%; curve c: Yb_2SiO_5; curve d: Yb_2O_3. The wave-like behaviour in the range 300-700 cm^{-1} is due to the interference fringes in a thin sample.

5.3.6 Eu^{3+} doped samples

Due to Eu^{3+} $4f^6$ configuration, the fundamental manifold is the *J*-singlet $^7F_0$; thus, no hot bands are expected (see Section 2.4.1). The first excited manifolds $^7F_{1,2,3}$ lie at energies lower than 2000 cm^{-1} [56], thus they should not be detected in a silica glass due to the overlapping of fundamental vibrational absorptions.

Figure 5.20 portrays the spectra of some samples doped with different Eu^{3+} amounts (0, 0.1, 1, 3, and 10mol%) and bands due to CF transitions can be detected already at Eu^{3+} 1mol%. In the investigated range (2100-5500 cm^{-1}) there are also the bands related to Si–OH stretching and combination modes. By increasing the Eu^{3+} concentration from 0.1 to 3mol%, the spectra show some changes:

1. broad and weak bands grow, as due to the presence of Eu^{3+}, at ~ 2670, 2826, 3020, 3900, 4526, and 4760 cm^{-1};
2. the ~3670 cm^{-1} peak, attributed to Si–OH stretching mode, smoothly decreases;

3. a bump at ~3600 cm^{-1} overlaps the Si–OH peak in the Eu^{3+} 1 and 3mol% samples, being more marked in the latter.

In the Eu^{3+} 10mol% doped sample the changes become significant:

1. the Eu^{3+} related absorptions are characterized by rather sharp lines;
2. the Si–OH peaks are no longer detected;
3. the bump at ~3600 cm^{-1} detected in the lower-concentration samples disappears;
4. the O–Si–O asymmetric stretching overtone at ~2260 cm^{-1} is heavily modified: a peak at 2238 cm^{-1} due to Eu^{3+} is superimposed to the intrinsic one at ~2260 cm^{-1};
5. the baseline increases by increasing the wave number.

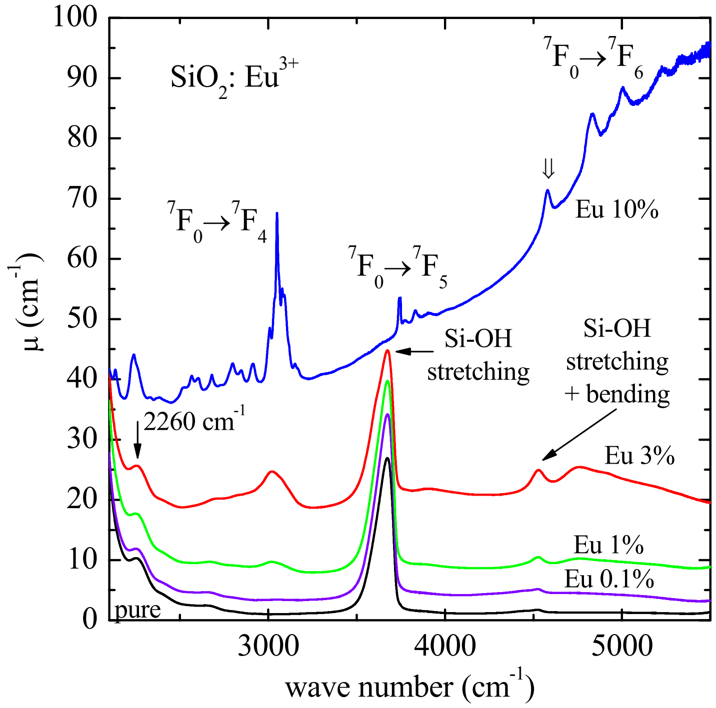

Figure 5.20 Optical absorption spectra measured at RT on SiO$_2$ samples doped with different Eu^{3+} amounts (0, 0.1, 1, 3, and 10mol%) in the region of Eu^{3+} $^7F_0 \rightarrow ^7F_{4,5,6}$ transitions.

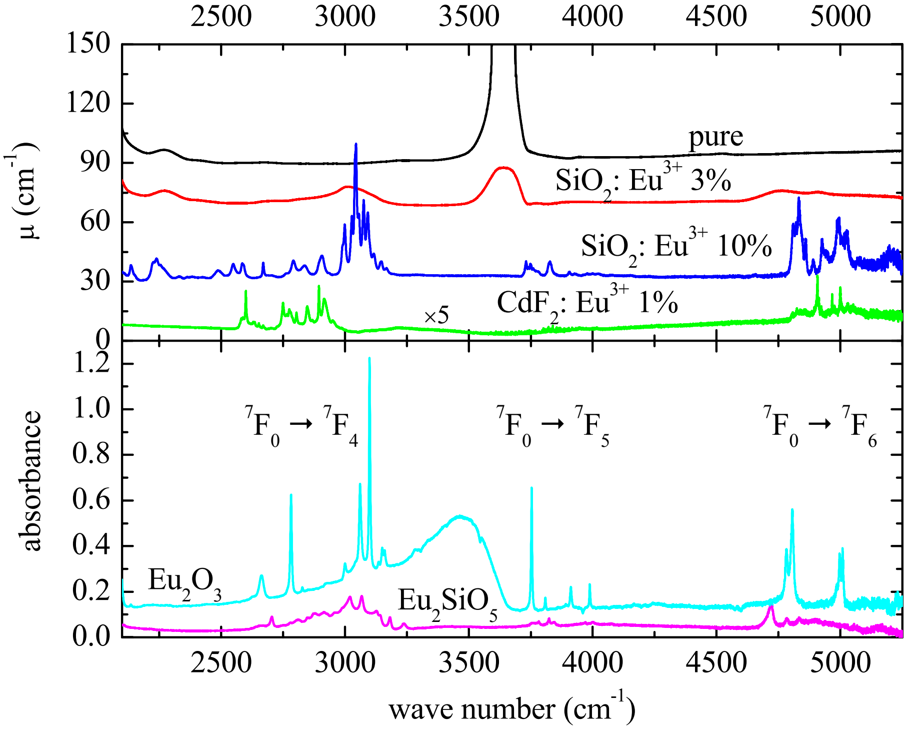

Figure 5.21 Optical absorption spectra measured at 9 K in the region of Eu^{3+} $^7F_0 \rightarrow {}^7F_{4,5,6}$ transitions. Upper panel: SiO_2 samples doped with Eu^{3+} 0, 3, and 10mol%; CdF_2: Eu^{3+} 1%. Lower panel: Eu_2O_3 and Eu_2SiO_5.

The Eu^{3+} 10 and 3mol% samples and the pure one were measured at low temperature to better investigate the unusual, for a glass matrix, narrow peaks shown by Eu^{3+} (see 1.); the spectra obtained are reported in Figure 5.21 and compared with the spectra measured at 9 K on a crystal CdF_2: Eu^{3+} 1% and two CsI pellets of Eu_2SiO_5 and Eu_2O_3. The absorptions in the Eu^{3+} 3mol% doped sample remain broad even at 9 K, while the Eu^{3+} 10mol% doped sample shows a line rich spectrum: by lowering the temperature the lines become narrower and their number increases. Moreover, the band due to the O–Si–O asymmetric stretching overtone (at ~2260 cm^{-1}) is only a weak shoulder in the Eu^{3+} 10mol% sample with respect to the 3mol% one.

The oxide powder was submitted to preliminary thermal treatments at T~1000 °C for one hour to remove some adsorbed moieties (e.g. water), responsible for spurious lines detected in the absorption spectra at ~850, 1087, 1494, 3410, and 3594 cm^{-1}; however, the treatment was unable to remove traces of carbonate groups (broad bands at ~1406 and 1530 cm^{-1}) [119], very likely introduced along the oxide synthesis procedure [120].

To better study the modifications induced by high Eu^{3+} doping levels on the fundamental matrix modes, measurements on CsI pellets containing chips of pure and doped samples were performed in the 200-2000 cm^{-1} range. The results are collected in Figure 5.22, and, as in previous cases, spectra of oxyorthosilicate and oxide pellets are reported for comparison. As already shown in Figure 5.2, the Eu^{3+} 10mol% sample is almost completely "milky" except for some transparent fragments; Figure 5.22 reports the spectra of two pellets prepared with different fragments: the differences are clear. While the spectrum of the transparent part is similar to that of Eu^{3+} 3mol% sample, in the other one additional absorptions appear and the peaks due to intrinsic O–Si–O vibrational modes shift towards low wave numbers and change shape.

The changes induced by doping increase up to 3mol% are:

1. the marked decrease of the absorption related to O–Si–O fundamental vibrations;
2. a modest "red shift" of the main peak at ~1100 cm^{-1};
3. the appearance of two shoulders growing around ~920 and ~567 cm^{-1}.

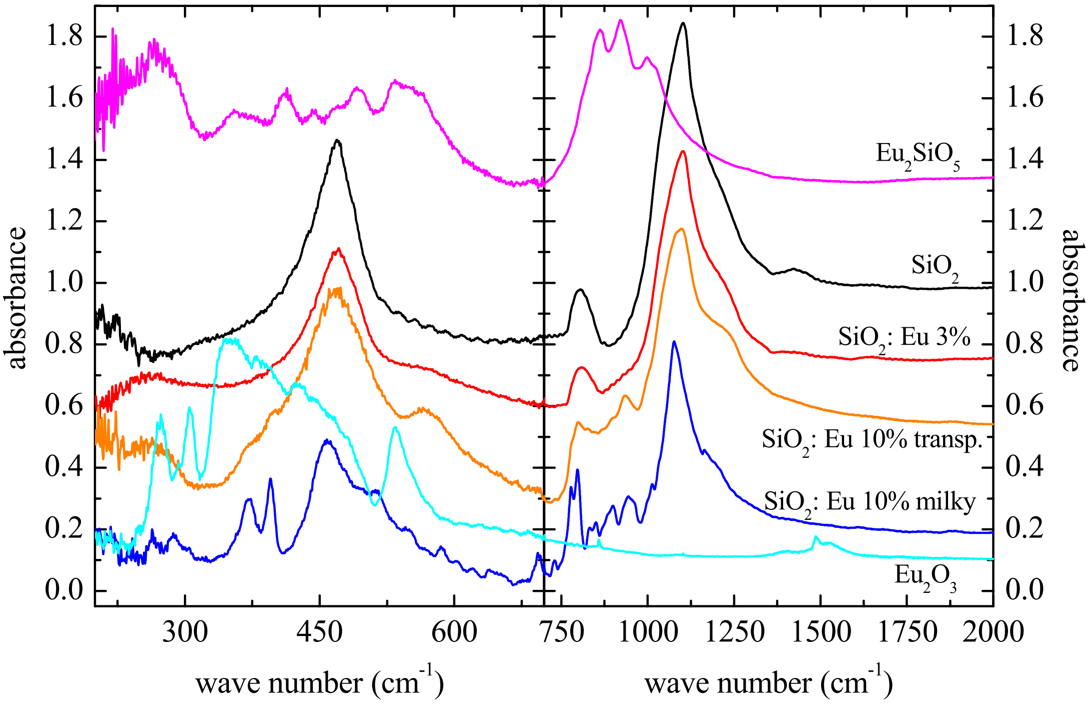

Figure 5.22 Optical absorption spectra measured at RT on CsI pellets of SiO_2: Eu^{3+} 0, 3, and 10mol%, Yb_2SiO_5, and Yb_2O_3.

Moreover, microreflectance measurements were performed and are collected in Figure 5.23 and Figure 5.24; in the former, the spectrum of a Eu_2SiO_5 pellet is reported as a reference. The spectra of the 1 and 3mol% samples show the same modifications already underlined for other RE^{3+}. In contrast, the spectrum of the milky 10mol% sample is completely different: the fundamental bands changes radically, and new peaks appear (Figure 5.23). On the other hand, the microreflectance spectrum of a partially transparent fragment of the 10mol% sample is more similar to that of the undoped sample (Figure 5.24). Measurements on both faces (top and bottom) of the milky sample were performed, due to their different appearance (Figure 5.24): the top face displays an intermediate behaviour between that of the bottom one and that of the transparent fragment.

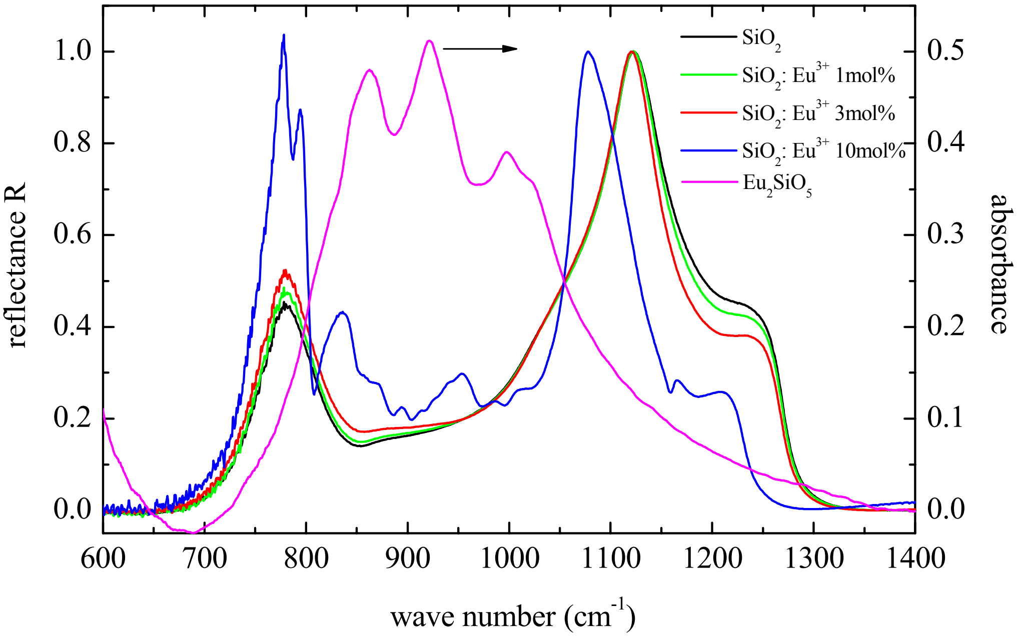

Figure 5.23 Microreflectance spectra of SiO_2 samples doped with different amounts of Eu^{3+} (0, 1, 3, and 10mol%); the spectrum of a Eu_2SiO_5 pellet is reported as reference. All the spectra are normalized to the maximum.

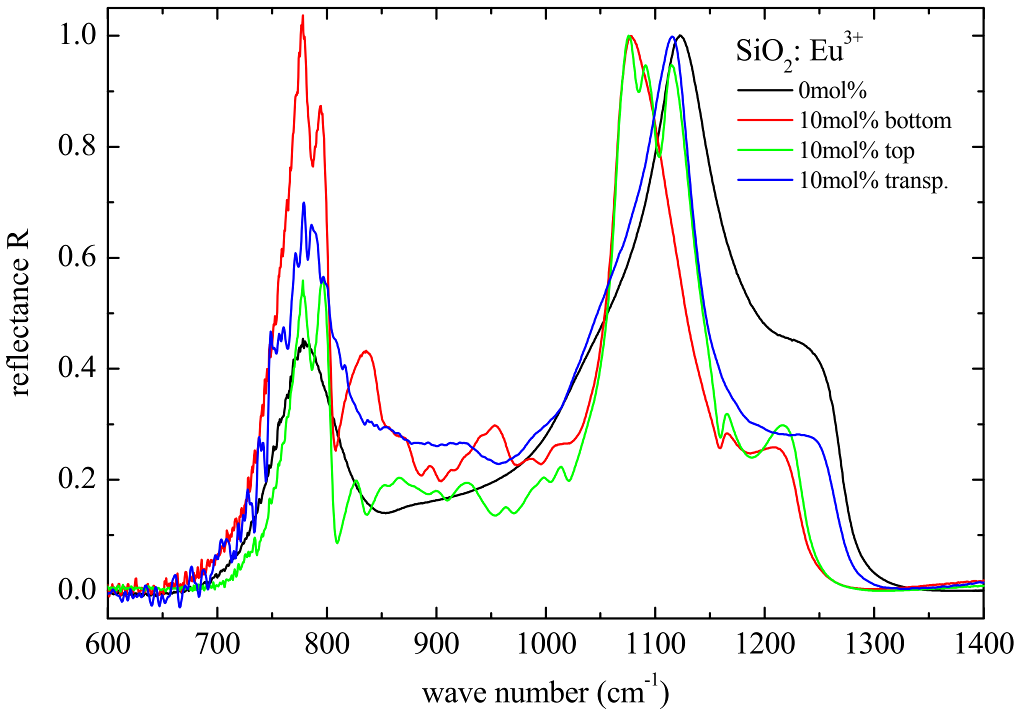

Figure 5.24 Microreflectance spectra of SiO$_2$ Eu^{3+} 10mol% and undoped samples. All the spectra are normalized to the maximum.

The difference between top and bottom face is confirmed also by AFM images (Figure 5.25): at the same observation scale, the former (panel B) is “smooth”, while the latter (panel A) is rough. In fact, the root mean square roughness of the top face is ~33 nm, while that of the bottom face is ~110 nm.

Finally, the vibrational spectra were taken even in the regions where overtones and combinations of the fundamental modes are expected to originate absorptions. They are displayed in Figure 5.26 for different samples and pellets.

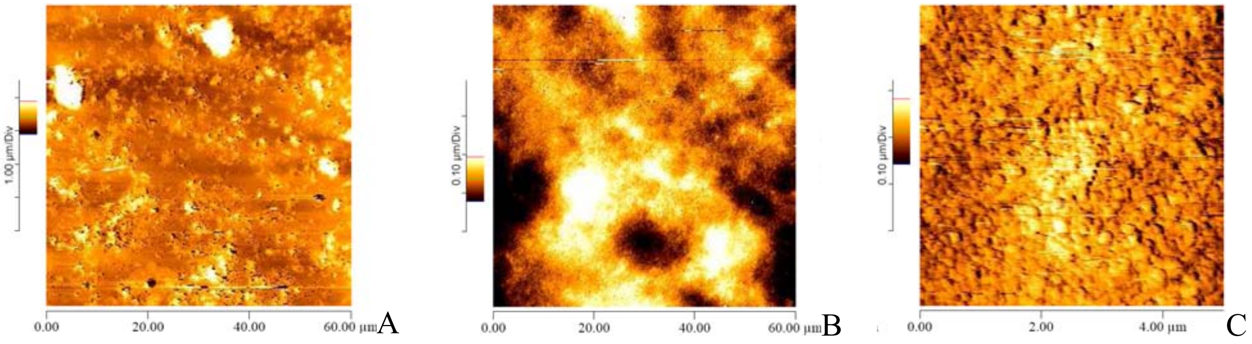

Figure 5.25 AFM topographic images of the SiO$_2$ Eu^{3+} 10mol% sample. Panel A and B: 60×60 µm images of the bottom and top face, respectively; panel C: 5×5 µm image of the top face.

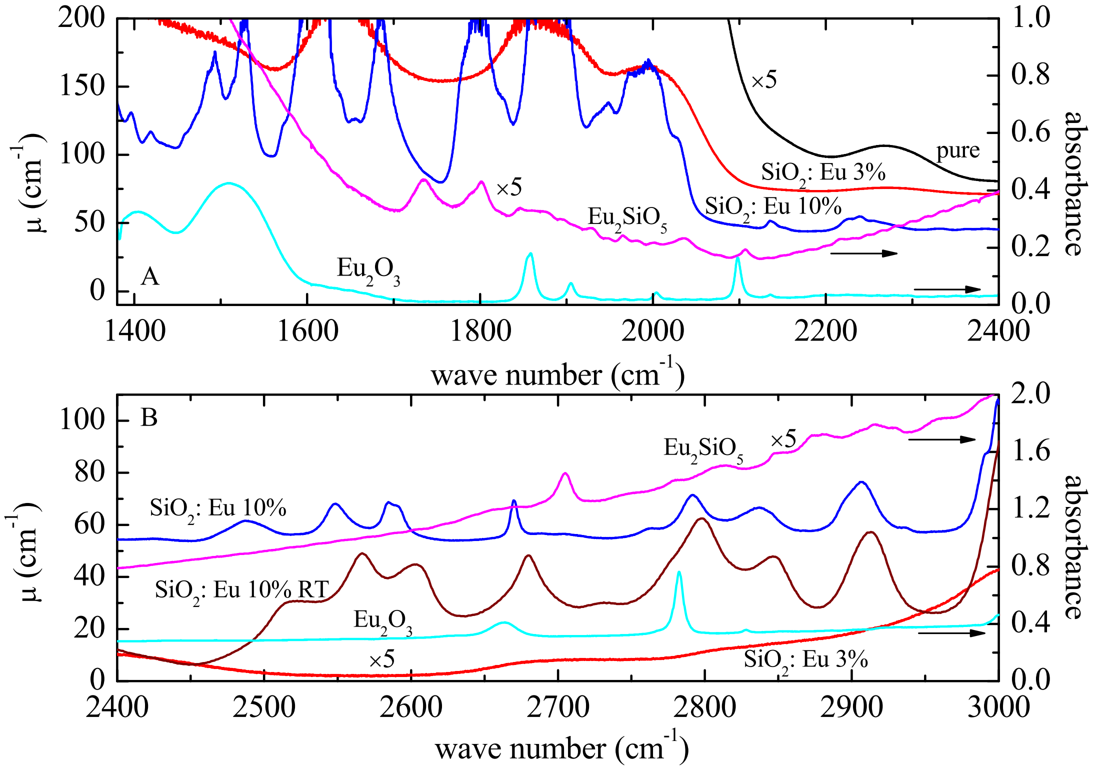

Figure 5.26 Optical absorption spectra measured at 9 K in the regions of the vibrational overtones and combinations. Panel A: Δn=2 region; panel B: Δn=3 region.

5.3.7 TEM and EDS measurements

TEM measurements were performed on heavy doped samples with the aim to make apparent possible nanostructures embedded in the silica matrix, as in the case of Ce^{3+} doped samples prepared in reducing atmosphere [113].

Figure 5.27 and Figure 5.28 portray TEM images performed on Gd^{3+} 3mol% and Yb^{3+} 4mol% samples, respectively, before (panels A) and after (panels B) RTT. In both cases the presence of nanoclusters is evident, and their sizes grow with the RTT (compare panels A and B). Panels D and panels E report EDS spectra obtained on the RTT samples by focusing the beam within the amorphous matrix or within a cluster, respectively: they demonstrate that Yb^{3+} is mainly located inside the clusters.

Very similar results were obtained for SiO_2: Tb^{3+} 10mol%.

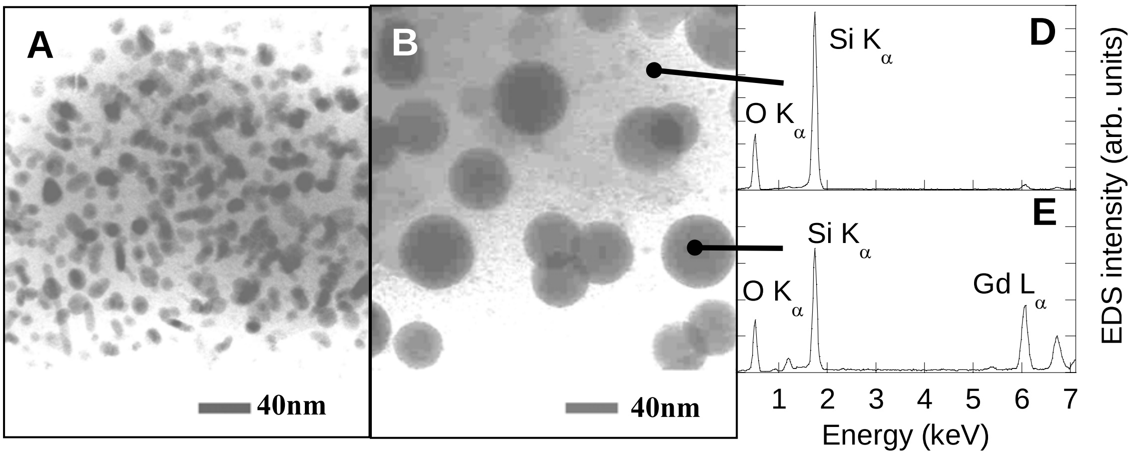

Figure 5.27 TEM images of SiO_2: Gd^{3+} 3mol% before (panel A) and after (panel B) RTT. EDS spectra obtained on SiO_2: Gd^{3+} 3mol% after RTT: different spectra were collected focusing the electron beam within the matrix (panel D) or within a cluster (panel E) [121].

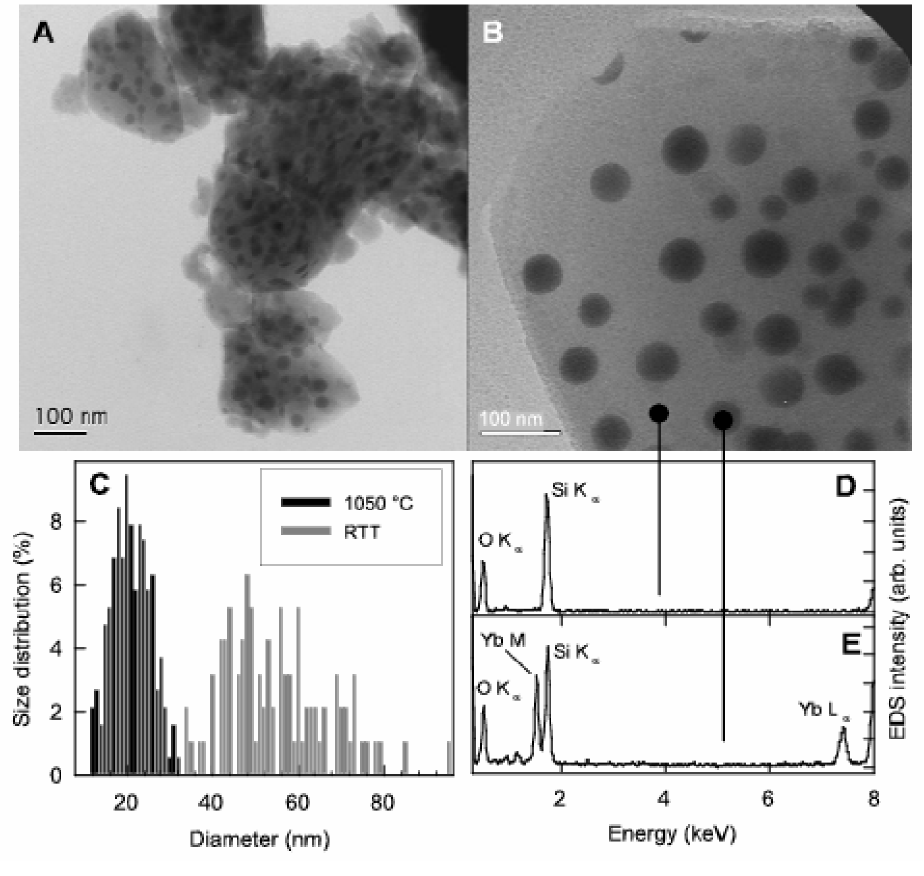

Figure 5.28 TEM images of SiO_2 : Yb^{3+} 4mol% before (panel A) and after (panel B) RTT. Statistical size distribution (panel C) of the clusters evaluated over 190 and 98 aggregates before and after RTT, respectively. EDS spectra of SiO_2: Yb^{3+} 4mol% after RTT. The spectra were collected focusing the electron beam on the matrix (panel D) or on the cluster (panel E) [122].

Figure 5.29 and Figure 5.30 display TEM images taken on two Eu^{3+} doped samples: 3 and 10mol%, respectively. The clusters are evident in both samples, being larger in the heavy doped one; high resolution images (panels B) show the clusters “structure”. EDS spectra taken on nanocluster rich regions are shown in Figure 5.31: only the heavy doped sample (panel B) evidences a clear pattern due to an ordered environment.

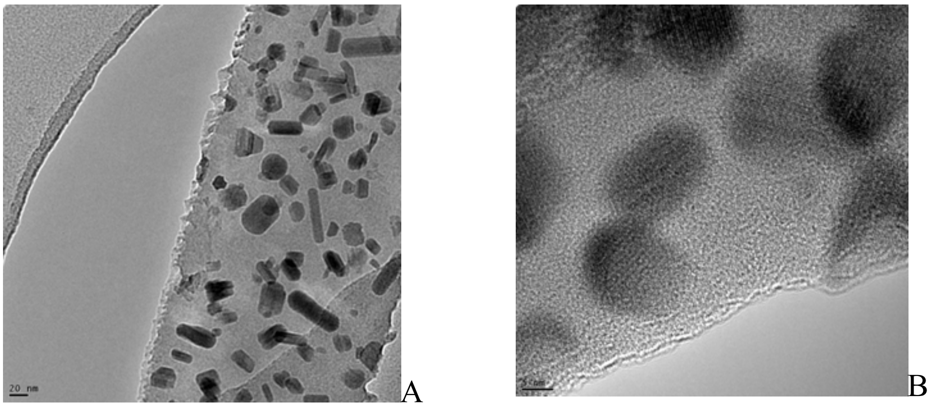

Figure 5.29 TEM images of SiO_2 : Eu^{3+} 3mol%. Panel A: 20 nm, panel B: 5 nm.

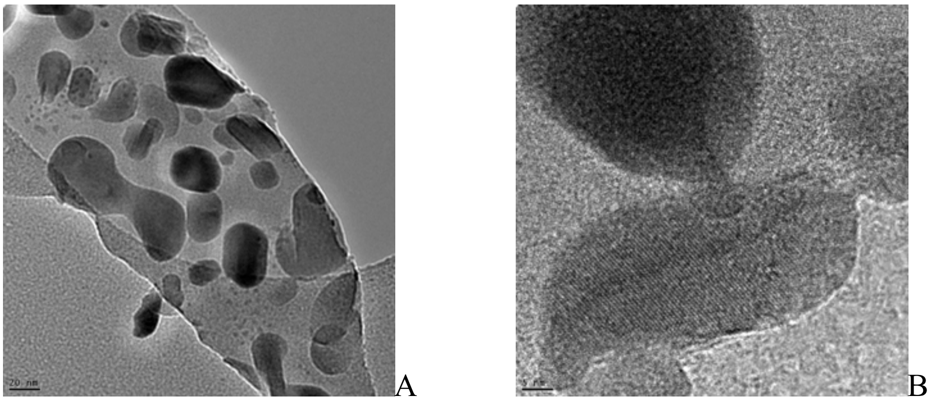

Figure 5.30 TEM images of SiO_2 : Eu^{3+} 10mol%. Panel A: 20 nm, panel B: 5 nm.

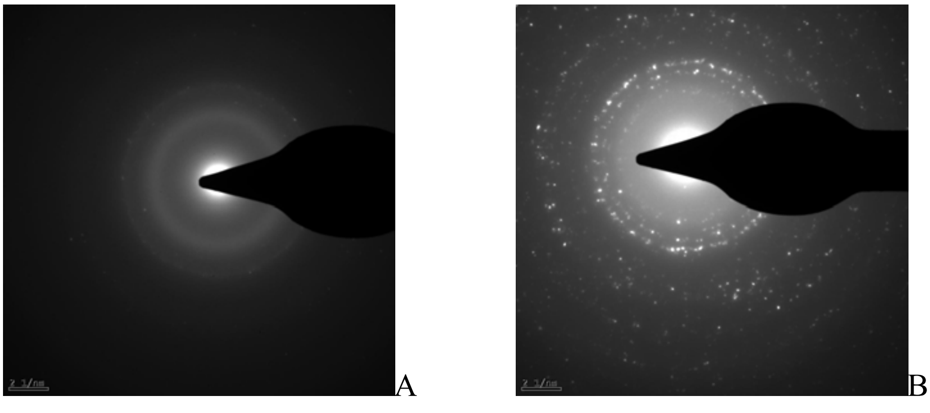

Figure 5.31 EDS spectra of SiO_2: Eu^{3+} 3 (panel A) and 10mol% (panel B).

5.4 DISCUSSION

5.4.1 Crystal field spectra

Ce^{3+}, Gd^{3+}, Tb^{3+}, Yb^{3+}, and Eu^{3+} are characterized by $4f^1$, $4f^7$, $4f^8$, $4f^{13}$ and $4f^6$ configurations, respectively [56]. In silica *f-f* electronic transitions are partially allowed by the crystal field (CF) originated from nearest neighbours and probed by the RE^{3+}. Since Ce^{3+} and Yb^{3+} have either one more or one less electron with respect to a closed shell configuration, they exhibit only one CF transition, i.e. $^2F_{5/2} \rightarrow {}^2F_{7/2}$ and $^2F_{7/2} \rightarrow {}^2F_{5/2}$, respectively, which fall in the infrared (IR). The lowest excited manifold of Gd^{3+} ($^6P_{7/2}$) lies in the UV, at wave numbers higher than 32000 cm^{-1}, thus no electronic absorptions should occur in the spectral range investigated; this was confirmed by measurements. For Tb^{3+} and Eu^{3+} (one more or one less electron with respect to Gd^{3+}) a few transitions ($^7F_6 \rightarrow {}^7F_{5,4,3,2,1,0}$ and $^7F_0 \rightarrow {}^7F_{1,2,3,4,5,6}$, respectively) fall in mid-IR [56]. Spectra portrayed in Figure 5.4, Figure 5.13, Figure 5.16, and Figure 5.20 show the absorptions arising from the CF transitions mentioned above, indeed proving the presence of a given RE in silica samples in its trivalent state. Particular attention must be paid to Ce^{3+} doped samples: previous studies over samples grown in oxidizing atmosphere demonstrated the presence of a large amount of Ce^{4+}, both atomically dispersed in the silica matrix and in CeO_2 clusters [108, 111, 112]. Figure 5.32 compare the spectra of two Ce-doped samples sinterized in oxidizing and in reducing atmosphere (curves a and b, respectively): the weak shoulder at ~2130 cm^{-1} suggests that only a small fraction of dopant enters the glass as Ce^{3+} in the former case. Thus, the reducing atmosphere is effective in avoiding the Ce^{3+} oxidation to Ce^{4+} [113]. Nevertheless, the structured absorption displayed by Ce^{3+} doped silica in the 2000-3500 cm^{-1} range at 9 K (Figure 5.5 and Figure 5.32) shows more 'lines' than the four expected at low temperature, i.e. for transitions from the lowest sublevel of the ground manifold $^2F_{5/2}$ to the four sublevels of the unique excited manifold $^2F_{7/2}$. This result suggests that more than one disordered environments are probed by the ions. In any case, the bands remain broad even at 9 K: thus the probed environments are amorphous.

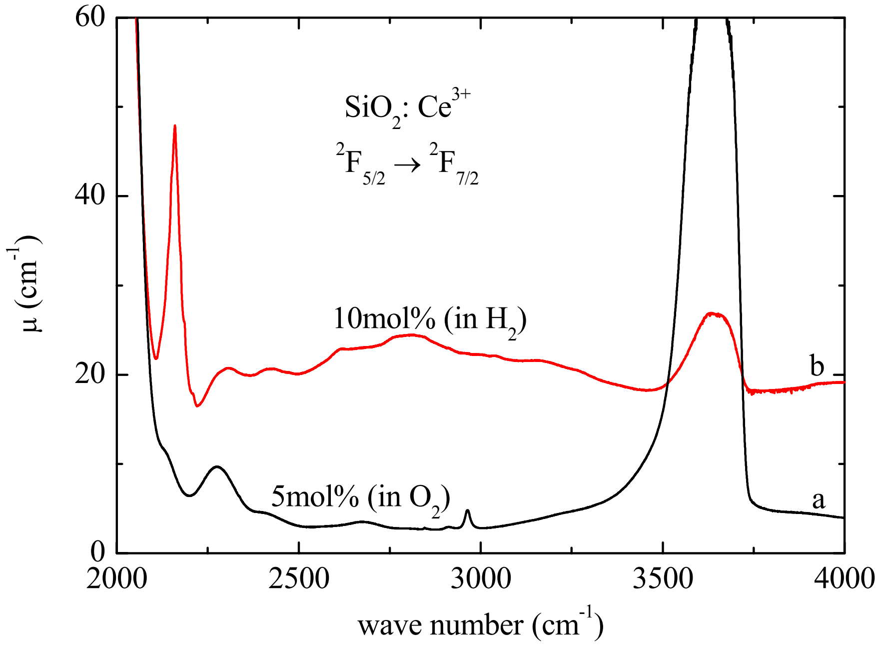

Figure 5.32 Optical absorption spectra measured at 9 K on SiO_2: Ce^{3+} in the region of Ce^{3+} $^2F_{5/2} \rightarrow {}^2F_{7/2}$ transition. Curve a: 5mol%, oxidizing atmosphere; curve b: 10mol%, reducing atmosphere.

In the cases of Tb^{3+} and Yb^{3+} too, the CF absorption bands remain broad at low temperature (Figure 5.13 and Figure 5.17): this means that the ions are embedded in disordered environments. Furthermore, the absorptions due to Tb^{3+} CF transitions (Figure 5.13) do not show any meaningful change if the samples are submitted to RTT. Since EDS measurements evidenced that the RE^{3+} is mainly located inside the clusters (see Section 5.3.7), this means that the RTT neither distroy the cluster nor change their amorphous structure. On the contrary, the cluster size increases, as supported by TEM images (see Figure 5.28).

The RT spectra of silica samples in the region of the Yb^{3+} $^2F_{7/2} \rightarrow {}^2F_{5/2}$ transition (Figure 5.16) maintain the absorption shape practically unchanged over the whole concentration range explored (0.1-4mol%). In Figure 5.33 the 10244 cm^{-1} peak amplitude is reported as a function of the Yb^{3+} content: it exhibits a nearly linear dependence (the addition of a small quadratic contribution improves the fit). Both results confirm that Yb^{3+} is located in undistinguishable, amorphous environments both in the diluted solid solutions and within Yb^{3+} clusters (shown in Figure 5.28).

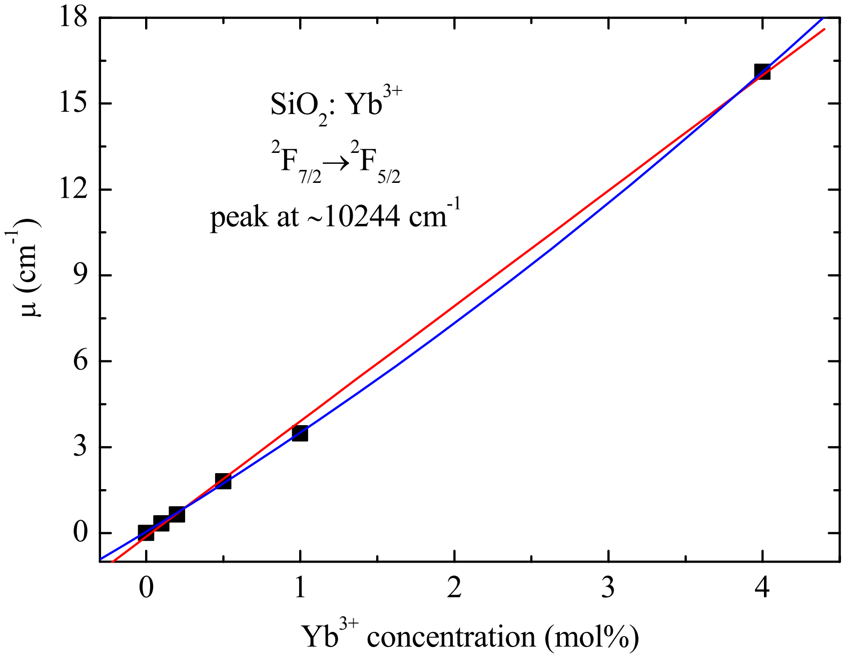

Figure 5.33 10244 cm^{-1} line amplitude measured at RT on Yb^{3+} doped samples as a function of the dopant concentration. The data are fitted to first (red line) and second (blue line) order polynomial functions.

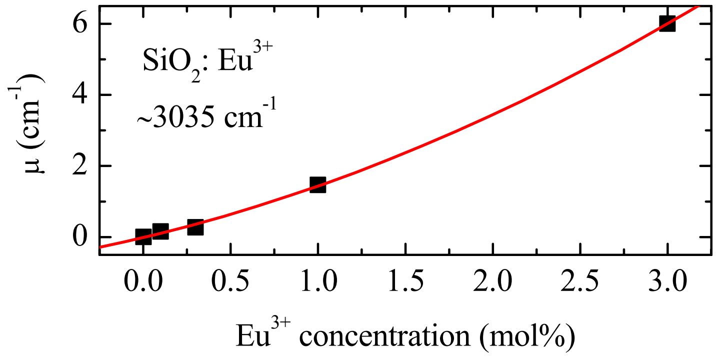

Figure 5.34 Line amplitude of the band at~3035 cm^{-1} measured at RT on Eu^{3+} doped samples as a function of the RE^{3+} concentration. The data are fitted to a second order polynomial function.

The same analysis was done for the band at ~3035 cm^{-1} in the spectra of Eu^{3+} doped samples; the result is displayed in Figure 5.34. The supralinear trend suggests that clustering may occur at high Eu^{3+} doping levels, as supported by TEM and EDS images (Figure 5.30 and Figure 5.31).

Moreover, while the CF absorption bands due to Eu^{3+} $^7F_0 \rightarrow {}^7F_{4,5,6}$ transitions appear as broad bands, both at RT and 9 K, for concentrations up to 3mol% (Figure 5.20 and

Figure 5.21), they are well structured in the spectra of the Eu^{3+} 10mol% sample, even at RT. This suggests the RE^{3+} is probing ordered environments, as for Er^{3+} in SnO_2 nanocrystals embedded in silica [123], but at variance with the behaviour of other analyzed RE^{3+}. On the other hand, the sharp lines are "broader" with respect to the absorption lines due to CF transitions in a crystal (see the comparison with the spectrum of a CdF_2: Eu^{3+} 1mol% crystal in Figure 5.21); thus, the probed environment is rather ordered, but not as ordered as in a single crystal. Moreover, the number of detected CF absorption lines is much larger than that expected (maximum 9, 11, and 13 for the $^7F_0 \rightarrow {}^7F_{4,5,6}$ transitions, respectively, since the fundamental manifold is a singlet): this means that Eu^{3+} experiences different surroundings. Such a conclusion might be verified by measuring the spectrum of the Eu^{3+} 10mol% sample in the region of the singlet-to-singlet $^7F_0 \rightarrow {}^5D_0$ transition (~17000 cm^{-1}): here only one line is predicted for each environment probed by Eu^{3+}. Unfortunately, the light scattering, evidenced by the baseline increase at increasing wave numbers in the IR region (see Figure 5.20), becomes too strong in the visible, thus precluding the detection of the weak line induced by the $^7F_0 \rightarrow {}^5D_0$ transition.

The $^7F_0 \rightarrow {}^7F_{1,2,3}$ transitions are expected to lie at energies below ~2000 cm^{-1} [56], thus they cannot be directly monitored in the Eu^{3+} doped silica massive samples, due to the overlapping of the dominant O–Si–O vibrational absorption peaks. Nevertheless, an indirect information about the separation of the lowest excited manifold $^7F_1$ from the ground one, $^7F_0$, can be extracted from the position of the peak at 4577 cm^{-1} appearing in the RT spectrum of the Eu^{3+} 10mol% sample (Figure 5.20). Since it is no longer detectable at 9 K (Figure 5.21), the starting level of the transition originating the absorption should be populated at RT and empty at 9 K, i.e. the transition should start from an excited sublevel of the ground manifold. But this is not possible, because the ground manifold $^7F_0$ is not split by CF (J=0). Thus, the sublevel may belong to the first excited manifold $^7F_1$. The separation between the 4577 cm^{-1} absorption and the first peak on its high energy side (4828 at RT and 4809 cm^{-1} at 9 K, respectively) allows estimating, at least roughly, the position of the $^7F_1$ manifold with respect to the ground one. The value obtained (232÷251 cm^{-1}) well accounts for the population of the $^7F_1$ manifold at RT. The first Eu^{3+} CF transition ($^7F_0 \rightarrow {}^7F_1$) is reported to occur around 300 cm^{-1} in $LaCl_3$ single crystals [56]. Looking for direct confirmations of these values, the spectra of sample pellets were analyzed (Figure 5.22); peaks between 250 and 300 cm^{-1} are monitored indeed in the Eu^{3+} 10mol% doped silica pellet and a broad band appears around 240 cm^{-1} in the Eu^{3+} 3mol% one. Although they should be ascribed to Eu^{3+} because they are absent in the pure silica pellet, they cannot be unequivocally attributed to an Eu^{3+} CF transition ($^7F_0 \rightarrow {}^7F_1$): in that range the concomitant presence of much stronger absorptions related to Eu–O group vibrations is expected (as shown by the spectra of Eu_2O_3 and Eu_2SiO_5 pellets).

Possible candidates for Eu^{3+} clusters composition are Eu-oxyorthosilicate (Eu_2SiO_5) and Eu-oxide (Eu_2O_3): the absorption spectra measured at 9 K in the region of first CF transitions on pellets containing polycrystalline powders are collected in Figure 5.21. A direct comparison of the positions of the Eu^{3+} CF absorption lines detected in the spectrum of the Eu^{3+} 10mol% sample with those in the spectra of the two pellets did not provide an exact correspondence neither with Eu_2SiO_5 nor with Eu_2O_3. However there are more coincidences with the former than with the latter.

The analysis of the EDS spectra of the heavy doped sample in a cluster rich region (Figure 5.31), which is in progress, should clarify the problem. Preliminary EDS results suggest that even Eu_2SiO_5 does not match the composition of clusters occurring at high Eu^{3+} doping levels. A new candidate might be the Eu-orthosilicate oxyapatite $Eu_5Si_3O_{13}$, where $(SiO_4)^{4-}$ groups are anyway present.

5.4.2 OH$^-$ and related species

5.4.2.1 OH$^-$ concentration

The bands at ~3670 and 4520 cm^{-1} are due to the stretching and combination (stretching+bending) modes of Si–OH groups [115], respectively. From the amplitude and/or area subtended to these peaks, it is possible to evaluate the OH concentration (C_{OH}) [124]. This analysis was performed for the majority of the massive samples, and the results are collected in Table 5.2. In several cases the band related to the stretching mode at ~3670 cm^{-1} was too intense (either out of scale or affected by detector non linearity) to allow the calculation of C_{OH} (fifth column); thus, only the value obtained from the combination band at ~4520 cm^{-1} is reported (last column).

Table 5.2 reports also the thickness of each sample. In fact, the C_{OH} depends on the sample thickness: OH$^-$ groups leave easily the matrix during thermal treatments if the sample is thin [69, 108]. This accounts for some very low C_{OH} values listed in Table 5.2.

Table 5.2 OH contents (mol%) calculated from Si–OH stretching (fifth column) and combination (last column) bands for SiO_2 samples doped with different RE^{3+}. The thickness of the samples is reported in the fourth column.

Dopant	C_{RE} (mol%)	C_{RE} (mol%)	d (cm)	C_{OH} (mol%) stretch	C_{OH} (mol%) comb
Ce^{3+}	0		0.105	0.40	0.47
	0.001		0.105	0.56	0.68
	0.003		0.11	0.71	0.93
	0.01		0.105	0.64	0.76
	0.03		0.141	0.61	0.87
	0.1		0.135		1.02
	0.3		0.1		1.29
	1		0.115		1.01
	3		0.11		1.09
	10		0.065	0.09	0.19
Gd^{3+}	0.05		0.14		0.97
	0.1		0.135		1.02
	1		0.085		0.64
	3		0.141		0.89
	8		0.033	0.23	0.21
RTT	0.05		0.137		0.90
RTT	0.1		0.171		0.79
RTT	0.5		0.153		1.04
RTT	1		0.094		0.74
RTT	3		0.171		0.95
RTT	8		0.076	0.18	0.15
Gd^{3+}, Ce^{3+}	0.1	1	0.069		0.47
	0.5	1	0.065	0.45	0.41
white	1	1	0.213		1.77
transp	1	1	0.171		0.85
	3	1	0.069		0.62
	5	1	0.081		0.47
	8	1	0.103		0.45
RTT	1	1	0.195		1.02
RTT	3	1	0.02	0.61	
RTT	8	1	0.099		0.42
	0.1	0.1	0.085		0.79

Dopant	**C_{RE} (mol%)**	**C_{RE} (mol%)**	**d (cm)**	**C_{OH} (mol%) stretch**	**C_{OH} (mol%) comb**
	0.5	0.1	0.108		0.97
	1	0.1	0.077		0.51
	3	0.1	0.085		0.66
	5	0.1	0.121		0.35
	8	0.1	0.047	0.22	0.22
RTT-white	1	0.1	0.182		1.34
RTT-transp	1	0.1	0.132		0.87
RTT	3	0.1	0.07		0.74
RTT	5	0.1	0.103		0.62
RTT	8	0.1	0.07	0.33	0.30
Tb^{3+}	0.001		0.126		1.18
	0.003		0.125		1.21
	0.01		0.095		1.28
	0.03		0.116		1.12
	0.1		0.1	0.82	1.03
	0.3		0.142		1.23
	1		0.122		1.42
	3		0.134		1.69
	10		0.07	0.52	2.00
Yb^{3+}	0		0.092	0.55	0.61
	0.005		0.1		1.26
	0.01		0.09		1.18
	0.02		0.137		1.24
	0.05		0.036	0.12	0.23
	0.1		0.11		0.96
	0.2		0.12		1.31
	0.5		0.115		1.02
	1		0.11		1.04
	4		0.1	0.76	0.87
Eu^{3+}	0		0.118	0.40	0.46
	0.001		0.146		0.71
	0.003		0.119		1.28
	0.01		0.1		1.32
	0.03		0.095		1.37
	0.1		0.066	0.47	0.65
	0.3		0.042	0.07	0.16
	1		0.055	0.50	0.76
	3		0.051	0.42	1.57

The values obtained for Tb^{3+} and Eu^{3+} heavily doped samples are strongly affected by the superposition of the CF absorption bands to the combination mode one (see Figure 5.13); this is stressed by the large difference between the values obtained from the stretching (C_{OH}=0.52mol%) and combination (C_{OH}=2mol%) bands in the Tb^{3+} 10mol% sample. Owing to this, the relative values will not be considered.

Nevertheless, it is possible to find a general trend: C_{OH} initially increases with respect to the OH content of undoped samples (C_{OH}=0.43-0.58mol%), then it decreases by increasing the RE^{3+} doping. C_{OH} evaluated for Yb^{3+} doped samples is displayed in Figure 5.35 as a function of the Yb^{3+} content (C_{Yb}), and compared to that of an undoped sample (C_{OH}^{0}). High doping levels, e.g. Gd^{3+} 8mol% or Ce^{3+} 10mol%, induces a strong decrease of the OH content, even with respect to that of an undoped sample; see, for example, Figure 5.4 or Figure 5.7. The limit case is represented by the Eu^{3+} 10mol% sample: Figure 5.20 shows how the OH related bands are no longer detectable in its spectrum.

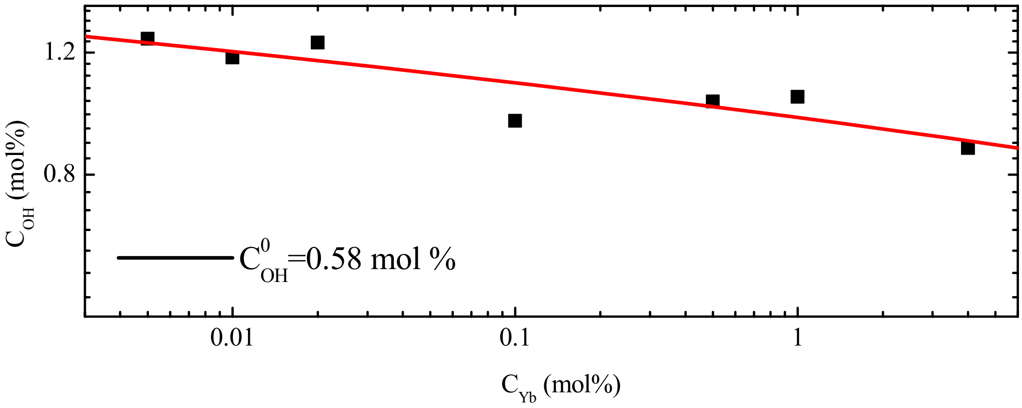

Figure 5.35 C_{OH} evaluated for Yb^{3+} doped samples as a function of the Yb^{3+} content; the OH content of a pure sample (C_{OH}^{0}) is reported for reference.

The initial increase followed by a decrease of C_{OH} as a function of C_{RE} can be interpreted as follows. At low doping levels, the RE^{3+} is present as an isolated defect in the glassy matrix: it substitutes for Si^{4+}, thus requiring charge compensation which may be easily offered by an OH^{-}. At higher doping levels, RE clustering starts until phase separation may occur, as shown by TEM images (see Section 5.3.7). Now charge compensation provided by OH is no longer needed. Thus, the Si–OH content decreases again since OH groups can be desorbed during the annealing at 1050 °C. Recent molecular-dynamics modeling of Eu^{3+} in an ideal OH-free silica showed that a few Eu^{3+} pairs are already present at Eu^{3+} content of 1mol% in addition to dominating isolated

Eu^{3+}; by increasing the doping level large Eu^{3+} clusters are formed at the expense of both Eu^{3+} pairs and isolated Eu^{3+} ions [125].

5.4.2.2 Other features

Spectra measured on Gd^{3+} doped and Ce^{3+}-Gd^{3+} co-doped samples show a weak band at ~4250 cm^{-1} in addition to the peak due to OH^- combination stretching+bending mode at ~4520 cm^{-1} (see Figure 5.7 and Figure 5.11). The amplitude of this additional band increases by increasing the Gd^{3+} doping level, and it disappears in samples submitted to RTT.

It is more pronounced in co-doped samples, but it is not related to the presence of Ce^{3+}: in fact it does not appear in Ce^{3+} doped samples prepared in oxydizing atmosphere (Figure 5.36). It was not detected for other investigated RE. This means that it is related to the presence of Gd^{3+}. It cannot be attributed to any Gd^{3+} electronic transition (see Section5.4.1), but rather to a vibrational absorption due to a combination mode (stretching+bending) of an OH perturbed by the presence of nearby Gd^{3+} ion (or ions).

An interaction between Gd^{3+} and OH^- is feasible, because Gd^{3+}, substituting for Si^{4+}, may be locally charge compensated by an OH^-, substituting for an O^{2-} (see Section 5.4.2.1). The amplitude of the 4250 cm^{-1} peak shows quadratic dependence as a function of the Gd^{3+} concentration in Ce^{3+}-Gd^{3+} co-doped samples (Figure 5.37). The quadratic law suggests that the complex responsible for the 4250 cm^{-1} peak is a Gd^{3+} dimer interacting with OH^-, perturbing its vibrational modes, and causing the peak shift from 4520 to 4250 cm^{-1}.

TEM measurements show as the RTT induces an increase of the cluster dimensions, at the expenses of small aggregates. This could justify the disappearance of the peak in samples submitted to RTT: the treatment breaks the dimers. A similar result was found for Ce^{3+}-doped silica, where Ce^{3+} dimers, monitored by an electronic transition occurring at 2.4 eV, disappeared in samples submitted to an RTT [108].

Thus, the additional line at 4250 cm^{-1} can be due to a Si-OH combination mode perturbed by neighbouring Gd^{3+} dimers.

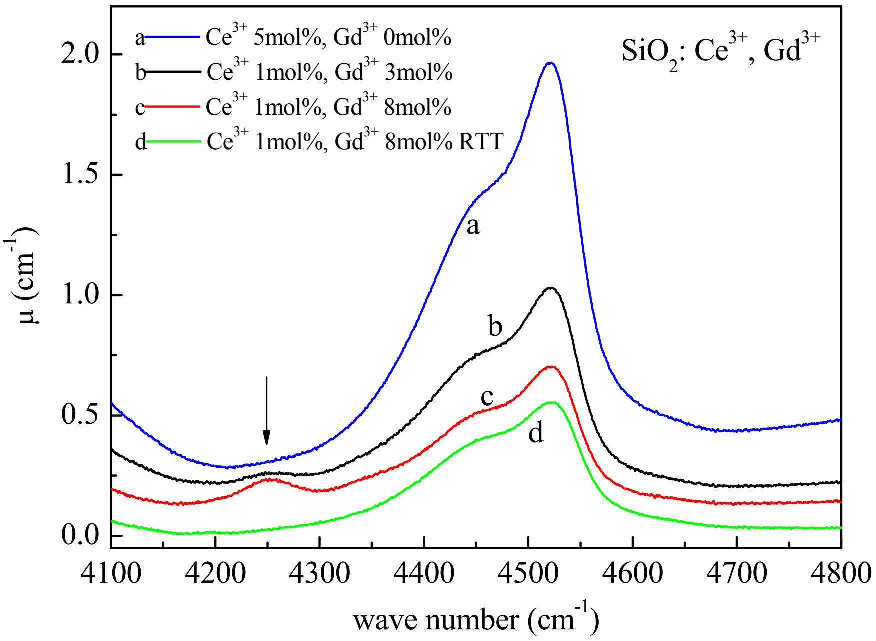

Figure 5.36 Absorption spectra measured in the region of the OH^- combination mode on SiO_2: Ce^{3+}, Gd^{3+} co-doped samples. Curve a: Ce^{3+} 5mol%; curve b:Ce^{3+} 1mol%, Gd^{3+} 3mol%; curve c:Ce^{3+} 1mol%, Gd^{3+} 8mol%; curve d: Ce^{3+} 1mol%, Gd^{3+} 8mol% submitted to RTT.

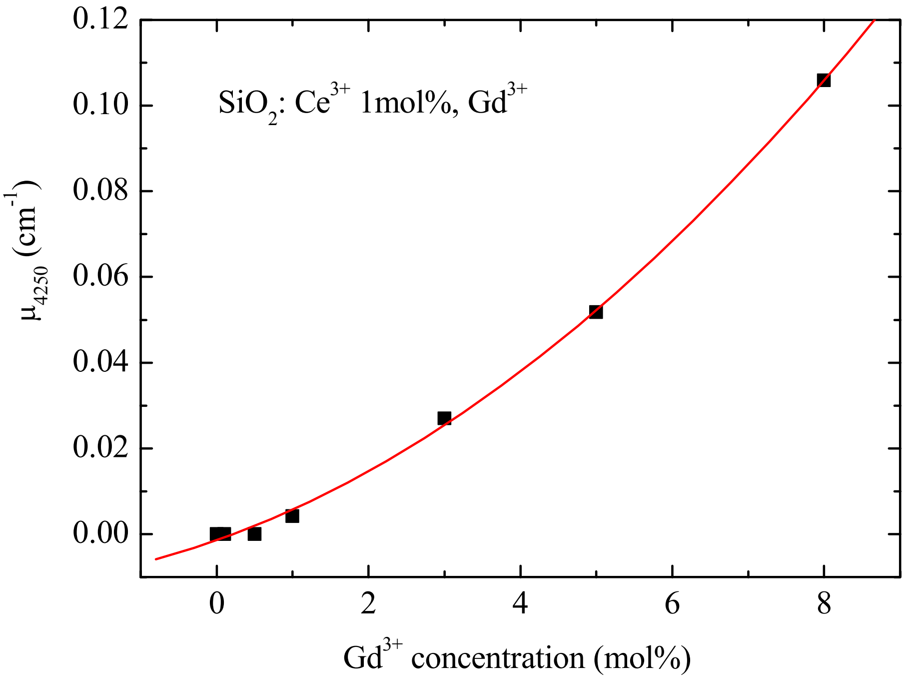

Figure 5.37 Amplitude of the band at 4250 cm^{-1} as a function of the Gd^{3+} concentration in Ce^{3+} 1mol%, Gd^{3+} co-doped samples. The continuous line is a fitting according to a quadratic low.

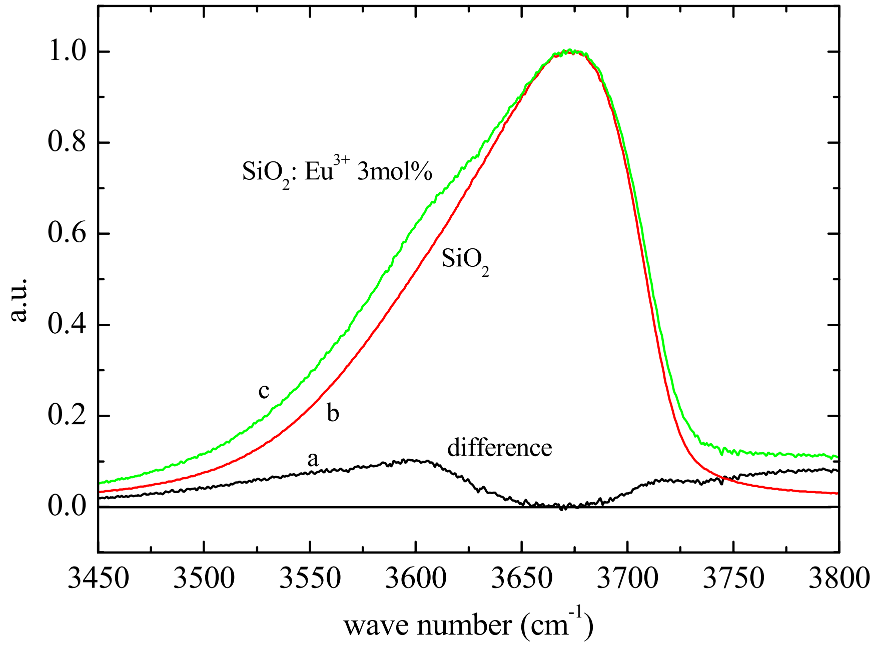

Figure 5.38 Difference spectra (curve a) between the normalized spectrum of a pure SiO_2 sample (curve b) and that of a SiO_2: Eu^{3+} 3mol% (curve c) in the region of the additional bump at 3600 cm^{-1}.

Spectra of Eu^{3+} 1 and 3mol% samples show a bump at 3600 cm^{-1} overlapping the Si–OH peak at RT; it is absent in undoped silica and its amplitude increases with the RE^{3+} concentration (Figure 5.20). The additional contribution due to Eu^{3+} doping is clearly put in evidence in Figure 5.38 by the difference spectrum (curve a) between the Eu^{3+} 3mol% doped sample spectrum (curves c) and that of an undoped SiO_2 sample (curves b), both normalized at the maximum at 3673 cm^{-1}. This suggests that Eu^{3+} may be responsible of it. Two hypotheses may be put forth to explain its origin.

1. It is related to an Eu^{3+} CF transition: in this case it should be present in the Eu^{3+} 10mol% doped silica spectrum as a well isolated strong peak, since no disturbing overlapping of the Si–OH band occurs. But it is not present, neither at RT (Figure 5.20) nor at 9 K (Figure 5.21); moreover, no Eu^{3+} CF line was monitored around 3600 cm^{-1} in any of the Eu^{3+} doped systems investigated.
2. It is associated with an OH (or Si–OH) group perturbed by a neighbouring Eu^{3+}, as in the previous case of Gd^{3+} bump at 4250 cm^{-1}. This hypothesis requires the simultaneous presence of both Eu^{3+} and OH (or Si-OH) groups: this is the case of Eu^{3+} 1 and 3mol% doped samples, but not of the Eu^{3+} 10mol%, where OH is

> absent. An interaction between OH groups and Eu^{3+} is well known to take place in sol-gel silica: it causes Eu^{3+} fluorescence quenching and favours hole burning within the Eu^{3+} $^5D_0 \rightarrow {}^7F_0$ emission line [126].

Thus the 3600 cm^{-1} bump monitored in the Eu^{3+} 1 and 3mol% doped samples can be reasonably attributed to a Si-OH stretching mode perturbed by one or more neighboring Er ions.

5.4.3 Vibrational modes

The fundamental vibration modes of O–Si–O groups are responsible for the 'reststrahlen' monitored by microreflectance (Figure 5.6, Figure 5.8, Figure 5.9, Figure 5.14, Figure 5.23, and Figure 5.24) and absorption (Figure 5.10, Figure 5.12, Figure 5.15, Figure 5.19, Figure 5.22, and Figure 5.26) spectra of silica samples. The modes and the related transverse (TO) and longitudinal optical (LO) frequencies in undoped silica (see Figure 5.39) are the rocking at ~460 cm^{-1} (TO_1) and ~505 cm^{-1} (LO_1), the bending at ~810 cm^{-1} (TO_2) and ~820 cm^{-1} (LO_2), the antisymmetric stretching (AS) at ~1075 cm^{-1} (TO_3) and ~1255 cm^{-1} (LO_3) [117]. Two different AS modes have been distinguished according to the two Si-adjacent oxygens oscillating either in phase (AS_1) or out of phase (AS_2). The disorder typical of a glass matrix causes a mechanical coupling of the two AS modes, thus introducing an additional pair of LO and TO modes at ~1165 cm^{-1} (LO_4) and at ~1200 cm^{-1} (TO_4), respectively, with an inversion with respect to the usual sequence of the LO and TO frequencies [118].

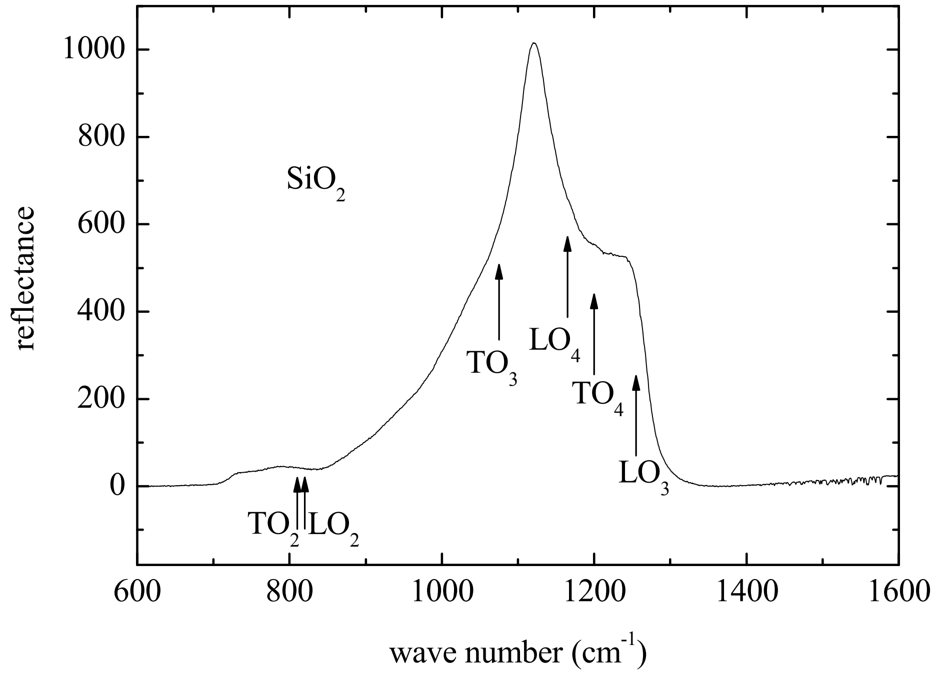

Figure 5.39 Microreflectance spectra of an undoped SiO_2 sample. The arrows indicate the position of the optical frequencies.

5.4.3.1 Microreflectivity spectra

The reflectivity spectra were in the recent past exploited to monitor the effects produced by increasing doses of implanted ions (e.g. Ar, N, Cu) into silica films. They consist in a shift of the vibrational frequencies to lower values, and in a decrease and broadening of the peaks; a subsequent sample annealing at high temperature causes a partial recovery of the spectra [117]. The shift and the shoulder, appearing at ~1040 cm^{-1}, are attributed to the Si–O–Si bond-breaking [127]. In the present case, at variance with the implanted films where the foreign ions are concentrated only in a thin layer, RE^{3+} should be uniformly distributed along the sample thickness, although some departure from uniformity was occasionally detected in Eu^{3+} doped samples (see Figure 5.1 and Figure 5.2).

To summarize the characteristics induced by submitting the sample to RTT and increasing the RE^{3+} concentration, microreflectance spectra in the 650-1350 cm^{-1} range, measured on undoped sol-gel silica samples (both before and after RTT) and doped with different amounts of Tb^{3+}, are compared in Figure 5.40, panel A. To better appreciate the shape changes, the spectra are normalized to the reflectivity maximum occurring around 1120 cm^{-1} and difference spectra with respect to that of the undoped sample are displayed in panel B.

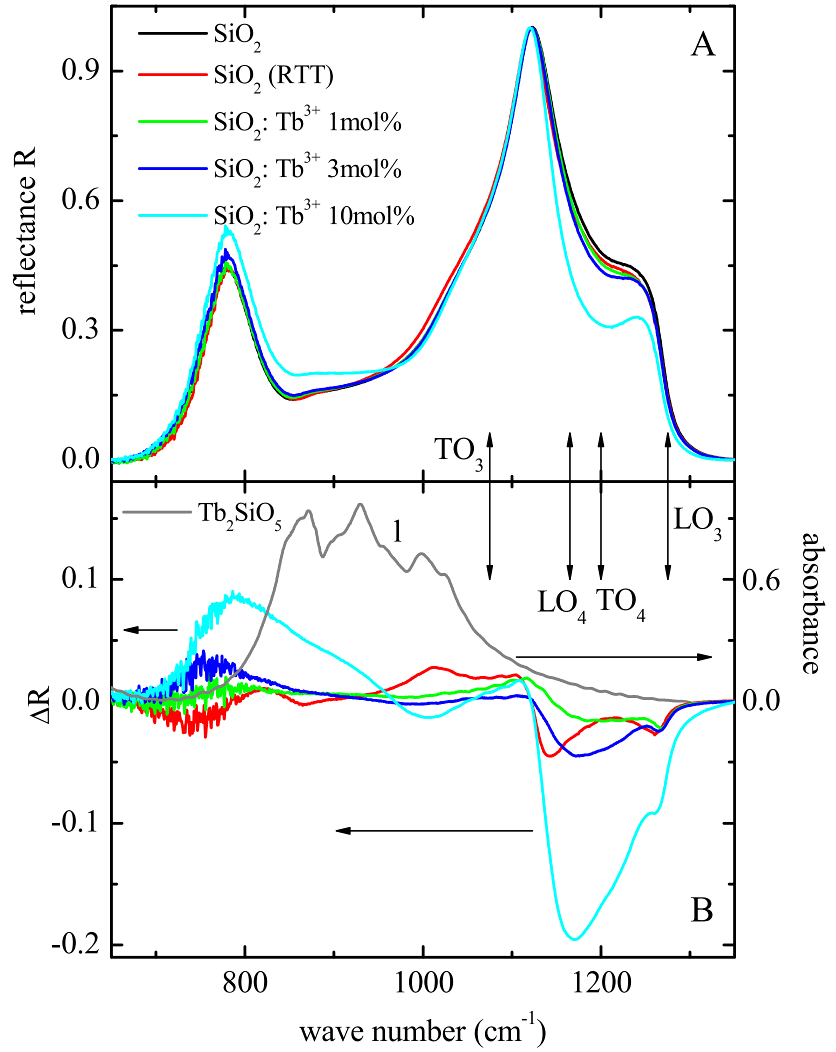

Figure 5.40 Panel A: RT microreflectance spectra of SiO_2 samples undoped (before and after RTT) and doped with different Tb^{3+} concentrations. Panel B: difference microreflectance spectra, the reference being the spectrum of the undoped sample. The RT absorption spectrum of a Tb_2SiO_5 pellet is shown for comparison.

The major features for the undoped sample are a peak at 1123 cm^{-1} and a shoulder at ~1230 cm^{-1}, both related to O–Si–O antisymmetric stretching modes, and a peak at ~780 cm^{-1}, related to the bending mode.

With respect to the spectrum of the undoped sample, RTT induces a weak bump at ~1020 cm^{-1}; moreover, common effects produced by both RTT and Tb^{3+} doping (but also by Ce^{3+}, Gd^{3+}, and Eu^{3+} up to 3mol%; see Figure 5.6, Figure 5.8, Figure 5.9, Figure 5.23, and Figure 5.24) are:

1. a slight shift towards low wave number of the reflectivity maximum at ~1123 cm^{-1};
2. an increase of the dip at ~1200 cm^{-1} by increasing the RE^{3+} concentration.

An additional, relevant change as a consequence of RE^{3+} doping is the progressive increase of the signal in the range 650-1000 cm^{-1}.

Thus, by increasing RE^{3+} amount, the reflectivity decreases mainly in two spectral regions: that of the LO_3 frequency and that of the TO_4 and LO_4 frequencies. The LO modes are sensitive to long range electrostatic interactions: the presence of the RE^{3+} (which may substitute for Si^{4+}) modifies such an interaction, decreasing the number of the original O–Si–O active modes. In the case of LO_4 and TO_4 modes, which arise from the mechanical coupling induced by disorder [118], the RE^{3+} may interrupt the sequence of interacting modes, thus decreasing the total interaction strength.

Furthermore the RTT, which causes a partial freezing of a high temperature arrangement of the glassy network, induces a reflectivity increase at ~1020 cm^{-1}, i.e. very close to the peak at ~1040 cm^{-1}, detected in Cu-implanted silica films and attributed to the Si–O–Si bond-breaking [127]: the similarity suggests that such effects are induced by RTT as well. A further support is supplied by the moderate 'red' shift of the peak at ~1123 cm^{-1} detected as a consequence of both the RTT and RE^{3+} doping. The larger atomic mass of dispersed RE^{3+} ions, which substitute for some of the lighter Si^{4+} in the Si–O–Si chains, may contribute to the 'red shift'. The shoulder at ~1020 cm^{-1} was monitored also in the spectrum of the Eu^{3+} 3mol% sample (Figure 5.23).

The increase of the reflectivity in the 650-1000 cm^{-1} region induced by increasing the RE^{3+} doping, may be attributed to vibrational modes of RE-clusters, i.e. of a separated phase containing RE, Si, and O. The absorption spectrum of a Eu_2SiO_5 pellet, portrayed in Figure 5.40, panel B for comparison, shows the fundamental vibrational peaks actually in that region; thus, the separated phases might have a composition similar to that of Eu_2SiO_5.

Figure 5.41 displays the spectra measured on the samples with 10mol% content of different RE^{3+}: Ce^{3+}, Tb^{3+}, and Eu^{3+}. It stresses once more the drastic changes induced by Eu^{3+} 10mol% doping with respect to the same doping level of other RE^{3+}. Figure

5.23 shows the large differences with respect to the spectrum of the Eu^{3+} 3mol% sample. Figure 5.24 demonstrates the sample is not homogeneous: spectra taken on different parts of the sample (see Figure 5.2 and Figure 5.25) differ one to each other and are quite different from that of the undoped sample.

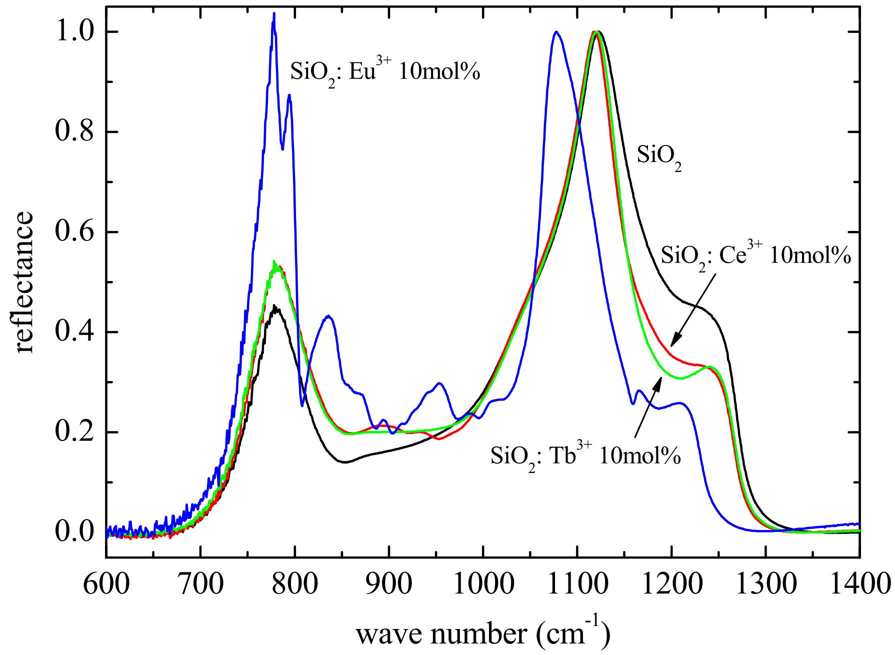

Figure 5.41 Microreflectance spectra of SiO_2 samples undoped and doped with 10mol% of different RE^{3+}: Ce^{3+}, Tb^{3+}, and Eu^{3+}.

In the Eu^{3+} 10mol% spectra, the intrinsic silica antisymmetric stretching modes are heavily modified: the reststrahlen peak at 1123 cm^{-1} shifts to ~1115 and 1116 cm^{-1} (top face and transparent part, respectively) while two side peaks (doublet) appear at ~1076 and 1091 cm^{-1} (top face). The microreflectivity spectrum of the bottom face of the milky piece displays a unique broad peak at ~1078 cm^{-1}, which looks as an envelope of the above mentioned doublet. In all cases the high energy contribution to the pure silica reststrahlen appears strongly reduced. This means that the silica matrix has been strongly modified.

Moreover, a set of well structured peaks appear between 750-1100 cm^{-1}, i.e. in the region of vibrational absorptions of Eu_2SiO_5 (see Figure 5.23); the detailed pattern of these additional peaks depend on the specific area of the sample investigated (Figure 5.24).

The results emphasize that phase separation occurs within silica with the formation of clusters or nanoclusters (see Section 5.4.1) with a rather ordered structure and a composition which recalls that of Eu_2SiO_5, while the residual silica network appears heavily modified.

5.4.3.2 IR absorption spectra

The changes induced by RE^{3+} doping in the region of the fundamental vibration modes of O–Si–O were monitored also by measuring the absorption spectra of sample pellets (see Figure 5.10, Figure 5.12, Figure 5.15, Figure 5.19, and Figure 5.22).

Once more, the case of Tb^{3+} can be used as reference. Figure 5.42 (the same as Figure 5.15 to with the difference spectrum is added) clearly summarizes the changes, indicated by arrows. It is important to underline that it resembles the microreflectance difference spectrum (Figure 5.40), at least in the common 650-1350 cm^{-1} range.

As in the case of microreflectance, it is possible to identify some changes, with respect to an undoped sample, common to absorption spectra measured on samples doped with different RE^{3+} (concentration level up to 3mol% for Eu^{3+}). They are:

1. a marked decrease of the absorption in all the regions of O–Si–O fundamental vibrations;
2. a small "red-shift" of the main peak at ~1100 cm^{-1};
3. the appearance of two shoulders growing around ~940 and ~554 cm^{-1} (these positions slightly change with the RE^{3+}: ~880 cm^{-1} for Gd^{3+}, ~920 and 567 cm^{-1} for Eu^{3+}; they do not appear in Yb^{3+} spectra, but the maximum doping level analyzed was 4mol%).

The first two points have been already discussed in the previous Section (5.4.3.1): the decrease of the vibrational peaks can be ascribed to Si–O–Si bond-breaking [127], while the red-shift can be due to the substitution of the heavy RE^{3+} ions (e.g., m_{Eu}~196 amu) for a fraction of the lighter Si^{4+} ones (m_{Si}~28 amu).

The bump at ~940 cm^{-1} displayed in Figure 5.42 (curve b) falls in the same range where the intrinsic vibrations of SiO_4 tetrahedra occur in Tb_2SiO_5 (curve c). The weak shoulder at ~554 cm^{-1} (curve b) recalls peaks displayed by Tb_2SiO_5 in the 520-580 cm^{-1} range and related to RE-O vibrational modes (curve c). Recent Raman scattering measurements performed on Y_2SiO_5 and Lu_2SiO_5 single crystals ascribed peaks detected in the 500-700 cm^{-1} range to SiO_4 groups bending modes [128]. On the contrary, no clear correspondence is found between the features induced in silica by heavy Tb^{3+} doping (curve b) and the spectrum of Tb-oxide (curve d), which remains practically flat at least in the 700-2000 cm^{-1} range and shows a huge peak around 400 cm^{-1}: no trace of it can be identified in curve b. Such results suggest that Tb^{3+} clusters should have a composition similar to that of Tb-oxyorthosilicate rather than that of the Tb-oxide. The shoulders at ~940 and ~554 cm^{-1} (curve b) support the attribution, but, remaining broad, at variance with the corresponding, structured absorptions of polycrystalline Tb_2SiO_5, stress once more that Tb clusters are amorphous. Similar results were obtained from Raman scattering spectra measured on silica samples doped with Gd^{3+}, Tb^{3+}, or Yb^{3+} [122]: the appearance of two bands, whose position varies from 836 to 891 cm^{-1} and from 930 to 1018 cm^{-1} from sample to sample, occurs. They are related to the RE^{3+} doping and, in particular, suggest that amorphous aggregates could have a structure resembling that of oxyorthosilicates [122].

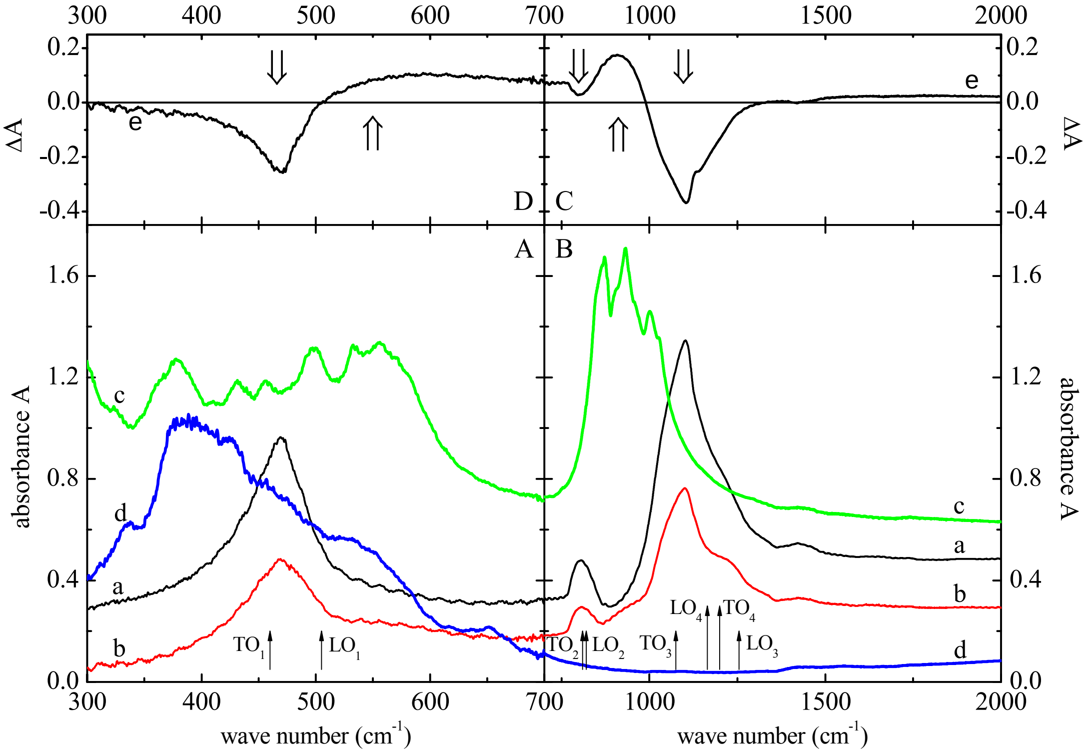

Figure 5.42 Optical absorption spectra measured at RT of CsI pellets. Curve a: undoped SiO_2; curve b: SiO_2: Tb^{3+} 10mol%; curve c: Tb_2SiO_5; curve d: Tb_4O_7. Curve e is the difference spectrum between curve b and curve a: the up and down arrows indicate the regions of increasing and decreasing absorption, respectively.

Quite different patterns are exhibited by the spectra measured on pellets containing chips of Eu^{3+} 10mol% sample, related to two different portions of the same sample, the former being partially transparent and the latter being completely milky (Figure 5.22). In addition to a more marked 'red shift' of the main peak, from ~1102 cm^{-1} in the undoped sample to ~1096 cm^{-1} and ~1077 cm^{-1} in the transparent and milky samples, respectively, the main changes are represented by the appearance of new peaks, which are more defined in the milky sample. By lowering the temperature of the last sample, such peaks sharpen gradually and look more resolved (Figure 5.43): this usually occurs for the absorption spectra of ordered structures. The similarity of the additional peaks with those of Eu_2SiO_5 pellet is evident, while no correspondence can be found with the nearly flat background of the Eu_2O_3 pellet. This strongly supports the hypothesis of nanoclusters with a structure similar to that of Eu-oxyorthosilicate growing in heavily Eu^{3+} doped silica, suggested also by the CF analysis. Furthermore, the shape of the peaks at ~842, 900, and 944 cm^{-1} for the Eu^{3+} doped milky silica recalls rather closely that of the peaks occurring at ~863, 922, and 997 cm^{-1} for the Eu_2SiO_5 pellet and due to SiO_4 groups symmetric and antisymmetric stretching modes [128]. The two peaks below 320 cm^{-1} may be attributed either to Eu–O vibrations or to the Eu^{3+} CF $^7F_0 \rightarrow {}^7F_1$ transition (Section 5.4.1) or to both.

The spectrum of the partially transparent Eu^{3+} 10mol% doped sample looks as intermediate between those of Eu^{3+} 3mol% and milky Eu^{3+} 10mol% doped silica. This suggests the coexistence of amorphous and nearly ordered Eu_2SiO_5-like clusters.

The marked shift and decrease of the peaks related to O–Si–O fundamental vibration modes evidence the great modifications induced by the heavy doping level on the silica matrix, due to the presence of Eu-rich clusters which breaks the Si–O sequences. A shift of the main peak to lower frequencies (by about 10-25 cm^{-1}) was also reported for silicate oxides, as a consequence of heavy doping with lanthanide oxides [129].

Thus, the results agree with those coming from the analysis of the CF spectra (Section 5.4.1) and emphasize that, at Eu^{3+} 10mol% doping level, segregation of an Eu-rich, nearly ordered phase takes place within the silica matrix, as supported by TEM and EDS images (Figure 5.30 and Figure 5.31). Molecular-dynamics modelling of Eu^{3+}-ion clustering in SiO_2 glass demonstrated that clustering is already present at 1mol%, but phase separation becomes apparent at 5mol% doping.

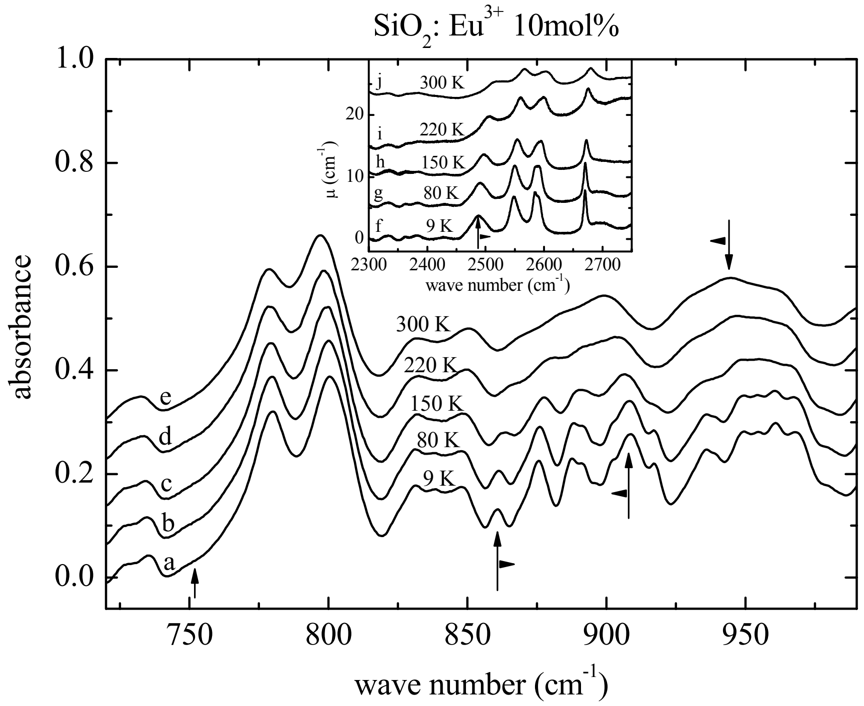

Figure 5.43 Optical absorption spectra measured at different temperatures on CsI pellets of SiO_2: Eu^{3+} 10mol%.

A further insight on the stretching modes of SiO_4 tetrahedra within the Eu_2SiO_5-like nanoclusters in the milky sample can be derived by inspecting the related spectra at higher wave numbers, i.e. in the spectral regions where the weaker absorptions due to combination and overtone modes are expected to occur (see Figure 5.26 and Figure 5.43). Panel A and B in Figure 5.26 display the results in the region of $\Delta n=2$ and $\Delta n=3$, respectively, where n is the quantum number which labels the energy levels of an anharmonic oscillator. The anharmonicity of high energy stretching modes of SiO_4 tetrahedra has been demonstrated, for example in sillenite single crystals [59]. In panel A the 9 K spectra of a few massive silica samples are displayed in the 1380-2400 cm^{-1} range: the undoped silica shows clearly the bump at ~2275 cm^{-1} due to an intrinsic O-Si-O overtone mode [114], followed by a steep increase due to the strong absorption originated by excitation of other vibrational combination modes. The spectra of the Eu^{3+} 3 and 10mol% samples exhibit peaks in the spectral region where the pure sample is completely opaque: a few broad bands the former, a lot of structured peaks the latter. Moreover the bump at ~2275 cm^{-1} is, at least, strongly reduced. Both these features confirm that silica matrix is deeply modified. The peaks below 2100 cm^{-1} of the heavy doped sample are too strong to be attributed to the partially forbidden Eu^{3+} CF $^7F_0 \rightarrow {}^7F_3$ transition; more likely they can be associated with the first overtones (Δn=2) of the absorptions displayed in the 820-980 cm^{-1} range (Δn=1) by the relative pellet (Figure 5.22). Also combinations of two different modes may contribute to the 1500-1900 cm^{-1} spectrum: at least one of them should be IR active [59]. The peak structure is similar to that displayed by the spectrum measured at 9 K on the Eu_2SiO_5 pellet, while it is different from that of the Eu_2O_3 pellet (the doublet recorded around 1450 cm^{-1} in this spectrum is due to carbonate contamination [119] and the narrow peaks above 1800 cm^{-1} may be attributed to Eu^{3+} CF lines within the $^7F_0 \rightarrow {}^7F_3$ transition). This, together with the previous considerations on the silica matrix, confirms once more the conclusion drawn from the above analysis of the fundamental vibration spectra: the undoped silica modes are in part substituted by those of nanoclusters with a Eu_2SiO_5-like composition. The change from broad bands in the Eu^{3+} 3mol% doped sample to a sequence of structured peaks in the Eu^{3+} 10mol% one suggests the presence of amorphous Eu_2SiO_5-like phases in the former and of more ordered Eu_2SiO_5-like clusters in the latter.

In the region displayed in Figure 5.26, panel B, where the Eu^{3+} lines due to CF $^7F_0 \rightarrow {}^7F_4$ transition occurs (2750-3050 cm^{-1} [56]), also the absorptions induced by third harmonics (Δn=3) of SiO_4^- vibrational modes (and combinations of three modes) are expected. The set of broad peaks below 2620 cm^{-1} exhibited by the Eu^{3+} 10mol% doped sample (both in RT and 9 K spectra) may be attributed to Δn=3 transitions. In the Eu_2SiO_5 pellet no absorption clearly attributable to Δn=3 vibrational transitions can be distinguished below 2600 cm^{-1}, due to the high dilution within the pellet; the Eu_2O_3 pellet, as expected, shows only lines due to Eu^{3+} CF transitions. The Eu^{3+} 3mol% doped silica spectrum displays broad weak CF absorptions but no peak attributable to Δn=3 vibrational modes, due to the lower Eu^{3+} concentration and, as a consequence, to a lower content of the Eu_2SiO_5-like phase.

Possible associations among the fundamental frequency (ω_1, Δn=1, measured on pellets, Figure 5.22) and the related overtones (ω_2, Δn=2; ω_3, Δn=3, measured on the massive sample, Figure 5.26) for a set of selected modes in Eu^{3+} 10mol% doped silica are listed in Table 5.3. If the associations are correct, in the framework of Morse anharmonic oscillator model, the ratio ω_n/n plotted vs. n should give a straight line [59, 130], according to the equation

$$\frac{\omega_n}{n} = \omega_0 - \omega_0 x_e \left(n+1\right), \qquad 5.1$$

where ω_0 is the natural oscillation frequency and x_e is the anharmonicity parameter.

Table 5.3 Frequencies of the fundamental (ω_1) and overtone (ω_2 and ω_3) modes. The first column indicates the temperature at which the peak position was measured. The values in the last four columns (natural oscillation frequency ω_0, anharmonicity parameter x_e, and binding energy D_e) were derived according to eq. 5.1 and 5.2.

T (K)	ω_1 (cm^{-1})	ω_2 (cm^{-1})	ω_3 (cm^{-1})	ω_0 (cm^{-1})	$x_e \times 10^3$	D_e (cm^{-1})	D_e (eV)
9	752*	1492	2220*	764	7.9	24321	3
9	860.8	1690*	2487	892.6	17.8	12528	1.6
9	908	1805	2688	920.2	6.5	35279	4.4
300	944	1876	2797.7	955.3	6	40140	5

*** Shoulder.**

Figure 5.44 shows the linear dependence found indeed for the vibrational modes listed in Table 5.3; fifth and sixth column report the values of ω_0 and x_e derived by fitting the experimental data. The anharmonicity parameters are in the 6-8$\times10^{-3}$ range for the 752, 908, and 944 cm^{-1} modes, in agreement with the value found for SiO_4 stretching modes in the $Bi_{12}SiO_{20}$ sillenite (5.9 $\times10^{-3}$ [59]); the value obtained for that at 860.8 cm^{-1} is higher (~17.8$\times10^{-3}$). However, this rather high value is along with the remarkable 'blue shift' suffered by the mode as the temperature is increased from 9 to 300 K: this is particularly evident for the ω_3 frequency which shifts from 2487 to ~2517 cm^{-1} (see inset in Figure 5.43). Usually by increasing the temperature the vibrational peak frequencies shift towards lower values due to lattice thermal expansion (as it happens indeed for the peaks at 908 and 944 cm^{-1} listed in Table 5.3 and characterized by lower x_e, see Figure 5.43), unless the anharmonicity contribution prevails [131], as probably in the case of 860.8 cm^{-1} peak.

From the anharmonicity parameter x_e, the binding energy D_e can be evaluated as

$$D_e = \frac{\omega_0}{4x_e}. \qquad 5.2$$

D_e and β are the parameters appearing in the expression of the Morse potential as a function of distance r

$$U(r-r_e) = D_e\left[1-e^{-\beta(r-r_e)}\right]^2 \qquad 5.3$$

where r_e is the equilibrium distance [130]. The values so obtained are listed in the last two columns of Table 5.3: those related to the 752, 908, and 944 cm^{-1} modes, are quite close to that reported for SiO_4 stretching modes in the $Bi_{12}SiO_{20}$ sillenite (4.7 eV [59]), while that related to the 860.8 cm^{-1} mode is lower, due to the already emphasized higher anharmonicity.

It is important to notice that, even if the high Eu^{3+} doping level induces heavy changes in the silica matrix, here the anharmonicity parameter was derived in a glass and not in a crystal matrix.

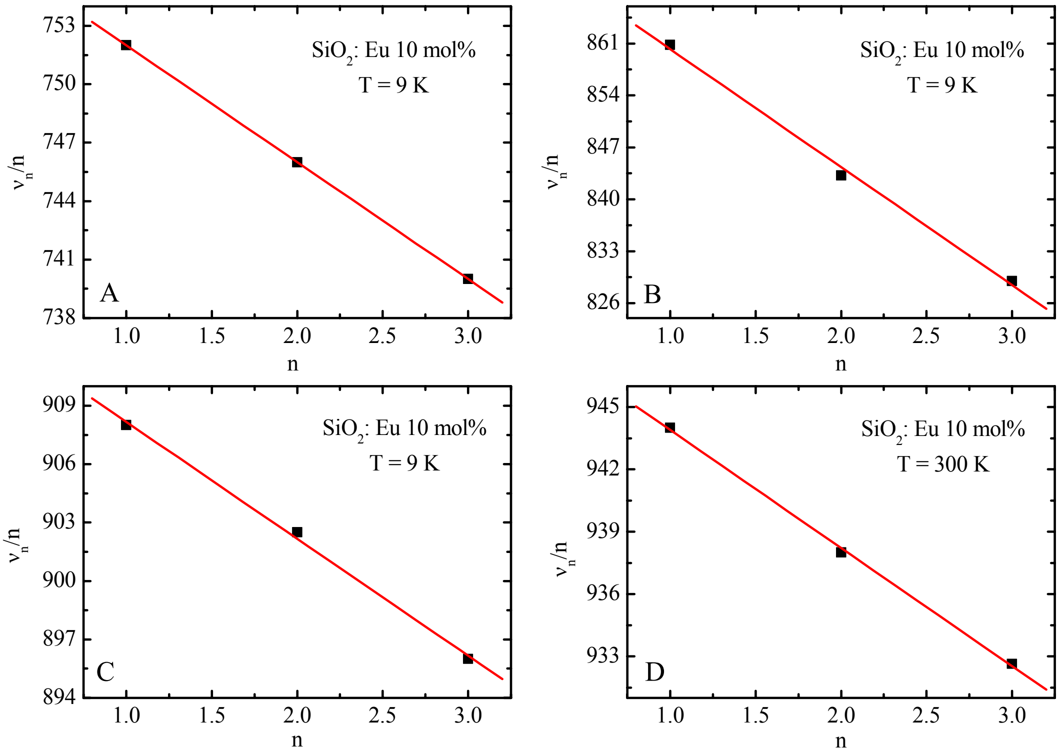

Figure 5.44 Linear dependence of the vibrational modes listed in Table 5.3 derived according to eq. 5.1.

5.5 CONCLUSION

The effects of RE^{3+} (RE=Ce, Gd, Tb, Yb, and Eu) incorporation in sol-gel silica matrix were studied by means of FTIR spectroscopy, with the support of TEM, EDS, and Raman spectroscopy measurements. Particular attention was paid to OH^- content (Section 5.4.2), matrix modifications (Section 5.4.3), and cluster formation (Section 5.4.1).

All the analyses performed evidence that with increasing the doping level the silica matrix changes and formation of RE-rich clusters occurs; the dimensions of the aggregates increase with the RE^{3+} concentration and as a consequence of RTT. The separate phases remain amorphous in the case of Ce^{3+}, Gd^{3+}, Tb^{3+}, and Yb^{3+}, even at high concentration levels, while they assume nearly ordered arrangements in the case of Eu^{3+} 10mol%.

Good candidate for the cluster structure is the RE-oxyorthosilicate $(RE)_2SiO_5$: such a phase rather than the oxide may be favoured just due to the survival within the oxyorthosilicate of tetrahedral SiO_4 groups which, very likely, contribute to reduce the mismatch with the host silica matrix.

Actually, recent results from EDS measurement analysis seem to rule out even this hypothesis and introduce a new candidate: the Eu-orthosilicate oxyapatite $Eu_5Si_3O_{13}$. The considerations which supported the hypothesis of $(RE)_2SiO_5$-like clusters are still valid, due to the presence in both the orthosilicates of the groups $(SiO_4)^{4-}$. The EDS analysis is still in progress.

In any case, the formation of rather ordered nanophases in Eu^{3+} doped silica matrix was proven, in addition to the amorphous clusters evidenced in silica doped with other RE^{3+} ions. Nanocrystals might be obtained even in those system possibly by modifying synthesis conditions.

Nanocrystals embedded in amorphous SiO_2 could directly serve as luminescent phases, or as nanometric hosts for a different activator in the case of low intrinsic luminescent yield.

Anyway, the understanding of the nanophase nature which spontaneously form in the silica network as a consequence of heavy RE^{3+} doping is an important step for tailoring silica based nanocomposites, since it gives indications on which nanophases are expected to be more favourably incorporated due to a low mismatch with the silica matrix. For this reason, the present work could be extended to samples doped with Eu^{3+} concentrations in the range 3-10mol% and submitted to proper thermal annealing to produce Eu-rich nanocrystals, possibly of controlled size, embedded in a transparent host silica.

6 CONCLUSIONS

In the present work the optical properties of rare earth (RE) ions embedded in different matrices were studied mainly by means of high resolution Fourier transform absorption spectroscopy in wide wave number (200-25000 cm^{-1}) and temperature (9-300 K) ranges. Complementary techniques (microreflectance, linear dichroism, specific heat, photoluminescence, TEM, EDS, and AFM measurements) were employed to provide a more complete and sound description of the analyzed phenomena (see Appendix).

A number of materials was investigated being promising candidates for applications in photonics. The present work reports only the results related to materials for which the high resolution spectroscopy was crucial to get a deep insight on the RE^{3+} environments[1], i.e.:

1. BaY_2F_8 (BaYF) single crystals doped with Er^{3+}, Tm^{3+}, and Ho^{3+} (Chapter 2);
2. YPO_4 single crystals doped with Ho^{3+} (Chapter 3);
3. $YAl_3(BO_3)_4$ (YAB) single crystals doped with Pr^{3+} (Chapter 4);
4. SiO_2 glasses doped with Ce^{3+}, Gd^{3+}, Tb^{3+}, Yb^{3+}, and Eu^{3+} (Chapter 5).

---

[1] The high resolution spectroscopy gave also a substantial contribution to the ligand field understanding in a Tm^{3+}-based ‘double-decker’ phtalocyanine complex which can be regarded as a single molecule magnet for applications in quantum computation and information storage (see Publication 4). Preliminary analyses of crystal field were also carried out on $Lu_3Al_5O_{12}$ (LuAG) and $YAlO_3$ (YAP) doped with Ce^{3+} and Pr^{3+}.

The careful analysis of the narrow line rich spectra measured as a function of temperature, sample orientation, and incident light polarization brought to the absorption line attribution, allowing to build the energy level scheme for:

1. Tm^{3+} and Ho^{3+} in BaYF (Section 2.4.1; actually, a refinement with respect to Ref. [28]);
2. Ho^{3+} in YPO_4 (Section 3.4.1);
3. Pr^{3+} in YAB (Section 4.4.1).

The experimental data fitting according to a single-ion Hamiltonian model supplied a valuable support to unravel the complex energy level scheme originated by the line rich spectra. It confirmed the attribution validity in the cases of RE^{3+} embedded in BaYF and YPO_4. On the other hand, the agreement between experimental results and theoretical calculations was not found satisfactory in the case of YAB: Pr^{3+}, confirming both the difficulties already encountered for other Pr^{3+}-doped systems [88-92] and the limits of the single-ion model. Moreover, the free ion and crystal field (CF) parameters were determined: those obtained for Tm^{3+} and Ho^{3+} in BaYF were compared with those related to Nd^{3+}, Dy^{3+}, and Er^{3+} in the same matrix. The free ion parameters slightly increase by increasing the atomic number, while the CF ones slightly decrease or remain more or less constant along the series, as expected. Further theoretical calculations are in progress.

The dichroic spectra analysis allowed not only to refine the line attribution (e.g. by distinguishing between lines very close one to each other), but also to identify the orientation both of the dielectric ellipsoid and of the dipole moments μ associated with a few optical transitions in BaYF and YAB (Sections 2.4.2 and 4.4.2). The results suggest that the dipole moments are oriented along preferential directions within the crystal.

RE^{3+} ions embedded in matrices can also be exploited as microscopic probes sensitive to the environments. In fact, thanks to the high resolution, it was possible to make evident the fine structures decorating the absorption lines due either to the hyperfine nuclear interaction (of Ho^{3+} in BaYF and YPO_4, and of Pr^{3+} in YAB; Sections 2.4.4, 3.4.2, and 4.4.4, respectively) or to roto-electronic transitions, i.e. caused by the simultaneous excitation of an electronic transition and hindered rotation modes (in Er^{3+} and Tm^{3+} doped BaYF samples; Section 2.4.3).

The role of RE^{3+} as environment probes was extensively exploited also in the study of silica glasses. The analyses of CF (Section 5.4.1) and vibrational (Section 5.4.3) spectra measured on SiO_2 glasses doped with Gd^{3+}, Ce^{3+}, Tb^{3+}, Yb^{3+}, and Eu^{3+} evidenced the matrix modifications and the formation of RE^{3+} aggregates by increasing the doping level. The aggregate structure is amorphous and close to that of RE-oxyorthosilicate $(RE)_2SiO_5$ in all cases except for Eu^{3+}, which can originate ordered phases, as confirmed by EDS images.

APPENDIX

1 FOURIER TRANSFORM SPECTROSCOPY

The Fourier Transform (FT) spectroscopy is based on the Michelson interferometer (see Figure 1). The electro-magnetic radiation is emitted by a source (S) and divided by a beam-splitter (b/s) into two beams which reflect on two mirrors, a fixed and a movable one. Then, the two beams come back to the b/s, where they interfere. The radiation intensity monitored by the detector as a function of the path length difference (introduced by the movable mirror) is the source S interferogram. Its inverse FT is the source radiation spectrum. The basic principles of FT spectroscopy are well known and can be found in a more detailed form in Ref. [132, 133]. In the following the main characteristics of the apparatus are described.

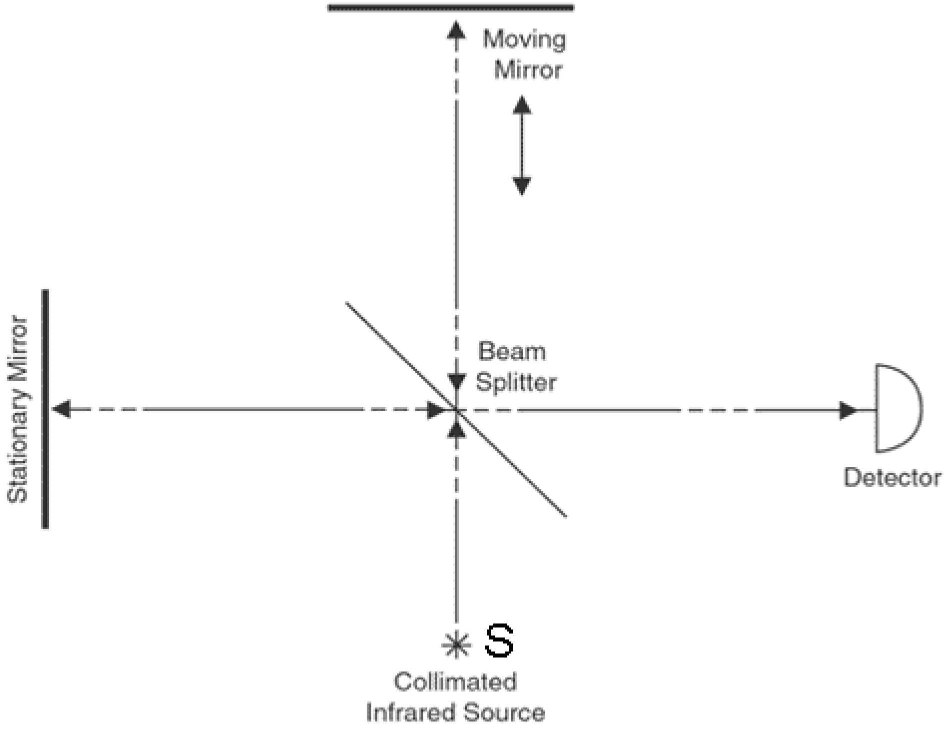

Figure 1 Michelson interferometer.

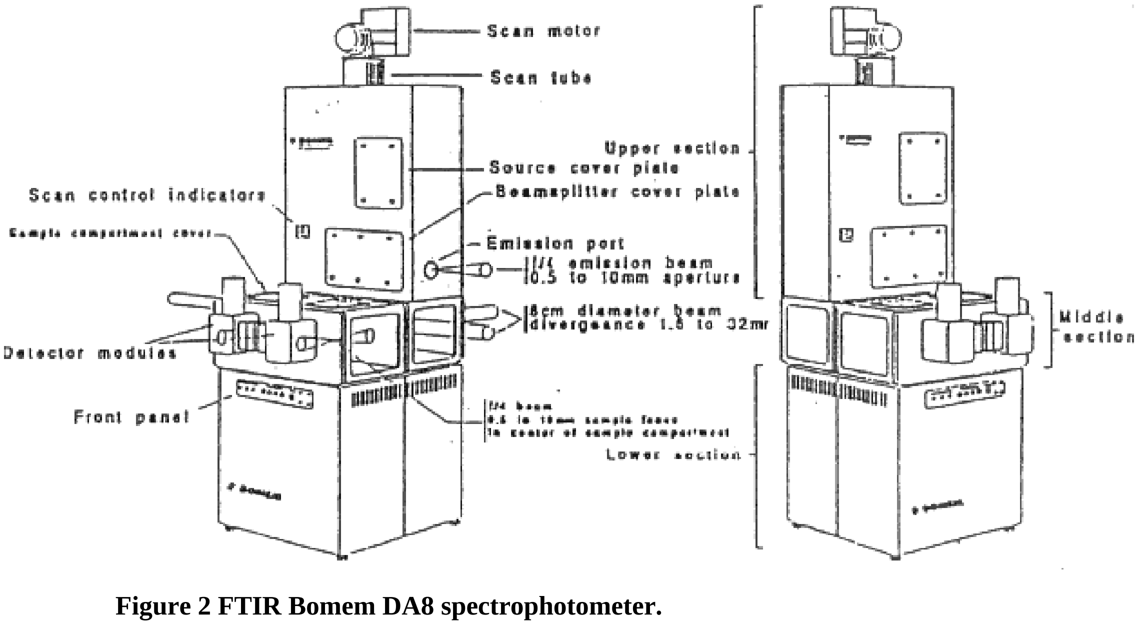

Figure 2 FTIR Bomem DA8 spectrophotometer.

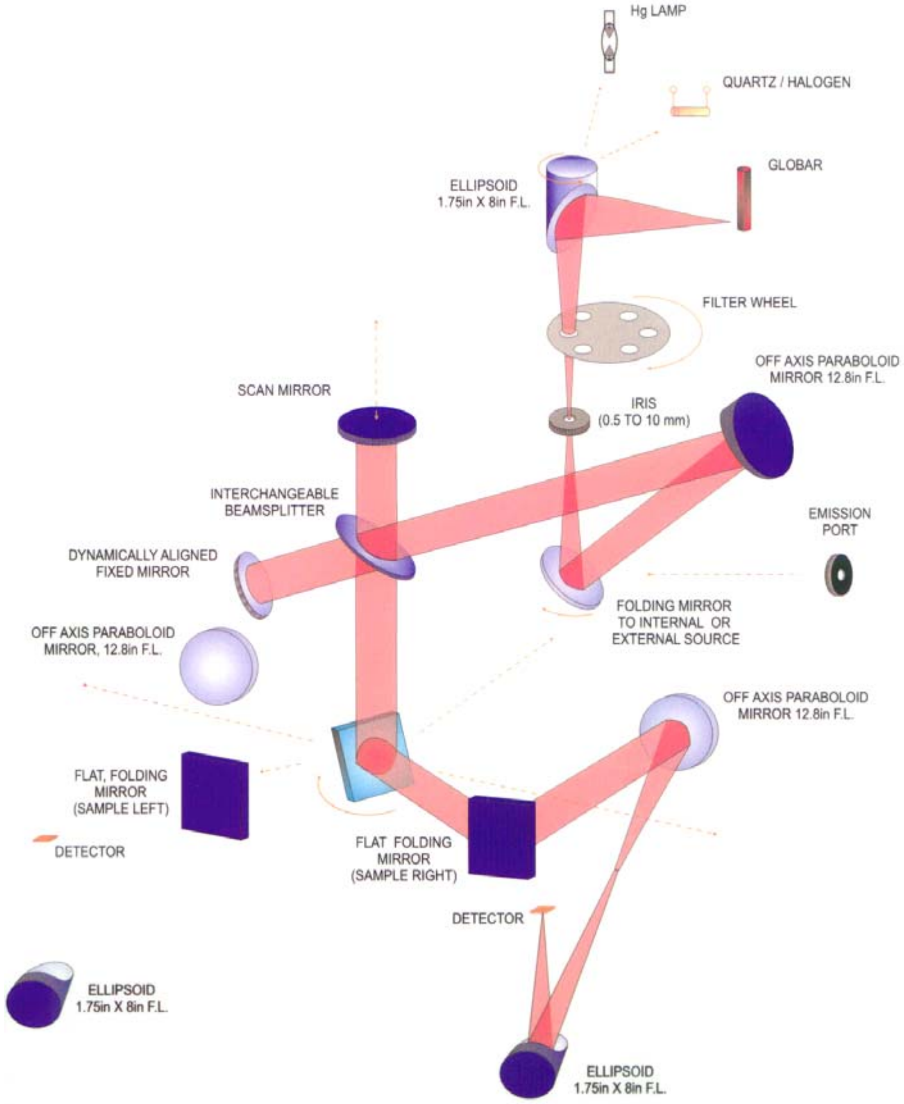

Figure 3 Bomem DA8 scheme.

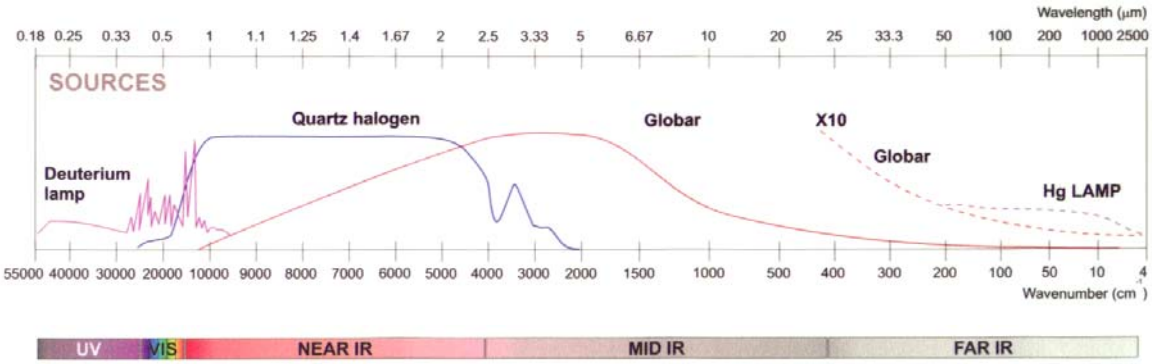

Figure 4 Source working ranges.

1.1 Fourier Transform spectrophotometer Bomem DA8

The optical absorption spectra were measured in the present work, by means of a Fourier Transform spectrophotometer Bomem DA8.

It actually consists of a spectrophotometer (Figure 2), an H.P.V.P. (high performance vectorial processor) and a personal computer. The apparatus scheme is illustrated in Figure 3. It works in the spectral range 5-50000 cm^{-1}, by means of different radiation sources (Figure 4):

1. Mercury Lamp: 5-200 cm^{-1};
2. Globar Lamp: 200-10000 cm^{-1};
3. Halogen Quartz Lamp: 2000-25000 cm^{-1};
4. Deuterium Lamp: 25000-55000 cm^{-1};

and several types of beam-splitters (Figure 5):

1. different Mylar films b/s: 10-850 cm^{-1}. The range 10-500 cm^{-1} can be covered by a hyper-splitter;
2. Germanium film deposited on KBr slab: 450-10000 cm^{-1};
3. TiO_2 film deposited on a quartz slab: 4000-25000 cm^{-1};
4. Aluminium film deposited on a quartz slab: 8500-55000 cm^{-1}.

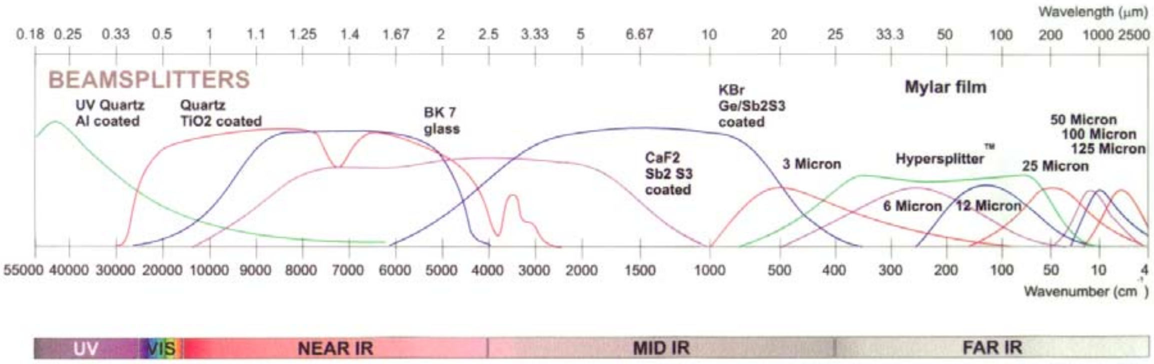

Figure 5 Beam-splitter working ranges.

The available detectors, indicated by blue arrows in Figure 6, are:

1. Silicon bolometer: 10-700 cm^{-1};
2. DTGS (Deuterium TriGlycine Sulphate): 10-700 cm^{-1};
3. MCT (Mercury Cadmium Telluride): 500-6000 cm^{-1};
4. High sensitivity MCT: 800-5000 cm^{-1};

5. InSb: 2000-14000 cm^{-1};
6. Si: 8500-55000 cm^{-1}.

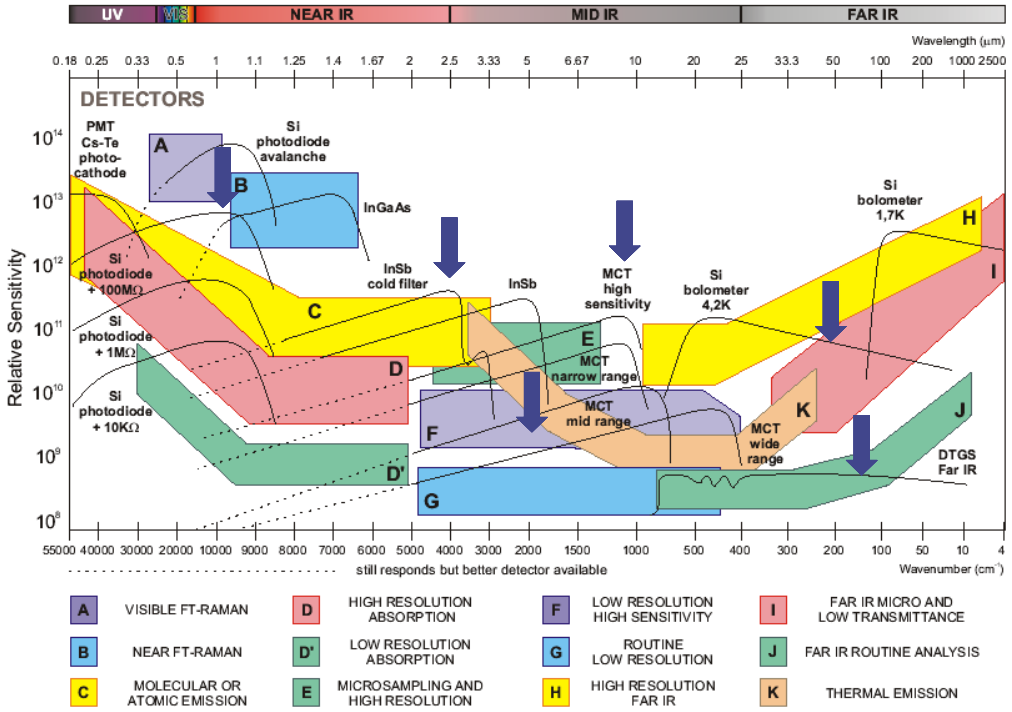

Figure 6 Detector working ranges. The arrows indicate the available detectors.

The detector 1 requires liquid helium cooling, while 3, 4, and 5 need liquid nitrogen cooling. The sample and optics compartments (Figure 2) are maintained under a pressure of ~0.3 Torr, thus reducing the presence of gaseous CO_2 or H_2O which have strong absorptions in the IR region.

A single beam procedure is adopted to obtain optical absorption spectra, i.e. two measurements are performed: the former with the sample and the latter (the reference) with the same experimental set up but without the sample. By knowing the intensity of light transmitted by the sample I and the reference intensity I_0, the absorption spectrum of the sample, or optical density *O.D.* (absorbance), is

$$O.D. = \log_{10}\frac{I_0}{I}. \qquad 1$$

The absorption coefficient can be derived from equation 1 as:

$$\mu = \frac{\ln 10 \cdot O.D.}{\Delta x} \tag{2}$$

where Δx is the sample thickness.

Optical densities higher than 1 cannot be detected correctly due to some non-linearity problems induced by the detectors (e.g. MCT detector).

The spectral resolution is related to the maximum displacement of the movable mirror by

$$\Delta\sigma = 1/L \tag{3}$$

where σ is the wave number ($\sigma = 1/\lambda$). In the Bomem DA8 spectrophotometer the maximum displacement is L=50 cm, thus the maximum apodized (the apodization function should be introduced to correct the problems due to finite FT integration limits) resolution is 0.02 cm^{-1} (0.01 cm^{-1} non-apodized).

1.2 Accessories

1.2.1 Cryocooler

To measure low temperature spectra, the samples are assembled in a 22SC model Cryodine Refrigerator from CTI Cryogenics equipped with KRS5 and fused silica windows. Thanks to an inverse Carnot Cycle operating on gaseous Helium, the samples are cooled down to 9 K. A temperature controller allowed to change T in the 9-300 K range. A dynamic vacuum (~10^{-6} Torr) is maintained inside the cryocooler by a pump system independent of that of Bomem DA8.

1.2.2 Polarizer

A gold grid polarizer deposited onto a KRS5 substrate allows to perform measurements with linearly polarized light in the IR region (500-10000 cm^{-1}). The home-made polarizer holder can be placed in the Bomem DA8 sample compartment and allows changing the direction of the light electric field without breaking the spectrophotometer vacuum.

1.2.3 Microscope

An IR PLAN microscope from Spectra Tech (Stamford, CT) can be coupled to the Bomem DA8 by means of a mirror system to perform microreflectance measurements at room temperature in the 500-6000 cm^{-1} range. The reflectance standard is usually a gold layer. The high sensitivity MCT is used as a detector (see Section 1.1).

2 OTHER EXPERIMENTAL TECHNIQUES

2.1 Specific-heat measurements

The specific heat measurements were performed by Prof. G. Carini and co-workers at the Physics Department of the University of Messina in the 1.5-25 K range using an automated relaxation calorimeter, operating according to the thermal relaxation method. Temperatures were measured by calibrated commercial germanium thermometers. The random error was less than 3-4%.

2.2 Luminescence measurements

Photoluminescence spectra on YPO_4 crystals were obtained by Prof. J. Garcia Solé and co-workers at the Material Physics Department of the Universidad Autonoma de Madrid using an Optical Parametric Oscillator (OPO Quanta Ray) as excitation source. This OPO provides 10 ns pulses with an average energy of 10 mJ and wavelength tunability from about 400 nm to about 2000 nm; the emitted light was focused onto a double-grating monochromator (SPEX 500 M), followed by a CCD-Si detector. Measurements were made at 10 K by using a liquid He cryostat.

2.3 AFM measurements

Atomic force microscopy (AFM) images were obtained by means of an AFM Autoprobe from CP-Research, Thermomicroscopes. The acquisition mode was the contact one.

2.4 TEM measurements

Transmission electron microscopy (TEM) images were taken in the framework of a cooperation with the Department of Materials Science of the University of Milano-Bicocca (Prof. A. Vedda and co-workers) using a JEOL 2000 CX FII at 150 kV, both in transmission and diffraction mode, and a JEOL 2010 at 200 kV, equipped with an energy dispersive spectrometer (X-EDS), detecting X-rays from the samples.

3 THE NEW POLARIZER HOLDER

The chance to perform linear dichroism measurements in the wave number range 500-10000 cm^{-1} was an important work tool. In some cases it should be useful to extend the spectral range to the region 10000-28500 cm^{-1}. Thus, a Glan-Thompson polarizer and a proper polarizer holder was designed (Figure 7) and realized (Figure 8).

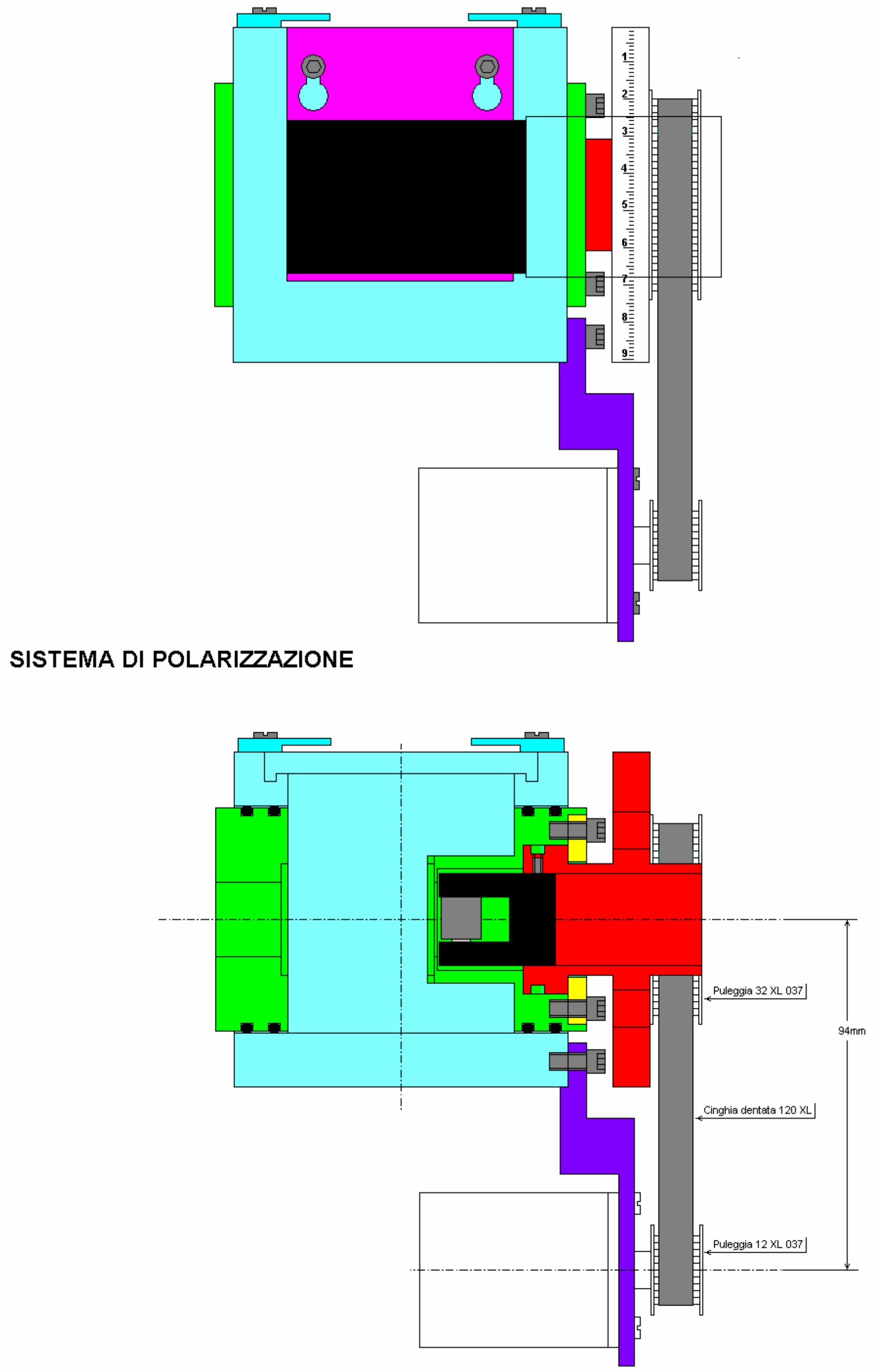

Figure 7 Design of the polarizer holder.

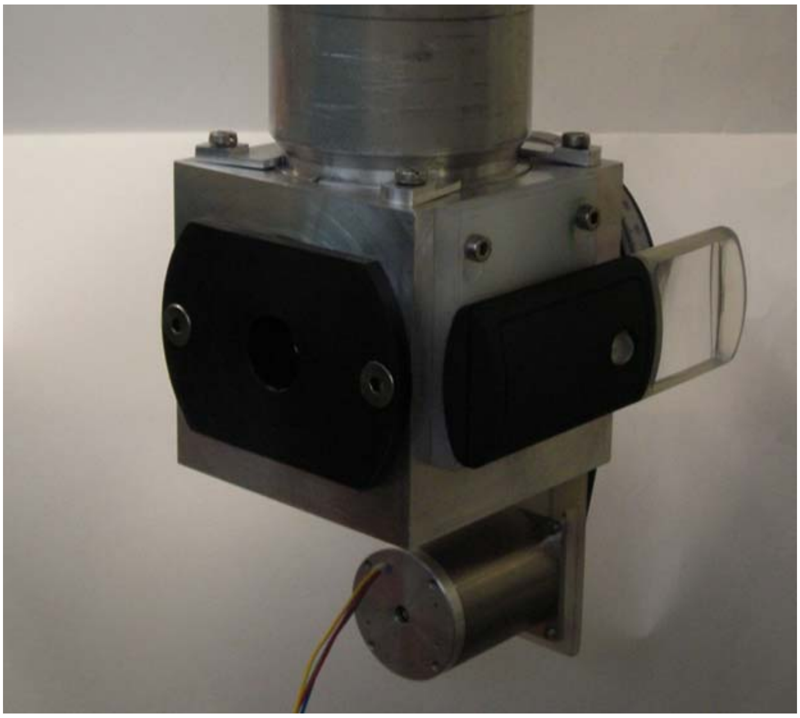

Figure 8 Two pictures of the polarizer holder.

REFERENCES

[1] G. Amoretti, Formulazione microscopica delle interazioni fondamentali nel magnetismo, XXII corso G.N.S.M., L'Aquila, 1990.

[2] B. G. Wybourne, *Spectroscopic Properties of Rare Earths*, Interscience, New York, 1965.

[3] A. Abragam and B. Bleaney, *Electron paramagnetic resonance of transition ions*, Clarendon Press, Oxford, 1970.

[4] B. Di Bartolo, *Optical Interactions in Solids*, John Wiley & Sons, New York, 1968.

[5] N. Magnani, G. Amoretti, A. Baraldi, and R. Capelletti, Eur. Phys. J. B **29**, 79 (2002).

[6] N. Magnani, G. Amoretti, A. Baraldi, and R. Capelletti, Radiat. Eff. Defects Solids **157**, 921 (2002).

[7] R. Capelletti, A. Baraldi, E. Buffagni, N. Magnani, and M. Mazzera, Chapter 1 – Rare earths as a probe of environment and electron-phonon interaction in optical materials: high resolution absorption spectroscopy and theoretical analysis, in Rare earths: Research and Applications, ed. Keith N. Delfrey, Nova Science Publishers, New York, 2008, pp. 25-77 (ISBN 978-1-60456-218-7).

[8] D. J. Newman and B. K. C. Ng, *Crystal Field Handbook,* Cambridge University Press, Cambrigde, 2000.

[9] N. I. Agladze and M. N. Popova, Solid State Communic. **55**, 1097 (1985).

[10] A. Baraldi, R. Capelletti, M. Mazzera, N. Magnani, I. Földvari, and E. Beregi, Phys. Rev. B **76**, 165130 (2007).

[11] N. I. Agladze, E. A. Vinogradov, and M. N. Popova, Sov. Phys. JETP **64**, 716 (1986).

[12] A Ellens, H. Andres, A. Meijerink, and G. Blasse, Phys. Rev. B **55**, 173 (1997); and A Ellens, H. Andres, M. L. ter Heerdt, R. T. Wegh, A. Meijerink, and G. Blasse, Phys. Rev. B **55**, 180 (1997).

[13] P. Dumas, Y. J. Chabal, and G. S. Higashi, Phys. Rev. Lett. **65**, 1124 (1990).

[14] P. Beneventi, P. Bertoli, and R. Capelletti, Mikrochim. Acta [Suppl.] **14**, 491 (1997).

[15] G. Blasse, Int. Rev. Phys. Chem. **11**, 71 (1992).

[16] G. Blasse, A. Meijerink, and C. de Mello Donegà, J. Alloys Compd. **225**, 24 (1995).

[17] A Ellens, S. Schenker, A. Meijerink, and G. Blasse, J. Lumin. **69**, 1 (1996).

[18] D. E. Mc Cumber, J. Lumin. **85**, 171 (2000).

[19] A. Toncelli, M. Tonelli, A. Cassanho, and H. P. Jenssen, J. Lumin. **82**, 291 (1999).

[20] A. A. Kaminskii, S. E. Sarkisov, F. Below, and H.-J. Eichler, Opt. Quantum Electron. **22**, S95 (1990).

[21] M. Pollnau, W. Lüthy, H. P. Weber, T. Jensen, G. Huber, A. Cassanho, H. P. Jenssen, and R. A. MacFarlane, Opt. Lett. **21**, 48 (1996).

[22] G. Galzerano, F. Cornacchia, D. Parisi, A. Toncelli, M. Tonelli, and P. Laporta, Opt. Lett. **30**, 854 (2005).

[23] L. F. Johnson and H. J. Guggenheim, IEEE J. Quantum Electron. **10**, 442 (1974).

[24] G. Galzerano, M. Marano, S. Longhi, E. Sani, A. Toncelli, M. Tonelli, and P. Laporta, Opt. Lett. **28**, 2085 (2003).

[25] M. Marano, G. Galzerano, S. Taccheo, P. Laporta, E. Sani, A. Toncelli, and M. Tonelli, Opt. Mat. **24**, 327 (2003).

[26] L. H. Guilbert, J. Y. Gesland, A. Bulou, and R. Retoux, Mat. Res. Bull. **28**, 923 (1993).

[27] J. B. Amaral, M. A. Couto Dos Santos, M. E. G. Valerio, and R. A. Jackson, Appl. Phys. B **81**, 841 (2005).

[28] A. Baraldi, R. Capelletti, M. Mazzera, P. Riolo, G. Amoretti, N. Magnani, E. Sani, A. Toncelli, and M. Tonelli, phys. stat. sol. (c) **2**, 248 (2005).

[29] A. Baraldi, E. Buffagni, R. Capelletti, M. Mazzera, N. Magnani, G. Carini Jr., and G. D'Angelo, Phys. Rev. B **80**, 155121 (2009).

[30] F. Cornacchia, D. Parisi, C. Bernardini, A. Toncelli, and M. Tonelli, Opt. Express **12**, 1982 (2004).

[31] A. Baraldi, R. Capelletti, M. Mazzera, A. Ponzoni, G. Amoretti, N. Magnani, A. Toncelli, and M. Tonelli, Phys. Rev. B **72**, 075132 (2005).

[32] G. H. Dieke, *Spectra and Energy Levels of Rare Earth Ions in Crystals,* John Wiley & Sons, New York, 1968.

[33] W. T. Carnall, G. L. Goodman, K. Rajnak, and R. S. Rana, J. Chem. Phys. **90**, 3443 (1989).

[34] G. Turrell, *Infrared and Raman Spectra of Crystals,* Academic Press, London, 1972, pp. 153-158.

[35] R. D. Shannon, R. C. Shannon, O. Medenbach, and R. X. Fischer, J. Phys. Chem. Ref. Data **31**, 931 (2002).

[36] R. M. Macfarlane, A. Cassanho, and R. S. Meltzer, Phys. Rev. Lett. **69**, 542 (1992).

[37] A. Baraldi, R. Capelletti, M. Mazzera, A. Ponzoni, G. Amoretti, E. Sani, and M. Tonelli, Radiat. Eff. Defects Solids **158**, 241 (2003).

[38] K. R. Martin, C. Peng, S. Kleekajai, P. Blaney, E. Diamond, W. B. Fowler, M. Stavola, and R. González, Physica B **401-402**, 421 (2007).

[39] L. W. Molenkamp and D. A. Wiersma, J. Chem. Phys. **80**, 3054 (1984).

[40] M. M. Koza, M. R. Johnson, R. Viennois, H. Mutka, L. Girard, and D. Ravot, Nature Mater. **7**, 805 (2008).

[41] M. Hartmann, R. E. Miller, J. P. Toennies, and A. Vilesov, Phys. Rev. Lett. **75**, 1566 (1995).

[42] H. U. Beyeler, Phys. Rev. B **10**, 2614 (1974).

[43] H. U. Beyeler, J. Chem. Phys. **60**, 4123 (1974).

[44] W. D. Seward and V. Narayanamurti, Phys. Rev. **148**, 463 (1966); and V. Narayanamurti, W. D. Seward, and R. O. Pohl, Phys. Rev. **148**, 481 (1966).

[45] L. Pauling, Phys. Rev. **36**, 430 (1930).

[46] R. W. Dreyfus, Phys. Rev. **188**, 1340 (1969).

[47] A. A. Kaminskii, M. Bettinelli, A. Speghini, H. Rhee, H. J. Eichler, and G. Mariotto, Laser Phys. Lett. **5**, 367 (2008).

[48] M. Laroche, S. Girard, J. Margerie, R. Moncorgé, M. Bettinelli, and E. Cavalli,. J. Phys.: Condens. Matter **13**, 765 (2001).

[49] P. S. Peijzel, P. Vergeer, A. Meijerink, M. F. Reid, L. A. Boatner, and G. W. Burdick, Phys. Rev. B **71**, 045116 (2005).

[50] P. S. Peijzel, A. Meijerink, R. T. Wegh, M. F. Reid, and G. W. Burdick, J. Solid State Chem. **178**, 448 (2005).

[51] P.-J. Becker, H. G. Kahle, and D. Kuse, phys. stat. sol. **36**, 695 (1969).

[52] P.-J. Becker, phys. stat. sol. **38**, 379 (1970).

[53] D Neogy, H. Sen, and B. M. Wanklyn, J. Magn. Magn. Mater. **78**, 387 (1989).

[54] L. van Pieterson, M. F. Reid, G. W. Burdick, and A. Meijerink, Phys. Rev. B **65**, 045114 (2002).

[55] E. D. Reed, Jr and H. W. Moos, Phys. Rev. B **8**, 980 (1973).

[56] A. A. Kaminskii, *Laser Crystals*, 2nd ed., Springer-Verlag, Berlin, 1990.

[57] R. Faoro, F. Moglia, M. Tonelli, N. Magnani, and E. Cavalli, J. Phys.: Condens. Matter **21**, 275501 (2009).

[58] R. W. Mooney and S. Z. Toma, J. Chem. Phys. **46**, 3364 (1967).

[59] R. Capelletti, P. Beneventi, L. Kovács, W. B. Fowler, Phys. Rev. B **66**, 174307 (2002).

[60] L. Kovács, R. Capelletti, and M. Gospodinov, Vib. Spectrosc. **46**, 69 (2008).

[61] N. I. Agladze, M. N. Popova, G. N. Zhizhin, V. J. Egorov, and M. A. Petrova, Phys. Rev. Lett. **66**, 477 (1991).

[62] M. N. Popova, and N. I. Agladze, Mol. Phys. **102**, 1315 (2004).

[63] J. P. D. Martin, T. Boonyarith, and N. B. Manson, J. Lumin. **63**, 297 (1995).

[64] J. P. D. Martin, T. Boonyarith, N. B. Manson, M. Mujaji, and G. D. Jones, J. Phys.: Condens. Matter **5**, 1333 (1993).

[65] N. M. Strickland and G. D. Jones, Mol. Phys. **102**, 1345 (2004).

[66] J.-P. R. Wells, G. D. Jones, M. F. Reid, M. N. Popova, and E. P. Chukalina, Mol. Phys. **102**, 1367 (2004).

[67] M. Mujaji, G. D. Jones, and R. W. G. Syme, Phys Rev. B **48**, 710 (1993).

[68] M. J. Weber, *Handbook of Optical Materials*, CRC Press, Boca Raton, 2003.

[69] M. Mazzera, Fourier transform spectroscopy of Rare Earth in Insulating materials for Photonics, PhD Thesis, University of Parma, Italy, 2006.

[70] D. Jacque, J. Capmany, F. Molero, Z. D. Luo, and J. García Sole, Opt. Mater. **10**, 211 (1998).

[71] H. Jiang, J. Li, J. Wang, X.-B. Hu, H. Liu, B. Teng, C.-Q. Zhang, P. Dekker, and P. Wang, J. Cryst. Growth **233**, 248 (2001).

[72] P. A. Burns, J. M. Dawes, P. Dekker, J. A. Piper, J. Li, and J. Wang, Opt. Commun. **207**, 315 (2002).

[73] M. Laroche, M. Bettinelli, S. Girard, and R. Moncorgé, Chem. Phys. Lett. **311**, 167 (1999).

[74] M. H. Bartl, K. Gatterer, E. Cavalli, A. Speghini, and M. Bettinelli, Spectrochim. Acta Part A **57**, 1981 (2001).

[75] Gy. Mészáros, E. Sváb, E. Beregi, A. Watterich, and M. Tóth, Physica B **276-278**, 310 (2000).

[76] E. Beregi, E. Hartmann, L. Malicskó, and J. Madarász, Cryst. Res. Technol. **34**, 641 (1999).

[77] Á, Péter, K. Polgár, and E. Beregi, J. Cryst. Growth **209**, 102 (2000).

[78] A. Baraldi, R. Capelletti, N. Magnani, M. Mazzera, E. Beregi, and I. Földvari, J. Phys.: Condens. Matter **17**, 6245 (2005).

[79] G. W. Burdick and F. S. Richardson, Chem. Phys. **228**, 81 (1998).

[80] M. D. Faucher and O. K. Moune, Phys. Rev. A **55**, 4150 (1997).

[81] M. J. Weber, Handbook of Laser Science and Technology: Supplement 2, CRC, 1995.

[82] *IEEE standard on piezoelectricity: an American national standard*, Institute of Electrical and Electronics Engineers, 1988.

[83] R. Martínez Vázquez, R. Osellame, M. Marangoni, R. Ramponi, and E. Diéguez, Opt. Mater. **26**, 231 (2004).

[84] K. Wang, J. Zhang, J. Li, J. Wang, H. Zhang, C. Fang, X. Zhao, and Q. Zhang, J. Cryst. Growth **285**, 388 (2005).

[85] L. Kovács, M. Mazzera, E. Beregi, and R. Capelletti, Appl. Phys. B **94**, 273 (2009).

[86] G. Carini, private communication.

[87] M. Mazzera, A. Baraldi, R. Capelletti, E. Beregi, I. Földvári, phys. stat. sol. (c) **4**, 860 (2007).

[88] G. D. Jones and N. M. Strickland, J. Lumin. **102-103**, 166 (2003).

[89] E. P. Chukalina, M. N. Popova, E. Antic-Fidancev, and J. P. Chaminade, Phys. Lett. A **258**, 375 (1999).

[90] M. N. Popova, E. P. Chukalina, B. Z. Malkin, A. I. Iskhakova, E. Antic-Fidancev, P. Porcher, and J. P. Chaminade, Phys. Rev. B **63**, 075103 (2001).

[91] P. Goldner and O. Guillot-Noël, Mol. Phys. **102**, 1185 (2004).

[92] P. Goldner and O. Guillot-Noël, J. Alloys Compd. **451**, 682 (2008).

[93] S. Bertaina, S. Gambarelli, A. Tkachuk, I. N. Kurkin, B. Malkin, A. Stepanov, and B. Barbara, Nature Nanotec. **2**, 39 (2007).

[94] E. Fraval, M. J. Sellars, and J. J. Longdell, Phys. Rev. Lett. **95**, 030506 (2005).

[95] M. J. Weber, J. Lumin. **100**, 35 (2002).

[96] G. Blasse, Chem. Mater. **6**, 1465 (1994).

[97] C. W. E. van Eijk, Nucl. Instrum. Methods Phys. Res. A **460**, 1 (2001).

[98] E. Mones, I. Veronese, F. Moretti, M. Fasoli, G. Loi, E. Negri, M. Brambilla, N. Chiodini, G. Brambilla, and A. Vedda, Nucl. Instrum. Methods Phys. Res. A **562**, 449 (2006).

[99] E. Auffray, D. Bouttet, I. Dafinei, J. Fay, P. Lecoq, J. A. Mares, M. Martini, G. Mazé, F. Meinardi, B. Moine, M. Nikl, C. Pedrini, M. Poulain, M. Schneegans, S. Tavernier, and A. Vedda, Nucl. Instrum. Methods Phys. Res. A **380**, 524 (1996).

[100] S. Baccaro, R. Dall'Igna, P. Fabeni, M. Martini, J. A. Mares, F. Meinardi, M. Nikl, K. Nitsch, G. P. Pazzi, P. Polato, C. Susini, A. Vedda, G. Zanella, and R. Zannoni, J. Lumin. **87-89**, 673 (2000).

[101] A. Vedda, N. Chiodini, D. Di Martino, M. Fasoli, S. Keffer, A. Lauria, M. Martini, F. Moretti, G. Spinolo, M. Nikl, N. Solovieva, and G. Brambilla, Appl. Phys. Lett. **85**, 6356 (2004).

[102] J. A. Mares, M. Nikl, K. Nitsch, N. Solovieva, A. Krasnikov, and S. Zazubovich, J. Lumin. **94-95**, 321 (2001).

[103] Y. Kondo, K. Tanaka, R. Ota, T. Fujii, and Y. Ishikawa, Opt. Mater. **27**, 1438 (2005).

[104] I. R. Martín, J. Méndez-Ramos, F. Delgado, V. Lavín, U. R. Rodríguez-Mendoza, V. D. Rodríguez, and A. C. Yanes, J. Alloys Compd. **323-324**, 773 (2001).

[105] N. Chiodini, M. Fasoli, M. Martini, F. Morazzoni, E. Rosetta, R. Scotti, G. Spinolo, A. Vedda, M. Nikl, N. Solovieva, A. Baraldi, R. Capelletti, and R. Francini, Radiat. Eff. Defects Solids **158**, 463 (2003).

[106] A. Vedda, A. Baraldi, C. Canevali, R. Capelletti, N. Chiodini, R. Francini, M. Martini, F. Morazzoni, M. Nikl, R. Scotti, and G. Spinolo, Nucl. Instrum. Methods Phys. Res. A **486**, 259 (2002).

[107] A. Baraldi, R. Capelletti, N. Chiodini, C. Mora, R. Scotti, E. Uccellini, and A. Vedda, Nucl. Instrum. Methods Phys. Res. A **486**, 408 (2002).

[108] A. Vedda, N. Chiodini, D. Di Martino, M. Fasoli, F. Morazzoni, F. Moretti, R. Scotti, G. Spinolo, A. Baraldi, R. Capelletti, M. Mazzera, and M. Nikl, Chem. Mater. **18**, 6178 (2006).

[109] K. Saito and A. Ikushima, J. Appl. Phys. **91**, 4886 (2002).

[110] B. M. Tissue, Chem. Mater. **10**, 2837 (1998).

[111] D. Di Martino, A. Vedda, G. Angella, M. Catti, E. Cazzini, N. Chiodini, F. Morazzoni, R. Scotti, and G. Spinolo, Chem. Mater. **16**, 3352 (2004).

[112] A. Vedda, N. Chiodini, D. Di Martino, M. Fasoli, M. Martini, A. Paleari, G. Spinolo, M. Nikl, N. Solovieva, A. Baraldi, and R. Capelletti, phys. stat. sol. (c) **2**, 620 (2005).

[113] M. Fasoli, A. Vedda, A. Lauria, F. Moretti, E. Rizzelli, N. Chiodini, F. Meinardi, and M. Nikl, J. Non-Cryst. Solids **355**, 1140 (2009).

[114] A. Agarwal, K. M. Davis, and M. Tomozawa, J. Non-Cryst. Solids **185**, 191 (1995).

[115] K. M. Davis and M. Tomozawa, J. Non-Cryst. Solids **201**, 177 (1996).

[116] D. L. Ou and A. B. Seddon, J. Non-Cryst. Solids **210**, 187 (1997).

[117] P. Mazzoldi, A. Carnera, F. Caccavale, M. L. Favaro, A. Boscolo-Boscoletto, G. Granozzi, R. Bertoncello, and G. Battaglin, J. Appl. Phys. **70**, 3528 (1991).

[118] C. T. Kirk, Phys. Rev. B **38**, 1255 (1988).

[119] J. M. Luiz, J. R. Matos, I. Giolito, and M. Ionashiro, Thermochim. Acta **254**, 209 (1995).

[120] M. R. Davolos, S. Feliciano, A. M. Pires, R. F. C. Marques, and M. Jafelicci Jr., J. Solid State Chem. **171**, 268 (2003).

[121] D. Di Martino, N. Chiodini, M. Fasoli, F. Moretti, A. Vedda, A. Baraldi, E. Buffagni, R. Capelletti, M. Mazzera, M. Nikl, G. Angella, and C. B. Azzoni, J. Non-Cryst. Solids **354**, 3817 (2008).

[122] A. Vedda, N. Chiodini, M. Fasoli, A. Lauria, F. Moretti, D. Di Martino, A. Baraldi, E. Buffagni, R. Capelletti, M. Mazzera, P. Bohacek, and E. Mihokova, IEEE Transactions on Nuclear Science, accepted for publication.

[123] S. Brovelli, A. Baraldi, R. Capelletti, N. Chiodini, A. Lauria, M. Mazzera, A. Monguzzi, and A. Paleari, Nanotechnol. **17**, 4031 (2006).

[124] K. M. Davis, A. Agarwal, M. Tomozawa, and K. Hirao, J. Non-Cryst. Solids **203**, 27 (1996).

[125] N. D. Afify and G. Mountjoy, Phys. Rev. B **79**, 024202 (2009).

[126] M. Nogami and T. Hayakawa, Phys. Rev. B **56**, R14235 (1997).

[127] H. Amekura, N. Umeda, N. Okubo, and N. Kishimoto, Nucl. Instrum. Methods Phys. Res. B **206**, 1101 (2003).

[128] L. Zheng, G. Zhao, C. Yan, X. Xu, L. Su, Y. Dong, and J. Xu, J. Raman Spectrosc. **38**, 1421 (2007).

[129] J. R. Ferraro, J. J. Hazdra, and W. Boettner, J. Chem. Phys. **57**, 4540 (1972).

[130] W. B. Fowler, R. Capelletti, and E. Colombi, Phys. Rev. B **44**, 2961 (1991).

[131] Z. Y. Zhang, Phys. Lett. A **143**, 413 (1990).

[132] A. Borghesi, La spettroscopia a trasformata di Fourier in Spettroscopie e processi veloci nei semiconduttori, Scuola Nazionale del G.N.S.M., Castro Marina, 1990.

[133] R. J. Bell, *Introductory Fourier Transform Spectroscopy*, Academic Press, New York, 1972.

ACKNOWLEDGEMENTS

Thanks to:

- Prof. R. Capelletti, Prof. A. Baraldi, and Dr. M. Mazzera (University of Parma) for everything.
- Dr. N. Magnani (Institute for Transuranium Elements, Karlsruhe, Germany) for theoretical calculations.
- Prof. M. Tonelli and co-workers (University of Pisa) for supplying BaY_2F_8 samples.
- Prof. G. Carini and co-workers (University of Messina) for specific heat measurements.
- Prof. M. Bettinelli and co-workers (University of Verona) for supplying YPO_4 samples.
- Prof. J. Garcia Solé and co-workers (Universidad Autonoma de Madrid, Spain) for photoluminescence measurements.
- Dr. I. Földvari (Research Institute for Solid State Physics and Optics, Budapest, Hungary) for supplying $YAl_3(BO_3)_4$ samples.
- Prof. A. Vedda and co-workers (University of Milano-Bicocca) for supplying SiO_2 samples and TEM and EDS images.
- Prof. L. Cristofolini (University of Parma) for AFM measurements.

PUBLICATIONS

1. N. Magnani, A. Baraldi, E. Buffagni, R. Capelletti, M. Mazzera, S. Brovelli, and A. Lauria, *A Crystal-Field Study of Erbium Oxide and Fluoride*, phys. stat. sol. (c) **4**, 1209 (2007).
1. A. Baraldi, E. Buffagni, R. Capelletti, M. Mazzera, S. Brovelli, N. Chiodini, A. Lauria, F. Moretti, A. Paleari, and A. Vedda, *FTIR Spectroscopy to Investigate the Role of Fluorine on the Optical Properties of Pure and Rare Earth-doped Sol-gel Silica*, J. Non-Cryst. Solids **353**, 564 (2007).
2. R. Capelletti, A. Baraldi, E. Buffagni, N. Magnani, and M. Mazzera, *Chapter 1 – Rare earths as a probe of environment and electron-phonon interaction in optical materials: high resolution absorption spectroscopy and theoretical analysis*, in *Rare earths: Research and Applications*, ed. Keith N. Delfrey, Nova Science Publishers, New York, 2008, pp. 25-77 (ISBN 978-1-60456-218-7).
3. D. Di Martino, N. Chiodini, A. Fasoli, F. Moretti, A. Vedda, A. Baraldi, E. Buffagni, R. Capelletti, M. Mazzera, M. Nikl, G. Angella, and C. B. Azzoni, *Gd-incorporation and luminescence properties in sol-gel silica glasses*, J. Non-Cryst. Solids **354**, 3817 (2008).
4. N. Magnani, R. Caciuffo, E. Colineau, F. Wastin, A. Baraldi, E. Buffagni, R. Capelletti, S. Carretta, M. Mazzera, D. T. Adroja, M. Watanabe, and A. Nakamura, *Low-energy spectrum of a Tm-based double-decker complex*, Phys. Rev. B **79,** 104407 (2009).

5. A. Baraldi, E. Buffagni, R. Capelletti, M. Mazzera, N. Magnani, G. Carini Jr., and G. D'Angelo, *Hindered rotations probed by rare earths in crystals:* Er^{3+} *and* Tm^{3+} *in* BaY_2F_8, Phys. Rev. B **80**, 155121 (2009).
6. R. Capelletti, A. Baraldi, E. Buffagni, N. Magnani, and M. Mazzera, *Rare earth crystal field spectra as a probe of librational motions in* BaY_2F_8 *solid state laser crystals*, J. Phys.: Conf. Ser., accepted for publication.
7. R. Capelletti, A. Baraldi, E. Buffagni, M. Mazzera, N. Magnani, E. Martin Rodriguez, J. Garcia Sole, and M. Bettinelli, *Optical spectroscopy of* YPO_4 *single crystals doped with* Ho^{3+}, *Spectroscopy of Lanthanide Materials II,* Special Edition of Spectroscopy Letters, accepted for publication.
8. A. Vedda, N. Chiodini, M. Fasoli, A. Lauria, F. Moretti, D. Di Martino, A. Baraldi, E. Buffagni, R. Capelletti, M. Mazzera, P. Bohacek, and E. Mihokova, *Evidences of rare-earth nanophases embedded in silica using vibrational spectroscopy*, IEEE Transactions on Nuclear Science, accepted for publication.